ISOSPIN MIXING IN LIGHT NUCLEI

by

John Franklin Wilkerson

A dissertation submitted to the faculty of The University of North Carolina at Chapel Hill in partial fulfillment of the requirements for the degree of Doctor of Philosophy in the Department of Physics and Astronomy.

Chapel Hill

1982

Approved by:

_____
Advisor

_____
Reader

_____
Reader

JOHN FRANKLIN WILKERSON. Isospin Mixing in Light Nuclei. (Under the direction of EDWARD J. LUDWIG.)

Abstract

Isospin mixing in light nuclei has been directly studied through isospin-forbidden resonances corresponding to high-lying T=3/2 states in A=4n+1, T_z=-1/2 nuclei.

High-lying T=3/2 states in A=25, 29, 33, and 37, T_z=|1/2| nuclei were identified by the isospin-allowed (p,t) and (p,^{3}He) reactions at a single angle with an incident proton energy of 42.4 MeV. Comparisons of angular distributions measured at 60 MeV for ^{27}Al(p,t)^{25}Al, ^{27}Al(p,^{3}He)^{25}Mg, ^{31}P($\vec{p}$,t)^{29}P, and ^{31}P($\vec{p}$,^{3}He)^{29}Si were used to assign T=3/2 levels in the A=25 and A=29, T_z=|1/2| nuclei.

A measurement system utilizing a high-resolution polarized proton beam was developed at Triangle Universities Nuclear Laboratory to measure ($\vec{p}$,p) scattering over isospin-forbidden resonances. The polarized-beam energy excitation functions were analyzed to extract all resonance parameters from the results of a single experiment. A system was developed to measure directly the beam energy spread. Parameters for several previously studied first T=3/2 resonances in the A=4n+1, T_z=-1/2 nuclei were remeasured to confirm the validity of our new measurement and analysis techniques. High-lying T=3/2 isospin-forbidden resonances in ^{17}F, ^{25}Al, ^{29}P, ^{33}Cl, and ^{37}K were studied and proton elastic-scattering reduced widths were extracted by a model-independent helicity amplitude analysis. The results of the present study indicate that the

isospin mixing in a given nucleus does not increase monotonically with increasing excitation energy. The present study, in conjunction with previous work, indicates that the isospin mixing exhibits a smooth dependence with mass number A and is largely independent of nuclear structure. There is an oscillation of period A=8 displayed by the average T=3/2 reduced widths and the first T=3/2 state reduced widths and by the average reduced widths for each nucleus. This behavior is not explained by conventional isospin-mixing mechanisms.

Acknowledgments

I would first like to express special appreciation to my advisor, Dr. Ed Ludwig, for the continued encouragement, support, and enthusiasm he has shown during the course of my studies. I also owe special thanks to Dr. Bill Thompson for his helpful ideas and discussions, along with his assistance in the analysis and interpretation of the data. I am very grateful for the help and advice Dr. Tom Clegg has given to me, and for the continued interest he has shown in my project. I would like to thank Ed, Bill, and Tom for their careful reading of this dissertation and for their helpful comments. Dr. Rick Anderson deserves thanks for his assistance during the experiments and for the helpful discussions and ideas he offered. I am privileged to have been able to work in such an enjoyable and productive environment.

I appreciate the help given during the many experiments taken at TUNL and value the friendship of fellow students Barry Burks, Dr. Steve Tonsfeldt, and Robert Varner. I would also like to thank Chris Westerfeldt for his useful ideas and his continual efforts to upgrade and keep the TUNL high-resolution system in good working order. I am indebted to Dr. Dick Purser for his helpful discussions and ideas, and for his collaboration in the beam resolution experiments.

I am grateful to Dr. Will Jacobs for his advice and for his help in making the measurements at Indiana. The help of fellow collaborators Dr. H. Nann and Dr. Y. Aoki, and the support of the entire IUCF staff made this experiment very successful. I would like to thank Dr. Dick Kouzes and the Princeton cyclotron staff for their efforts in making the

experiment at Princeton possible, along with Dr. Y. Tagishi who helped with the measurements. The work at IUCF and Princeton was supported in part by the National Science Foundation.

Thanks go to Sidney Edwards, Paul Carter, and Bob Rummel at TUNL for their efforts to keep the lab functioning and also for time spent in implementing various projects. The beam resolution experiments would have not been possible without the invaluable advice and help of Al Lovette and the craftsmanship of Bob Hogan of the TUNL instrument shop. Thanks also to Ralph Lewter and the UNC instrument shop for their contributions to various projects. I would like to acknowledge the excellent preparation of figures by Mrs. D. (Mike) Bailey and the photographic work of Ron Nelson. I also appreciate the support given this project by Dr. Ed Bilpuch, the laboratory director. This dissertation was supported in part by the Department of Energy.

Finally, I would like to thank my parents for their support and encouragement. I would especially like to thank my wife Millicent for her continued patience and help during the writing of this dissertation. Her assistance during the final preparation was invaluable to me.

TABLE OF CONTENTS

1. Introduction 1

1.1 Overview 1

1.1.1 Isospin Mixing Observed by First T=3/2 State Decays . . . 4

1.1.2 Isospin Mixing Observed by First T=2 State Decays 8

1.1.3 Previous Conclusions on Isospin Mixing Obtained from the T=3/2 and T=2 Measurements 8

1.2 Statement of Dissertation Purpose 10

1.3 Measurement Techniques and Requirements 11

1.4 Outline of Dissertation Presentation 13

2. Location and Identification of T=3/2 States 15

2.1 Introduction 15

2.2 Identification of the Lowest T=3/2 States 16

2.3 Previous Results 19

2.4 Transfer Reactions 19

2.4.1 (p,t) and (p,^{3}He) Two-Nucleon Transfer Reactions 26

2.4.2 Theory 27

2.4.3 Experimental Considerations 32

2.5 Energy-Excitation Functions 35

2.5.1 (p,γ) Reaction 36

2.5.2 (p,p) Reaction 37

2.6 Summary of Techniques 41

3. (p,t) and (p,^{3}He) Measurements - Princeton 43

3.1 Introduction 43

3.2 Experiment--Targets 44

3.3 Experiment--Setup 49

3.4 Experiment--Analysis 51

3.5 Measurements - Calibration Reactions 52

3.5.1 States in ^{25}Al and ^{25}Mg 54

3.5.2 States in ^{29}P and ^{29}Si 61

3.5.3 States in ^{33}Cl and ^{33}S 62

3.5.4 States in ^{37}K and ^{37}Ar 75

3.6, Summary 81

4. (p,t) and (p,^{3}He) Measurements - Indiana 83

4.1 Introduction 83

4.2 Experiment--Targets 84

4.3 Experiment--Setup and Data Acquisition 86

4.4 Experiment--Analysis 92

4.5 Experiment--Measurements 99

4.5.1 States in ^{25}Al and ^{25}Mg 101

4.5.2 States in ^{29}P and ^{29}Si 108

4.6 Summary of IUCF Results 124

4.7 Summary of (p,t) and (p,^{3}He) Measurements 127

5. Introduction to High-Resolution ($\vec{p}$,p) and (p,p) Investigations 128

5.1 Description of T=3/2 Isospin-Forbidden Resonance Measurements 128

5.1.1 Relationship of Resonance Parameters and Isospin Admixtures 128

5.1.2 Measurement Techniques Used to Extract the Resonance Parameters 131

5.1.3 A Single Measurement Technique to Extract Resonance Parameters 134

5.2 Overview of Present High-Resolution Measurements 136

5.3 Outline of High-Resolution Measurements Presentation 136

5.4 Review of Previous T=3/2 Resonance Measurements 136

5.4.1 High-lying T=3/2 States in ^{13}N 137

5.4.2 High-lying T=3/2 States in ^{17}F 138

5.4.3 High-lying T=3/2 States in ^{21}Na 141

5.4.4 High-lying T=3/2 States in ^{25}Al 141

5.4.5 High-lying T=3/2 States in ^{29}P 142

5.4.6 High-lying T=3/2 States in ^{33}Cl 142

5.4.7 High-lying T=3/2 States in ^{37}K 143

6. $(\vec{p},p)$ and (p,p) Investigations - Analysis 144

6.1 Introduction 144

6.2 (p,p) Resonance Analysis Methods 144

6.2.1 Helicity Amplitude Analysis Method 146

6.2.2 Inclusion of Energy Resolution Parameters 148

6.2.3 The Grid-Search Calculations 148

6.3 Resolution Effects 151

6.3.1 Energy Straggling 153

6.3.2 Incident Beam Resolution 159

6.3.3 Target Doppler Broadening 161

6.3.4 Atomic-Excitation Effects 169

6.4 Analysis Codes and Method 169

6.4.1 Preliminary Data Analysis 170

6.4.2 Resolution Calculations 173

6.4.3 Helicity Amplitudes Analysis Code - T32GRD 173

6.5 T32GRD Fitting Analysis Procedures 177

6.6 Determination of Resonance Parameters and Estimation of Errors 179

6.7 Test and Assessment of Analysis Methods 180

7. $(\vec{p},p)$ and (p,p) Investigations - High-Resolution Beams 184

7.1 Introduction 184

7.2 TUNL High-Resolution Beam Transport 185

7.3 High-Resolution Beam Energy Regulation 186

7.4 High-Resolution Polarized Beams. 192

7.5 Monitoring High-Resolution Performance 201

7.6 Summary 206

8. $(\vec{p},p)$ and (p,p) Investigations - Direct Beam Resolution Measurements 207

8.1 Introduction 207

8.2 Measurement Principle 208

8.3 System Design 213

8.3.1 Analyzing Magnet 214

8.3.2 Object Slit SL1 and Acceptance Slit SL2 221

8.3.3 Total Beam Phase Space Sampling 223

8.3.4 The Image Slit 228

8.3.5 Beam Position Scanning at the Image Slit 231

8.4 Ideal Experimental Measurement Procedures. 231

8.5 Actual Measurement Procedures. 233

8.6 Measurement Results 236

8.7 Summary and Recommendations 244

9. $(\vec{p},p)$ and (p,p) Investigations - Magnet Analyzing System Calibration 246

9.1 Introduction 246

9.2 Experimental Setup 247

9.3 Experimental Techniques 250

9.3.1 Consistent Beam Transport Procedures 250

9.3.2 Monitoring Procedures 252

9.3.3 Data Acquisition Methods 252

9.3.4 Target Preparation 254

9.4 Results of Calibration Measurements 255

9.4.1 Analysis of (p,n) Threshold Data 255

9.4.2 The (p,p) Resonance Analysis 263

9.4.3 Error Estimation 265

9.4.4 Magnet Analysis System Calibration 267

9.5 Discussion and Summary 268

10. $(\vec{p},p)$ and (p,p) Investigations - Experiments 271

10.1 Introduction 271

10.2 Targets and Target Preparation 271

10.3 Beamline and Chamber Setup and Geometry 277

10.4 Measurement Procedures 280

10.5 Data Acquisition 281

11. $(\vec{p},p)$ and (p,p) Data I. - A = 13, 17, 25 285

11.1 Introduction 285

11.2 First T=3/2 Resonance in ^{13}N 288

11.3 First T=3/2 Resonance in ^{17}F 291

11.4 Second T=3/2 Resonance in ^{17}F 294

11.5 First T=3/2 Resonance in ^{25}Mg 294

11.6 Second T=3/2 Resonance in ^{25}Mg 299

11.7 Higher T=3/2 Resonances in ^{25}Mg 302

11.8 Summary of A=13, 17, and 25 306

12. $(\vec{p},p)$ and (p,p) Data II. - A = 29 307

12.1 Introduction 307

12.2 First T=3/2 Resonance in ^{29}P 307

12.3 Second T=3/2 Resonance in ^{29}P 310

12.4 Search for the Third T=3/2 Resonance in ^{29}P 313

12.5 Fourth T=3/2 Resonance in ^{29}P 319

12.6 Sixth T=3/2 Resonance in ^{29}P 319

12.7 Seventh T=3/2 Resonance in ^{29}P 322

12.8 Summary of A=29 Measurements 322

13. $(\vec{p},p)$ and (p,p) Data III. - A = 33 and 37 329

13.1 Introduction 329

13.2 First T=3/2 Resonance in ^{33}Cl 329

13.3 Second T=3/2 Resonance in ^{33}Cl 332

13.4 Third T=3/2 Resonance in ^{33}Cl 334

13.5 Higher T=3/2 Resonances in ^{33}Cl 339

13.6 First T=3/2 Resonance in ^{37}K 339

13.7 Second T=3/2 Resonance in ^{37}K 342

13.8 Third T=3/2 Resonance in ^{37}K 347

13.9 Summary of Measurements 347

14. Isospin Mixing and Proton Reduced Widths 348

14.1 Introduction 348

14.1.1 Isospin-Mixing Mechanisms 348

14.1.2 Isospin-Mixing Interactions 349

14.1.3 Isospin-Mixing Calculations 351

14.2 Systematic Behavior of Reduced Widths 354

14.2.1 Comparison of A-Dependences of Reduced Widths 355

14.2.2 Comparison of A-Dependences of Average Reduced Widths 359

14.2.3 Comparison of Excitation-Energy Dependences of Reduced Widths 362

14.2.4 Comparison of Spin and Parity Dependences of Reduced Widths 370

14.3 Summary of Observed T=3/2 States Reduced Widths Behavior . . 370

14.4 Conclusion on Isospin Mixing 380

15. Recommendations and Summary 383

15.1 Suggestions for Theoretical Investigations 383

15.2 Suggestions for Future Experimental Investigations 385

15.3 Summary 388

Appendix A 390

Appendix B 393

References 395

1. Introduction

1.1 Overview. The concept of isospin, in which the proton and neutron are described as different states of the same particle, has proven to be very fruitful in understanding nuclear structure. Isospin was first introduced by Heisenberg [Hei32]. Although the charge dependence of the Coulomb interaction breaks isospin symmetry, the general charge independence of the strong (hadronic) force is vividly illustrated when examining the nuclear level structures of isobaric multiplets. A fundamental question of nuclear physics is: "To what extent is the observed isospin symmetry breaking caused by the Coulomb force and to what extent is it caused by the strong force?"

The strength of the Coulomb interaction has made the search for an answer to this question very difficult. Many experiments have been performed to study charge independence and charge symmetry of nuclear forces. Charge independence states that the pp np and nn forces are equal to each other, while charge symmetry is the weaker statement that pp and nn forces are identical. A general review of these experiments and their consequences can be found in [Hen69, Bli73, Hen79]. Thus far, all observed isospin impurities of nuclear states can be attributed to the Coulomb interaction [Ber72].

A brief review of isospin formalism and nomenclature is necessary to understand some of the terms and concepts used in this chapter and

the following chapters. The isospin projection of a nucleus is $T_z=\frac{1}{2}(N-Z)$, where N is the number of neutrons and Z is the number of protons. (Sometimes T_z is referred to as T_3, and in high energy physics the sign convention may be reversed.) From the definition of T_z, it should be clear that different T_z values correspond to different nuclei. For most nuclei the ground state total isospin T is equal to T_z. Isospin formalism uses the same spin algebra introduced by Pauli for angular momentum calculations, except that the operators are in charge space.

An isospin multiplet is defined as a series of nuclei with the same number of total nucleons A and total isospin T, that has 2T + 1 isospin projections T_z. If there were no charge dependent forces, then the energy levels of the isospin projection states would be identical. However, the Coulomb force displaces the levels. For example, the A=13, T=3/2 isospin multiplet members are ^{13}B ($T_z=+3/2$), ^{13}C ($T_z=+1/2$), ^{13}N ($T_z=-1/2$), and ^{13}O ($T_z=-3/2$). In the $T_z=|3/2|$ isospin multiplet members, the lowest nuclear levels correspond to total isospin T=3/2 levels. However, in the $T_z=|1/2|$ isospin multiplet nuclei, the lowest energy levels correspond to total isospin T=1/2 states. The total isospin T=3/2 levels occur at high excitation energies in the $T_z=|1/2|$ nuclei. The first T=3/2 levels occur at 5-15 MeV for the A=4n+1, $T_z=|1/2|$ ($9 \leq A \leq 41$) isospin multiplets. Levels in a nucleus with total isospin greater than the ground state total isospin are referred to as $T_>$ (T upper) states while the nuclear levels with the same isospin as the target nucleus are called $T_<$ (T lower) states. A more complete introduction to isospin in nuclear physics can be found in most graduate level nuclear physics texts [Fra74, Pre75]. A comprehensive review of

isospin in nuclear physics is given in [Wil69].

A direct method to measure isospin admixtures in light nuclei is the observation of isospin-forbidden particle decays of $T_>$ states in $T_<$ nuclei. The isospin mixing is characterized by the total decay width Γ of the $T_>$ state and partial decay widths corresponding to decay of energetically allowed but isospin-forbidden states. The widths observed for the isospin-forbidden particle decays are a measure of the isospin admixtures in these nuclear states. It is possible for these isospin admixtures to be in the compound nucleus state, the state of the decaying particle, the final state, or any combination of these three states.

Observation of the decay of T=3/2 states in A=4n+1, $T_z=|1/2|$ nuclei or the decay of T=2 states in A=4n, $T_z=0$ nuclei, are two of the best experimental methods available to study isospin mixing. The only isospin-allowed decay channels for the first T=3/2 states in the A=4n+1 nuclei or the first T=2 states in the A=4n nuclei are the electromagnetic γ-decays. These decay channels are very weak, with decay widths of only a few eV. The observed decay widths for the measured T=3/2 and T=2 states are 40 eV to several keV. Thus, the total decay widths and partial decay widths of these first T=3/2 or T=2 states are dominated by the isospin-forbidden particle decays. Measurement of these widths yields a very sensitive test of the isospin mixing of these states.

Systematic measurements of the decay of the first T=3/2 states in A=4n+1 nuclei (for $9 \leq A \leq 41$) and of the lowest T=2 states in A=4n

nuclei (for $8 \leq A \leq 44$) have been performed [Ade73, Fre76, Iko76, McD76]. The current research was motivated by the results from some of these measurements.

1.1.1 Isospin Mixing Observed by First T=3/2 State Decays. The isospin-forbidden proton decay of the first T=3/2 states in A=4n+1, $T_z=-1/2$ nuclei to the ground state of the corresponding A=4n, $T_z=0$ final state nuclei have been observed for the T=3/2 states in A=4n+1 nuclei for $9 \leq A \leq 41$. A summary of these measurements is given in [Iko76]. The isospin mixing of these decays is characterized by the reduced elastic proton width $\gamma^2_{p_o}$. The reduced width is defined as

$$\gamma^2_{p_o} = \frac{\Gamma_{p_o}}{2 \cdot P_c} \qquad 1\text{-}1$$

where the Coulomb penetrability P_c removes the angular momentum and kinematic factors from the partial width Γ_{p_o}. The reduced elastic proton width $\gamma^2_{p_o}$ represents the probability of decay of the T=3/2 state to the final A=4n ground state and hence is a measure of the overlap of the analog T=3/2 state and final target T=0 state wave functions. The overlap of the wave functions results from isospin admixtures in one or more of these states.

The results of the reduced proton widths for the first T=3/2 state elastic proton decays are presented in Fig. 1-1. The reduced widths are plotted versus the mass number A of the final A=4n $T_z=0$ states. The observation of most of these widths is accomplished by (p,p) elastic scattering on A=4n self-conjugate target nuclei. The isospin-forbidden

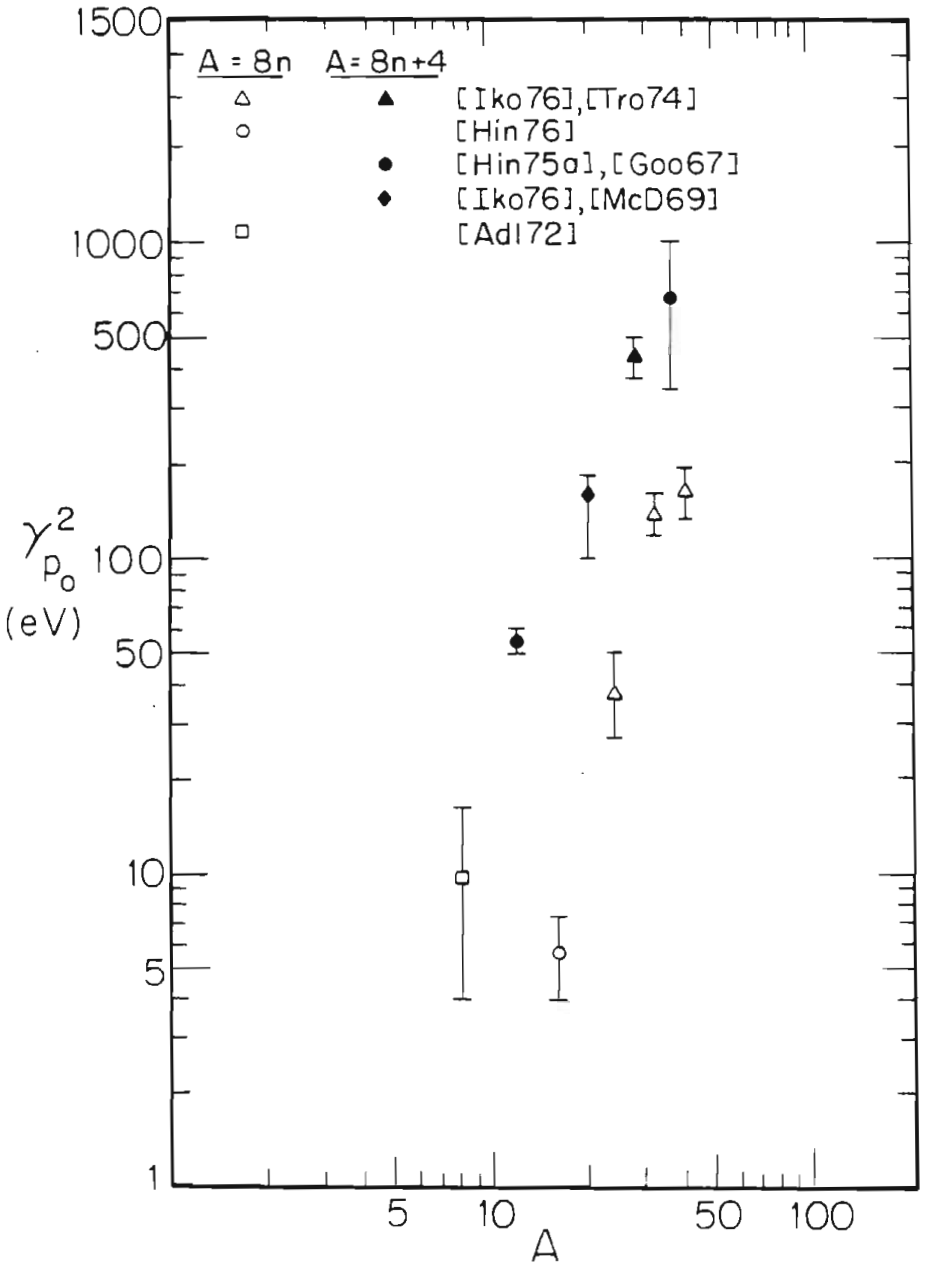

Figure 1-1 The reduced proton widths $\gamma^2_{p_o}$ for the p_o decays of the first T=3/2 states in A=4n+1 T_z=-1/2 nuclei to the T_z=0 A=4n ground states are plotted versus mass number A. The oscillation of the reduced widths for A=8n (open points) and A=8n+4 (solid points) target nuclei is apparent. See Table 1-1 for sources.

T=3/2 resonances and corresponding proton partial widths are obtained by measuring (p,p) energy excitation functions. The details of how these measurements are made will be described in later chapters. The resonance parameters of these first T=3/2 states are presented in Table 1-1.

The general trend of the increasing elastic proton reduced widths with increasing A is expected from isospin mixing models [MDo60, Ari71, Aue71, Lev73, Ber72]. However, the magnitudes of the reduced widths are overestimated. The ratio of the measured reduced widths γ_p^2 divided by the predicted reduced widths $\gamma_{s.p.}^2$ calculated using the extreme single particle model is $\sim 10^{-4}$. This ratio indicates that the isospin admixtures only contribute $\sim 10^{-2}$ to the wave function amplitudes. The systematic A=8n period oscillation exhibited by the reduced widths of A=8n to A=8n+4 final state nuclei is not explained by any model.

Other information relevant to determining the source of isospin mixing can come from the decay of T=3/2 states in T_z=-1/2 nuclei to excited states of the residual nuclei and from the neutron decay of the T=3/2 states in T_z=+1/2 nuclei. Measurements for some of the inelastic proton decay channels for these same first T=3/2 states have been measured [McD76]. A comparison of the decays of the lowest 2^+ inelastic levels for the same T=3/2, A=4n+1 T_z=-1/2 nuclei does not reveal any oscillation between the A=8n+4 and A=8n final state nuclei.

The neutron decay of the T_z=+1/2, T=3/2 states (the mirror states of the T_z=-1/2 T=3/2 states) have been observed for A=4n+1 nuclei for $A \leq 25$ [McD76, Wei76, Hin81]. The lowest T=3/2 states in T_z=+1/2 nuclei are neutron bound for $A > 25$, and hence no neutron decays will be

Table 1-1 Decay Parameters for the First T=3/2 States in A=4n+1 T_z=-1/2 Nuclei as Determined Previous Measurements.

A=4n T_z=0	A=4n+1 T_z=-1/2	J^π	E_x (MeV)	Γ (eV)	Γ_p (eV)	γ_p^2 [a] (eV)
^{8}Be	^{9}B	$3/2^-$	14.6550 ± .0025 [b]	275 ± 93	30 ± 17 [f]	10 ± 6
^{12}C	^{13}N	$3/2^-$	15.0645 ± .0002 [c]	1100 ± 90	210 ± 11 [g]	55 ± 3
^{16}O	^{17}F	$1/2^-$	11.1933 ± .0023 [d]	200 ± 40	19 ± 3 [d]	12 ± 5
^{20}Ne	^{21}Na	$5/2^+$	8.973 ± .003 [e]	750 $^{+\ 50}_{-\ 250}$	150 $^{+\ 10}_{-\ 50}$ [h]	165 $^{+\ 13}_{-\ 65}$
^{24}Mg	^{25}Al	$5/2^+$	7.901 ± .002 [e]	155 ± 50	26 ± 9 [a]	38 ± 13
^{28}Si	^{29}P	$5/2^+$	8.379 ± .003 [e]	360 ± 50	300 ± 40 [a]	435 ± 60
^{32}S	^{33}Cl	$1/2^+$	5.544 ± .001 [e]	115 ± 15	115 ± 15 [a]	140 ± 20
^{36}Ar	^{37}K	$3/2^+$	5.047 ± .003 [e]	40 ± 20	40 ± 20 [i]	680 ± 340
^{40}Ca	^{41}Sc	$3/2^+$	5.940 ± .004 [e]	55 ± 5	55 ± 5 [j]	165 ± 30

a) [Iko76] b) [Ajz79] c) [Hue74] d) [Hin76] e) [End78]

f) [McD76] g) [Hin75a] h) [McD69] i) [Goo67] j) [Tra74]

observed for these states. There is no observed oscillation of neutron reduced widths between the A=8n and A=8n+4 target nuclei, for which neutron decay can be observed. However, the widths of these resonances are approximately an order of magnitude larger than those for the T_z=-1/2 mirror decays.

1.1.2 Isospin Mixing Observed by First T=2 State Decays. A comprehensive study of p_o and p_1 proton decays and α_0 and α_1 decays of the lowest T=2 states occurring in A=4n nuclei was performed [Fre79]. The reduced widths of the T=2 elastic proton p_o decays were similar in size to the T=3/2 p_o reduced widths. Both the p_o and α_0 reduced widths may exhibit an oscillatory behavior between the A=8n and A=8n+4, T=2 states. However, the large error bars on some of the reduced width values make it impossible to make a definite conclusion on the periodic behavior.

1.1.3 Previous Conclusions on Isospin Mixing Obtained from the T=3/2 and T=2 Measurements. A variety of conclusions have been reached from an examination of the reduced width information extracted from the combined T=3/2 and T=2 measurements and from prior calculations of isospin mixing. A summary of these conclusions follows:

(1) Both the T=3/2 and T=2 reduced widths are in general smaller than the widths predicted by theory [Iko76, Fre79].

(2) The systematic behavior with mass of the reduced widths indicates that the mixing is not primarily a result of chance admixtures of $T_>$ states with nearby $T_<$ states of the same J^π.

(3) The similarity of magnitude and slopes of the reduced widths as a

function of mass number for both the T=2 and T=3/2 states indicates that a general isospin mixing mechanism is present in the light nuclei, independent of gross nuclear structure effects such as shell closure.

(4) There is no explanation for the A=8n periodic behavior exhibited by the first T=3/2 p_o decays.

(5) The difference in magnitude of reduced widths for the T=3/2 A=4n+1, T_z=-1/2 and T_z=+1/2 decays requires isotensor (two-body) as well as isovector mixing [McD78].

(6) The isospin-mixing mechanisms for mixing with the antianalog state in the compound nucleus or mixing with the monopole compound state involve very small isotensor terms [McD78].

(7) The difference in magnitude of reduced widths for the T=3/2, A=4n+1 T_z=-1/2 and T_z=+1/2 decays implies that the isospin mixing is not dominated by the A=4n final nucleus contributions [McD76].

(8) The lack of periodic behavior displayed by the reduced widths of the T=3/2 state decays to the lowest 2^+ states may indicate that the oscillation of the reduced widths does not result directly from isospin mixing , but results from the nuclear structure of the T=3/2 states and target A=4n ground states [McD76].

The conclusions numbered 1 through 6 above are strongly supported by the accumulated experimental evidence. However, the conclusions reached in 7 and 8 are less well supported.

The experimental evidence and the above list of conclusions raise several questions:

(1) Where is the isospin mixing taking place and what are the

dominant mechanisms?

(2) How does the isospin mixing change as a function of excitation energy in a particular nucleus?

(3) To what extent is the periodic behavior displayed by the T=3/2 p_o reduced widths due to nuclear structure?

(4) Can the magnitude of the T=3/2 or T=2 reduced widths be described by nuclear structure, such as shell model arguments?

(5) Does this periodic behavior indicate a charge dependence of the nuclear force?

An experimental method to probe these questions is to study isospin-forbidden formation and decay of high-lying T=3/2 states in the same A=4n+1 or A=4n nuclei as were studied for the first isospin-forbidden states. However, since the A=8n periodic behavior is strongly displayed by the T=3/2 states in the T_z=-1/2 nuclei, the logical course of study would be to examine the higher T=3/2 states.

1.2 Statement of Dissertation Purpose. The intent of this dissertation is to perform a systematic study of high-lying T=3/2 states in T_z=-1/2 A=4n+1 nuclei. The purpose of this study is twofold: 1) To attempt to determine the isospin mixing mechanisms involved in light nuclei, and 2) To see if the periodic behavior exhibited by the decay of the first T=3/2 to the A=4n p_o levels persists in the higher T=3/2 p_o decays.

Measurements of the resonance properties of the second T=3/2 states in several of the A=4n+1 nuclei were made to study the possible periodic behavior of p_o reduced widths. In an attempt to deduce possible

isospin mixing dependences, measurements of resonance parameters of many high-lying T=3/2 states in the same T_z=-1/2 nucleus were also performed for several A=4n+1 nuclei. The contributions of different isospin mixing mechanisms to the total isospin admixtures should change with increasing excitation energy in the T_z=-1/2 nucleus.

1.3 Measurement Techniques and Requirements. Before discussing the techniques required to measure the resonance properties of higher-lying T=3/2 states, it is useful to review the techniques used to measure the first T=3/2 states. The extraction of the reduced widths for the lowest T=3/2 states in T_z=-1/2 nuclei was performed by measuring (p,p) energy excitation functions, except for the A=9 decay which was observed by other means [McD76a, Ad171, Ad172, Ber73]. The observation of the isospin-forbidden resonances which have very narrow widths required making measurements with high incident beam energy resolution. An incident beam energy spread comparable to the resonance width (~ 500 eV) was necessary. Finding the energy location of these weak first T=3/2 resonances was not a problem, because the location of these T=3/2 states had been determined from super-allowed β^+-delayed proton decay measurements (see Table 2-1 for references). These β^+-delayed proton decay measurements had the further advantage of uniquely identifying the isospin of the T=3/2 levels. The observation of a narrow resonance does not identify the isospin of the resonance.

However, the measurement of (p,p) excitation functions alone was not sufficient to extract both the resonance total width and partial width. The branching ratios Γ_p / Γ for the decay of these first T=3/2

states to the p_o channel had been determined by other measurement techniques (see Table 2-1 for references). The combination of the (p,p) measurements and the branching ratios allowed extraction of the reduced proton widths γ_p^2.

The measurements of the high-lying T=3/2 states performed in the present research required the same high-resolution techniques as the measurements of the first T=3/2 resonances with three additional complications:

(1) The locations of the high-lying T=3/2 states in the A=4n+1 nuclei were known for only a few nuclei. The energy determination for most of these known states was accurate to only ~ 50 keV.

(2) There is no distinct β^+-delayed proton decay signature for the high-lying states which can be used to determine their isospin (see Chapter 2).

(3) The branching ratios for the high-lying T=3/2 states are not available for the few high-lying T=3/2 states which had been identified (see Chapter 2), thus the (p,p) measurements alone are insufficient to determine the reduced widths.

To overcome these complications in the systematic study of isospin mixing performed in the present research, the following experimental techniques were developed and used:

(1) and (2) The (p,t) and (p,^{3}He) reaction measurements were used to locate and identify the T=3/2 states.

(3) New polarized beam high-resolution ($\vec{p}$,p) measurement techniques and analysis codes were developed which allowed the complete

determination of the resonance parameters, including the determination of the branching ratio. Thus, the reduced proton widths could be extracted from a single measurement.

1.4 Outline of Dissertation Presentation. In order to locate, identify, and measure the reduced widths of the high-lying T=3/2 states it was necessary to use a variety of nuclear measurement and analysis techniques. The dissertation can be divided into three principal parts describing the techniques used and results achieved.

The first part details the measurements used to locate and identify the T=3/2 states. The previously identified high-lying T=3/2 states and a review of the available measurement techniques used to locate and identify T=3/2 levels in $T_z=|1/2|$ nuclei are explained in Chapter 2. The (p,t) and (p,^{3}He) results from measurements at the Princeton University cyclotron and at the Indiana University Cyclotron Facility are presented in Chapters 3 and 4, respectively.

The second part of the dissertation deals with the high-resolution (p,p) and ($\vec{p}$,p) measurements performed at Triangle Universities Nuclear Laboratory (TUNL). A review of the previous measurements of high-lying T=3/2 states, and an explanation of the experimental techniques involved in measuring high-resolution resonances are covered in Chapter 5. The necessary analysis methods to extract the reduced widths are then discussed in Chapter 6. Chapters 7, 8, 9, and 10 explain the high-resolution measurement hardware and experimental details. The data from the (p,p) and ($\vec{p}$,p) measurements are given in Chapters 11, 12 and 13.

The final part (Chapters 14 and 15) presents a summary of the current models of isospin mixing along with a compilation of the extracted high-lying T=3/2 state reduced widths. The results of the systematic behavior exhibited by the high-lying T=3/2 states' reduced widths are discussed in context with the current mixing models, along with implications for future theoretical and experimental work.

2. Location and Identification of T=3/2 States

2.1 Introduction. In order to perform a systematic study of isospin-mixing for T=3/2 states in A=4n+1 nuclei, it is necessary to locate and identify positively the T=3/2 states in an efficient manner. This identification is made difficult by the large number of surrounding T=1/2 levels in the $T_z=|1/2|$ nuclei; these occur in the same region of excitation energies as the T=3/2 states. The density of T=1/2 levels is high because the T=3/2 states of interest occur in the A=4n+1 compound nucleus at excitation energies ranging from 5 to 12 MeV. The typical level spacing of states at these energies is ~ 45 to 70 keV, as calculated using the program LEVD based on Gilbert and Cameron level densities [Gil65]. There are several methods available to identify T=3/2 levels in $T_z=-1/2$ nuclei. This chapter will review these methods and discuss the relative merits and faults of each. The following two chapters will then discuss the measurements performed to locate T=3/2 levels.

2.2 Identification of the Lowest T=3/2 States. For the lowest T=3/2 levels in these $T_z=-1/2$ nuclei, the isospin identification can be accomplished by observing the β^+-delayed proton decay; a $T_z=-3/2$ parent ground-state β^+ decays to its $T_z=-1/2$, T=3/2 daughter state which then proton decays (isospin-forbidden) to a $T_z=0$ nucleus [Ear74]. Figure 2-1 shows an example of this transition in the A=29 isobaric multiplet.

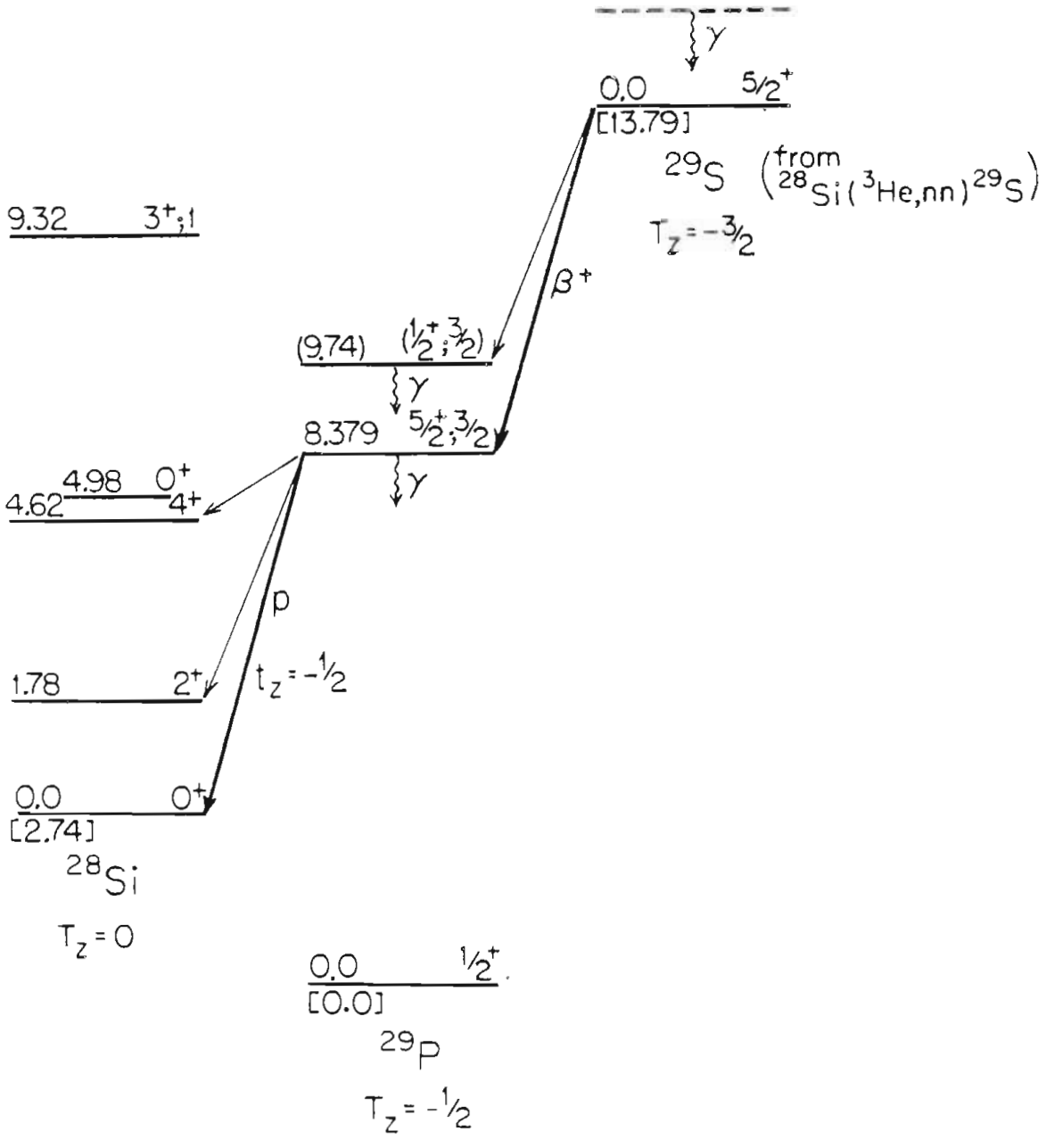

Figure 2-1 Level diagram showing β^+-delayed proton decay transition for A=29 system.

Because the lowest T=3/2 state in the T_z=-1/2 nucleus has the same total isospin and J^π as the parent state, this β^+-decay goes predominantly by a super-allowed Fermi transition, where a pure Fermi decay transition has $\Delta T=0$, $\Delta J=0$, and $\Delta\pi=0$. Calculation of log(ft) values, based on relative proton intensities which have been in turn calibrated to absolute log(ft) values known from β^+-decays from other reactions, yields a definite assignment of isospin for the super-allowed decay [Har74]. Thus, because of the strong proton decay signature, the lowest T=3/2 states have been accurately found and identified for most $A \leq 40$ T_z=-1/2 nuclei [Ajz79, Ajz82, End78].

There are problems in locating the higher T=3/2 states since the β^+ decay of a parent excited state cannot compete with the γ-decay to its ground state, and the β^+-delayed proton decay method is not feasible. In theory, one could predict the location of the high-lying T=3/2 states in the $T_z=|1/2|$ nuclei from the excitation energy of the lowest T=3/2 state in the T_z=-1/2 nuclei and the excitation energies of the excited states in the $T_z=|3/2|$ parent nuclei. An example of this can be seen in Fig. 2-2, where the A=29 isobaric multiplet members are shown. The members have been shifted in energy so that all the lowest T=3/2 parent and daughter states are at the same energy. The absolute energies of the members' ground states relative to ^{29}Si are shown in brackets located below each ground state.

The high-lying T=3/2 daughter states are never found at the energies predicted by the parent state locations, but may be shifted upwards or downwards in energy (~ 100-200 keV) depending on nuclear

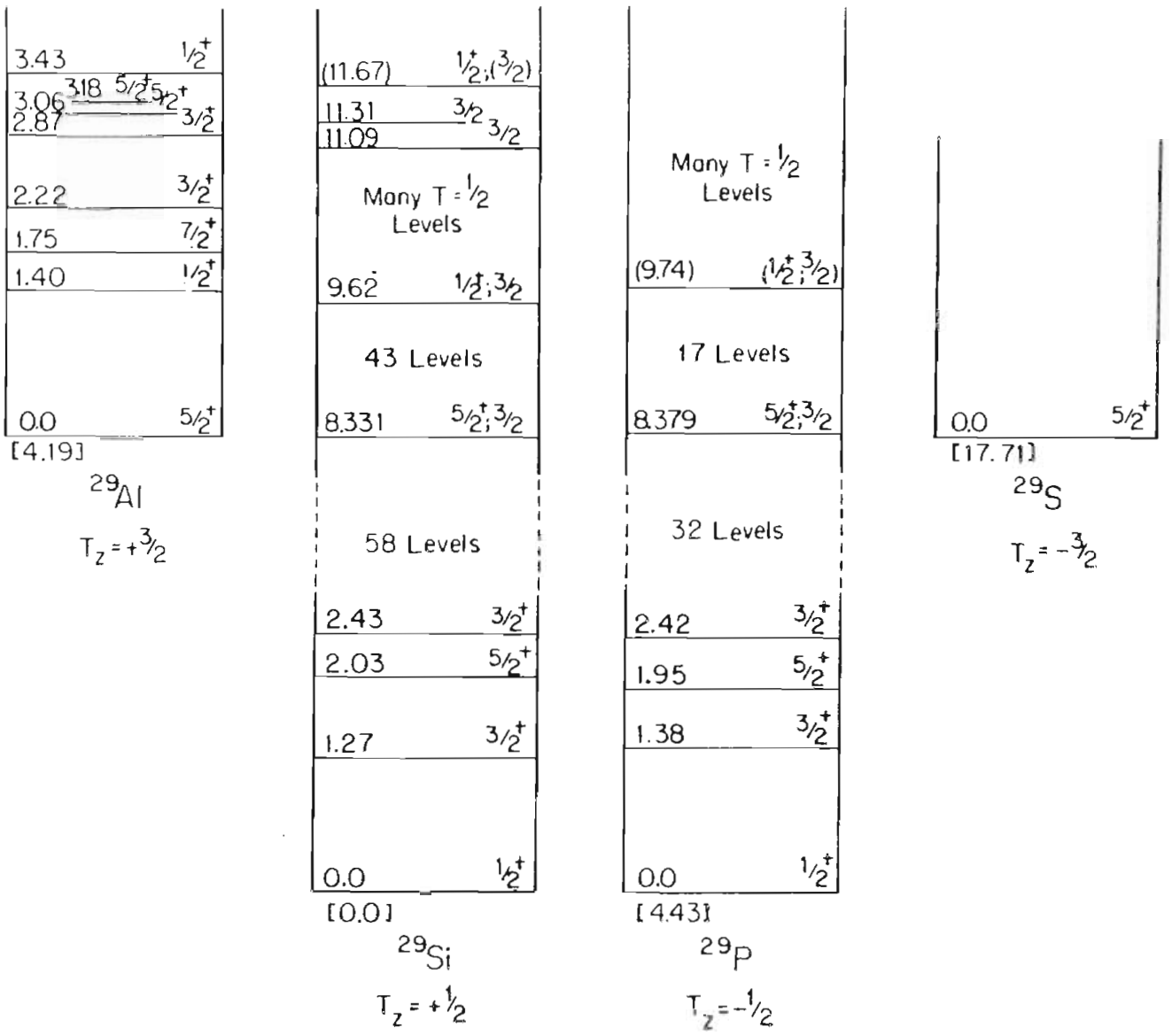

Figure 2-2 The A=29 Isobaric Multiplet. Energies have been shifted to align the T=3/2 parent and daughter states.

structure effects which cannot be predicted exactly. Unfortunately, many of the previous measurements have depended too strongly on the expected energy locations of the high-lying T=3/2 states in the T_z=1/2 nuclei based on the parent nucleus' excited-state locations. Thus, there are several identifications of T=3/2 states we have found to be incorrect. These misidentifications will be discussed later. Experimental methods to locate and identify these high-lying T=3/2 states in the T_z=|1/2| nuclei will be discussed after presenting the previous results.

2.3 Previous Results. In Table 2-1 a summary of known T=3/2 states found in T_z=|1/2| nuclei for A = 13, 17, 21, 25, 29, 33, and 37 is presented. The table lists the method(s) used to assign the isospin to the levels. In most of the cases the T=3/2 level in the T_z=-1/2 nucleus has been identified by the β^+-delayed proton decay. Many of the assignments are based on a combination of experimental data acquired by different methods. Even though none of the experiments alone uniquely identify the isospin, the sum of experimental evidence makes a persuasive case.

In general, there is very little available information on high-lying T=3/2 states in T_z=|1/2| nuclei, particularly for T_z=-1/2 nuclei, which are the levels for which we wish to determine the resonance properties by taking $(\vec{p},p)$ energy excitation functions. Also, the excitation energies of the known high-lying T=3/2 states are usually known to lesser accuracy.

2.4 Transfer Reactions. Several transfer reactions, including (p,t), (^{3}He,n), (^{3}He,p), and (^{3}He,α), have favorable ΔT selection rules

Table 2-1 T=3/2 Multiplets in Light Nuclei. Location of known T=3/2 levels in A = 13, 17, 21, 25, 29, 33, and 37 nuclei.

- ΔE is defined as E_x - E_x(first T=3/2 state) - E_x(T_z=+3/2 analog state).
- A T_z=|1/2| E_x energy surrounded by ( ) indicates that the state has been identified as a T=3/2 level but has not been assigned to a known or listed T_z=|3/2| state.
- A reference followed by * indicates the state was studied, but the experiment was not used to locate the T=3/2 state.
- A reference followed by [a] indicates the E_x given from this measurement varies by >50 keV from the accepted value.
- Multiple references are given in cases where the references contain different information.

Listed near the top of each isobaric multiplet table is the principal reference where more information can be found.

A = 13 [Ajz81]

^{13}B		^{13}C							^{13}N								^{13}O	
E_x	J^π	E_x	ΔE	(p,τ)	(τ,p)	(τ,α)	(d,t)	(n,n)	E_x	ΔE	(p,t)	(τ,n)	(p,p)	(p,α)	(p,γ)	β^+-p	E_x	ΔE
0.0	3/2$^-$	15.108	0.0	Cer66	Ade73 Mar77*				15.064	0.0	Cer66	Ade69	Lev69 Tho80*	Lev69			0.0	0.0
3.483									18.406	−0.14		Ade69	Lev69	Lev69			2.82	−0.66
3.543									(18.961	--)		Ade69	Lev69	Lev69				

Table 2-1 continued

A = 17 [Ajz82]

^{17}N		^{17}O							^{17}F								^{17}Ne	
E_x	J^π	E_x	ΔE	(p,τ)	(τ,p)	(τ,α)	(d,t)	(n,n)	E_x	ΔE	(p,t)	(τ,n)	(p,p)	(p,α)	(p,γ)	β^+-p	E_x	ΔE
0.0	$1/2^-$	11.079	0.0		Ade73*	Ade73* Det69	Mai77	Cie80 Hin81	11.193	0.0		Ade69	Hin76*	Hin76*	Har75*	Har71	0.0	0.0
1.374	$3/2^-$	12.466	0.01			Det69	Mai77	Cie80 Hin81	12.550	-0.02		Ade69	Hin76*	Hin76*	Har75*			
1.850	$1/2^+$	12.944	0.02			Det69	Mai77	Cie80 Hin81	13.080	0.04		Ade69	Skw74	Skw74	Har75*			
1.907	$5/2^-$	12.998	0.01			Det69		Cie80 Hin81	13.061	-0.04			Skw74	Skw74				
2.526	$5/2^+$	13.635	0.03			Det69	Mai77	Cie80 Hin81	13.781	0.06			Skw74	Skw74				
3.129	$7/2^-$	14.230	0.02			Det69[a]		Cie80 Hin81	14.304	-0.02			Hin76* Skw74	Hin76*	Har75*			
3.204	$3/2^-$								14.176	-0.22			Skw74		Har75*			
		7 additional levels					Mai77	Hin81 Cie80										

Table 2-1 continued

A = 21 [End78]

^{21}F		^{21}Ne							^{21}Na								^{21}Mg	
E_x	J^π	E_x	ΔE	(p,τ)	(τ,p)	(τ,α)	(d,t)	(α,n)	E_x	ΔE	(p,t)	(τ,n)	(p,p)	(p,α)	(p,γ)	β^+-p	E_x	ΔE
0.0	$5/2^+$	8.857	0.0	But68	McD68	Hen68	But68	McD76*	8.973	0.0	But68	Ade69	McD69*	McD69*	Bea70*	Sex73 Har65	0.0	0.0
0.280	$1/2^+$	9.139	0.00		McD68	Hen68	But68		9.220	−0.03	But68 Ben73a	Ade69	McD69*	McD69*	Bea70*		0.21	−0.07
1.101	−	9.963	0.01			Hen68	But68										1.08	−0.02
1.730 1.755		(10.604	0.02 −0.01)			Hen68											1.64	−0.09 −0.11
2.040 2.071		(10.904	0.01 −0.02)			Hen68											2.01	−0.03 −0.06

A = 25 [End78]

^{25}Na		^{25}Mg							^{25}Al								^{25}Si	
E_x	J^π	E_x	ΔE	(p,τ)	(τ,p)	(τ,α)	(d,t)	Other	E_x	ΔE	(p,t)	(τ,n)	(p,p)	(p,α)	(p,γ)	β^+-p	E_x	ΔE
0.0	$5/2^+$	7.790	0.0	Har66 Ben73a	Deh67	Det70		Wei76 Ber70	7.901	0.0	Har66 Ben73a		Iko76*		Rog77*	Ree66 McP65	0.0	0.0
0.90	$3/2^+$	7.864	−0.01	Har66 Ben73a	Deh67	Det70		Wei76 Ber70	7.970	−0.02	Ben73a		Iko76*		Rog77*		0.04	−0.05
1.069	$1/2^+$	8.836	−0.02			Det70[a]		Wei76									0.815	−0.25
2.202	$3/2^+$	9.999[A]	0.01					Ber70									1.963	−0.04
		5 additional levels				Det70												

o The Ber70 reference listed under Other refers to (γ,n) data and Wei76 is for (n,n) data

o The [A] indicates that the T=3/2 level was not listed by [End78].

Table 2-1 continued

A = 29 [End78]

- The Vig74 reference listed under Other refers to (α,nγ) and Cle78 is for (n,n)
- The [A] indicates that the E_x listed was not from [End78].
- The [B] indicates that the level was tentatively identified in [End78] as the T=3/2 level.

^{29}Al		^{29}Si							^{29}P								^{29}S	
E_x	J^π	E_x	ΔE	(p,τ)	(τ,p)	(τ,α)	(d,t)	Other	E_x	ΔE	(p,t)	(τ,n)	(p,p)	(p,α)	(p,γ)	β^+-p	E_x	ΔE
0.0	$5/2^+$	8.331	0.0	Har66		Det70		Vig74	8.379	0.0	Har66		Tei69 Iko76[e]		Bar72[e] Mor68[e]	Har66a	0.0	0.0
1.398	$1/2^+$	9.685[A]	-0.04			Det70[a]		Cle78	9.743[B]	-0.03			Tei69					
1.754	$7/2^+$																	
2.224	$3/2^+$																	
2.865	$3/2^+$	11.087	-0.11			Det70												
3.062	$5/2^+$	11.305	-0.09			Det70												
3.184	$5/2^+$																	
3.433	$1/2^+$	11.665	-0.10			Det70												

Table 2-1 continued

A = 33 [End78]

^{33}P		^{33}S							^{33}Cl							^{33}Ar	
E_x	J^π	E_x	ΔE	(p,τ)	(τ,p)	(τ,α)	(d,t)	Other	E_x	ΔE	(p,t)	(τ,n)	(p,p)	(p,α)	(p,γ)	β^+-p	E_x	ΔE
0.0	$1/2^+$	5.475	0.0	Vig71					5.544	0.0	Vig71		Iko76*		Esw72	Har71	0.0	0.0
1.432	$3/2^+$	6.905	0.10	Vig71					6.984	0.01	Vig71		Abb73				1.344	-0.09
1.848	$5/2^+$	7.337	0.01	Vig71					7.399	0.01	Vig71		Abb73		Esw72		1.786	-0.06
2.539	$3/2^+$	8.107	0.10	Vig71					8.100	0.02	Vig71							

A = 37 [End78]

^{37}Cl		^{37}Ar							^{37}K							^{37}Ca	
E_x	J^π	E_x	ΔE	(p,τ)	(τ,p)	(τ,α)	(d,t)	Other	E_x	ΔE	(p,t)	(τ,n)	(p,p)	(p,α)	(p,γ)	β^+-p	E_x	ΔE
0.0	$3/2^+$	4.993	0.0	Ben73b					5.047	0.0	Ben73b		Goo67			Sex74 Har66a	0.0	0.0
1.726	$1/2^+$	6.654	-0.07	Ben73b					6.670	-0.10	Ben73b						1.613	-0.11

for forming $T_>$ states in $T_<$ nuclei and have been used to identify T=3/2 levels in $T_z=|1/2|$ nuclei [Cer68]. These transfer reactions rely for isospin identification on enhancement of the T=3/2 levels relative to the surrounding T=1/2 levels. The identification is also based on these enhanced states having the correct J^π and being located near the excitation energy expected from the $T_z=|3/2|$ parent state values. The $(p,t)-(p,^3He)$ and $(^3He,p)-(^3He,n)$ reactions have a further advantage in that, with the same target nucleus and incident particle, T=3/2 mirror levels can be observed in both the $T_z=1/2$ and $T_z=-1/2$ nuclei. The $(p,t)-(p,^3He)$ reaction products can be observed with the same detectors and experimental setup; however, this is not true for the $(^3He,p)-(^3He,n)$ reactions, since the detection of protons requires very different experimental techniques than the detection of neutrons. Finally, a direct comparison of the (p,t) to $(p,^3He)$ cross sections can uniquely assign the isospin of a set of mirror states, and this comparison in most cases offers the best method to locate and assign isospin to states in $T_z=|1/2|$ nuclei. It is important to point out that when considered alone none of the reactions uniquely identifies the isospin of the observed levels; although, when considering the additional evidence of location and J^π (when determined), the assignments are more reliable. The details on how and why the (p,t) and $(p,^3He)$ reactions can be used to determine the isospin of $T_>$ levels will now be presented.

2.4.1 (p,t) and (p,^{3}He) Two-Nucleon Transfer Reactions. The use of (p,t) and (p,^{3}He) two-nucleon transfer reactions to identify the isospin of $T_>$ states located in $T_<$ nuclei is a well known and tested method [Cer64, Det65, Cer66, Fle68]. As will be discussed in Section 2.4.2, for a T_z=-1/2 target nucleus, the observed angular distributions of cross sections for the (p,t) and (p,^{3}He) reactions should be nearly the same in shape and magnitude for the T=3/2 states, except for the ratio of triton to ^{3}He wave numbers and Coulomb effects on the transition amplitudes. Thus, comparison of (p,t) and (p,^{3}He) cross section and analyzing power angular distributions yields a direct method to determine the isospin of the T=3/2 levels in T_z=|1/2| nuclei. Advantages of this procedure are that the population of the T=3/2 states is isospin-allowed, and in the (p,t) reaction the isospin selection rules and the simple structure of the T=3/2 states may enhance their population relative to the large number of surrounding T=1/2 states which have less coherent structure. Considering that the theory predicting the agreement in (p,t) and (p,^{3}He) cross sections assumes several simplifications such as zero-range and identical mass-3 wave functions, the experimental agreement is outstanding [Cer64, Det65, Cer66, Fle68].

Although the comparison method should work, there are several possible problems. Some of the high-lying T=3/2 states will have nuclear structure configurations which will not likely be populated by the (p,t) or (p,^{3}He) reaction, and thus will not be easily distinguished from the sea of T=1/2 levels. Also, the high-lying T=3/2 levels become less coherent with increasing excitation energy, and hence the states become

less prominent relative to the T=1/2 states. Finally, the (p,t) two-neutron transfer is predominantly an S=0 transfer and hence has J=L. Many of the states of interest have J^{π} configurations which proceed by L=2, resulting in most of the cross section angular distributions having similar shapes. However, these problems are shared by all the reaction methods.

The (p,t) and (p,^{3}He) comparison method for the identification of T=3/2 states has been used in several isobaric multiplets to identify the lowest T=3/2 state (see Table 2-1). A comparison of the (p,t)-(p,^{3}He) to the β^+-delayed proton decay assignments shows complete agreement between the methods. However, there is much less information on the identification of high-lying T=3/2 states. The second levels in A=25 [Ben73a] and A=37 [Ben73b] have been observed. There is also work reporting on several possible T=3/2 states in the A=33 system [Vig71]. However, this work is limited by very poor energy resolution in the (p,t) and (p,^{3}He) spectra, and has been found by the present work to have incorrect identifications.

2.4.2 Theory. For a direct two nucleon pickup reaction, such as (p,t) or (p,^{3}He) at sufficiently high energy, the zero-range distorted-wave Born approximation (DWBA) model can be used to predict cross section and analyzing powers [Aus70, Bae73, Gle75, Tow69]. For a pickup reaction A(a,b)B the cross section can be expressed as

$$\frac{d\sigma}{d\Omega}_{pick\text{-}up} = \frac{\mu_a \mu_b}{\{2\pi\hbar^2\}^2} \frac{k_b}{k_a} |T|^2 \qquad 2\text{-}1$$

where μ_i are the reduced masses, k_i are the center-of-mass (cm) wave numbers, and T is the transition amplitude between the initial and final configurations. Exact scattering theory describes this transition amplitude as

$$T = \langle \underline{\Psi}_f^- \mid (V_{aA} - \bar{U}_{aA}) \mid \underline{\Phi}_i^+ \rangle \qquad 2\text{-}2$$

with V_{aA} being the sum of all two-body interaction potentials between the nucleons in a and A, while $\bar{U}_{aA}$ is the optical potential for elastic scattering in the initial channel. The initial configuration of incident particle 'a' and initial state A is described by $\underline{\Phi}_i^+$ and the final configuration of residual nucleus B and outgoing particle b is described by $\underline{\Psi}_f^-$. The DWBA model is valid when the elastic channel is the dominant scattering channel and all other channels have weak effects on T. Perturbation methods then allow replacing the final state wave function by a product of the bound-state wave functions for B and b with the scattering distorted wave function χ_b^-. Then the transition amplitude in the DWBA approximation can be written

$$T = \langle \chi_b^- \varphi_b \underline{\Phi}_B \mid (V_{aA} - \bar{U}_{aA}) \mid \chi_a^+ \varphi_a \underline{\Phi}_A \rangle \qquad 2\text{-}3$$

where χ_i are the distorted waves and (+) and (-) denote that these wave functions must satisfy the asymptotic boundary conditions of outgoing and incoming spherical waves. The cross section for two-nucleon transfer in the DWBA zero-interaction-range approximation, neglecting spin-orbit coupling in the distorted waves, is then

$$\frac{d\sigma}{d\Omega}_{pick\text{-}up} = \frac{\mu_a \mu_b}{\{2\pi\hbar^2\}^2} \frac{k_b}{k_a} \frac{2s_b + 1}{2s_a + 1} D_o^2 \sum_{\Lambda}^{LSJT}$$

$$\times b_{ST}^2 (T_B N_B TN | T_A N_A)^2 [D(S,T)]^2$$

$$\times | \sum^{q_1 q_2} S_{AB}^{1/2}(q_1 q_2 : LSJT) B_{\Lambda}^{NL} |^2 \qquad 2\text{-}4$$

where s_i are the spins of the light particles, and D_o is a scale factor which is included due to the zero-range approximation and is usually determined by normalization of calculations to experimental values. The spectroscopic amplitudes b_{ST} for the particles a and b are discussed below. The Clebsch-Gordan coefficient for isospin is $(T_B N_B TN | T_A N_A)^2$, and D(S,T) is a spin-isospin exchange term for the interaction potential. The spectroscopic amplitude $S_{AB}^{1/2}$ contains all nuclear structure information and is a measure of the probability that the nucleons common to both the initial and final states will have the same configuration. The q_i terms are the transferred single-particle-state quantum numbers $[n_i l_i j_i]$, where there is a coherent sum over these states, and LSJT are the quantum numbers of the transferred pair when taken as a cluster. The scattering amplitude B_{Λ}^{NL} contains the distorted waves and form factor for the transferred nucleons in the zero-range interaction approximation, where Λ represents the magnetic substates of L. For more details than presented here refer to [Aus70, Bae73, Gle75, Tow69].

To take the ratio of (p,t) to (p,^{3}He) cross sections we should examine the isospin or reaction dependent terms in the DWBA cross section expression. The light-particle spectroscopic factor can be expressed for (p,t) and (p,^{3}He) reactions as

$$b_{ST}(p,t) = -\delta_{S,0}\delta_{T,1} \qquad 2\text{-}5a$$

$$b_{ST}(p,{}^3He) = -\frac{1}{\sqrt{2}}\left(\delta_{S,0}\delta_{T,1} - \delta_{S,1}\delta_{T,0}\right) \qquad 2\text{-}5b$$

where the triton and ^{3}He particles are assumed to be pure $^2s_{1/2}$ states. This spectroscopic factor simply says that in the case of (p,t) where two neutrons are transferred, the isospin transferred is T=1 and, because of the anti-symmetrization of the wave function, the spin transferred must be zero. In the case of the (p,^{3}He) reaction where a proton and neutron are transferred, either T=1 and S=0 or T=0 and S=1. Thus, the (p,t) reaction with isospin transfer of ΔT=1 is a good reaction to populate $T_>$ states when starting with a $T_<$ target nucleus. The isospin Clebsch-Gordan coefficients for the case of $T_B = T_A + 1$ are

$$(T_B N_B T N | T_A N_A)^2_{(p,t)} = \frac{1}{\{2T_A + 3\}\{T_A + 1\}} \qquad 2\text{-}6a$$

$$(T_B N_B T N | T_A N_A)^2_{(p,{}^3He)} = \frac{\{2T_A + 1\}}{\{2T_A + 3\}\{T_A + 1\}} \qquad 2\text{-}6b$$

where these will be the cases of interest for forming T=3/2 states.

The only other isospin or reaction dependent terms are the B_{Λ}^{NL} scattering amplitude and the wave numbers k_i. The wave numbers which vary according to the velocity of the outgoing triton or ^{3}He particle can be calculated exactly with the ratio of k_t to k_τ written as

$$\frac{k_t}{k_\tau} = \left[\frac{E_p^L A\{A+1\}^{-1} + Q_t'}{E_p^L A\{A+1\}^{-1} + Q_\tau'}\right]^{1/2} \qquad 2\text{-}7$$

where E_p^L is the incident proton lab energy and Q_i' is the Q-value for the reaction plus the excitation energy in the residual nucleus. The scattering amplitude B_Λ^{NL} is weakly dependent on the Q-value differences and the mass-3 wave function differences. For $A \leq 60$ the ratio of the scattering amplitudes has been estimated to be different by less than two percent because of mass-3 wave function differences, while the ΔQ differences for high incident proton energies are less than five percent [Har69], and hence the ratio of scattering amplitudes is assumed to be unity.

Thus, the predicted DWBA ratio of cross sections for (p,t) to $(p,{}^3He)$ for sufficiently high energies is

$$\frac{\frac{d\sigma}{d\Omega}_{(p,t)}}{\frac{d\sigma}{d\Omega}_{(p,{}^3He)}} = \frac{k_t}{k_\tau} \frac{2}{\{ 2T_A + 1 \}} \qquad 2\text{-}8$$

for the case of $T_B = T_A + 1$. One should note that up to this point no assumptions about target isospin have been made. For the particular case of a T_z=-1/2 target forming a T=3/2 state in a T_z=-1/2 nucleus, T_A = 1/2 only, so the ratio reduces to simply

$$\frac{\frac{d\sigma}{d\Omega}_{(p,t)}}{\frac{d\sigma}{d\Omega}_{(p,{}^3He)}} = \frac{k_t}{k_\tau} \, . \qquad 2\text{-}9$$

Therefore, the T=3/2 mirror states populated by the (p,t) and $(p,{}^3He)$ reactions should not only be the same shape, but when corrected by the ratio of wave numbers should also be the same magnitude. Note also that

the (p,^{3}He) spectroscopic factor allows population of T=1 and S=0 or T=0 and S=1 states; however, formation of the T=3/2 states allows only the T=1 and S=0 channel. For the T=1/2 states, both types of transfer are allowed, and thus the T=1/2 states observed by (p,^{3}He) should have no simple relationship in shape or magnitude to the corresponding mirror T=1/2 states populated by the (p,t) reaction.

From these comments and from previous experiments, one expects the comparison of experimental (p,t) and (p,^{3}He) cross sections and analyzing powers ratios and shapes to yield definitive assignments of the isospin of T=3/2 states in T_z=-1/2 nuclei. However, DWBA calculations do not always completely describe these observed shapes [Fle68, Nel74, Pig74, Mic75].

2.4.3 Experimental Considerations. The use of the (p,t) and (p,^{3}He) comparison method requires both a high incident proton beam energy $\geq$ 40 MeV and sufficient particle spectrum resolution to resolve and identify peaks. The first requirement is necessary because of the large negative ground-state Q-value for the reactions, ~ -15 MeV for the (p,t) and ~ -12 MeV for the (p,^{3}He) reactions, and the high excitation energy of the T=3/2 states, 5-12 MeV. See Fig. 2-3 for an example for the A=29 case. There is also the generally held belief that the outgoing triton or ^{3}He particles should be at least 20 MeV or greater in energy. This belief is based on some observed, but not well understood, energy dependences of the interactions of the mass-3 wave system [Nan74]. Thus, an incident proton energy of 40 MeV or more is required.

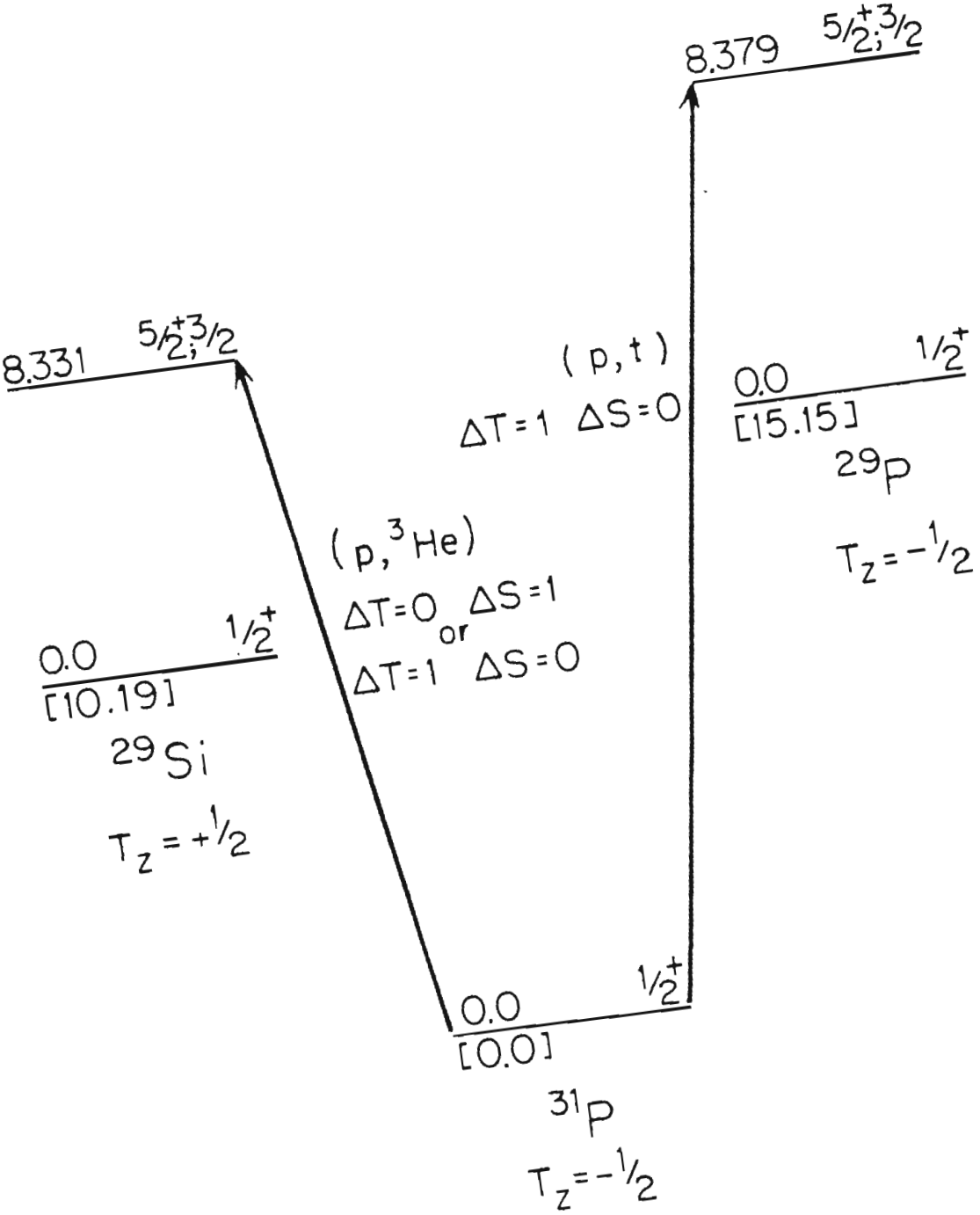

Figure 2-3 The (p,t) and (p,^{3}He) transitions for the lowest T=3/2 states in the T_z=|1/2| nuclei for the A=29 system.

Good resolution, ~ 15–45 keV, is necessary to resolve the particle spectrum peaks because of the high-density of T=1/2 states at excitation energies where the T=3/2 states occur. The typical spacing of T=1/2 levels for residual nuclei with A = 25 to 37 is ~ 45–75 keV calculated by using the level density program LVDN. The high incident particle energy requires the use of a magnetic spectrograph to acquire the necessary resolution. Earlier work [Har66, But68], with solid-state particle telescopes was of sufficient resolution, ~ 150–200 keV, to resolve the lowest T=3/2 states because of the large enhancement relative to the T=1/2 states; however, the high-lying states have less coherent nuclear structure at higher energies and the nuclear level density increases. This necessitates the best possible resolution. One can attribute several incorrect assignments of high-lying T=3/2 states to poor resolution. These examples will be discussed later. The experimental requirements of high incident beam energy and magnetic spectrograph restricted our performing these measurements to a couple of laboratories in the USA.

Another possible experiment to provide the identification of T=3/2 states is the measurement of A_y angular distributions. These results can help resolve possible ambiguities in cross section measurement comparisons because of target thickness normalization problems. In addition, most of the states of interest are populated by low-L transitions or mixtures of these transitions and have similar cross section magnitudes, while the analyzing powers for different L-transfers

or mixtures of L-transfers exhibit different angular distribution shapes [Har70, Nel70].

A final consideration in performing these experiments at an appropriate laboratory is the amount of time needed to acquire sufficient angular distributions for both (p,t) and (p,^{3}He) on an A = 25 to 37 system over a ~ 5 Mev range of excitation. Count rate estimates show that angular distributions can be obtained at forward angles in less than 2 to 3 days, even with polarized beam, which makes the (p,t) and (p,^{3}He) method of locating and identifying these states look very reasonable.

2.5 Energy-Excitation Functions. Observing the isospin-forbidden formation of the T=3/2 levels in T_z=-1/2 A=4n+1 nuclei can be accomplished with (p,γ) (p,α), and (p,p) energy-excitation functions taken on A=4n target nuclei. In all cases the identification relies on observing a narrow resonance in the expected energy region of the T=3/2 state. A narrow total resonance width, 100-1000 eV, is expected since the decay of the compound nucleus state is isospin-forbidden. This results in a long compound state lifetime, and hence the widths of these states are comparatively narrow. The expected excitation energy region is calculated, as for the reaction methods, by taking the excitation energy of the excited state in the T_z=-3/2 parent nucleus and adding it to the E_x energy of the accurately measured lowest T=3/2 level in the T_z=-1/2 nuclei. Then if a reasonably narrow resonance is observed with the expected ℓ or J^π, it is claimed to be the T=3/2 state. None of the methods can identify the isospin of the state.

2.5.1 (p,γ) Reaction. The advantage of using the (p,γ) reaction is that, although the formation of the T=3/2 level is isospin-forbidden, the γ decay of the $T_>$ state to the $T_<$ ground state or lower excited states is isospin-allowed. In contrast, the decay of the T=3/2 state by proton and α channels is isospin-forbidden. Also, because the T=3/2 levels in the T_z=-1/2 nucleus are analogs to the low-lying levels in the T_z=|3/2| parent nuclei, these levels are expected to have simple structure compared to the large number of surrounding T=1/2 levels, and hence the total cross sections for the T=3/2 levels should be enhanced relative to these surrounding T=1/2 levels. Thus, the identification of T=3/2 levels via the (p,γ) reaction relies on observing strong γ resonances of narrow width in the proper excitation energy region.

The use of the (p,γ) reaction to locate T=3/2 states has several serious deficiencies. First, and most importantly, the location of a strong narrow (p,γ) resonance in the neighborhood of an expected T=3/2 level does not in any way determine the isospin of the observed level. It is also known from (p,p) work [Tie69], in the E_x region of ^{29}P where the second T=3/2 state should be located, that there are many resonances with widths $\leq$10 keV. Although the T=3/2 state γ widths will be well below 1 kev, the experimentally measured widths are usually on the order of ~ 15 keV, since in many studies this width is dominated by target thickness and beam resolution. The fact that the electromagnetic γ-decay is much weaker than the charged particle decays makes it necessary to use targets thick enough to obtain reasonable yields. Since the experimental resolution is insufficient to distinguish resonances

$\leq$10 keV, and since many resonances of this approximate width are observed in the excitation energy regions where the T=3/2 states are expected to be found, the observation of a narrow resonance is not sufficient evidence for the state to have isospin T=3/2. Finally, the strength of the integrated (p,γ) cross section is proportional to $\Gamma_p\Gamma_\gamma/\Gamma$, where Γ_p is the total proton decay width, Γ_γ is the γ-decay width to the T_z=-1/2 ground states, and Γ is the total decay width. The γ-decay width depends on the γ-decay spin-parity selection rules for the particular initial and final state spin configuration [Wil60]. Hence, some T=3/2 states of unfavorable J^π will decay weakly and will not be predominant peaks in the (p,γ) spectra. Thus, it is likely that (p,γ) energy excitation functions will observe some of the T=3/2 levels, but they cannot be used to yield consistent, non-ambiguous isospin assignments.

An example of using the (p,γ) method to locate and identify T=3/2 states is work done in the A=33 system [Esw72] where narrow, strong (p,γ) resonances were observed in the expected E_x regions for the lowest and third T=3/2 states in ^{33}Cl. However, in the E_x region where the second T=3/2 state should be found there are no strong or narrow resonances seen, as shown in Fig. 2-4.

2.5.2 (p,p) Reaction. The use of (p,p) (or (p,α)) energy excitation functions to identify the isospin of the T=3/2 nuclear levels has several of the advantages and many of the disadvantages of the (p,γ) method. Because both the population and decay of most low-lying T=3/2 states are isospin-forbidden, these $T_>$ states are not only much narrower

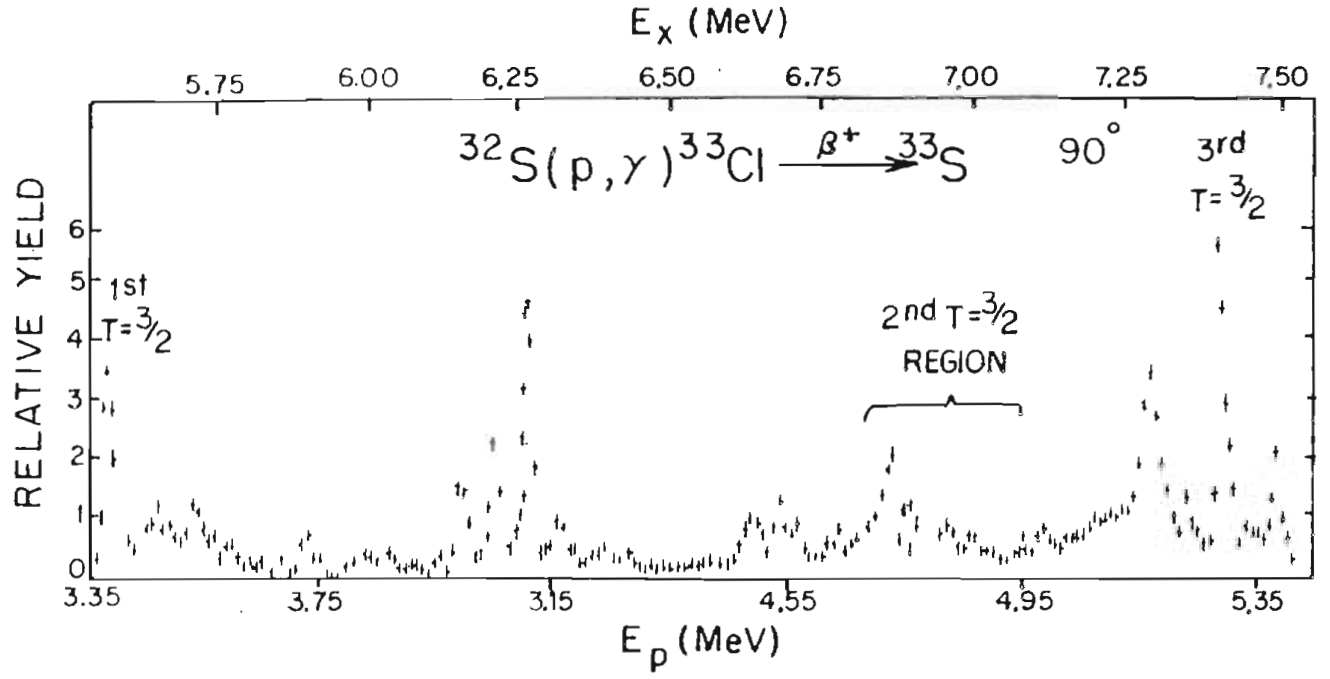

Figure 2-4 $^{32}S(p,\gamma)^{33}Cl$ excitation energy spectra [Esw72]. The first and third T=3/2 states are indicated. The region where the second T=3/2 state should occur is also marked.

than the surrounding $T_<$ levels, but they also exhibit much smaller effects in the cross section. Hence, very good total resolution of the same order as the resonance width is required in order to observe these resonances. Again, the identification of the T=3/2 states is based on observing a narrow resonance in the proper energy region of the compound nucleus. However, as in the (p,γ) case, observing a narrow resonance in the proper energy region does not determine the isospin of the level. Also, as mentioned in the (p,γ) case, there are examples of several narrow resonances in the energy region of expected T=3/2 resonances.

An example of the problems with the (p,p) method can be seen in work done on the A=33 system by [Abb73]. Here the third T=3/2 state has been incorrectly assigned to a fairly broad and strong resonance near the correct excitation energy. This energy was predicted from the parent excited state location. However, the actual T=3/2 resonance is about 10 keV lower than the strong resonance and can be observed as a slight bump in the cross section, as shown in Fig. 2-5. Our high-resolution scan across the actual T=3/2 state is also shown in the figure.

One improvement to the (p,p) method is to measure analyzing power excitation functions. This makes it possible to determine the J^π of the levels, and since the T=3/2 analog levels are of the same J^π as the parent states, this allows one to eliminate narrow resonances of the incorrect J^π. However, taking high-resolution, polarized (p,p) data is very difficult and also quite time consuming. The analysis of the excitation functions is also difficult. It is not feasible to search large energy regions around the expected T=3/2 state location, because

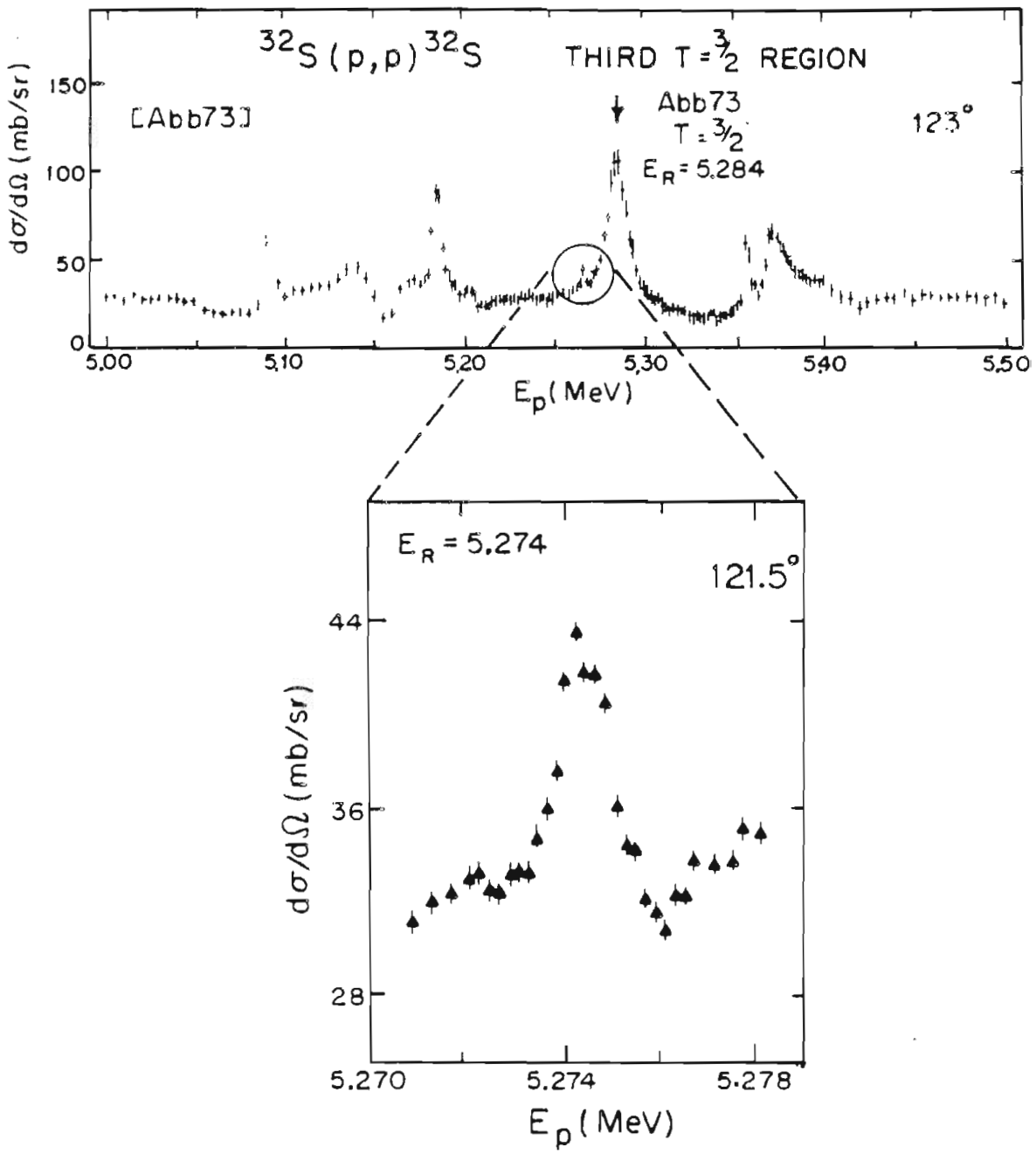

Figure 2-5 The upper figure is (p,p) cross section excitation function data from [Abb73] at $\theta_L = 123^\circ$. The state incorrectly identified by [Abb73] as the third T=3/2 state in ^{33}Cl is indicated by an arrow. Our high-resolution (p,p) data at $\theta_L = 121^\circ$ is shown in the lower figure for the third T=3/2 state, where the corresponding energy region in [Abb73] is circled.

small energy steps of 200–500 eV, good resolution, and sufficient statistics are necessary to observe the small isospin-forbidden effects. As an example, to cover a 200 keV energy region, for a typical high-resolution $(\vec{p},p)$ experiment at TUNL, would require 8 to 10 days of continuous uninterrupted beam time. Even with this, the isospin of any observed state of correct J^{π} will not be determined by the $(\vec{p},p)$ method.

The conclusion that is reached for the (p,p), (p,α), and (p,γ) energy excitation methods is that in many cases the narrow resonance observed in the expected energy region will in fact be the desired T=3/2 level. However, since there is no direct evidence that the states are T=3/2 levels, there will be many cases where the isospin of these narrow resonances will be misidentified.

2.6 Summary of Techniques. Each of the different methods described to locate and identify T=3/2 states has advantages and disadvantages. As detailed in this chapter, each method may lead to ambiguous results. The (p,t) and (p,^{3}He) comparison is by far the best choice, since it is the only method that can locate and uniquely assign isospin to the T=3/2 levels. A significant reason for its success is the fact that it requires the evaluation of two sets of different measurements. It has several experimental advantages: being able to use the same target and incident beam to identify states in both $T_z=|1/2|$ nuclei, being able to examine a large range of excitation energy in the residual nucleus with a single measurement, and requiring no elaborate calculations to identify the T=3/2 states. However, this measurement tells nothing of the resonance parameters of the state and hence no

information on isospin-mixing.

Certainly the most definitive way to assign T=3/2 levels would be to perform as many of the different experiments as possible and compare their results. Thus, the total sum of results would eliminate most ambiguities. However, this is clearly not feasible, especially when trying to identify many T=3/2 levels. We decided that the best way was first to take (p,t) and (p,^{3}He) data on several target nuclei and then look at suspect states indicated in the (p,t) data by using high-resolution (p,p) energy excitation functions of cross section and analyzing power over the energy regions corresponding to these levels. Although our principal objective was to obtain information on the T_z=-1/2 T=3/2 levels, the (p,t)-(p,^{3}He) work offers the additional advantage of yielding information about the T_z=1/2 states.

Although TUNL is uniquely equipped to perform the ($\vec{p}$,p) and (p,p) high-resolution experiments, it was necessary to go elsewhere to acquire the (p,t) and (p,^{3}He) data. The next two chapters present the results of the (p,t)-(p,^{3}He) experiments performed at the Princeton University Cyclotron and at the Indiana University Cyclotron Facility.

3. (p,t) and (p,^{3}He) Measurements - Princeton

3.1 Introduction. Targets of ^{27}Al, ^{29}P, ^{35}Cl, and ^{39}K were bombarded by the proton beam from the Princeton University Cyclotron to search for T=3/2 states in $T_z=|1/2|$ nuclei by using the (p,t) and (p,^{3}He) reactions. The availability of an incident proton beam of greater than 40 MeV and a QDDD high-resolution magnetic spectrometer made Princeton an ideal facility for performing a search for T=3/2 states. The selection of the A = 25, 29, 33, and 37 final state mass systems for study was based on the following criteria: (1) The need to study T=3/2 states in several different A = 4n+1 systems over a range of mass values in order to look for systematic behavior of isospin mixing as a function of A. (2) The ability to check our measurement method since a few T=3/2 states in the selected $T_z=-1/2$ member nuclei had been previously located and studied (see Table 2-1). (3) The desire to locate T=3/2 states at excitation energies which could be measured by $(\vec{p},p)$ high-resolution studies at TUNL.

Data were acquired at only one spectrograph lab angle in an effort to make as many identifications as possible of T=3/2 candidate states in the (p,t) spectra within the allocated beam time. We define candidate T=3/2 states in the (p,t) data as moderately-populated to strongly-populated states located in the energy region ($\pm$ 200 keV) where a T=3/2 state is expected to occur relative to the parent $T_z=|3/2|$ state

location (based on previous measurements, see Table 2-1). There was concern because of the lack of (p,t)-(p,^{3}He) measurements on high-lying T=3/2 states, that the expected enhancement of T=3/2 levels relative to T=1/2 levels might not occur, and the T=3/2 states might not be distinguishable from T=1/2 levels. It was hoped that the analysis of the (p,t) and (p,^{3}He) data could provide starting points for (p,p) excitation functions based on two criteria; (1) The location of strong levels in the (p,t) spectra and (2) the comparison of the cross section at a given angle for states at comparable excitation energies in the residual nuclei populated by the (p,t) and (p,^{3}He) reactions.

3.2 Experiment--Targets. Targets were made using the evaporation facilities at UNC and were then transported to Princeton in vacuum desiccators. The targets were mounted on target frames designed for the Princeton spectrograph chamber and were stored in special metal boxes built by the TUNL instrument shop. Targets with a range of thicknesses were made consistent by limiting the resolution broadening caused by energy-loss of tritons and helions in the targets to ~ 15-20 keV.

Self-supporting natural Al (100% ^{27}Al) foils were prepared by standard electron-gun evaporation [Mug79] using a commercial electron-gun [VEE01] and a vitreous carbon crucible [FLU01]. Evaporations were at ~ 10^{-6} Torr using a vibrating quartz crystal [SLO01] to monitor evaporation rate and thickness. The Al was evaporated onto glass slides coated with natural $BaCl_2$ release agent (~ 200 $\mu g/cm^2$). The glass slides were located ~ 10 cm from the crucible. After evaporation the bell-jar was brought up to atmospheric pressure

with Ar gas. The Al foils were then removed from the glass slides and mounted on target frames by standard floating techniques [Mug79] using deionized distilled water. Target thicknesses were checked by both an α-particle energy loss measurement with an ^{241}Am source and also by proton scattering at 5 MeV, an energy of known cross section [El166]. Agreement between the methods was better than 10%.

Preparation of phosphorus targets presented special problems because of its chemical properties. Under a typical 10^{-4} to 10^{-6} Torr vacuum used for evaporation, phosphorus evaporates at ~ 375°C. Phosphorus vapor below a temperature of 800°C is in the molecular form of P_4 which condenses on surfaces as yellow phosphorus. The yellow phosphorus is unstable and burns on contact with air. However, at higher temperatures, ~ 1000°C, the phosphorus dissociates to P_2 and condenses as red phosphorus, which is not spontaneously combustible [Hoo64]. Thus, to evaporate only the red phosphorus, a special crucible and oven assembly was built [Tze78]. The phosphorus would evaporate in a crucible at ~ 350–400°C and then pass through an oven kept at a temperature of over 1000°C. The crucible and oven, both made of spectroscopic graphite, were built by the TUNL instrument shop. A Pyrex cylinder joined and insulated the crucible from the oven. Resistive heating with 0.03" tantalum wire coils was used with separate current power supplies for heating the crucible and oven.

The natural (red) P (100% ^{31}P) was evaporated onto target frames with carbon or carbon and Formvar ($C_5H_8O_2$) backings located ~ 8 cm from the top of the oven. The carbon backings, ~10 $\mu g/cm^2$ thick, were

obtained from a commercial source [ARI01]. The backing materials were selected because they are very strong even for small thicknesses. Backings as thin as possible were used to minimize contaminant peaks. The evaporation procedure was as follows: (1) The crucible was loaded with red phosphorus in an Ar atmosphere, mounted in the bell jar, and pumped down to ~ 10^{-6} Torr. (2) The oven was raised to a temperature of 1100–1200^{o}C. (3) The ionization tube was turned off and the bell jar sealed off from the vacuum pumping system. (This is because phosphorus contaminates the diffusion pump oil.) (4) The crucible was heated slowly while the Pyrex cylinder was watched for signs of phosphorus. (5) The evaporation was continued until the desired thickness was reached. Then the crucible heating current was slowly reduced to zero and after a few minutes the oven temperature was reduced. (6) After about 15 minutes for cooling, the bell jar was let up to about 500 mTorr of air. This caused any yellow phosphorus to ignite. (Normally there was a flash on the bell-jar surface caused by small amounts deposited there.) The flow of air was continued into the bell-jar until the pressure approached atmospheric pressure. Then the bell-jar was roughed back down to 5–10 mTorr with the mechanical pump. The mechanical pump was vented outside of the building. Vapors of various phosphorus compounds appeared as the roughing pump reduced the pressure below their vapor pressure. Note that it was important not to let the bell-jar up to atmospheric pressure and expose it to the room because some of the phosphorus compounds formed are toxic [Ste67].

(7) Step 6 was repeated two or more times until there were no vapors visible inside the bell-jar when roughing down, which indicated that the

majority of the phosphorus compounds were gone. The bell-jar was then let completely up to atmospheric pressure and opened. The targets were removed, placed in a desiccator, and placed under vacuum. It was found that exposing the targets to air for an hour or more caused the targets to crack and break.

Because of the limited crucible volume, several evaporations were necessary to make targets of thickness 100–250 $\mu g/cm^2$. The thickness of the evaporation was monitored by the vibrating crystal technique. Several targets were examined at TUNL using a low-energy proton beam to investigate the stability of the targets as a function of beam current and energy loss. The targets showed no deterioration for currents up to 1 μA. No target deterioration was expected at Princeton because although the incident proton beam would deposit more energy in the targets, cyclotron beams have a much greater cross-sectional area meaning less energy deposited per unit area.

The ^{35}Cl targets were made by resistively heating $BaCl_2$ (99.73% isotopically enriched ^{35}Cl [OAK01]) and evaporating the material onto carbon and Formvar backings mounted on target frames. A tantalum (0.005") open boat was used with the target frames located ~ 10 cm away, with a typical pressure of 10^{-7} Torr. The $BaCl_2$ was heated in an oven before being placed in the boat to drive off water and yield a smoother evaporation. The thicknesses of the targets were checked by a vibrating crystal during the evaporation, by the energy loss of α particles from a ^{241}Am source, and by Rutherford scattering of 5 MeV protons from Ba. Unlike other evaporations described here, in the $BaCl_2$ evaporation the

target frames were spaced far apart and there was a variance of target thickness with frame position. Targets from several locations were measured to determine this position-to-thickness relationship. The absolute determination of these target thicknesses is accurate to ~ 20%.

The evaporation of natural K (93.3% ^{39}K) targets required special techniques. Potassium forms oxides in air and is therefore quite unstable and dangerous to handle. To make stable potassium targets the potassium was first evaporated at ~ 10^{-5} Torr pressure by resistive heating techniques onto carbon, or carbon and Formvar, backed frames. (Potassium has a vapor pressure of 60°C at 10^{-6} Torr.) Then still under vacuum, a thin layer of gold in a separate tungsten dimple boat was evaporated over the potassium layer, forming a sandwich to protect the potassium from air. The potassium material was prepared for evaporation by cutting off a small piece of oxide-free potassium in an Ar atmosphere glove bag with the potassium immersed in mineral oil. The potassium used in the evaporation was wiped clean of mineral oil in the glove bag before being placed in the molybdenum (0.005") open boat, and immediately pumped down to vacuum. Care was taken to outgas slowly the potassium with a shield between the target frames and boat in order to evaporate any mineral oil left on the potassium sample. Both the potassium and gold evaporations were monitored by the vibrating crystal technique.

During all evaporations appropriate safety precautions for the handling and disposal of dangerous materials were followed. Gloves were always worn to minimize contact of targets with moisture and

contaminants. All targets were stored under vacuum until used in the experiment. Transfers of targets during the experiment to the target rod were performed in an Ar-filled glove bag.

3.3 Experiment--Setup. A dispersion matched 42.4 MeV proton beam from the Princeton AVF (Azimuthally Varying Field) cyclotron was used during the (p,t) and (p,^{3}He) measurements in conjunction with the QDDD (quadrupole-dipole-dipole-dipole) magnetic spectrograph. (See Fig. 3-1.) The QDDD spectrograph is well suited for high-resolution nuclear spectroscopy because of its high dispersion (8.72 MeV-mm/keV) and its large solid angle (14.7 msr) [Kou74]. The spectrograph was adjusted each run to correct for the kinematic spread of the particular nuclear reaction. Unlike many spectrographs where the adjustment for kinematics is made by physically adjusting the focal plane, in the QDDD the correction is applied by a multipole lens located between two dipoles, and also by a hexapole at the entrance to the spectrograph.

For each target an energy excitation region of ~ 4 MeV above the lowest T=3/2 states in the residual nuclei was observed with the spectrograph for both the (p,t) and (p,^{3}He) reactions. Because of the large dispersion, the energy acceptance for the detectors at the focal plane is about six percent in energy which required taking 4 to 5 spectrograph bites to cover the ~ 4 MeV energy excitation region. The difference in triton and ^{3}He charge and momentum (because of Q-value differences) for the reactions required taking separate spectrograph bites for each reaction. The spectrograph settings for each run were determined by using the program RELKIN [Kou80]. The beam was stopped in

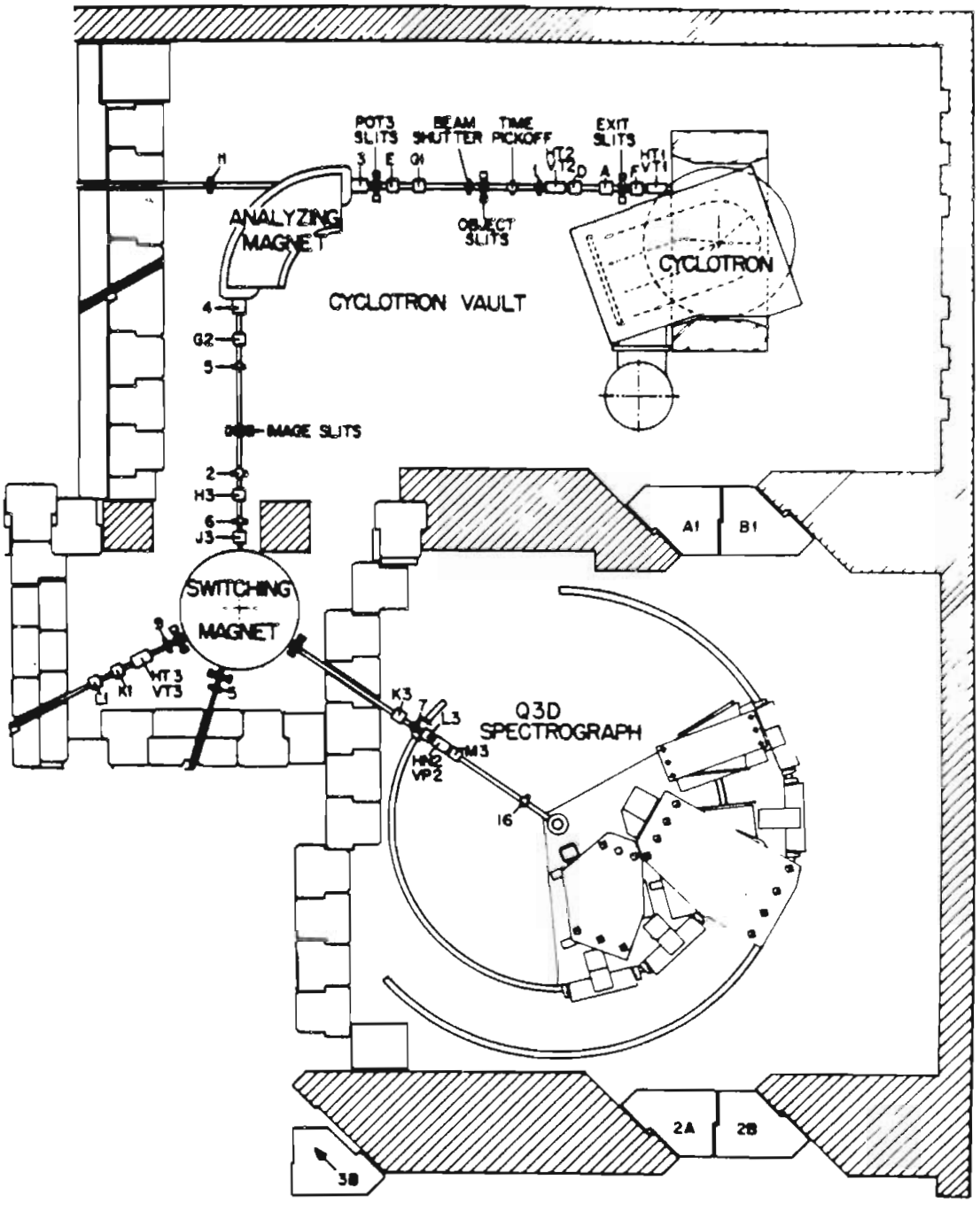

Figure 3-1 Princeton University cyclotron laboratory diagram showing QDDD spectrograph and associated beam transport.

a continuous-flow water Faraday cup with a remote storage container located away from the target to reduce radioactive background counts from the stop.

The tritons and helions were detected using a 60-cm resistive division position sensitive type gas proportional counter (PSGP) backed by a plastic scintillator [Kou74]. Particle-identification was obtained from the PSGP counter which yields mass and position information while the scintillator identified the charge, Z, of the particle. Data were acquired using the Princeton Eclipse S/230 computer and the code ACQUIRE [Kou78]. All measurements were made with the QDDD at a laboratory angle of 15^{o}.

3.4 Experiment—Analysis. The data tape from the Eclipse was translated at TUNL to VAX 11/780 compatible form. Sums and channel numbers for the (p,t) and (p,^{3}He) spectra were obtained by peak-fitting methods using the TUNL XSYS [Gou81] and peak-fitting code SPECTR [Var82].

The energy calibrations of peaks were calculated at TUNL on the VAX using the code CALIB [Kou74], which is specifically for use with QDDD data. The radius of curvature, ρ, for a particle from a specific reaction is calculated by a relativistic kinematics routine which also includes energy loss of incident and outgoing reaction products in the target and target backing. The relationship of radius of curvature to channel number is

$$\rho = a + b(k) * (x - x_{o}) + c * (x - x_{o})^{2} + \ldots \qquad 3\text{-}1$$

where x is the spectra channel number, and k is the kinematic parameter defined as

$$k = -\frac{1}{\rho}\frac{dp}{d\theta} \qquad 3\text{-}2$$

with p the outgoing reaction particle momentum. The kinematic parameter accounts for the finite acceptance angle of the spectrograph and the kinematical energy spread for the reaction being observed over this angular range $d\theta$. The code takes the changing dispersion into effect to first order with

$$b(k) = \frac{b_o}{(1 + 0.35k)} \; . \qquad 3\text{-}3$$

The channel x_o is the channel that is not affected by changes in k. Known reference reactions are used to calibrate the focal plane and to determine the constants a, b_o, and c. The code then calculates the excitation energies of the final state nucleus for the given spectrograph settings. All calculations of ρ were to second order in x.

3.5 Measurements - Calibration Reactions. Six separate calibration runs were taken at five different spectrograph settings for precisely determined energy states in ^{26}Si, ^{27}Si, and ^{25}Al. The reactions and calibration states observed are listed in Table 3-1. The lowest T=3/2 state for each particular reaction was included in the calibration for that set of data, except for ^{35}Cl(p,^{3}He)^{33}S data where the lowest T=3/2 state is obscured by a contaminant peak. The error in the calibration was checked by comparing the states which occurred in

Table 3-1 Princeton QDDD Calibration Reactions.

A summary of reactions used to calibrate the QDDD detector spectra to energy.

Run	Reaction	Freq (MHz)	k	E_x (MeV)	Channel
5	$^{28}Si(p,t)^{26}Si$	58.998	0.023	0.451	825.8
				0.945	615.0
				1.612	365.7
				1.790	306.3
8	$^{28}Si(p,t)^{26}Si$	50.178	0.028	1.796	726.0
				2.783	222.0
11	$^{28}Si(p,d)^{27}Si$	50.179	0.028	0.000	661.0
				0.780	379.0
				0.957	321.0
14	$^{28}Si(p,t)^{26}Si$	51.183	0.023	1.796	335.5
37	$^{27}Al(p,\tau)^{25}Mg$	32.569	0.021	0.000	493.6
				0.585	324.7
				0.975	225.3
43	$^{27}Al(p,\tau)^{25}Mg$	28.196	0.024	7.788	495.7

the energy overlap region of consecutive bites. Normally, the overlap region between bites was ~0.3–0.5 MeV. For the (p,t) data the energy assignment error was determined, from the agreement of calculations with known peaks and from the energy overlap regions, to be $\pm$ 7 keV. (For a few peaks which were on the edges of the detector, or near contaminant peaks, or which had very few counts, the error was $\pm$ 15 keV.)

For the (p,^{3}He) reactions, there were few calibration peaks in the higher channels, so an artificial calibration was input based on agreement between the ^{31}P(p,^{3}He)^{29}Si overlap peaks for three separate runs. This calibration was then used for the (p,^{3}He) data from other targets and checked against those reactions' overlap peaks, with good agreement. The energy assignment error for the (p,^{3}He) reactions was determined similarly to the (p,t) error estimate, with the additional problem that energy loss of the ^{3}He particles in the targets was significant. Thus, the energy assignment of (p,^{3}He) peaks is $\pm$ 12 keV, with a few peaks determined to only $\pm$ 25 keV.

3.5.1 States in ^{25}Al and ^{25}Mg. ^{27}Al(p,t)^{25}Al data were taken over an energy excitation region in ^{25}Al of 7.67 - 11.50 MeV on a target of 120 μg/cm^2 Al. Five separate bites were taken with an observed resolution of 18–20 keV. A composite figure obtained by combining the data from the different energy bites is shown in Fig. 3-2. The ^{27}Al(p,^{3}He)^{25}Mg data cover an energy excitation region of 7.06–10.69 MeV in ^{25}Mg. Three bites were taken over this region. An example of the energy overlap of bites is Fig. 3-3 where all ^{27}Al(p,^{3}He)^{25}Mg bites are shown separately. The observed resolution was 23–28 keV, in which the

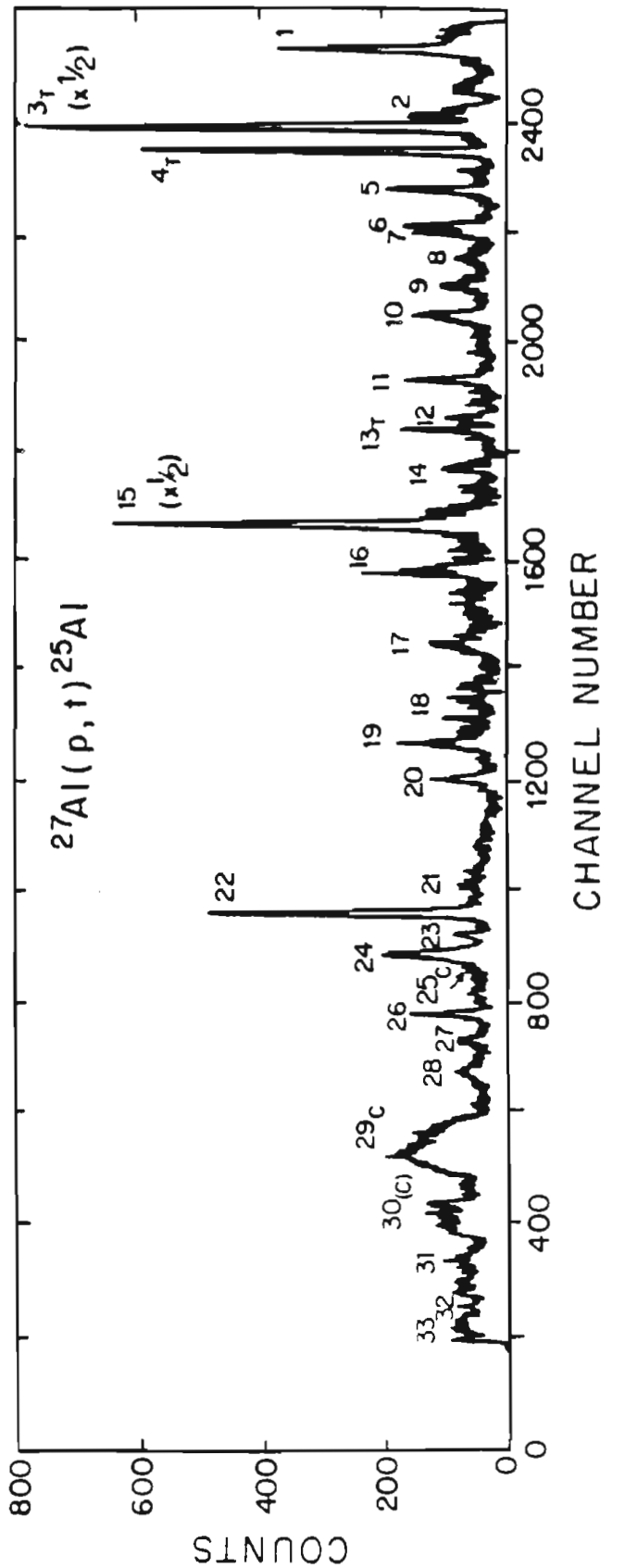

Figure 3-2 Composite ^{27}Al(p,t)^{25}Al spectra at $\theta_L = 15^\circ$ with an incident proton energy of 42.4 MeV.

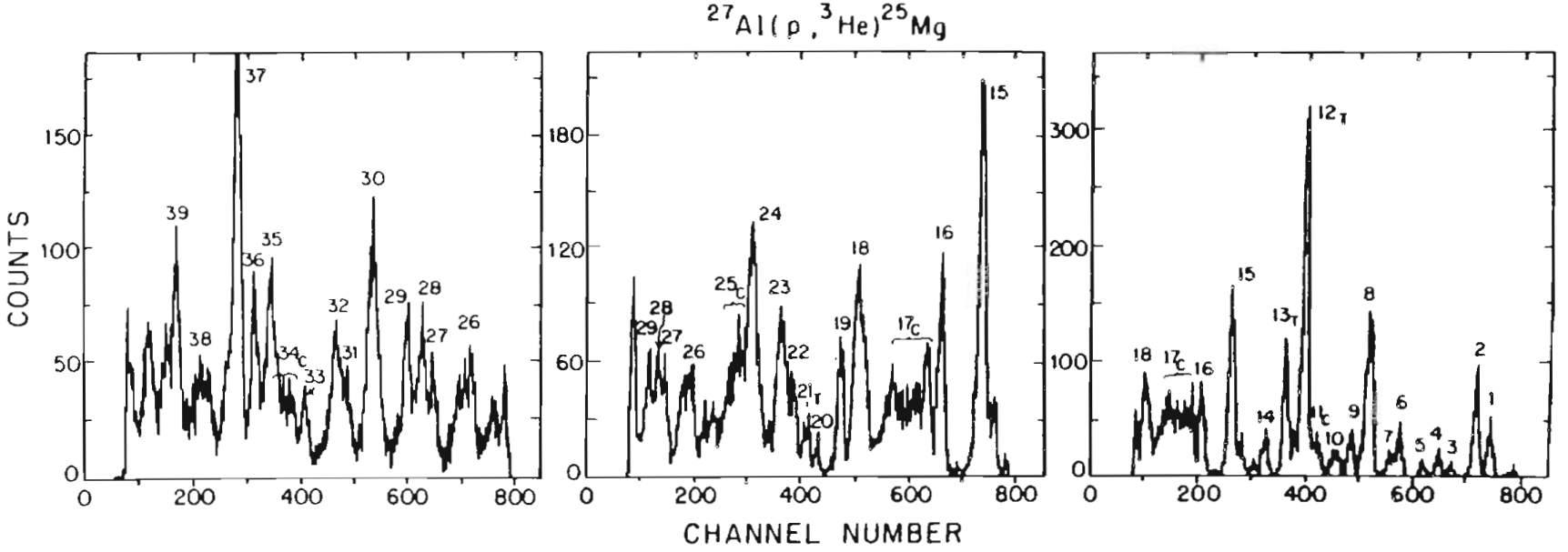

Figure 3-3 Spectra from three ^{27}Al(p,^{3}He)^{25}Mg bites taken with E_p = 42.4 MeV and $\theta_L = 15^{o}$. Note the energy overlap of the bites and the dispersion of the spectra as a function of position.

Table 3-2a Summary Explaining Excitation Energies and Cross Sections Tables.

- Peaks which are labeled subscript "c" represent contaminant peaks in the spectra. The contaminant final state E_x and nucleus are listed.

- Peaks labeled subscript "T" are T=3/2 states as determined by Princeton, Indiana University Cyclotron Facility, or TUNL measurements or a combination of two or more measurements (see text for details of the identifications).

- Peaks labeled subscript "t" are the most likely T=3/2 candidate states (see text for details of identifications).

- For the (p,^{3}He) data the adjusted cross section which has been multiplied by the ratio of triton and ^{3}He wave number is given. This normalizes the (p,^{3}He) data to the (p,t) data as explained in Chapter 2.

- Cross section errors are the statistical errors. There may be absolute errors up to 20%. See individual sections for absolute error determination.

Table 3-2b $^{27}Al(p,t)^{25}Al$ Excitation Energies and Cross Sections.

- Excitation energy errors are ± 7 keV except for cases shown to only 10's of keV where the error is ± 15 keV.
- See Table 3-2a for an explanation of notation.

Peak	E_x (MeV)	$\frac{d\sigma}{d\Omega}$ ± Δ ($\mu b/cm^2$)		Peak	E_x (MeV)	$\frac{d\sigma}{d\Omega}$ ± Δ ($\mu b/cm^2$)	
01	7.69	——		18	9.770	1.06	0.04
02	7.867	1.76	0.08	19	9.847	2.25	0.07
03_T	7.898	19.79	0.26	20	9.978	2.03	0.06
04_T	7.968	6.43	0.15	21	10.262	0.53	0.03
05	8.082	2.10	0.08	22	10.343	6.12	0.11
06	8.193	1.80	0.08	23	10.410	0.62	0.03
07	8.217	1.19	0.06	24	10.465	3.18	0.08
08	8.294	0.69	0.05	25_c *	5.92	------	^{14}O *
09	8.385	1.28	0.07	26	10.642	1.81	0.06
10	8.479	1.60	0.07	27	10.706	0.84	0.04
11	8.714	1.91	0.08	28	10.776	1.56	0.06
12	8.828	1.12	0.09	29_c *	3.35	------	^{10}C *
13_T	8.858	1.64	0.11	30_c *	6.59	------	^{14}O *
14	8.96	1.2	0.09	31	11.30	----	
15	9.135	18.44	0.39	32	11.44	----	
16	9.293	1.72	0.11	33	11.50	----	
17	9.523	2.80	0.15				

Table 3-2c $^{27}Al(p,^{3}He)^{25}Mg$ Excitation Energies and Cross Sections.

- Excitation energy errors are ± 12 keV except for cases shown to only 10's of keV where the error is ± 25 keV.
- See Table 3-2a for an explanation of notation.

Peak	E_x (MeV)	$\frac{d\sigma}{d\Omega}$ (μb/cm²)	± Δ	$\frac{k_t}{k_\tau}\frac{d\sigma}{d\Omega}$ (μb/cm²)	Peak	E_x (MeV)	$\frac{d\sigma}{d\Omega}$ (μb/cm²)	± Δ	$\frac{k_t}{k_\tau}\frac{d\sigma}{d\Omega}$ (μb/cm²)
01	7.078	3.57	0.16		21_T	8.789	1.80	0.09	1.59
02	7.122	7.43	0.23		22	8.842	2.79	0.11	2.47
03	7.206	0.67	0.07		23	8.894	7.84	0.18	
04	7.246	1.33	0.10		24	9.027	----		
05	7.298	0.90	0.08		25_c *	0.72	---------- ^{10}B *		
06	7.387	3.07	0.15		26	9.34	----		
07	7.423	1.75	0.11		27	9.48	1.51	0.07	
08	7.505	12.30	0.30		28	9.517	3.21	0.11	
09	7.581	3.30	0.16		29	9.563	3.09	0.11	
10	7.646	2.17	0.13		30	9.685	7.63	0.17	
11_c *	3.95	---------- ^{14}N *			31	9.79	----		
12_T	7.786	23.41	0.41	20.86	32	9.83	5.08	0.14	4.47
13_T	7.867	8.65	0.25	7.71	33	9.95	2.3	0.06	2.0
14	7.964	2.89	0.15		34_c *	1.74	---------- ^{10}B *		
15	8.130	12.31	0.29		35	10.085	3.77	0.12	3.30
16	8.275	(6.8)	0.22		36	10.159	2.80	0.10	2.45
17_c *	0.00	---------- ^{10}B *			37	10.237	10.03	0.19	8.78
18	8.569	(11.7)	0.29		38	10.38	----		
19	8.648	3.16	0.12		39	10.511	2.55	0.10	
20	8.731	0.67	0.05	0.59					

Table 3-3 T=3/2 levels for A = 25 $T_z=|1/2|$ nuclei. Identification of T=3/2 levels by $^{27}Al(p,t)^{25}Al$ and $^{27}Al(p,^3He)^{25}Mg$.

- ΔE (in MeV) is defined as $E_x - E_x$(first T=3/2) - E_x(^{25}Na analog).
- A peak number with the subscript $_T$ indicates the state is the T=3/2 state. (See text.)
- A peak number with the subscript $_t$ indicates the most likely T=3/2 candidate.
- An E_x followed by a superscript ^{I} indicates the T=3/2 state was identified by the IUCF measurements.
- The previously known states, as listed in Table 2-1 are shown in columns 1, 2, 4, and 5.
- All energies are given in MeV.

^{25}Na		^{25}Mg		$^{27}Al(p,^3He)^{25}Mg$				^{25}Al		$^{27}Al(p,t)^{25}Al$					^{25}Si	
E_x	J^π	E_x	ΔE	Peak	E_x	ΔE	$\frac{d\sigma}{d\Omega}_{Rel}$	E_x	ΔE	Peak	E_x	ΔE	$\frac{d\sigma}{d\Omega}_{Rel}$	E_R	E_x	ΔE
0.0	$5/2^+$	7.788	0.0	12_T	7.786^I	0.0	1.00	7.901	0.0	03_T	7.898^I	0.0	1.00	5.861	0.0	
0.090	$3/2^+$	7.864	-0.01	13_T	7.867^I	-0.01	0.37	7.970	-0.02	04_T	7.968^I	-0.02	0.32	5.934	0.04	-0.05
1.069	$1/2^+$	8.836	-0.02	20	8.731	-0.12	0.03			12	8.828	-0.14	0.06	6.830	0.815	-0.25
				21_T	8.789^I	-0.07	0.08			13_T	8.858^I	-0.11	0.08	6.861		
				22	8.842	-0.01	0.12			14	9.135	0.17	0.93	7.150		
2.202	$3/2^+$			32	9.83	-0.16	0.22			19	9.847	-0.25	0.11	7.891	1.963	-0.24
				33_t	9.95	-0.04	0.10			20_t	9.978	-0.12	0.10	8.028		
2.417	$(7/2^+)$			35	10.085	-0.12	0.16			21_t	10.262	-0.05	0.03	8.324	2.373	-0.04
				36	10.159	-0.04	0.12			22	10.343	0.03	0.31	8.408		
				37	10.237	0.03	0.43			23	10.410	0.10	0.03	8.478		
2.788										26_t	10.642	-0.04	0.09	8.719	2.606	-0.18
										27	10.706	0.02	0.04	8.786		

target resolution is included. Although the average target thickness was known to be 120 $\mu g/cm^2$, it is suspected from the observed resolution that the target was of non-uniform thickness.

The excitation energies and cross sections for the observed peaks are presented in Table 3-2, with contaminant peaks identified and labeled with subscript "c". For reference, Table 3-2a lists the special symbols and notation used to present the data in Tables 3-2b, 3-2c, 3-4, 3-6, and 3-8. The errors listed for the cross sections are statistical. Table 3-3 presents the excitation energies for the candidate T=3/2 states along with their predicted (p,p) resonance energies. In cases where several possible peaks are in the excitation region where an analog state is expected, all are listed. For convenience, states which have been determined to be T=3/2 states by (p,t)-(p,^{3}He) angular distribution data taken at IUCF (to be presented in the next chapter), or by a combination of the Princeton (p,t)-(p,^{3}He) data and TUNL ($\vec{p}$,p) data (also to be presented in later chapters), or by previous results, are indicated by a subscript "T", although the isospin of these states was not assigned by the single-angle (p,t) and (p,^{3}He) data alone. States which are the most likely T=3/2 states, but have less evidence from which to uniquely assign isospin are indicated by subscript "t".

3.5.2 States in ^{29}P and ^{29}Si. An energy excitation region of 7.72-12.31 MeV in ^{29}P was covered by measurements of five ^{31}P(p,t)^{29}P energy bites during six runs with an experimental resolution of 12-15 keV. Four bites covering an energy excitation region in ^{29}Si of 7.74-12.18 MeV were measured for the ^{31}P(p,^{3}He)^{29}Si reaction where the

observed resolution was 18-25 keV. A 110 $\mu g/cm^2$ phosphorus target with 11 $\mu g/cm^2$ of carbon and ~20 $\mu g/cm^2$ Formvar backing was used for both the (p,t) and (p,^{3}He) measurements. Composite spectra for the two reactions are shown in Figs. 3-4 and 3-5. None of the composite figures from the Princeton work are exactly linear on the x-axis, but the energies assigned to the peaks are correct since they are calculated by the program CALIB which accounts for the changing spectrograph dispersion. The target backing introduces several strong contaminant peaks. The peaks are very broad as a result of kinematical broadening, since the spectrograph is optimized for the kinematics corresponding to the heavier phosphorus target. Excitation energies and cross sections are presented in Table 3-4 for both reactions. Table 3-5 is a summary of T=3/2 and possible T=3/2 states. In several cases in the (p,^{3}He) data the contaminant peaks obscure any possible ^{31}P(p,^{3}He)^{29}Si peaks. Note that several doublet peaks in the (p,^{3}He) data are indicated by superscripts "A" and "B". The doublets were assigned based on their peak widths and confirmed as ^{29}P states by the IUCF angular distribution data measurements. It can be seen that for many cases the later (p,p) resonance work at TUNL and/or (p,t)-(p,^{3}He) angular distributions from Indiana usually eliminated all but one candidate state for assignment as a T=3/2 state.

3.5.3 States in ^{33}Cl and ^{33}S. States in ^{33}Cl from 5.31-9.57 MeV were observed with a resolution of 23-26 keV during six runs covering four energy bites on ^{35}Cl(p,t)^{33}Cl. After taking several (p,t) and (p,^{3}He) bites it was discovered that the $BaCl_2$ target was unstable under the beam of 0.7-1.0 μA and that the target had been evaporating. Thus,

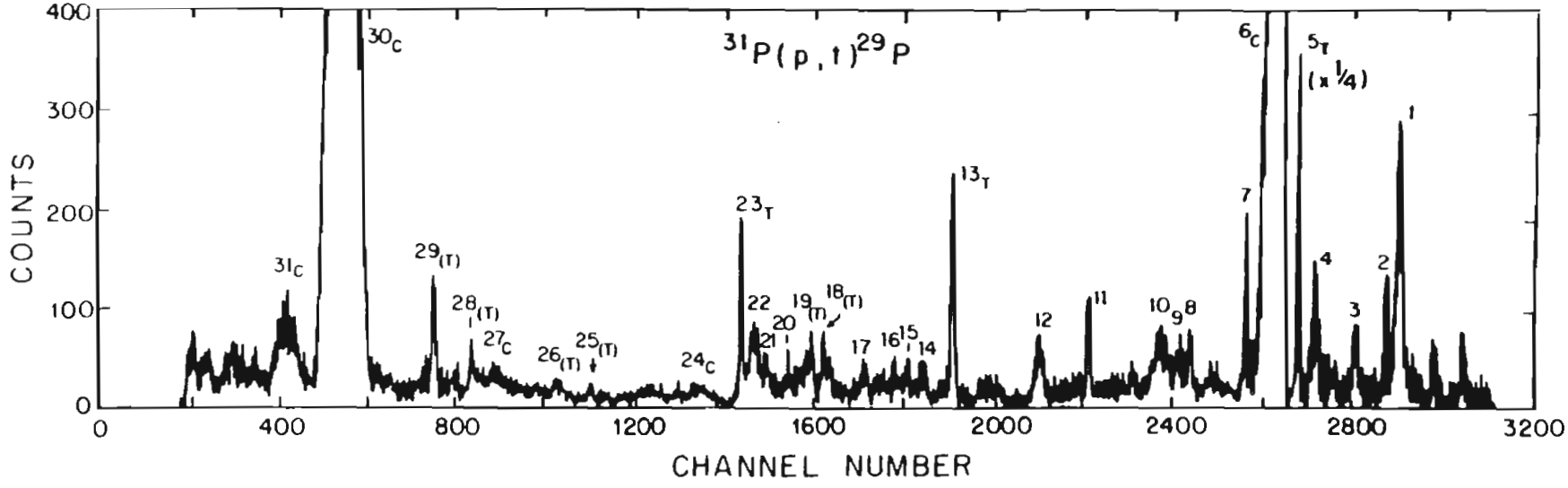

Figure 3-4 Composite $^{31}P(p,t)^{29}P$ spectra at $\theta_L = 15^o$ with an incident proton energy of 42.4 MeV. The broad strong peaks are contaminant peaks from the target backing.

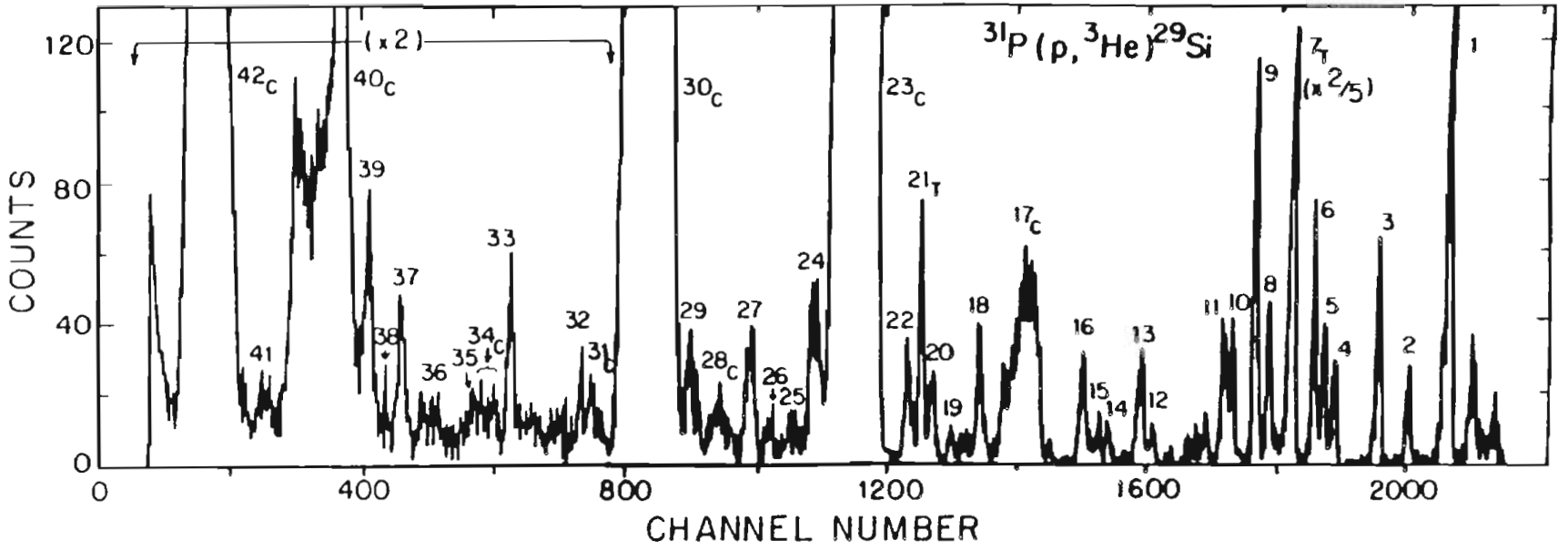

Figure 3-5 Composite $^{31}P(p,^{3}He)^{29}Si$ spectra at $\theta_L = 15^{o}$ with an incident proton energy of 42.4 MeV. The broad strong peaks are contaminant peaks from the target backing.

Table 3-4a $^{31}P(p,t)^{29}P$ Excitation Energies and Cross Sections.

° Excitation energy errors are ± 7 keV except for cases shown to only 10's of keV where the error is ± 15 keV.
° See Table 3-2a for an explanation of notation.

Peak	E_x (MeV)	$\frac{d\sigma}{d\Omega}$ ± Δ ($\mu b/cm^2$)	Peak	E_x (MeV)	$\frac{d\sigma}{d\Omega}$ ± Δ ($\mu b/cm^2$)
01	7.99	7.54 0.33	17	9.981	1.19 0.07
02	8.034	1.58 0.15	18	10.136	0.34 0.04
03	8.149	1.55 0.15	19	10.179	0.52 0.05
04	8.309	2.64 0.19	20	10.282	1.45 0.08
05_T	8.384	17.24 0.50	21	10.360	1.80 0.09
06_c *	0.0	------ ^{10}C *	22	10.423	3.86 0.13
07	8.602	1.75 0.16	23_T	10.48	2.45 0.11
08	8.80	----	24_c *	5.17	------ ^{14}O *
09	8.83	----	25	10.94	----
10	8.886	----	26	11.05	----
11	9.165	1.81 0.09	27_c *	5.92	------ ^{14}O *
12	9.370	4.21 0.14	28	11.356	1.34 0.08
13_T	9.659	3.54 0.13	29	11.480	1.98 0.09
14	9.765	----	30_c *	3.35	------ ^{10}C *
15	9.82	----	31_c *	6.59	------ ^{14}O *
16	9.865	----			

Table 3-4b $^{31}P(p,^{3}He)^{29}Si$ Excitation Energies and Cross Sections.

- Excitation energy errors are ± 12 keV except for cases shown to only 10's of keV where the error is ± 25 keV.
- See Table 3-2a for an explanation of notation.

Peak	E_x (MeV)	$\frac{d\sigma}{d\Omega}$ ± Δ ($\mu b/cm^2$)	$\frac{k_t}{k_\tau}\frac{d\sigma}{d\Omega}$ ($\mu b/cm^2$)	Peak	E_x (MeV)	$\frac{d\sigma}{d\Omega}$ ± Δ ($\mu b/cm^2$)	$\frac{k_t}{k_\tau}\frac{d\sigma}{d\Omega}$ ($\mu b/cm^2$)
01	7.848	1.61 0.13		19	9.560	0.59 0.05	
02	7.945	1.11 0.11		20	9.632	1.71 0.09	1.51
03	8.035	2.96 0.18		21_T	9.678	3.55 0.13	3.13
04	8.177	1.47 0.13		22	9.733	2.27 0.11	2.00
05	8.213	1.95 0.14		23_c *	0.0	---------- ^{10}B *	
06	8.245	2.80 0.17		24	10.11	6.07 0.22	
07_T	8.331	17.83 0.44	15.7	25	10.177	1.31 0.10	
08	8.404	2.39 0.16		26	10.24	1.19 0.10	
09	8.453	5.72 0.25		27^A	10.295	2.40 0.15	
10	8.540	1.82 0.14		27^B	10.315	1.36 0.12	
11	8.571	2.18 0.15		28_c *	5.11	---------- ^{14}N *	
12	8.862	0.58 0.08		29^A	10.472	1.20 0.12	1.04
13	8.899	2.13 0.10		29^B	10.498	2.52 0.16	2.19
14	9.000	.61 0.06		30_c *	0.72	---------- ^{10}B *	
15	9.035	.68 0.06		31_c *	5.69	---------- ^{14}N *	
16	9.083	2.18 0.11		32	10.87	----	
17_c *	3.95	---------- ^{14}N *		33	11.04	2.24 0.14	
18	9.449	2.37 0.11		34_c *	5.83	---------- ^{14}N *	

continued

Table 3-4b Continued

Peak	E_x (MeV)	$\frac{d\sigma}{d\Omega} \pm \Delta$ ($\mu b/cm^2$)	$\frac{k_t}{k_\tau}\frac{d\sigma}{d\Omega}$ ($\mu b/cm^2$)	Peak	E_x (MeV)	$\frac{d\sigma}{d\Omega} \pm \Delta$ ($\mu b/cm^2$)	$\frac{k_t}{k_\tau}\frac{d\sigma}{d\Omega}$ ($\mu b/cm^2$)
35	11.139	——		39	11.470	----	
36	11.265	0.94 0.09		40_c *	1.74	----------	^{10}B *
37	11.369	——		41	11.831	1.83 0.08	
38	11.415	----		42_c *	2.15	----------	^{10}B *

Table 3-5 T=3/2 levels for A = 29 $T_z=|1/2|$ nuclei. Identification of T=3/2 levels by $^{31}P(p,t)^{29}P$ and $^{31}P(p,^3He)^{29}Si$.

- ΔE (in MeV) is defined as E_x - E_x(first T=3/2) - E_x(^{29}Al analog).
- A peak number with the subscript $_T$ indicates the state is the T=3/2 state. (See text.)
- A peak number with the subscript $_t$ indicates the most likely T=3/2 candidate.
- An E_x followed by a superscript ^{I} or ^{i} indicates the T=3/2 state was identified by the IUCF measurements.
- A peak number with the superscript ^{A} or ^{B} is an unresolved doublet.
- The previously known states, as listed in table 2-1 are shown in columns 1, 2, 4, and 5.
- All energies are given in MeV.

^{29}Al		^{29}Si		$^{31}P(p,^3He)^{29}Si$				^{29}P		$^{31}P(p,t)^{29}P$					^{29}S	
E_x	J^π	E_x	ΔE	Peak	E_x	ΔE	$\frac{d\sigma}{d\Omega}_{Rel}$	E_x	ΔE	Peak	E_x	ΔE	$\frac{d\sigma}{d\Omega}_{Rel}$	F_R	E_x	ΔE
0.0	$5/2^+$	8.331	0.0	07_T	8.331^I	0.0	1.00	8.379	0.0	05_T	8.384^I	0.0	1.00	5.838	0.0	
1.398	$1/2^+$	9.685	-0.04	20_T	9.678^I	-0.05	0.20	9.743	-0.03	13_T	9.659^I	-0.13	0.21	7.159		
1.754	$7/2^+$									17	9.981	-0.15	0.07	7.492		
										18^t	10.136^i	0.00	0.02	7.653		
										19	10.179	0.05	0.03	7.697		
2.224	$3/2^+$			29^A	10.472	-0.08	0.07									
				29^B	10.498^I	-0.06	0.14			23_T	10.48^I	-0.13	0.14	8.10		
2.865	$3/2^+$									25	10.94	-0.32	----	8.48		
										26	11.05	-0.21	----	8.60		
3.062	$5/2^+$			37_T	11.369^I	-0.02	----			28_T	11.356^I	-0.09	0.08	8.916		
3.184	$5/2^+$			39_T	11.470^I	-0.05	----			29_T	11.480^I	-0.08	0.11	9.045		
3.433	$1/2^+$			$--_T$	11.72^I	-0.04	----			$--_T$	11.70^I	-0.12	----	9.27		

all but one of the energy bites were retaken with a new target while limiting the beam intensity to levels which did not deteriorate the target ($\leq$ 300 nA). The one bite not retaken was the lowest energy bite for $^{35}Cl(p,t)^{33}Cl$ where it was clear that other than the lowest T=3/2 state which was already known, there were no other T=3/2 states present. Thus, this lowest bite is not shown in the $^{35}Cl(p,t)^{33}Cl$ composite figure (Fig. 3-6) which covers a range of excitation beginning at 6.50 MeV. In an attempt to make a more stable and thicker target, a new target was made by placing two $BaCl_2$ targets together (with their backings away from each other) to form a sandwich and seal the $BaCl_2$ from the vacuum. The new target, ~ 260 $\mu g/cm^2$ of $BaCl_2$, was tested for stability by taking several runs with identical QDDD settings and comparing the yields.

The $^{35}Cl(p,^3He)^{33}S$ composite spectrum which consists of four energy bites and covers the energy excitation region in ^{33}S from 4.64-10.28 MeV with a resolution of 25-33 keV is shown in Fig. 3-7. Again there are problems with contaminant peaks in the $(p,^3He)$ spectra because of the backing materials, which for the sandwich target resulted in 19.5 $\mu g/cm^2$ of carbon and ~ 40 $\mu g/cm^2$ of Formvar. No discernible contaminant peaks for the barium isotopes were identified, most likely because of the low Q-value for reactions with contaminant nuclei, and thus high excitation energies for states populated in the residual nuclei. The cross section and excitation energies for the (p,t) and $(p,^3He)$ spectra are presented in Table 3-6 and the summary of T=3/2 states is listed in Table 3-7.

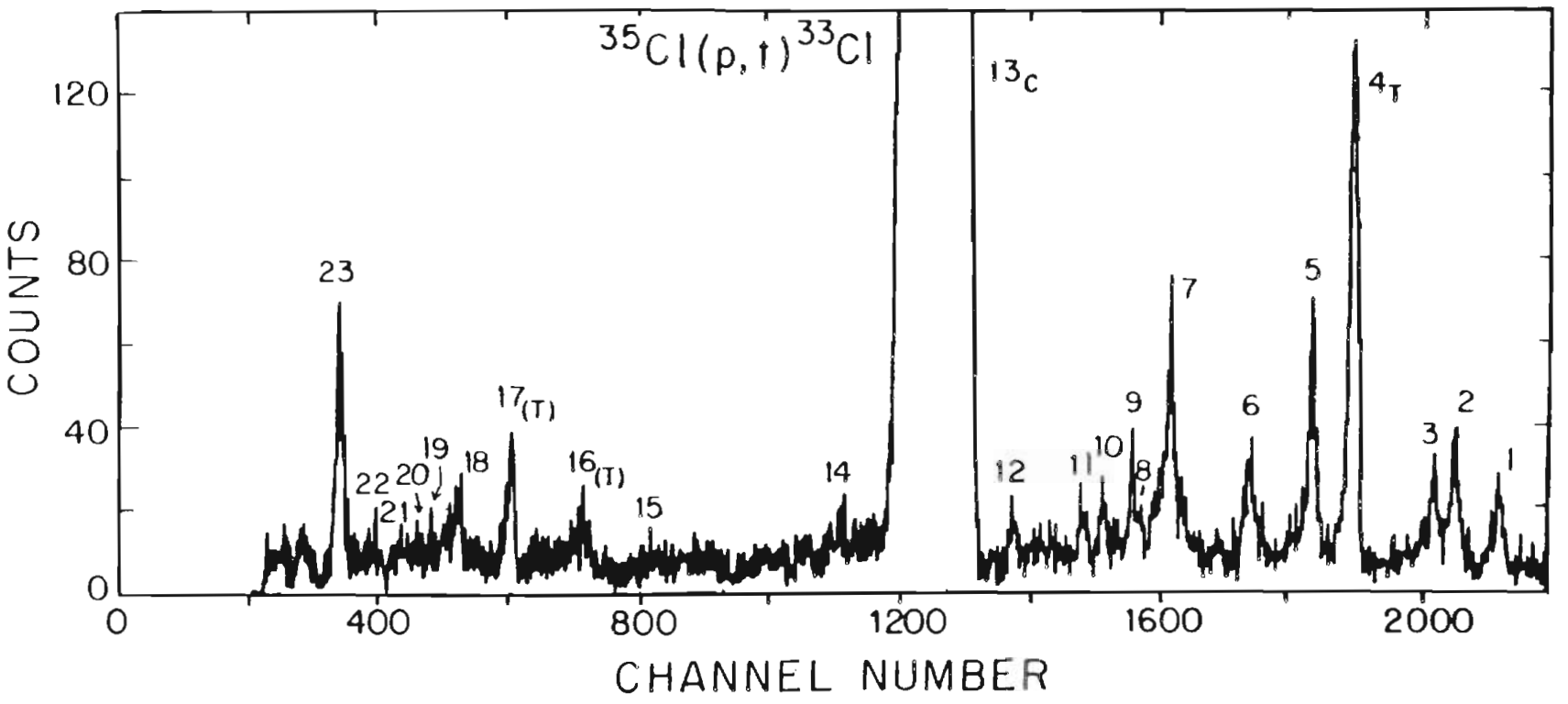

Figure 3-6 Composite ^{35}Cl(p,t)^{33}Cl spectra at $\theta_L = 15^o$ with $E_p = 42.4$ MeV. The broad contaminant peak is from the target backing. The bite containing the lowest T=3/2 state is not shown.

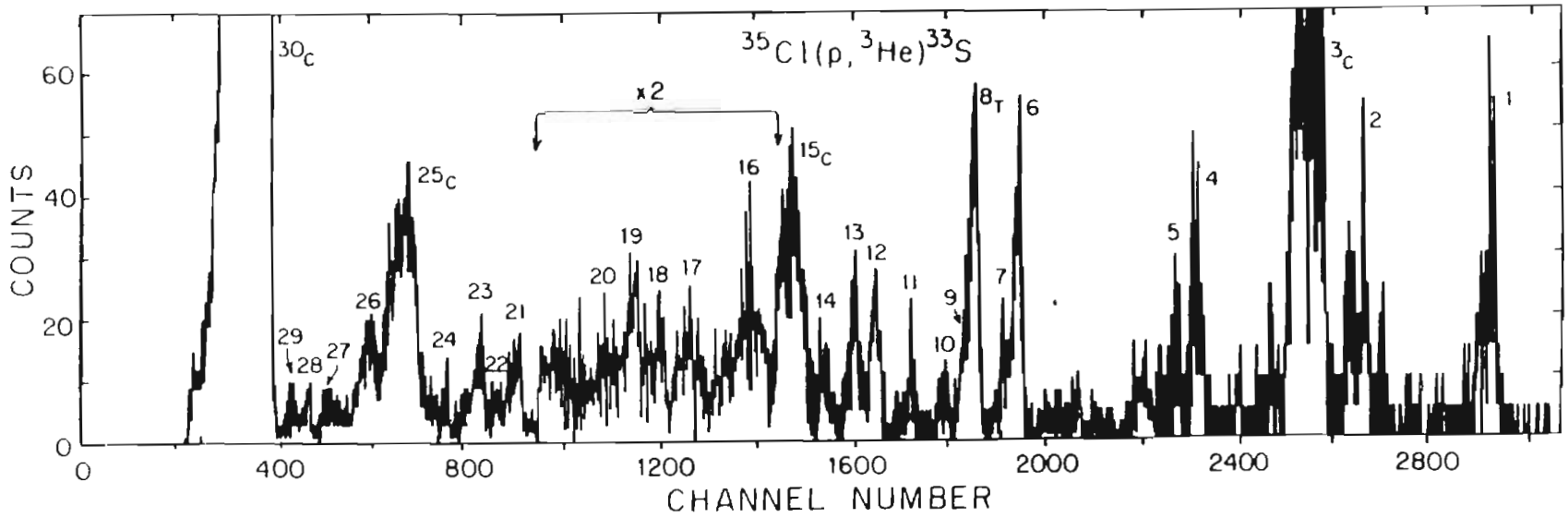

Figure 3-7 Composite $^{35}Cl(p,^{3}He)^{33}S$ spectra at $\theta_L = 15^{o}$ with an $E_p = 42.4$ MeV. The broad strong peaks are contaminants from the target backing. Here one obscures the lowest T=3/2 state.

Table 3-6a $^{35}Cl(p,t)^{33}Cl$ Excitation Energies and Cross Sections.

- Excitation energy errors are ± 7 keV except for cases shown to only 10's of keV where the error is ± 15 keV.
- See Table 3-2a for an explanation of notation.

Peak	E_x (MeV)	$\frac{d\sigma}{d\Omega}$ ± Δ ($\mu b/cm^2$)		Peak	E_x (MeV)	$\frac{d\sigma}{d\Omega}$ ± Δ ($\mu b/cm^2$)	
00_T	5.54(8)	----		12	7.764	3.1	0.19
01	6.539	----		13_c *	0.0	------	^{10}C *
02	6.626	----		14	8.259	0.6	0.08
03	6.669	----		15	8.681	----	
04_T	6.848	21.2	0.50	16	8.817	1.0	0.11
05	6.946	9.7	0.33	17	8.988	5.2	0.27
06	7.095	5.8	0.24	18	9.109	3.5	0.22
07	7.309	9.2	0.33	19	9.178	1.4	0.14
08	7.390	1.2	0.12	20	9.213	1.7	0.15
09	7.412	2.9	0.18	21	9.252	1.8	0.16
10	7.487	1.1	0.11	22	9.313	1.3	0.13
11	7.558	3.7	0.20	23	9.412	8.6	0.34

Table 3-6b $^{35}Cl(p,^{3}He)^{33}S$ Excitation Energies and Cross Sections.

- Excitation energy errors are ± 12 keV except for cases shown to only 10's of keV where the error is ± 25 keV.
- See Table 3-2a for an explanation of notation.

Peak	E_x (MeV)	$\frac{d\sigma}{d\Omega}$ ($\mu b/cm^2$)	± Δ	$\frac{k_t}{k_\tau}\frac{d\sigma}{d\Omega}$ ($\mu b/cm^2$)
01	4.770	9.1	0.96	
02	5.283	7.7	0.88	
03_c *	0.0	----------	^{14}N *	
04	6.125	7.0	0.84	
05	6.238	3.8	0.62	
06	6.723	14.6	0.70	
07	6.783	2.9	0.31	
08_T	6.903	20.3	0.83	17.83
09	6.957	2.9	0.31	2.5
10	7.042	2.2	0.27	
11	7.193	2.6	0.30	2.3
12	7.358	9.2	0.56	8.0
13	7.460	7.3	0.50	6.4
14	7.613	2.8	0.31	
15_c *	2.31	----------	^{14}N *	
16	8.030	9.1	0.43	
17	8.232	7.0	0.37	
18	8.348	4.0	0.28	
19	8.455	7.7	0.39	
20	8.575	----		
21	8.969	8.6	0.37	7.4
22	9.039	1.9	0.09	1.6
23	9.099	5.9	0.28	1.2
24	9.220	1.4	0.13	1.2
25_c *	3.95	----------	^{14}N *	
26	9.512	10.1	0.36	8.7
27	9.679	1.6	0.14	1.4
28	9.773	1.8	0.15	
29	9.841	1.2	0.13	
30_c *	0.0	----------	^{10}B *	

Table 3-7 T=3/2 levels for A = 33 $T_z=|1/2|$ nuclei. Identification of T=3/2 levels by $^{35}Cl(p,t)^{33}Cl$ and $^{35}Cl(p,^3He)^{33}S$.

- ΔE (in MeV) is defined as E_x - E_x(first T=3/2) - E_x(^{33}P analog).
- A peak number with the subscript $_T$ indicates the state is the T=3/2 state. (See text.)
- A peak number with the subscript $_t$ indicates the most likely T=3/2 candidate.
- The previously known states, as listed in table 2-1 are shown in columns 1, 2, 4, and 5.
- All energies are given in MeV.

^{33}P		^{33}S		$^{35}Cl(p,^3He)^{33}S$				^{33}Cl		$^{35}Cl(p,t)^{33}Cl$					^{35}Ar	
E_x	J^π	E_x	ΔE	Peak	E_x	ΔE	$\frac{d\sigma}{d\Omega}_{Rel}$	E_x	ΔE	Peak	E_x	ΔE	$\frac{d\sigma}{d\Omega}_{Rel}$	E_R	E_x	ΔE
0.0	$1/2^+$	5.475	0.0					5.544	0.0	00_T	5.548	0.0	----	3.371	0.0	
1.432	$3/2^+$	6.905	-.002	08_T	6.903	-.004	1.00	6.984	0.01	04_T	6.848	-0.13	1.00	4.714	1.344	-0.09
				09	6.957	0.05	0.14			05	6.946	-0.03	0.46	4.815		
1.848	$5/2^+$	7.337	0.01	11	7.193	-0.13	0.13	7.399	0.01	07	7.309	-0.09	0.43	5.189	1.786	-0.06
				12	7.358	0.04	0.45			08_T	7.390	-.006	0.06	5.273		
				13	7.460	0.14	0.36			09	7.412	0.02	0.14	5.296		
2.539	$3/2^+$	8.107	0.09	16	8.030	0.02	0.45	8.100	0.02							
3.275	+									15	8.681	-0.14	----	6.604		
										16	8.817	-0.01	0.05	6.744		
3.490	$5/2^+$			21	8.969	. 004	0.42			17_t	8.988	-0.05	0.25	6.921		
3.628	$7/2^+$			22	9.039	-0.06	0.09			18_t	9.109	-0.07	0.17	7.046		
				23	9.099	-.004	0.29			19	9.178	0.002	0.07	7.117		
				24	9.220	0.12	0.07			20	9.213	0.04	0.08	7.153		
4.05				26	9.512	-0.01	0.50			23	9.412	-0.19	0.41	7.358		
				27	9.679	0.15	0.08									

3.5.4 States in ^{37}K and ^{37}Ar. Four energy bites were taken for $^{39}K(p,t)^{37}K$ covering an energy excitation region in ^{37}K of 4.33-8.59 MeV. The $^{39}K(p,^{3}He)^{37}Ar$ energy bites covered an energy excitation region of 4.13-9.02 MeV which were also taken in four energy bites. The observed resolution was 26-32 keV for the (p,t) data and 40-48 keV for (p,^{3}He) data. This was not as good a resolution as desired. The composite spectra are presented in Figs. 3-8 and 3-9. Two different targets were used to acquire the data. The targets were cross-normalized in both the (p,t) and (p,^{3}He) case by repeating identical QDDD energy bites.

For all four targets there were a large number of outgoing deuterons, and hence the triton and deuteron windows had to be carefully set and monitored, especially for the higher bites. For all but one of the (p,t) bites the only evidence for deuteron "punch-through" were very small broad vestiges of peaks in the (p,t) spectra corresponding to very strong peaks in the (p,d) spectrum. However, there was one $^{39}K(p,t)^{37}K$ spectrum where deuterons from the (p,d) reaction did punch through into the triton spectra. These peaks are labeled in the figure and easily identified by their broad width. The excitation energies and cross sections are given in Table 3-8 while the identification of T=3/2 states is found in Table 3-9. The targets used were ~ 115 and ~ 170 $\mu g/cm^2$ thick potassium with ~ 60 $\mu g/cm^2$ of gold. There was no evidence for any known peak due to the Au. The carbon and Formvar backing material resulted in several large contaminant peaks in the (p,^{3}He) data.

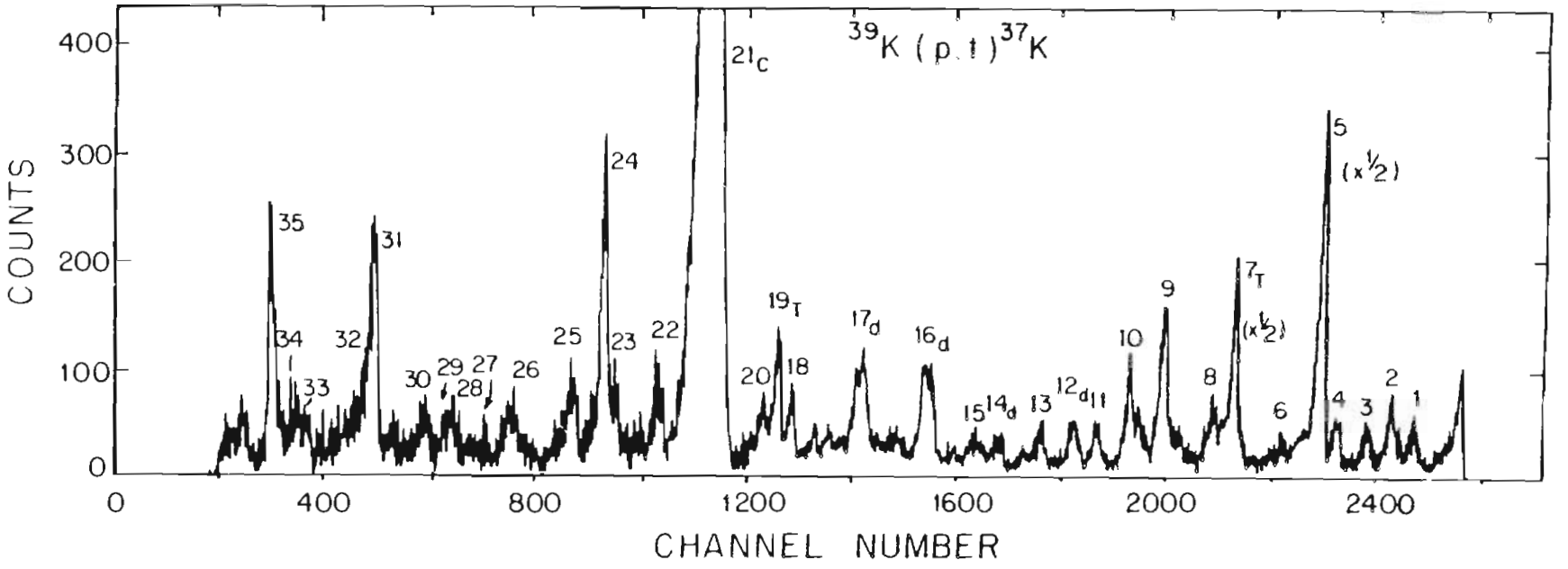

Figure 3-8 Composite $^{39}K(p,t)^{37}K$ spectra at $\theta_L = 15^\circ$ with an incident proton energy of 42.4 MeV. The broad peak is a contaminant peak from the backing. Note several deuteron punch-through peaks.

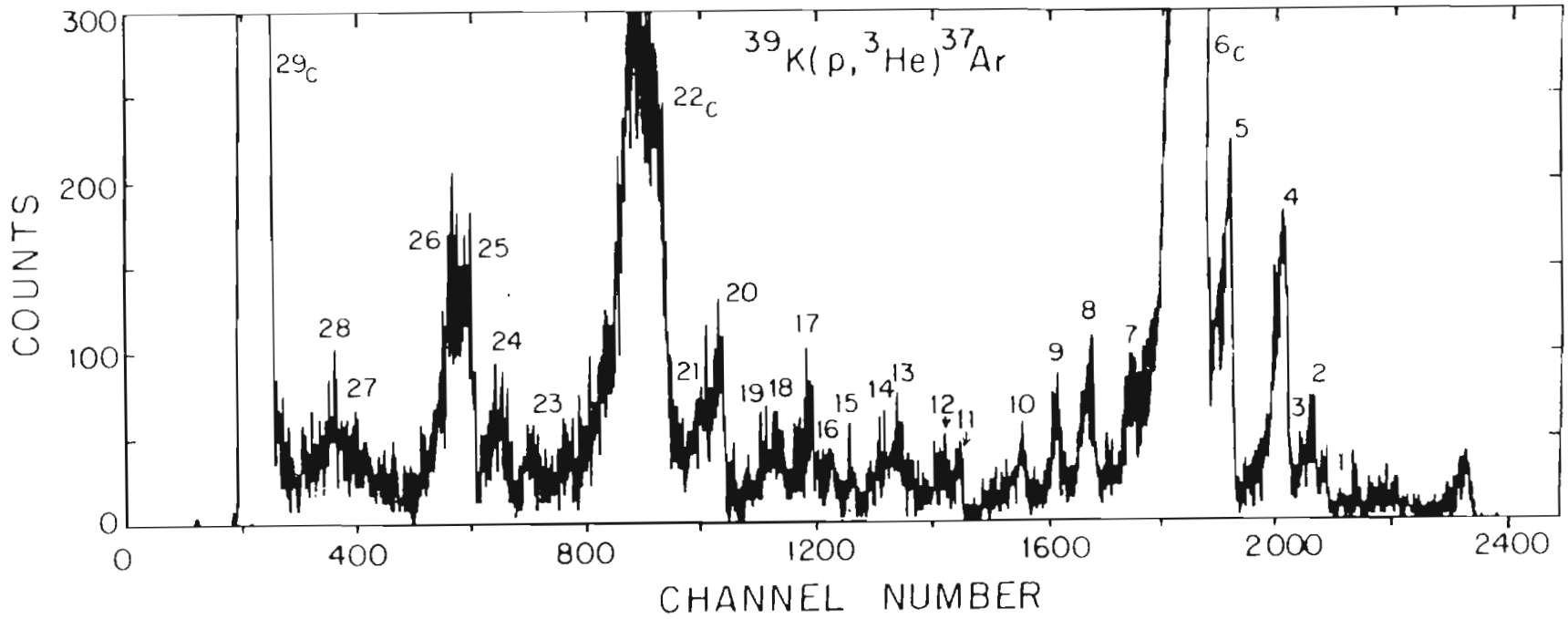

Figure 3-9 Composite $^{39}K(p,^{3}He)^{37}Ar$ spectra at $\theta_L = 15^{o}$ with an incident proton energy of 42.4 MeV. The broad strong peaks are contaminant peaks from the target backing.

Table 3-8a $^{39}K(p,t)^{37}K$ Excitation Energies and Cross Sections.

- Excitation energy errors are ± 7 keV except for cases shown to only 10's of keV where the error is ± 15 keV.
- See Table 3-2a for an explanation of notation.

Peak	E_x (MeV)	$\frac{d\sigma}{d\Omega}$ ± Δ ($\mu b/cm^2$)		Peak	E_x (MeV)	$\frac{d\sigma}{d\Omega}$ ± Δ ($\mu b/cm^2$)	
01	4.417	1.98	0.09	19	6.692	4.38	0.19
02	4.490	2.46	0.10	20	6.753	1.91	0.14
03	4.566	1.75	0.09	21_c *	0.0	------	^{10}C *
04	4.669	0.61	0.05	22	7.183	3.10	0.16
05	4.731	4.79	0.15	23	7.346	2.81	0.16
06	4.866	0.86	0.06	24	7.388	10.50	0.30
07_T	5.052	21.75	0.31	25	7.482	5.15	0.21
08	5.129	1.89	0.09	26	7.646	3.24	0.20
09	5.326	6.03	0.16	27	7.722	0.70	0.09
10	5.472	3.15	0.12	28	7.819	2.24	0.17
11	5.559	2.38	0.10	29	7.849	1.01	0.11
12_d		----		30	7.905	2.63	0.18
13	5.743	2.09	0.09	31	8.071	11.22	0.37
14_d		----		32	8.123	2.01	0.16
15	5.96	1.69	0.09	33	8.301	1.90	0.15
16_d		----		34	8.337	1.97	0.16
17_d		----		35	8.430	7.20	0.30
18	6.636	2.43	0.14				

Table 3-8b $^{39}K(p,^{3}He)^{37}Ar$ Excitation Energies and Cross Sections.

° Excitation energy errors are ± 12 keV except for cases shown to only 10's of keV where the error is ± 25 keV.
° See Table 3-2a for an explanation of notation.

Peak	E_x (MeV)	$\frac{d\sigma}{d\Omega}$ ± Δ ($\mu b/cm^2$)	$\frac{k_t}{k_\tau}\frac{d\sigma}{d\Omega}$ ($\mu b/cm^2$)	Peak	E_x (MeV)	$\frac{d\sigma}{d\Omega}$ ± Δ ($\mu b/cm^2$)	$\frac{k_t}{k_\tau}\frac{d\sigma}{d\Omega}$ ($\mu b/cm^2$)
01	4.588	1.14 0.11		16	6.56	1.71 0.14	1.48
02	4.635	2.39 0.16		17	6.657	3.95 0.25	3.42
03	4.684	0.92 0.11		18	6.826	2.4 0.18	2.08
04	4.750	16.84 0.56		19	6.88	1.0 0.09	
05_T	4.993	19.70 0.62	17.16	20	7.068	8.0 0.35	
06_c *	0.0	---------- ^{14}N *		21	7.14	5.2 0.29	
07	5.47	4.1 0.25		22_c *	2.31	---------- ^{14}N *	
08	5.684	5.5 0.30		23	7.832	1.94 0.16	
09	5.87	3.28 0.21		24	7.972	2.05 0.17	
10	5.90	2.18 0.16		25	8.066	11.54 0.40	9.85
11	6.103	1.47 0.13		26	8.127	7.92 0.33	6.76
12	6.155	1.23 0.12		27	8.53	----	
13	6.317	2.37 0.16		28	8.92	----	
14	6.360	1.28 0.12		29_c *	3.95	---------- ^{14}N *	
15	6.49	1.36 0.13					

Table 3-9 T=3/2 levels for A = 37 $T_z=|1/2|$ nuclei. Identification of T=3/2 levels by $^{39}K(p,t)^{37}K$ and $^{39}K(p,^3He)^{37}Ar$.

- ΔE (in MeV) is defined as E_x - E_x(first T=3/2) - E_x(^{33}Cl analog).
- A peak number with the subscript $_T$ indicates the state is the T=3/2 state. (See text.)
- A peak number with the subscript $_t$ indicates the most likely T=3/2 candidate.
- The previously known states, as listed in table 2-1 are shown in columns 1, 2, 4, and 5.
- All energies are given in MeV.

^{37}Cl		^{25}Mg		$^{39}K(p,^3He)^{37}Ar$				^{37}K		$^{39}K(p,t)^{37}K$					^{37}Ca	
E_x	J^π	E_x	ΔE	Peak	E_x	ΔE	$\frac{d\sigma}{d\Omega}_{Rel}$	E_x	ΔE	Peak	E_x	ΔE	$\frac{d\sigma}{d\Omega}_{Rel}$	E_R	E_x	ΔE
0.0	$3/2^+$	4.993	0.0	05_T	4.993	0.0	1.00	5.047	0.0	07_T	5.052	0.0	1.00	3.284	0.0	
1.726	$1/2^+$	6.654	-0.07	16	6.56	-0.16	0.09	6.670	-0.10	18	6.636	-0.02	0.11	4.912	1.613	-0.11
				17_T	6.657	-0.06	0.20			19_T	6.692	-0.09	0.20	4.969		
				18	6.826	0.11	0.13			20	6.753	-0.03	0.09	5.032		
3.087	$5/2^+$			25_T	8.066	-0.01	0.59			31_T	8.071	-0.07	0.52	6.387		
				26	8.127	0.05	0.40			32	8.123	-0.02	0.09	6.440		
3.103	$7/2^-$															

3.6 Summary. The (p,t) and (p,^{3}He) data were very successful in locating T=3/2 states and T=3/2 candidate states in $T_z=|1/2|$ nuclei. In many cases the comparison of the (p,t) and (p,^{3}He) data at only one angle, coupled with the energy where the state is located, yields an assignment of isospin. For the cases where several possible states were observed and the (p,t)-(p,^{3}He) comparisons were ambiguous, only a limited number of states needed to be studied with (p,p) excitation functions corresponding to energy regions where a (p,t) peak was observed. In most cases the (p,p) work at TUNL indicated a probable T=3/2 assignment where several candidate states resulted from the (p,t) analysis, since normally only one of the regions studied with (p,p) excitation functions exhibited a narrow resonance. Also, many of the suspected T=3/2 narrow resonances observed in the $T_z=-1/2$ nuclei using ($\vec{p}$,p) studies have shapes corresponding to the proper J^π. Finally, the isospin of many of the states in the A=25 and A=29 systems have been confirmed by angular distribution comparisons of (p,t) and (p,^{3}He) reactions observed at IUCF, which will be presented in the next chapter.

There are several important factors revealed from the (p,t) and (p,^{3}He) data: (1) Because of the high density of T=1/2 states at the excitation energies the T=3/2 states are observed, it is important to have very good energy resolution. It was clear from the poorer resolution potassium data that as the resolution decreases the ambiguities increase. (2) The expected strong enhancement of T=3/2 states over T=1/2 states in the $T_z=-1/2$ nuclei was seen for many cases. But, as seen for the states observed in ^{25}Al near where the third T=3/2

state should occur, the enhancement argument cannot always be relied upon. (3) The presence of strong contaminant peaks, especially in the (p,^{3}He) data, makes single-angle data of limited use. It might be possible to use a different, high-A backing to reduce this problem. (4) Taking data using four different targets was helpful in that the large amounts of data acquired with different resolution caused by different target thicknesses but similar backings could be compared. This eliminated many problems from deuteron punch-through, contaminant peaks, target resolution, and energy calibration.

Discussions on details of the identification of T=3/2 states will be discussed at the end of the next chapter after presenting the results of the (p,t) and (p,^{3}He) angular distribution data taken at IUCF.

4. (p,t) and (p,^{3}He) Measurements - Indiana

4.1 Introduction. Angular distributions for the ^{27}Al(p,t)^{25}Al, ^{27}Al(p,^{3}He)^{25}Mg, ^{31}P(p,t)^{29}P, and ^{31}P(p,^{3}He)^{29}Si reactions were measured using a 60-MeV incident proton beam at the Indiana University Cyclotron Facility (IUCF). These data were used to determine the levels having isospin of T=3/2 in the $T_z=|1/2|$ members of the A=25 and A=29 isobaric multiplets. A comparison of the (p,t) and (p,^{3}He) cross-section and analyzing-power angular distributions was utilized to determine the isospin assignments, as outlined in Section 2.4. It was hoped that these angular distribution measurements would confirm the T=3/2 assignments from the combined Princeton single-angle (p,t)-(p,^{3}He) measurements and the TUNL ($\vec{p}$,p) or (p,p) measurements.

An experimental proposal was submitted to and approved by the IUCF Program Advisory Committee for 12 eight-hour shifts of beam time. There were several advantages to performing the (p,t) and (p,^{3}He) angular distribution measurements at IUCF:

1) An acceptable energy resolution ~ 30 keV QDDM magnetic spectrograph (quadrupole-dipole-dipole-multipole) was available.

2) A polarized proton beam with an intensity of ~ 100-125 nA on target was available for analyzing-power data.

3) The acceleration system at IUCF allowed acquisition of data using higher incident proton beam energies than were available at other

laboratories.

The advantages of using polarized beams in measuring (p,t) and (p,^{3}He) reactions are the additional constraints of comparing the shapes and magnitudes of the analyzing powers. Also, the analyzing powers are independent of the target thickness normalization problems discussed in Section 2.4.3. Earlier work indicated the necessity of using higher incident proton energies, E_p, in measuring the (p,t) and (p,^{3}He) angular distributions [Nan74, Nan81]. These previous measurements using E_p = 35 to 45 MeV indicated that angular distributions were featureless for outgoing triton and ^{3}He energies below ~ 20 MeV, as shown in Fig. 4-6.

The IUCF measurements and analysis are described in Sections 4.2-4.6. A summary and discussion of the results from the (p,t) and (p,^{3}He) measurements made at IUCF and Princeton are presented in Section 4.7.

4.2 Experiment--Targets. The ^{27}Al and ^{31}P targets were prepared [Loz81] using the target making facilities at IUCF. Target thicknesses were chosen to allow data acquisition with little or no resolution broadening from triton or ^{3}He energy-losses in the targets. This limits energy-losses of the tritons or ^{3}He particles to 20-25 keV. The difference in the energy loss of tritons and ^{3}He particles required having two different target thicknesses for the (p,t) and (p,^{3}He) measurements, the (p,t) targets being about three times thicker than the latter.

The self-supporting aluminum targets were prepared by resistive evaporation techniques similar to those described in Chapter 3. The

phosphorus targets were produced by a settling-drying technique [Loz80]. After the proper amount of phosphorus had settled out of a solvent and dried, the targets were sprayed with a thin (10–15 $\mu g/cm^2$) layer of styrene to give the targets strength. A sandwich of phosphorus was formed by evaporating a thin 50–60 $\mu g/cm^2$ layer of gold onto the side of the phosphorus which was not sprayed with styrene. The sandwich was formed to eliminate possible phosphorus evaporation during proton beam bombardment. However, the experimental resolution when using these targets was much worse than estimated, implying large triton and ^3He energy-losses in the targets. The average target thicknesses were determined by weighing the targets, not by measuring a true thickness. The phosphorus used to make the targets was ground into a fine powder before being settled. The observed resolution indicates that these particles were much too large and that the size of the particles limited the resolution. There was no discernible difference in the spectrum resolution when using targets of 335 $\mu g/cm^2$ or 1.05 mg/cm^2 thickness.

The energy-losses of the ^3He particles in these targets prepared by the settling techniques resulted in spectrum resolution that was too poor to allow acquisition of useful $^{31}P(p,^3He)^{29}Si$ data. However, the resolution problems for the ^{31}P targets were discovered during the experiment, and new ^{31}P targets were produced using the evaporation methods described in Chapter 3. The targets prepared during the experiment were used for the $^{31}P(p,^3He)^{29}Si$ measurements. However, these targets were too thin, resulting in poorer counting statistics than desired.

4.3 Experiment--Setup and Data Acquisition. The (p,t) and (p,^{3}He) angular distributions were measured using the QDDD magnetic spectrograph [Ben73c] and a dispersion-matched 59.4-MeV incident proton beam produced by the IUCF separated-magnet, sector-focused, variable energy, isochronous, injector and main cyclotrons. The unpolarized proton beam was obtained from a positive-ion duoplasmatron source. An atomic-beam polarized ion source [ANA01, Gru81] provided the beam of polarized protons, for which the spin quantization axis was reversed every 30 seconds. All polarized beam data were acquired with the QDDM spectrograph located on one side of the beam. Figure 4-1 presents a schematic diagram of the IUCF laboratory and QDDM spectrograph.

The (p,t) data were detected using a helical-cathode position-sensitive proportional counter [Off75] followed by two plastic scintillators. During the (p,t) measurements the helical counter was used to obtain the position information from the time difference of the signals from the two ends of the cathode wire. The ΔE signals from the two scintillators were used for particle identification. The helical-cathode proportional counter was also used in detecting the position of the ^{3}He particles. However, the outgoing ^{3}He particles produced with the 60-MeV proton beam were stopped in the first scintillator. Thus, the particle identification for the ^{3}He data was obtained by using the ΔE signal from the first scintillator and the ΔE signal available from the anode of the helical counter. Signals generated from the second scintillator were used as anticoincidence gates on the proportional counter and first scintillator detector

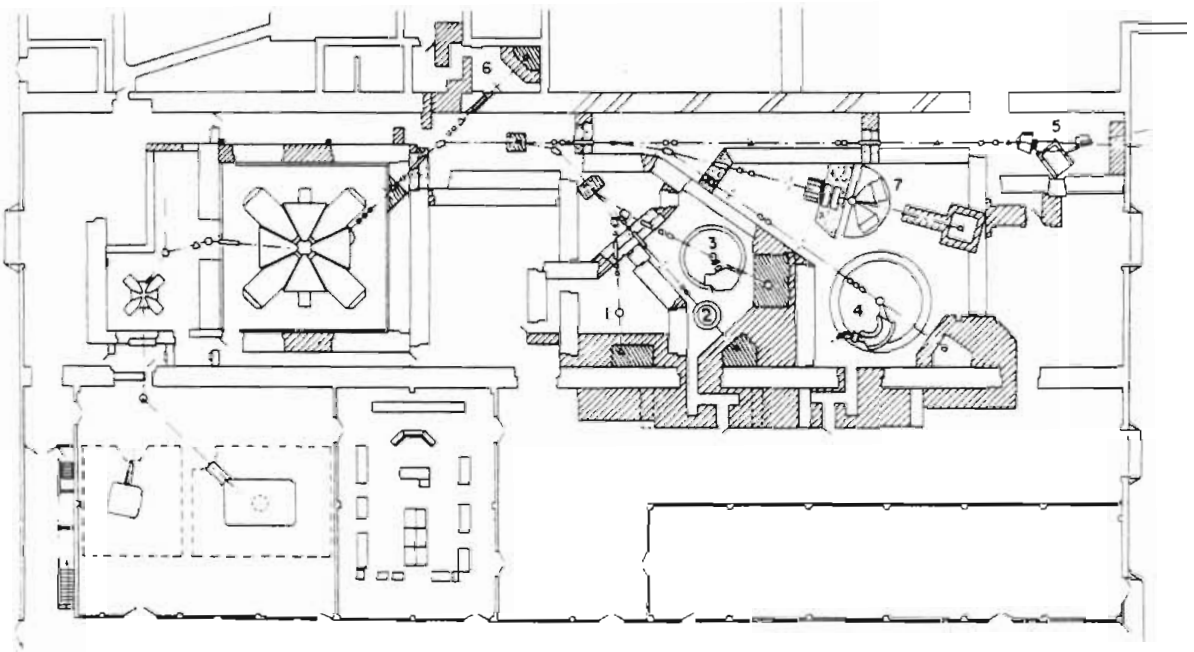

Figure 4-1 Indiana University Cyclotron Facility accelerator laboratory layout. The QDDM spectrograph (4) and associated beam transport used to make the (p,t) and (p,^{3}He) measurements are to the right of center in the figure.

signals. An incident beam energy of 75–80 MeV would result in the ^{3}He particles producing signals in both scintillation detectors, which allow the same particle identification setup for the (p,t) and (p,^{3}He) data. But at these higher incident beam energies, the dipole magnetic fields begin to saturate, resulting in poorer spectrum resolution.

The QDDM internal left-right, split Faraday cup was used to integrate the total incident beam charge. A beam monitor consisting of a 0.25" thick scintillator and a 1" by 1" NaI crystal detector was placed outside of the QDDM target chamber at $\theta_{lab} \simeq 26^{\circ}$ and ~ 88" from the center of the chamber. The monitor was used to trigger a pulser stored in the lower part of the monitor spectrum and in a scalar in order to obtain the true dead-time corrections. The monitor trigger was preferred over a beam current integration trigger for dead-time corrections because it accounted for instantaneous fluctuations in the beam intensity.

The polarization of the proton beam was monitored using a ^{4}He(p,p)^{4}He polarization monitor located between the injector cyclotron and main cyclotron. The proton beam between the two machines had E_p= 5.45 MeV. The polarization monitor consisted of two scintillators mounted on the left and right sides of the beam at $\theta_{lab} \simeq 112^{\circ}$. It was inserted into the beam, and measurements were made after approximately three (p,t) or (p,^{3}He) points had been measured. The average beam polarization was ~ 0.73. Previous studies indicated that no significant beam depolarization results from the passage of the beam through the main cyclotron or in the beam transport system to the target [Sch82,

Mi182].

For each target an energy region ~ 4 MeV was measured with the spectrometer for both the (p,t) and (p,^{3}He) reactions. The measured region in each residual nucleus corresponded to 4 MeV of excitation energy, starting just below where the first T=3/2 states occurred. For each angular distribution measurement, two magnetic field settings of the spectrometer were necessary to cover the 4-MeV region, because of the limited energy acceptance of the QDDM and its detectors. The energy acceptance for the (p,t) measurements was ~ 2.1 MeV/bite and the (p,^{3}He) energy acceptance was ~ 2.3 MeV/bite. The solid angle of the QDDM was 2.18 msr with a horizontal angular acceptance of 1.9° and a vertical acceptance of 3.67°.

Data were acquired using the on-line aquisition code DERIVE [Kou75]. The ^{27}Al(p,t)^{25}Al and ^{27}Al(p,^{3}He)^{25}Mg angular distributions were measured with an unpolarized proton beam. The lower and upper energy bite measurements were made at lab angles of 6°, 10°, 15°, 20°, 25°, and 30°. There was ~ 0.5 MeV of energy overlap between the two spectrograph bites. The observed triton spectrum resolution was 29-39 keV depending on the spectrograph angle, while the ^{3}He spectrum resolution varied from 48-52 keV. The ^{27}Al(p,t)^{25}Al measurements were made with a 818 $\mu g/cm^2$ thick target; for the ^{27}Al(p,^{3}He)^{25}Mg measurements the thickness was 334 $\mu g/cm^2$. Only the results for the lower-energy spectrograph bite covering the excitation energy region in the residual nuclei, where the first three T=3/2 states occur, will be presented here. The ^{27}Al(p,t)^{25}Al and ^{27}Al(p,^{3}He)^{25}Mg spectra taken at a

lab angle of 15^{o} for the lower energy spectrograph bite are shown in Fig. 4-2. The Princeton (p,t) and (p,^{3}He) spectra corresponding to a small portion of the IUCF spectra with a resolution of 15-20 keV are also shown.

The ^{31}P(p,t)^{29}P angular distributions for the lower spectrograph bite were taken at lab angles of 6^{o}, 10^{o}, 15^{o}, 20^{o}, 25^{o}, 30^{o}, and 38^{o}. The ^{31}P(p,^{3}He)^{29}Si measurements for the lower spectrograph bite were made at lab angles of 6^{o}, 10^{o}, 15^{o}, 20^{o}, 25^{o}, and 30^{o}. The ^{31}P(p,t)^{29}P upper spectrograph bite measurement angles were 6^{o}, 10^{o}, 15^{o}, 20^{o}, and 25^{o} in the lab frame, while the corresponding ^{31}P(p,^{3}He)^{29}Si measurements were taken at lab angles of 6^{o}, 10^{o}, and 15^{o}. A 1.05 mg/cm^{2} thick natural ^{31}P target prepared by the settling technique was used for the (p,t) measurements. The observed (p,t) spectra resolution, dominated by energy losses in the target, as discussed in Section 4.2, was 63-84 keV. The 10^{o} (p,t) data were remeasured using a thin $\sim$ 42 μg/cm^{2} ^{31}P target. This target was created by folding together two targets prepared by the oven and crucible evaporation technique, as discussed in Sections 3.2 and 4.2, to form a phosphorus sandwich, with carbon backings on both sides of the phosphorus. The (p,t) spectrum resolution taken with this target was 29 keV. The (p,t) measurements using the thin target were used to relate the thickness of this target to the 1.05 mg/cm^{2} target. The measurements were also made to identify (p,t) peaks that were unresolved in the thick target spectra. All ^{31}P(p,^{3}He)^{29}Si measurements were made using the thin 42 μg/cm^{2} ^{31}P target. The observed resolution for these measurements was 34-42 keV. The measurements of the (p,t) and (p,^{3}He) upper energy spectrograph bites had resolutions comparable to

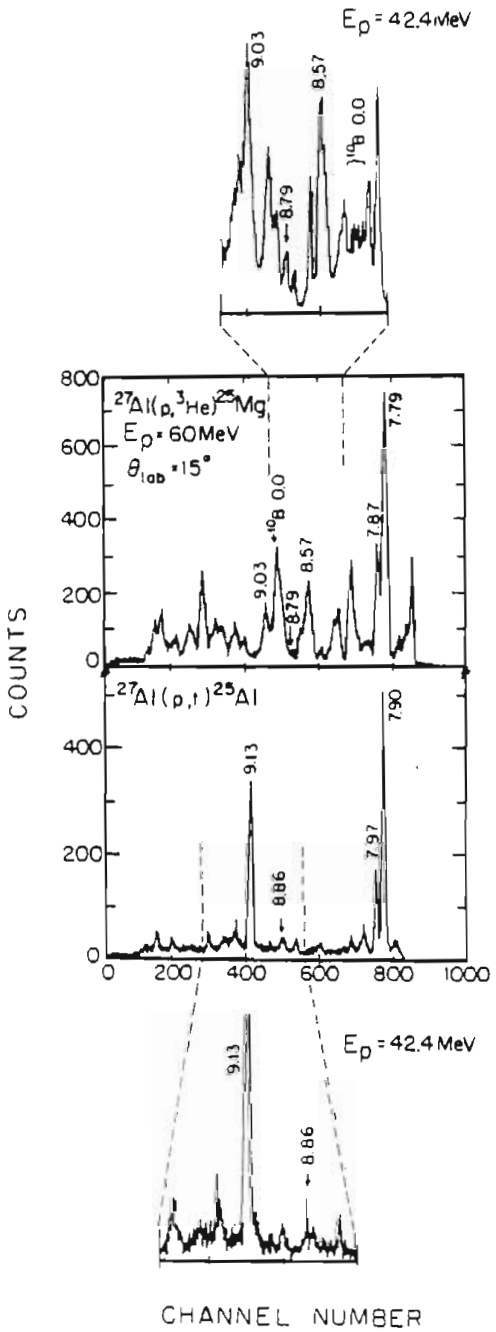

Figure 4-2 The ^{27}Al(p,t)^{25}Al and ^{27}Al(p,^{3}He)^{25}Mg spectra from the lower spectrograph bite measurement made at an angle of 15°. The cut-out spectra are the corresponding Princeton (p,t) and (p,^{3}He) measurements for the excitation energy region where the third T=3/2 state is expected. Note the different position of the ^{10}B contaminant peaks in the (p,^{3}He) data resulting from the different incident proton energies and scattering kinematics.

those for the lower bites. The $^{31}P(p,t)^{29}P$ and $^{31}P(p,^{3}He)^{29}Si$ spectra for data taken at 15^{o} are shown in Fig. 4-3. The poor resolution of the (p,t) data is obvious. The 10^{o} $^{31}P(p,t)^{29}P$ data taken with the thin target are shown in Fig. 4-4.

4.4 Experiment—Analysis. The IUCF data tapes were translated at TUNL to a VAX 11/780 compatible form for data analysis. The peak sums and channel numbers were extracted for all of the spectra by using consistent, careful, peak-fitting techniques. The peak-fitting code SPECTR [Var82] was used to analyze the data. The code SPECTR performs a χ^2 calculation which finds the best fit to the input data by searching peak centroid location, width, skewness, and background parameters.

The availability of the ~ 15 keV (p,t) and (p,^{3}He) spectra measured at Princeton was critical in allowing reliable extraction of the sums and peak channel numbers in the poorer resolution IUCF data. As mentioned in Section 3.6, good resolution is necessary because of the high density of states. However, the Princeton measurements were used to determine how many peaks were included in the peak-fitting searches, thereby increasing the reliability of the IUCF measurements.

The extraction of consistent peaks sums for the angular distributions was obtained only by following a very strict set of analysis procedures. Low energy $^{27}Al(p,t)^{25}Al$ and $^{27}Al(p,^{3}He)^{25}Mg$ spectrograph bites, containing only a few peaks corresponding to low-lying well-separated states, were measured to determine the skewness and peak width properties of the spectrograph detection system as a function of position. The widths, skewnesses, and peak centroids were

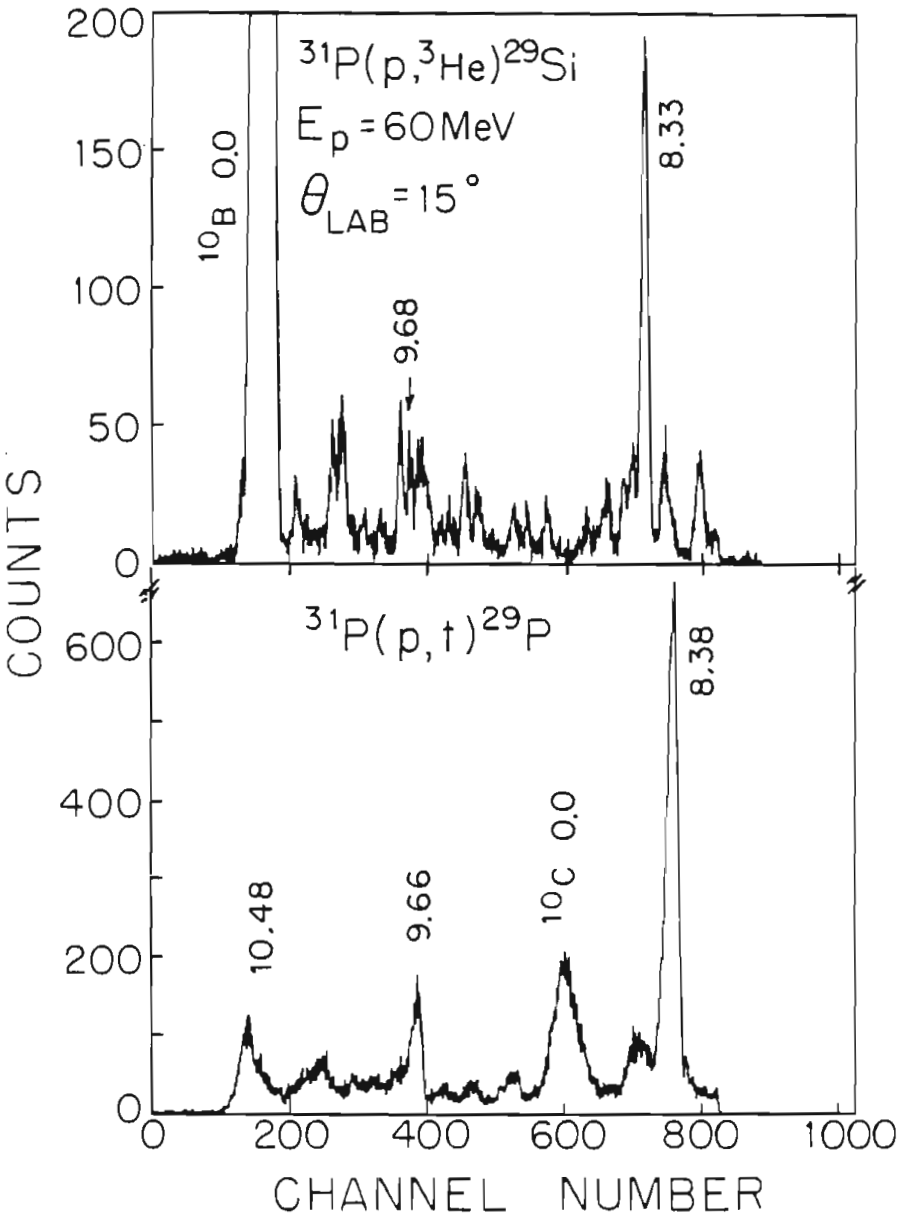

Figure 4-3 The $^{31}P(p,t)^{29}P$ and $^{31}P(p,^3He)^{29}Si$ spectra (sum of spin-up and spin-down) from the lower spectrograph bite measurement made at an angle of 15°. Notice the poorer (p,t) (65 keV) resolution resulting from the ^{31}P target produced by the settling technique.

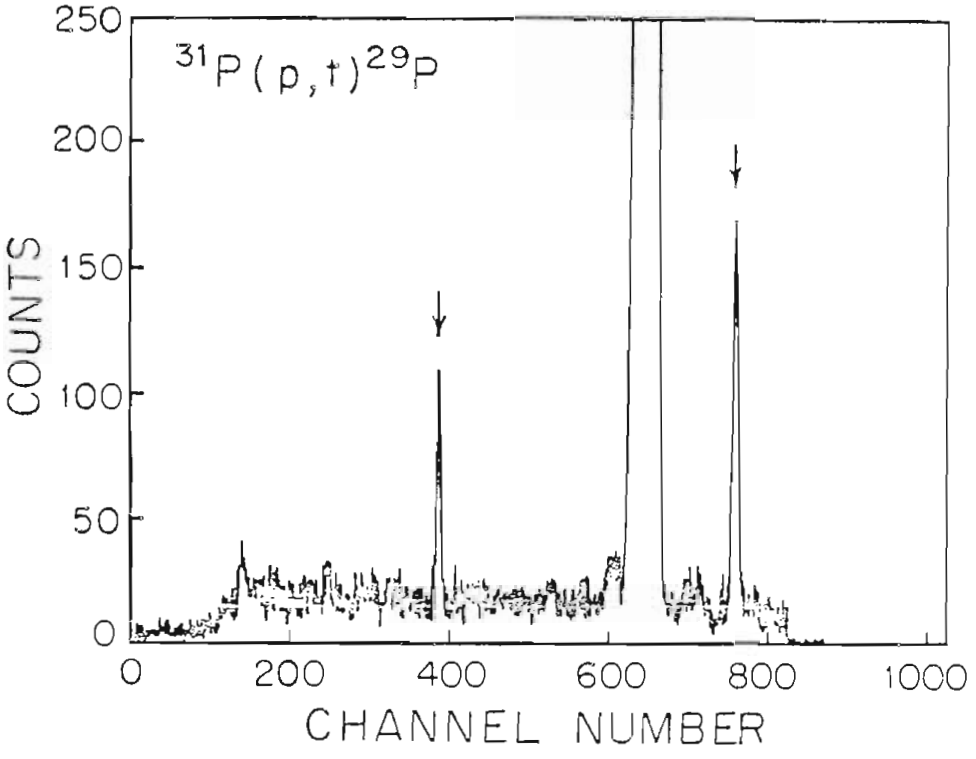

Figure 4-4 Good resolution $^{31}P(p,t)^{29}P$ spectra (sum of spin-up and spin-down) from the lower spectrograph bite measurement made at an angle of 10^{o}. This (p,t) measurement was made with the ~ 42 $\mu g/cm^2$ thin ^{31}P target prepared during the run. The first and second T=3/2 states are indicated by arrows. The spectrum resolution is 30 keV.

free and independent search parameters for each peak. There were essentially no background counts in these measurements. These tests indicated reasonably constant width and skewness as a function of detector position.

Each set of (p,t) or (p,^{3}He) angular distribution measurements consisted of spectra measured at different detector angles but covering the same energy excitation region. For each set of measurements, one or two energy region(s) in which a strong peak (or peaks) occurred at all angles was selected for initial analysis. The peak width and skewness determined at each angle from the analysis of all the peaks in this (these) region(s) were then used as fixed input for all other peaks in the spectra at this angle. This initial peak-fitting search was performed on the data from each angle with the peak widths, skewnesses, and centroids allowed to vary. At each angle the peak widths and skewnesses in the particular spectrum region were required to have the same width and skewness. The initial background was fixed at a constant value determined by visual inspection. Finally, different background values were searched in order to minimize the calculated χ^2 value.

The resulting set of centroids calculated from these initial fits was then used to determine the relative centroid locations; these were assumed independent of spectrograph angle. The channel differences between peaks in the spectra should not vary significantly from angle to angle for the small angular distribution region and the small energy excitation region covered in this work. Thus, the average relative centroid positions for all other peaks were determined by using the

large peak in the spectrum at each angle as the reference peak. The channel difference between this reference peak and the other peaks was computed for the data at each angle, then these relative locations were combined to determine the average angle-independent relative peak centroid positions.

The next step was to recalculate the fits with free widths and skewnesses, but with the relative centroid locations as fixed input. The centroid of the strong reference peak was allowed to vary. The widths and skewnesses were still required to be the same for all the peaks in a particular spectrum. The results of these calculations yielded the best-fit peak width and skewness for the spectra at each angle. However, the polarized beam data required one additional set of calculations, because for each angle two sets of data corresponding to the spin-up and spin-down proton beam were acquired. Thus, the best-fit widths and skewness were calculated for each angle of the polarized beam data by averaging the values determined from the individual spin-up and spin-down measurements. Values for the constant background were again searched to determine the minimum χ^2. However, the background determined in the initial step usually remained the χ^2 minimum value.

The final peak sums were calculated using the fixed average relative peak centroids, best-fit widths, and skewnesses. A best fit constant background for the final parameters was determined by varying the background subtraction and minimizing the calculated χ^2. This multistep fitting procedure was very time consuming, but was necessary to extract consistent angular distribution peak sums.

The remainder of the peaks in the particular spectrograph bite were then summed using each angle's average peak width and skewness determined from the above procedure. The number of necessary searches was then reduced to an initial search used to determine the relative peak centroid locations and a final calculation of sums using the derived average relative peak centroids. In both of these steps, the constant background was determined by obtaining the χ^2 minimum.

The contaminant peaks were carefully watched and considered when analyzing the data. Care was taken to track the contaminant peaks as they moved through the peaks of interest as the scattering angle was changed. The chief contaminant peaks were caused by the carbon backings and by carbon buildup on the targets. Calculations were also performed and the spectra were checked for other likely contaminant peaks resulting from ^{16}O and ^{28}Si.

The reliability of the extraction of peak-fit sums and peak centroid locations was tested by independently analyzing the peaks which occurred in the overlap regions between the upper and lower spectrograph energy bites. One of the most difficult sets of peaks to analyze was for the (p,t) peaks in the energy region surrounding the fourth T=3/2 state in ^{29}P. A comparison of the peak energies for the upper and lower bite measurements is presented in Table 4-1. The excellent self-consistency and agreement with the Princeton peak energies (also shown in Table 4-1) observed in this energy region indicate that the careful peak fitting procedures produced excellent results.

Table 4-1 Comparison of $^{31}P(p,t)^{29}P$ Fourth T=3/2 Energy Region Excitation Energies.

The excitation energies for the same energy levels observed in two separate spectrograph bite measurements at IUCF are compared along with the Princeton energies assignments. The IUCF data required extensive peak-fitting in order to extract the centroid locations. The peak locations from the two IUCF measurements were extracted independently of each other. All spectra were taken at lab angle of 15^{o}.

Princeton Data		IUCF Data			
		Lower bite		Upper bite	
Peak	E_x (MeV)	Rel Chan.	E_x (MeV)	Rel Chan.	E_x (MeV)
18	10.136	111.3	10.108	107.5	10.122
19	10.179	92.8	10.171	86.2	10.193
20	10.282	68.7	10.252	61.8	10.274
21	10.360	35.7	10.364	36.1	10.360
22	10.423	17.6	10.425	18.4	10.419
23	10.48	* 0 *	10.484	* 0 *	10.480

4.5 Experiment—Measurements. . The energy calibration of the spectra was determined by using the energy values extracted from the Princeton measurements. The extracted sums and errors for each measurement were normalized to the dead-time corrected total charge integrated during each run. The relative yields obtained from this procedure are presented instead of absolute cross sections. The absolute cross sections were not calculated because of the large uncertainty (~ 25%) in the absolute target thicknesses. The relative thicknesses of the targets were determined by measuring the same spectra with each target for the ground state and first few excited state transitions in the residual nuclei. These states produce strong energy-separated peaks with almost no surrounding background. The accuracy of the relative yields can be seen in Table 4-2. The table compares the relative counts for the fourth T=3/2 state as determined by the lower and upper bite angular distribution measurements.

The accurate measurement of relative yields requires an understanding of the detector efficiency. The efficiency was determined by examining the approximately constant continuum deuteron spectra in the $^{31}P(p,^{3}He)^{29}Si$ measurements. The detector was found to have essentially a constant detection efficiency from channels 130 to 815. Below or above these values, the efficiency rapidly dropped off. One dead section of the detector affecting ~ 10 channels was also discovered. Sums from peaks with any portion of the peak in the dead region were not used.

Table 4-2 Comparison of $^{31}P(p,t)^{29}P$ Fourth T=3/2 State Cross Sections and Analyzing Powers.

The cross sections and analyzing powers for the fourth T=3/2 state observed in two separate spectrograph bite measurements at IUCF are compared. The data required extensive peak-fitting in order to extract the peak sums. The peak locations and sums determined from the two bites were extracted independently of each other.

Angle (deg)	Lower bite $\frac{d\sigma}{d\Omega}$ (rel.)	Lower bite A_y	Upper bite $\frac{d\sigma}{d\Omega}$ (rel.)	Upper bite A_y
6	953	0.129	920	0.083
10	1316	-0.007	1166	0.052
15	1330	-0.104	1392	-0.147
20	845	-0.139	1060	-0.121
25	604	-0.122	656	-0.167
30	601	0.025	----	-----
38	573	0.08	----	____

The analyzing powers measured for the $^{31}P(\vec{p},t)^{29}P$ and $^{31}P(\vec{p},^3He)^{29}Si$ reactions were calculated from the asymmetries using the beam polarizations determined with the beam-polarization monitor.

4.5.1 States in ^{25}Al and ^{25}Mg. The angular distributions for the first and second T=3/2 states are shown in Fig. 4-5 for the $^{27}Al(p,t)^{25}Al$ and $^{27}Al(p,^3He)^{25}Mg$ cross-section measurements. All $(p,^3He)$ yields have been multiplied by the factor of k_t/k_τ, defined in Chapter 2, in order to make comparisons between the (p,t) and the $(p,^3He)$ reactions. There is excellent agreement for the first state between the (p,t) and $k_t/k_\tau \cdot (p,^3He)$ cross sections, confirming that this is indeed the T=3/2 state. The agreement between the (p,t) and $(p,^3He)$ data for the second T=3/2 state is not as good as for the first T=3/2 state. Possible causes of a discrepancy between the (p,t) and $(p,^3He)$ data might be (p,t) and $(p,^3He)$ cross-section normalization errors, systematic peak-fitting problems, or a nearby T=1/2 state which is nearly degenerate with the $(p,^3He)$ state. However, the first and second T=3/2 states are only 70 keV apart and the two peaks were fitted simultaneously. The good agreement between the first T=3/2 (p,t) and $(p,^3He)$ angular distribution measurements immediately eliminates any possible normalization or systematic peak-fitting errors. This disagreement in cross section for the second T=3/2 state was also observed in 40-MeV (p,t) and $(p,^3He)$ angular distribution measurements [Nan82].

If a degenerate T=1/2 state exists, it would have to lie within 1 or 2 keV of the T=3/2 state, based on the results of peak fitting the

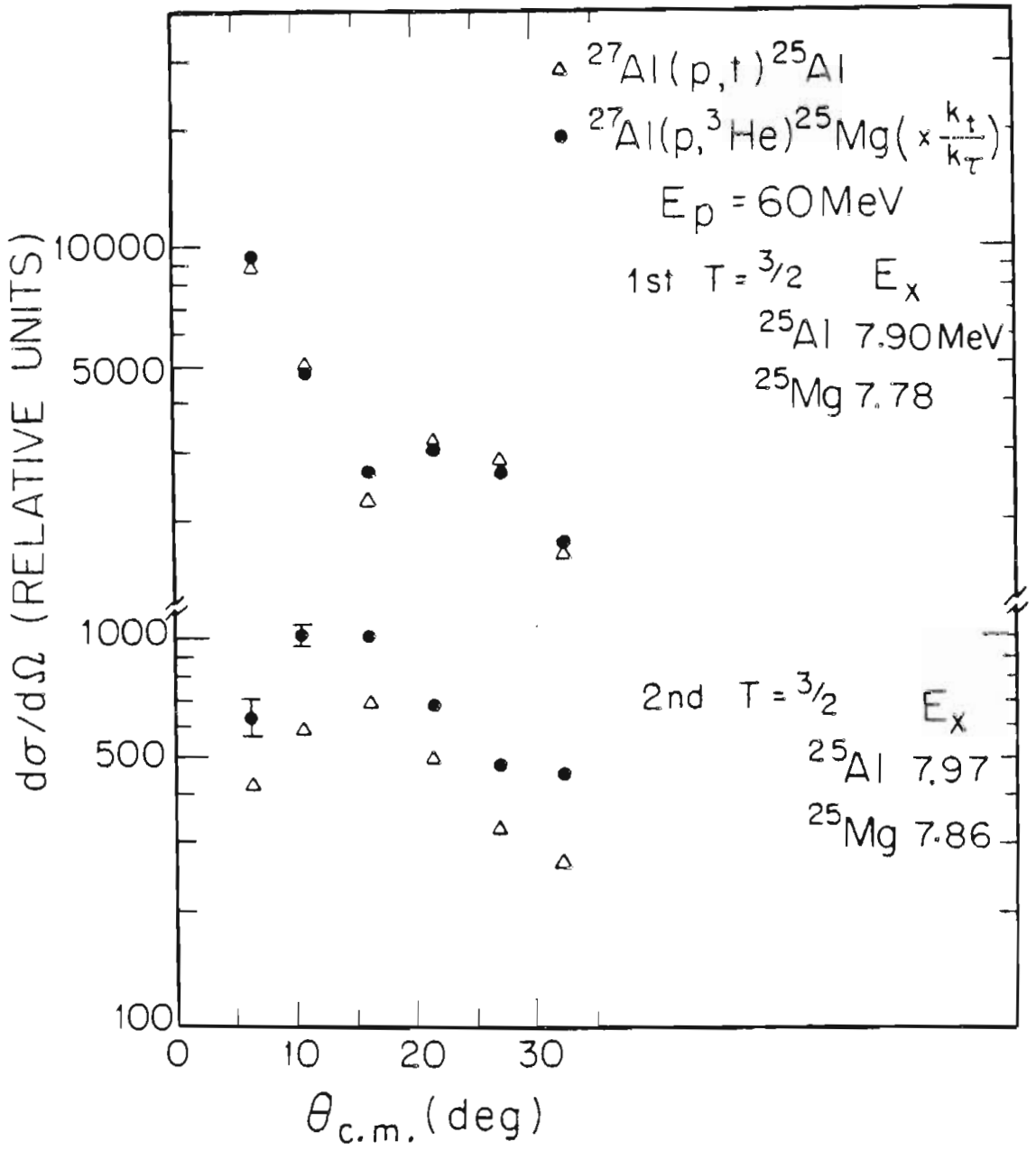

Figure 4-5 The $^{27}Al(p,t)^{25}Al$ (open triangles) and the $^{27}Al(p,^3He)^{25}Mg$ (solid dots) cross-section angular distribution comparisons for the first and second T=3/2 states in the $T_z=|1/2|$ A=25 nuclei. The $(p,^3He)$ data has been multiplied by a factor of k_t/k_τ. See Section 4.5.1 for discussion.

Princeton high-resolution $^{27}Al(p,^3He)^{25}Mg$ data (Fig. 3-3). There is a large T=1/2 state which occurs between the first and second T=3/2 states as observed by (p,p) scattering [Iko76]. However, this state was accounted for in the peak fitting. It might be possible for the second T=3/2 state to be a strong admixture of T=1/2 and T=3/2 wave function components with the same spin-parity. The $(p,^3He)$ reaction can populate the T=1/2 components by either J=0, T=1 or J=1, T=0 transfer and may result in a larger cross section than the (p,t) reaction which can only proceed by a J=0, T=1 transfer. It is also interesting to note that it is the magnitude of the (p,t) and $(p,^3He)$ comparison which disagrees, and that the shapes of the (p,t) and $(p,^3He)$ distributions are in good agreement. The total and reduced widths for the two T=3/2 states in ^{25}Al (presented in Chapter 11) show that although the reduced proton elastic widths are nearly the same for the two T=3/2 states ($\Gamma_p(1)=258$, $\Gamma_p(2)=330$), the second T=3/2 state in ^{25}Al has a total width 13 times greater than the first T=3/2 state ($\Gamma(1)=105$, $\Gamma(2)=1302$). The larger total width of the second state may indicate more T=1/2 admixtures.

The large (p,t) state at 9.14 MeV in ^{25}Al was thought to be the third T=3/2 state. This assignment was based on the relative strength with which the state was populated by the (p,t) reaction (see Fig. 3-2, peak 15, and Fig. 4-2). However, our angular distribution measurements of this $^{27}Al(p,t)^{25}Al$ state revealed that it is an $\ell = 0$ transition which indicates it is a $J^\pi = 5/2^+$ state (the ^{27}Al target nucleus ground state is a $5/2^+$ state). However, the third T=3/2 state should be a $1/2^+$ based on the parent analog state spin and parity. The (p,t) angular distribution is shown in Fig. 4-6, along with the measurement of [Nan81]

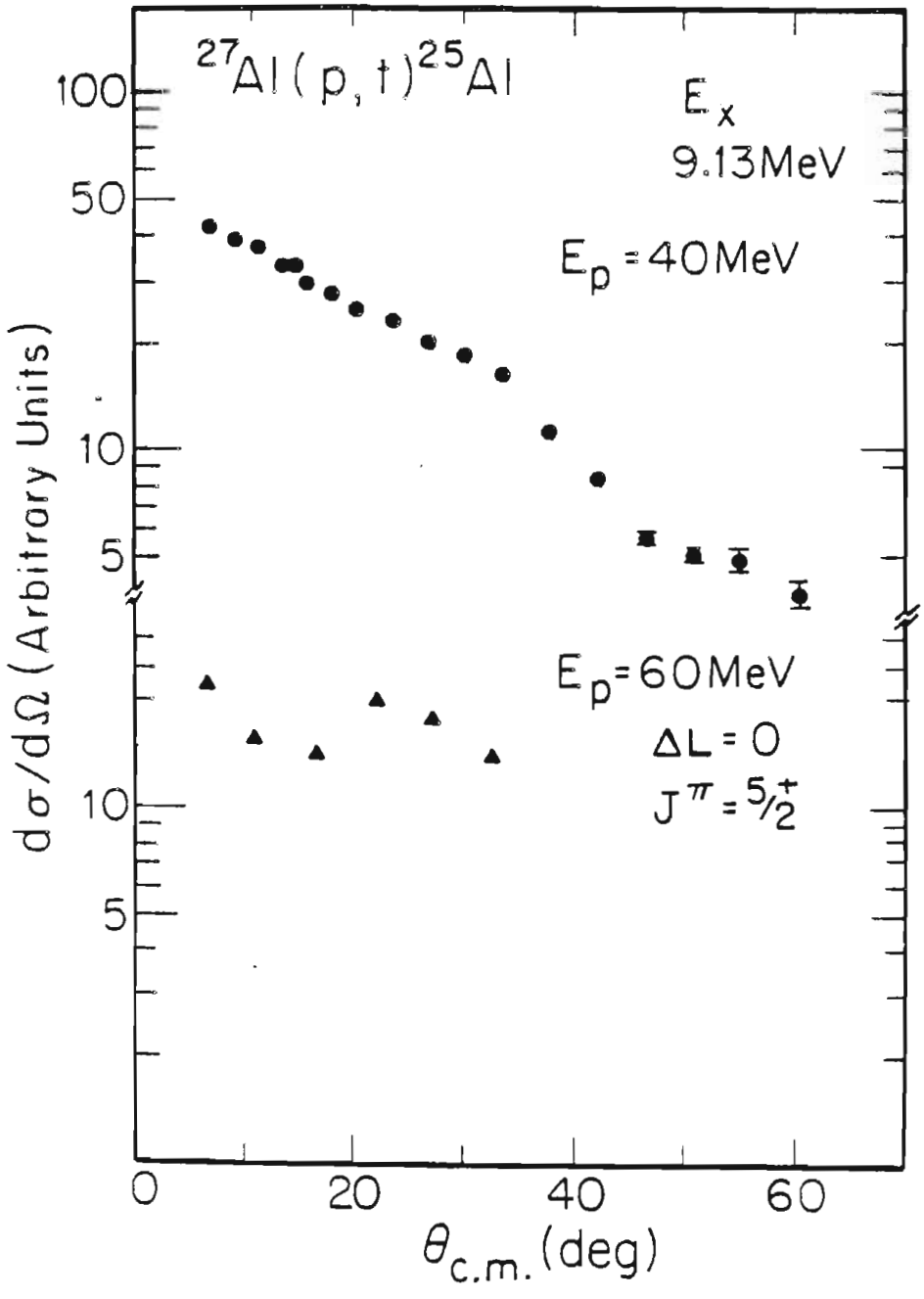

Figure 4-6 The $^{27}Al(p,t)^{25}Al$ angular distribution measured for the ^{25}Al 9.13-MeV state with incident proton beam energies of 40 MeV [Nan81] and 60 MeV from the present work. The 40-MeV data exhibits little structure in the angular distribution.

made with 40-MeV incident protons. The figure illustrates the problems with attempting to measure angular distributions when the outgoing triton energy becomes too small, which was mentioned in Section 4.1. The 40-MeV data, which are featureless, do not reveal any angular momentum information.

The third T=3/2 state in ^{25}Al is identified by this work at 8.86 MeV and the ^{25}Mg state at 8.79 MeV. The comparison of the angular distributions is shown in Fig. 4-7. There were two possible T=3/2 states in ^{25}Al which could be compared with one T=3/2 state in ^{25}Mg. Comparisons are shown in Fig. 6-7 for both ^{25}Al states compared with the single ^{25}Mg 8.79-MeV state. The selection of the 8.86-MeV ^{25}Al state as the T=3/2 state is based on the slightly better shape and magnitude agreement of the 8.86-MeV state with the ^{25}Mg state. The (p,p) measurements over these two states revealed a narrow resonance within 5 keV of the 8.86-MeV state predicted resonance energy. All of the observed states in the (p,t) and (p,^{3}He) energy region where the third T=3/2 state should occur are shown in Fig. 4-8. The (p,t) states are shown on the left and the (p,^{3}He) states are shown on the right. There has been no attempt to match (p,t) states with (p,^{3}He) states. The states are presented by increasing energy.

The results for the T=3/2 states in the A=25 $T_z=|1/2|$ nuclei are listed in Table 3-3. It was possible to observe only the first three T=3/2 states in the energy excitation region covered by the lowest spectrograph bite. However, more T=3/2 states may be revealed by the analysis of the upper spectrograph bite, which spans the energy regions

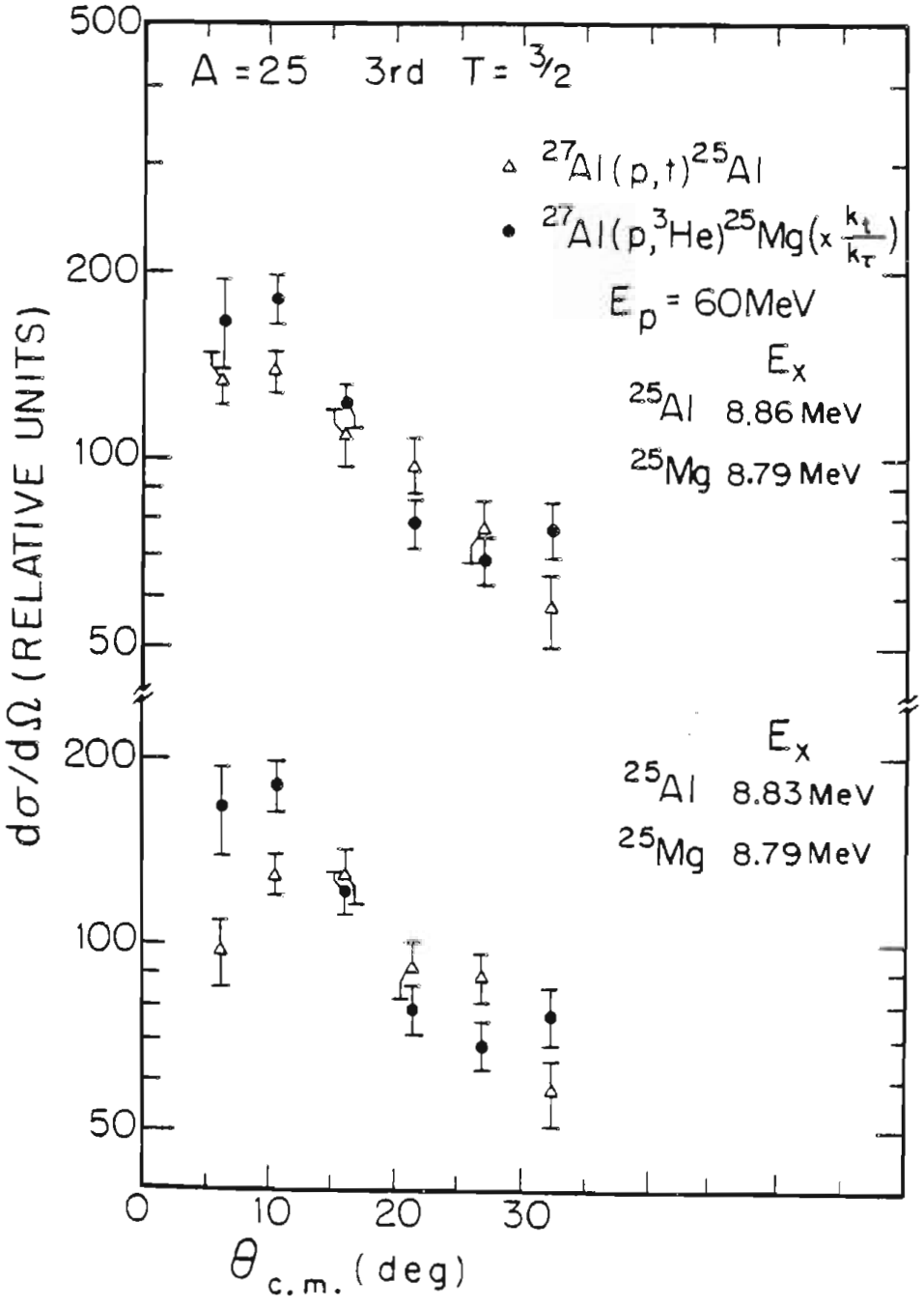

Figure 4-7 The ^{27}Al(p,t)^{25}Al (open triangles) and the ^{27}Al(p,^{3}He)^{25}Mg (solid dots) cross-section angular distribution comparisons for the third T=3/2 state in the T_z=|1/2| A=25 nuclei. Two (p,t) distributions compared favorably with the 8.79-MeV ^{25}Mg state. However, the 8.86-MeV ^{25}Al state was assigned as the T=3/2 state, based on the better agreement with the (p,^{3}He) measurements. The (p,^{3}He) data has been multiplied by a factor of k_t/k_τ.

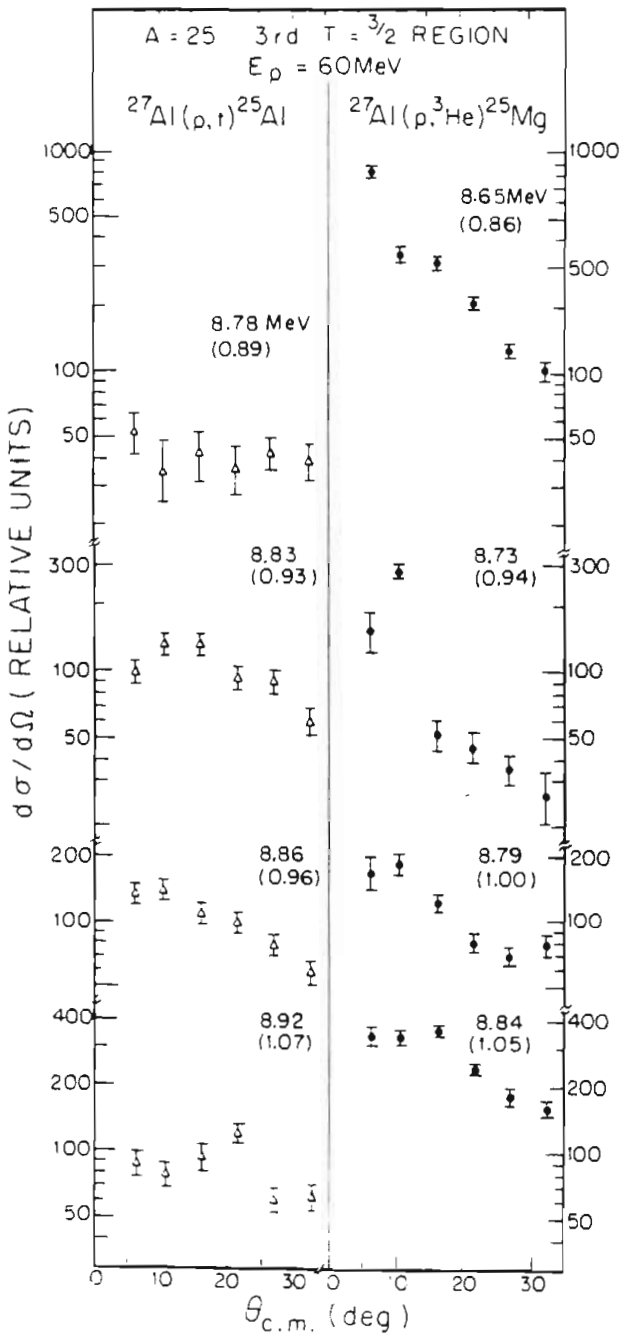

Figure 4-8 The $^{27}Al(p,t)^{25}Al$ (open triangles) and the $^{27}Al(p,^{3}He)^{25}Mg$ (solid dots) cross-section angular distributions for states in the energy region of the third T=3/2 state. The levels are presented by increasing energy, with no implied correlation between the (p,t) and (p,^{3}He) data. See Fig. 4-7 for the (p,t) and (p,^{3}He) comparisons.

where 3-4 more T=3/2 states should occur.

One problem which became evident when making the (p,t) and (p,^{3}He) measurements using the $J^\pi = 5/2^+$, ^{27}Al target nucleus is that, because of the target spin configuration, almost all of the transitions are $\ell = 2$. It would have been a great help to have analyzing-power data in addition to the cross-section data. Our measurement of only cross-section data resulted from the limited amount of beam time available.

4.5.2 States in ^{29}P and ^{29}Si. The ^{31}P($\vec{p}$,t)^{29}P and ^{31}P($\vec{p}$,^{3}He)^{29}Si measurements resulted in the isospin assignment of five previously unidentified T=3/2 levels in the $T_z=|1/2|$ A=29 nuclei. These five new levels are the second, fourth, sixth, seventh, and eighth T=3/2 states. In addition, a tentative isospin T=3/2 assignment was made the third T=3/2 state in ^{29}P.

The cross-section and analyzing-power comparisons of the first and second T=3/2 states are shown in Fig. 4-9. The addition of the analyzing-power data to the cross-section data enhances the probability of identification of these levels. The poor statistics for the ^{31}P($\vec{p}$,^{3}He)^{29}Si points are a result of the use of the very thin but good resolution target. The high density of T=1/2 levels necessitated using a thin target in order to resolve the states. The disagreement of the 25° and 30° (p,t) points for the second T=3/2 state may be caused by the ^{12}C(p,t)^{10}C contaminant peak which kinematically "walks through" the 9.66-MeV ^{29}P second T=3/2 state at these angles. These points are plotted as diamonds in the figures. Overall, there is very good

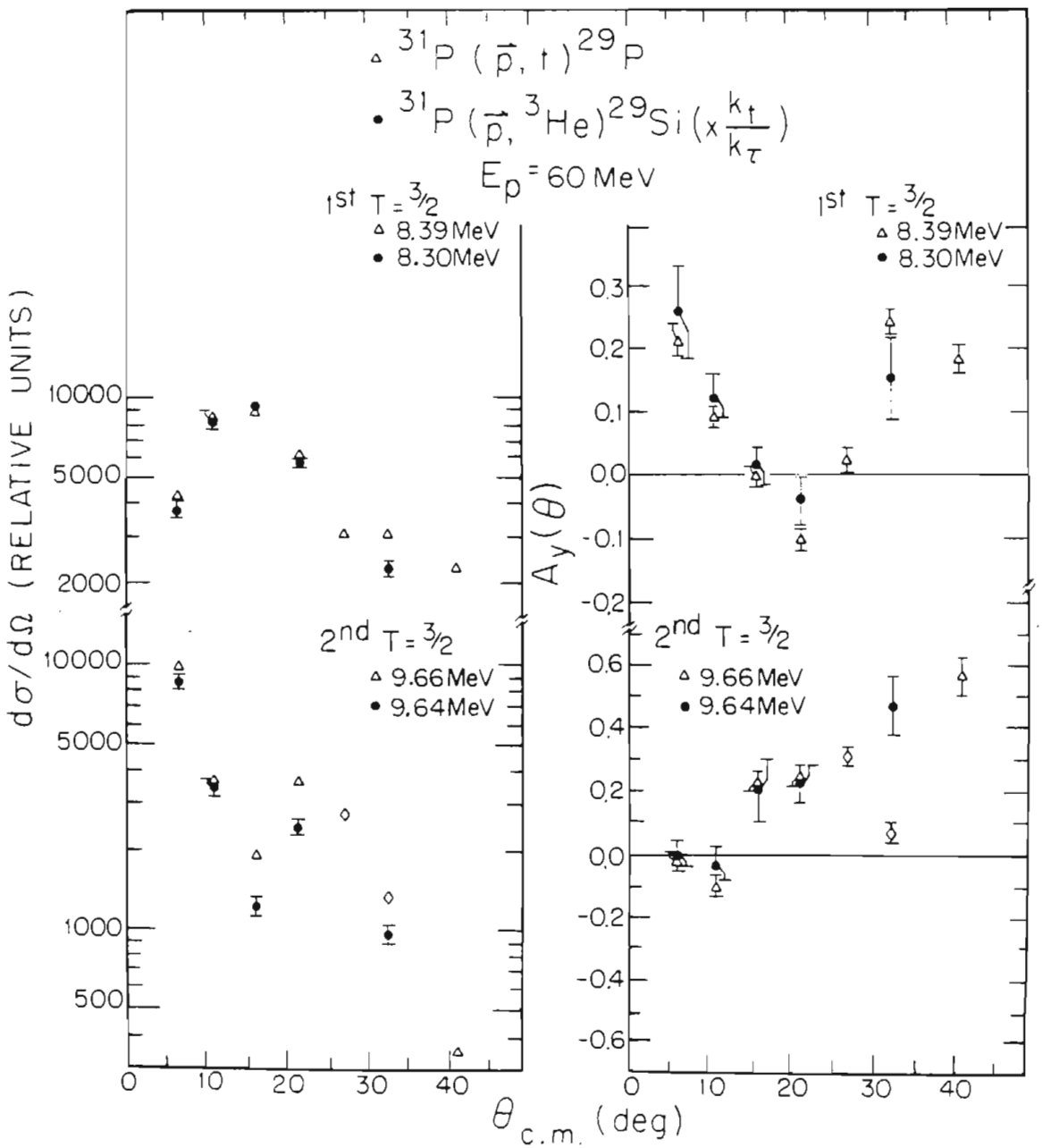

Figure 4-9 The $^{31}P(\vec{p},t)^{29}P$ (open triangles) and the $^{31}P(\vec{p},{}^{3}He)^{29}Si$ (solid dots) cross-section and analyzing-power angular distribution comparisons for the first and second T=3/2 states in the $T_z=|1/2|$ A=29 nuclei. The (p,^{3}He) cross-section data has been multiplied by a factor of k_t/k_τ. See Section 4.5.2 for discussion.

agreement between (p,t) and (p,^{3}He) results.

The (p,t) and (p,^{3}He) levels in the region where the third T=3/2 $7/2^+$ levels should occur are shown in Figs. 4-10 and 4-11, respectively. The ^{31}P target has a $J^\pi = 1/2^+$, which implies that the ℓ-transition must be a ℓ=4, and thus one might expect this state to be populated only weakly in the (p,t) and (p,^{3}He) reactions. The large T=1/2 states in the ^{31}P($\vec{p}$,^{3}He)^{29}Si spectra obscure any weak (p,^{3}He) states, and thus a definitive assignment of the isospin to levels in both of the $T_z=|1/2|$ nuclei was not possible. However, the (p,t) state at 10.14 MeV is tentatively assigned as the T=3/2 state, based on the cross-section angular distribution and by (p,p) measurements made over energy regions corresponding to both the 10.14- and 10.18-MeV states. Resonances were seen for both states, and the results of these measurements are discussed in Chapter 12. Realistic shell-model wave functions [Nan82a] were used in Distorted Wave Born Approximation (DWBA) calculations using a slightly modified version of DWUCK4 [Kun74, Aok82]. The results of the calculations for the first T=3/2 (p,t) angular distribution were in excellent agreement with the experimental results. The calculations for the third T=3/2 level were in reasonable agreement with the measurements at 25°, 30°, and 35°, but in very poor agreement with the forward angle data. However, the poor resolution resulting from the use of the settled ^{31}P targets probably filled in the expected ℓ = 4 minimum.

The fourth T=3/2 states in ^{29}P and ^{29}Si were identified at 10.48 MeV and 10.54 MeV, respectively. The comparison of the angular distributions is given in the upper half of Fig. 4-12. The (p,t) and

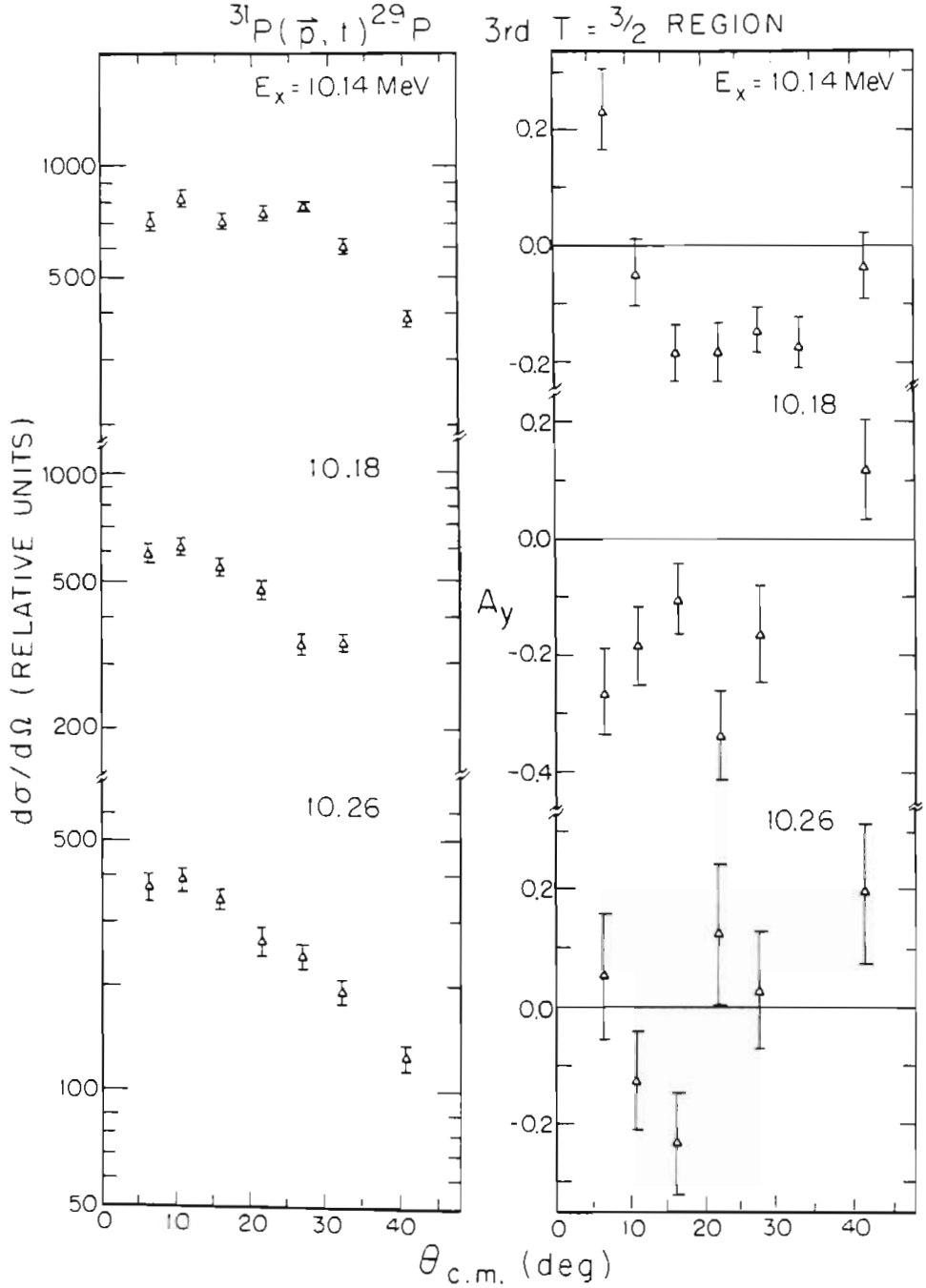

Figure 4-10 The $^{31}P(\vec{p},t)^{29}P$ cross-section and analyzing-power angular distributions for states in the energy region of the third T=3/2 state. The 10.14-MeV state has tentatively been assigned as the third T=3/2 state in ^{29}P. This state should be a $J^{\pi} = 7/2^{+}$ state and have $\ell = 4$ transfer.

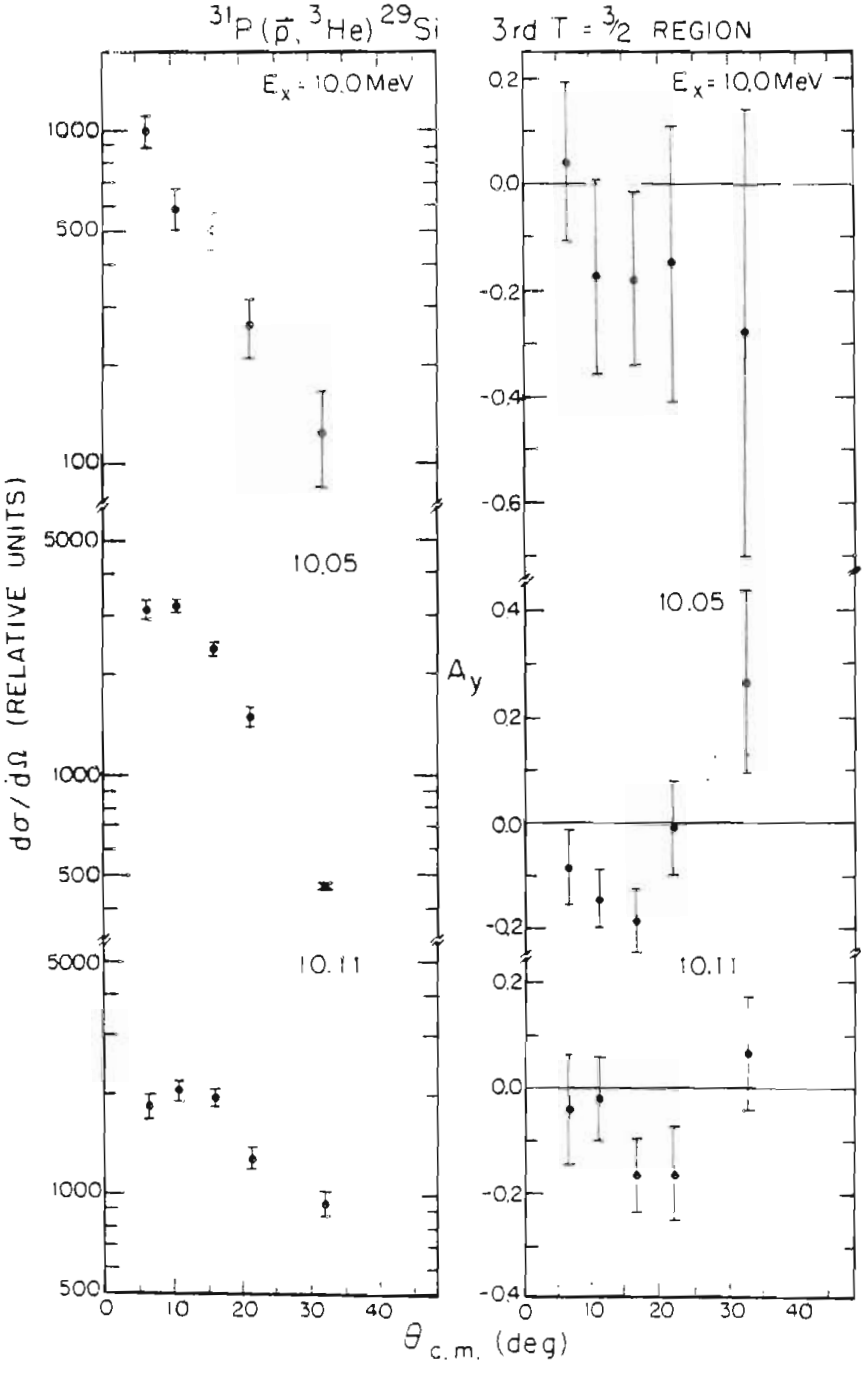

Figure 4-11 The $^{31}P(\vec{p},^{3}He)^{29}Si$ cross-section and analyzing-power angular distributions for states in the energy region of the third T=3/2 state. The third T=3/2 state in ^{29}Si should be a $J^{\pi} = 7/2^{+}$ state populated by $\ell = 4$ transfer. The strong T=1/2 states observed in this energy region were larger than any states observed in the corresponding energy region of the (p,t) spectra.

$(p,^3He)$ states in the region where the fourth T=3/2 states should occur are shown in Figs. 4-13 and 4-14. The $(p,^3He)$ peaks were obscured at several angles as a result of contaminant peaks. The overall agreement between the data is excellent.

No T=3/2 states could be assigned for the expected fifth T=3/2 levels in ^{29}P and ^{29}Si. These states were expected to be found in the upper spectrograph bite. However, only three $(p,^3He)$ angles were measured for the upper bite. The $(p,^3He)$ data were analyzed from only two of these angles because of the large $^{12}C(p,^3He)^{10}B$ contaminant state. The (p,t) and $(p,^3He)$ states in the region where the fifth T=3/2 state should occur are shown in Figs. 4-15 and 4-16.

The sixth T=3/2 states in ^{29}P and ^{29}Si were identified at energies of 11.25 MeV and 11.36 MeV, respectively. The comparison of the $^{31}P(\vec{p},t)^{29}P$ and $^{31}P(\vec{p},^3He)^{29}Si$ angular distributions is shown in the upper half of Fig. 4-17. The (p,t) and $(p,^3He)$ states in the energy region of the sixth T=3/2 state are shown in Figs. 4-18 and 4-19.

The comparisons of the angular distributions for the ^{29}P state at 11.48 MeV and the ^{29}Si state at 11.47 MeV are shown in lower half of Fig. 4-17. These states were identified as the seventh T=3/2 states, on the basis of the cross-section and analyzing-power measurements. The angular distributions for the (p,t) and $(p,^3He)$ states in the energy regions adjacent to these are shown in Figs. 4-20 and 4-21.

The eight T=3/2 states in ^{29}P and ^{29}Si were identified at energies of 11.70 MeV and 11.72 MeV, respectively. The (p,t) state was not

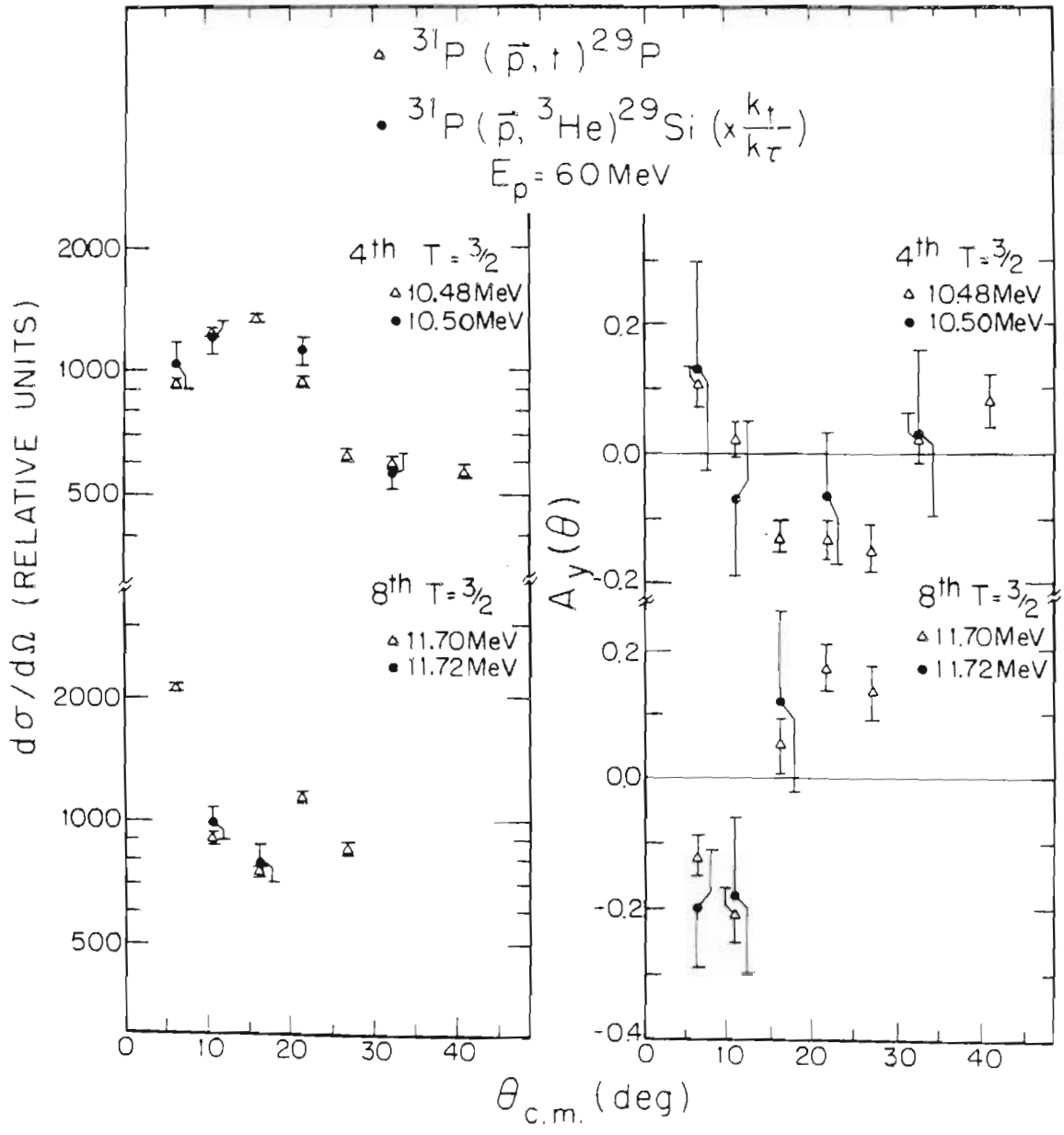

Figure 4-12 The $^{31}P(\vec{p},t)^{29}P$ (open triangles) and the $^{31}P(\vec{p},^{3}He)^{29}Si$ (solid dots) cross-section and analyzing-power angular distribution comparisons for the fourth and eighth T=3/2 states in the $T_z=|1/2|$ A=29 nuclei. The $(p,^{3}He)$ cross-section data have been multiplied by a factor of k_t/k_τ. See Section 4.5.2 for discussion.

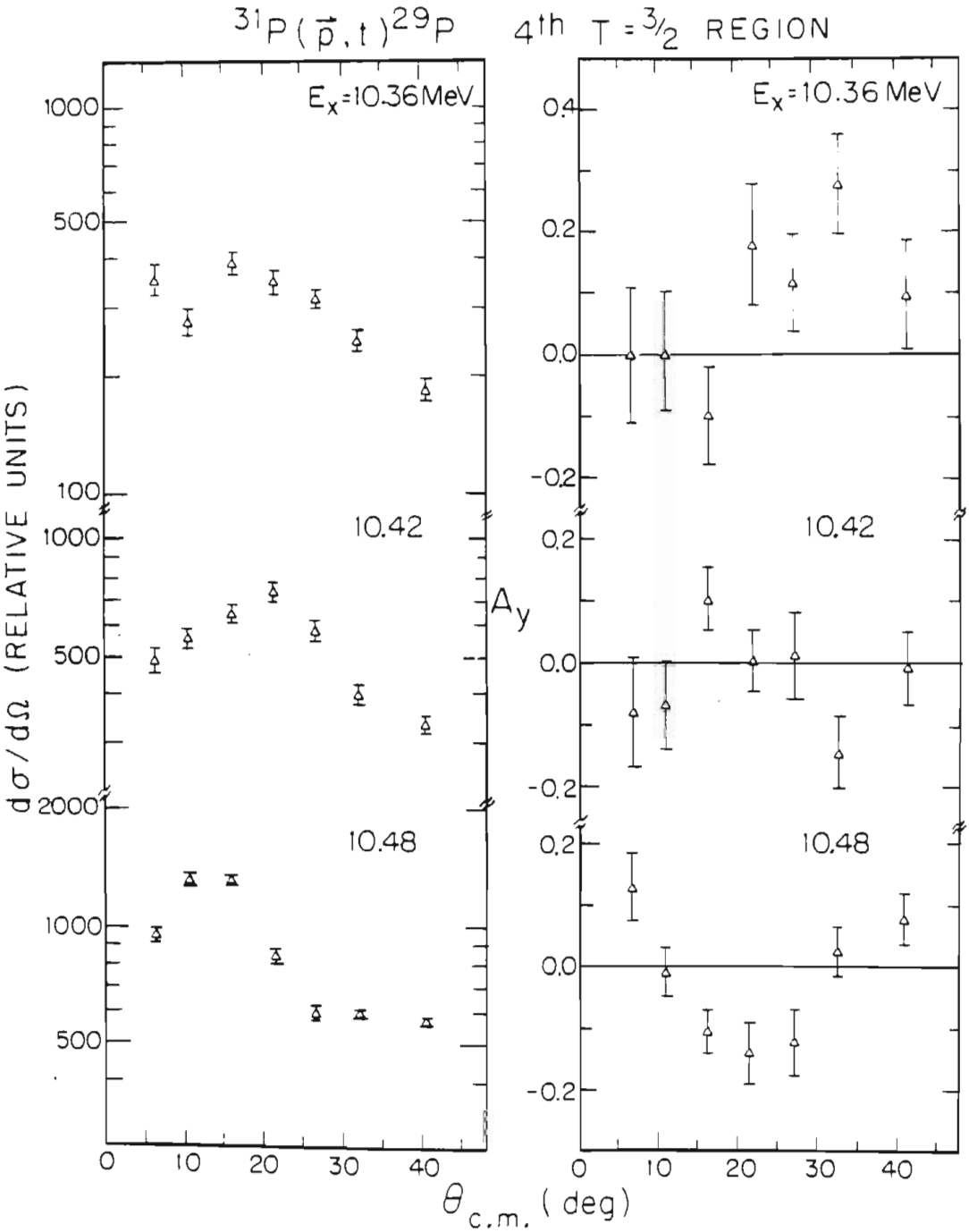

Figure 4-13 The $^{31}P(\vec{p},t)^{29}P$ cross-section and analyzing-power angular distributions for states in the energy region of the fourth T=3/2 state. The 10.48-MeV state has been assigned as the fourth T=3/2 state in ^{29}P. See Fig. 4-12.

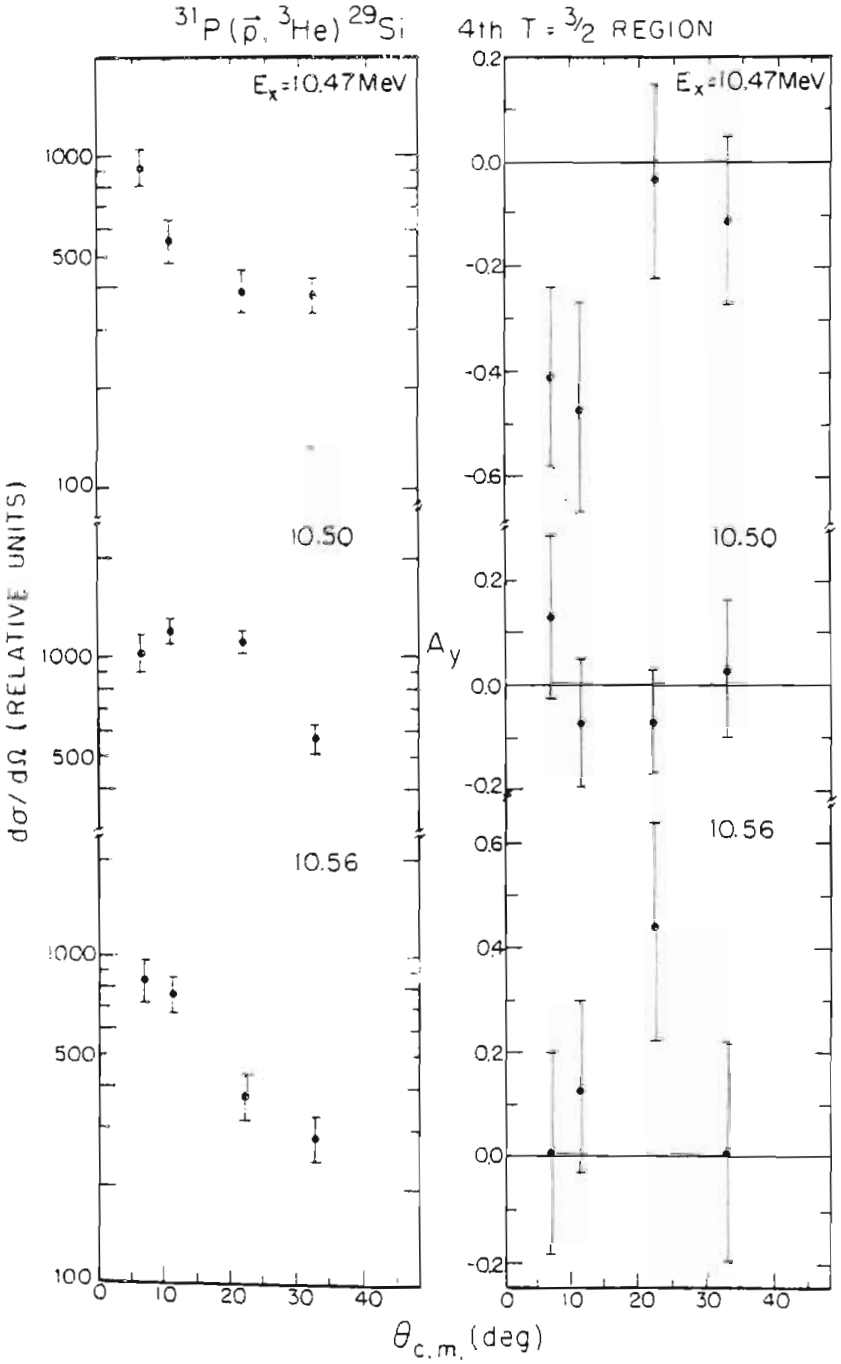

Figure 4-14 The $^{31}P(\vec{p},{}^{3}He)^{29}Si$ cross-section and analyzing-power angular distributions for states in the energy region of the fourth T=3/2 state. The 10.50-MeV state has been assigned as the fourth T=3/2 state in ^{29}Si. See Fig. 4-12.

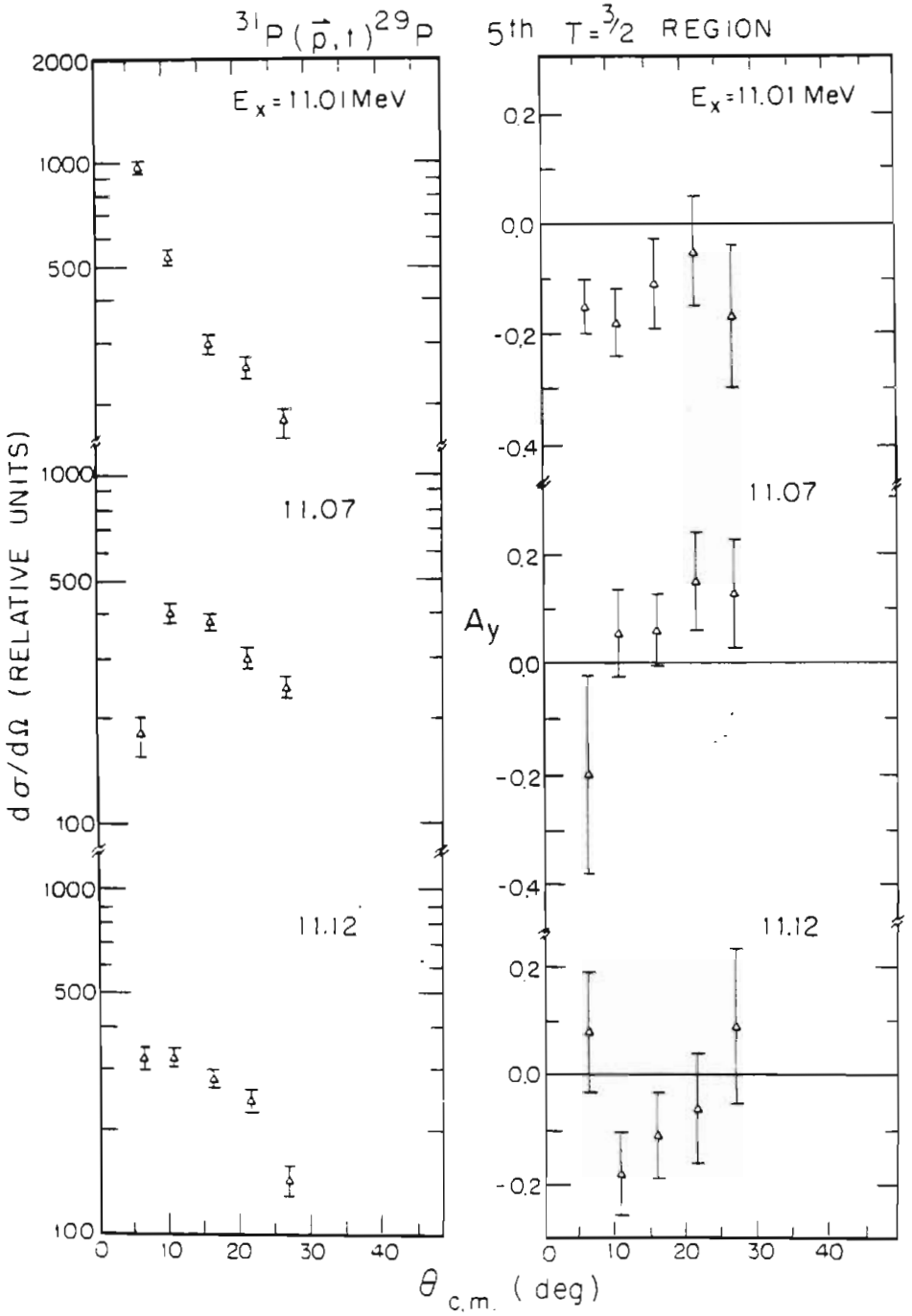

Figure 4-15 The $^{31}P(\vec{p},t)^{29}P$ cross-section and analyzing-power angular distributions for states in the energy region of the fifth T=3/2 state. No state in ^{29}P has been assigned as the fifth T=3/2 state. See Section 4.5.2 for discussion.

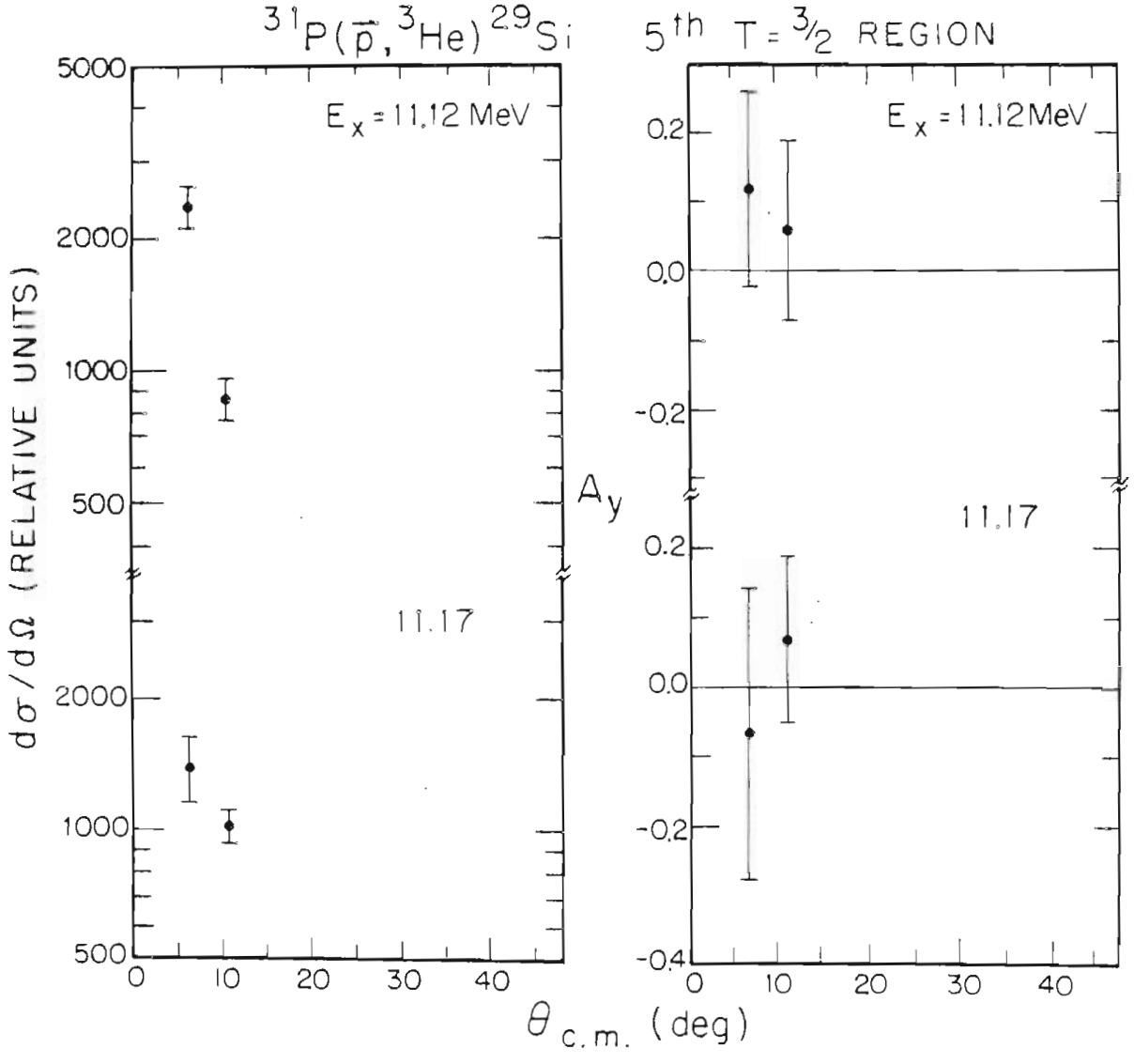

Figure 4-16 The $^{31}P(\vec{p},^{3}He)^{29}Si$ cross-section and analyzing-power two-angle distributions for states in the energy region of the fifth T=3/2 state. No state in ^{29}Si has been assigned as the fifth T=3/2 state. See Section 4.5.2 for discussion.

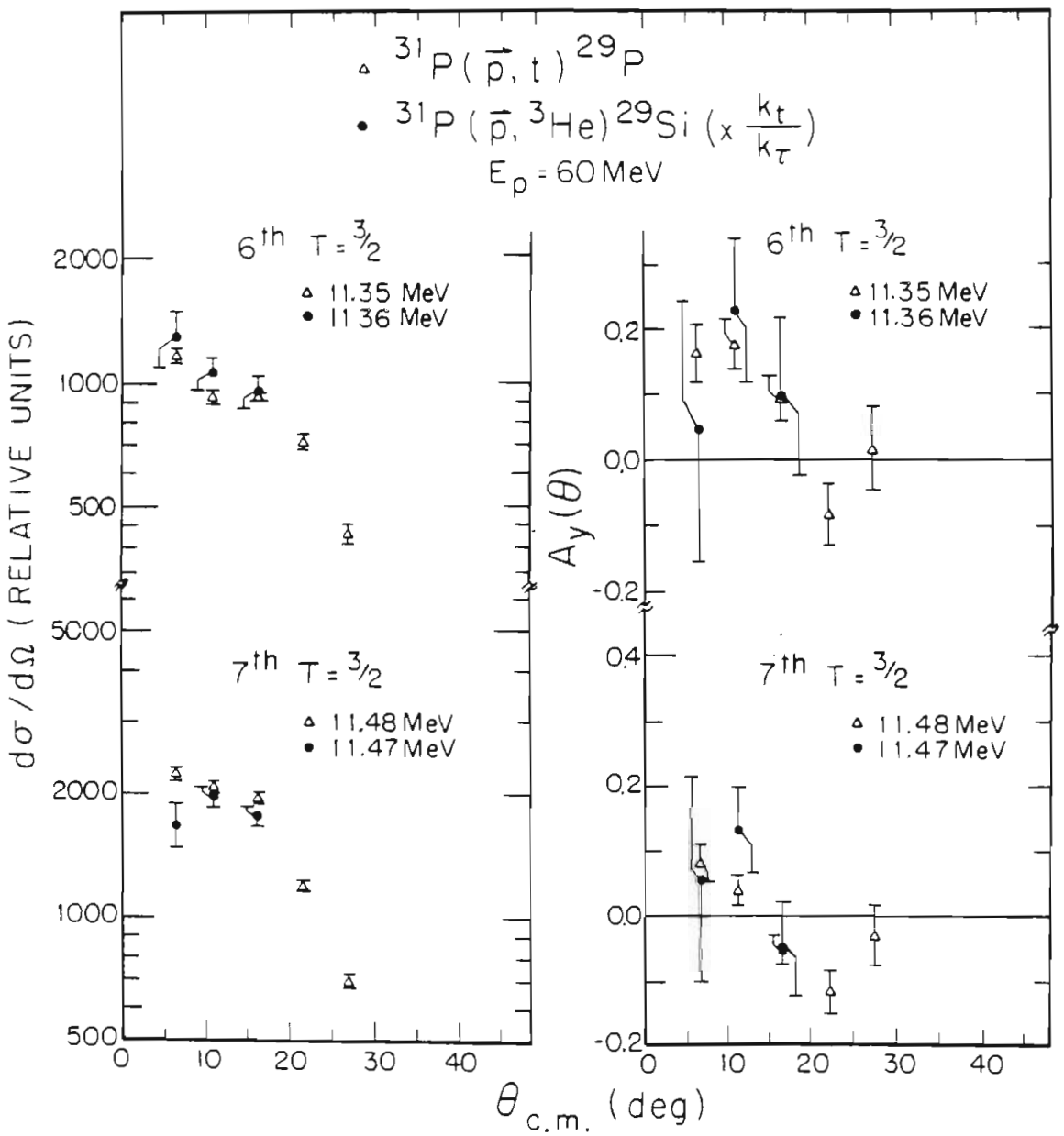

Figure 4-17 The $^{31}P(\vec{p},t)^{29}P$ (open triangles) and the $^{31}P(\vec{p},^{3}He)^{29}Si$ (solid dots) cross-section and analyzing-power angular distribution comparisons for the sixth and seventh T=3/2 states in the $T_z=|1/2|$ A=29 nuclei. The $(p,^{3}He)$ cross-section data has been multiplied by a factor of k_t/k_τ. See Section 4.5.2 for discussion.

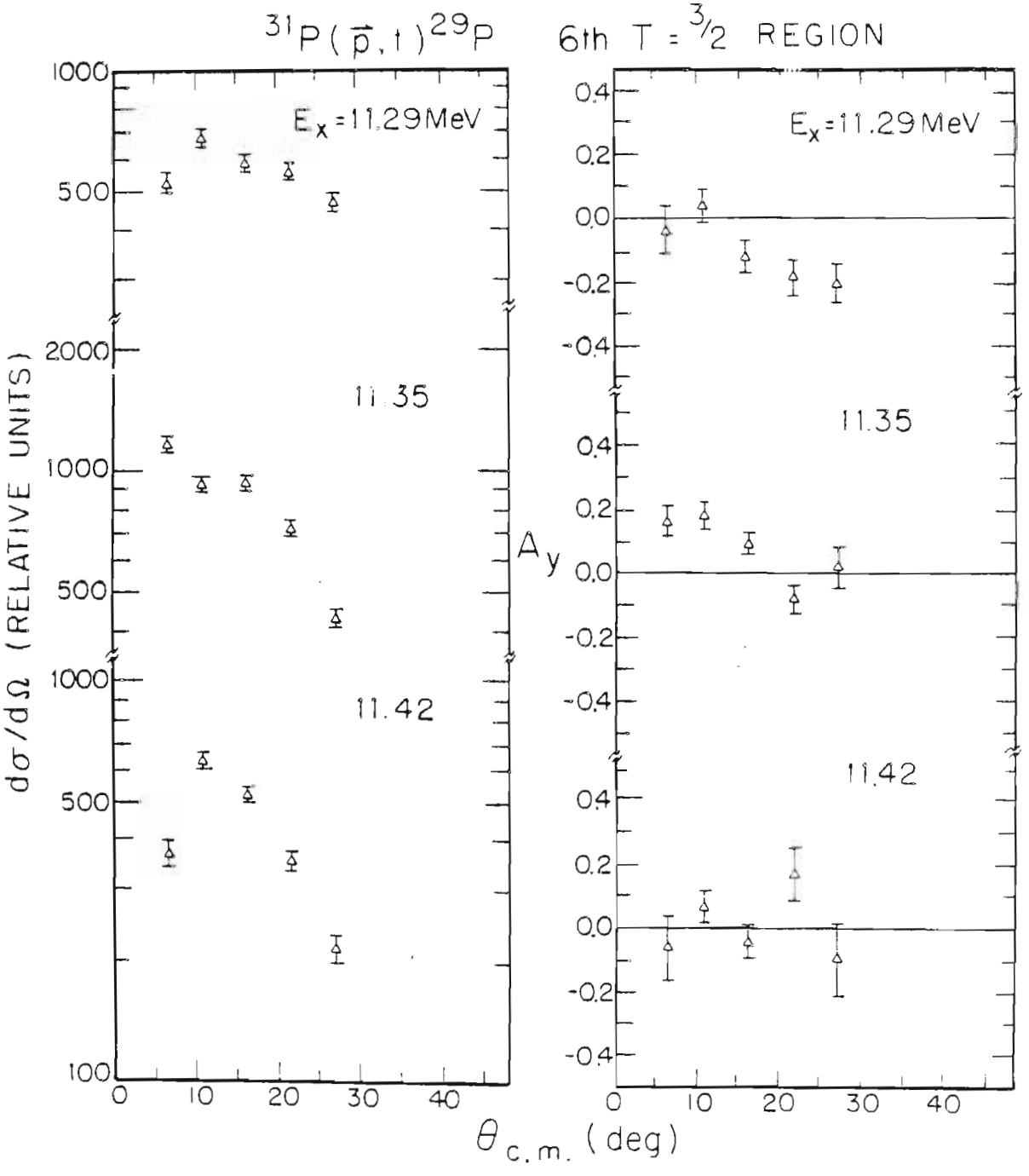

Figure 4-18 The $^{31}P(\vec{p},t)^{29}P$ cross-section and analyzing-power angular distributions for states in the energy region of the sixth T=3/2 state. The 11.35-MeV state has been assigned as the sixth T=3/2 state in ^{29}P. See Fig. 4-17.

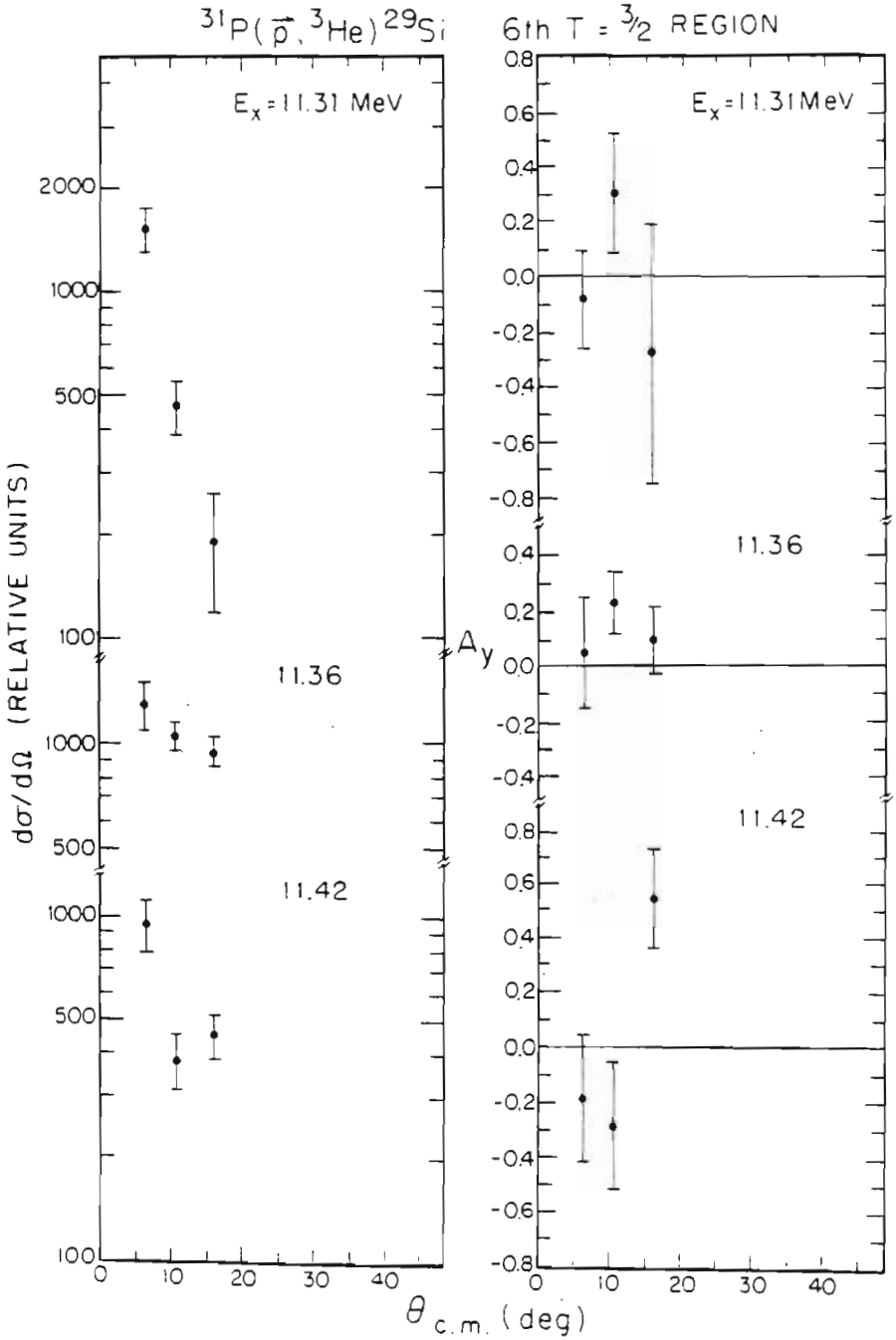

Figure 4-19 The $^{31}P(\vec{p},^{3}He)^{29}Si$ cross-section and analyzing-power angular distributions for states in the energy region of the sixth T=3/2 state. The 11.36-MeV state has been assigned as the sixth T=3/2 state in ^{29}Si. See Fig. 4-17.

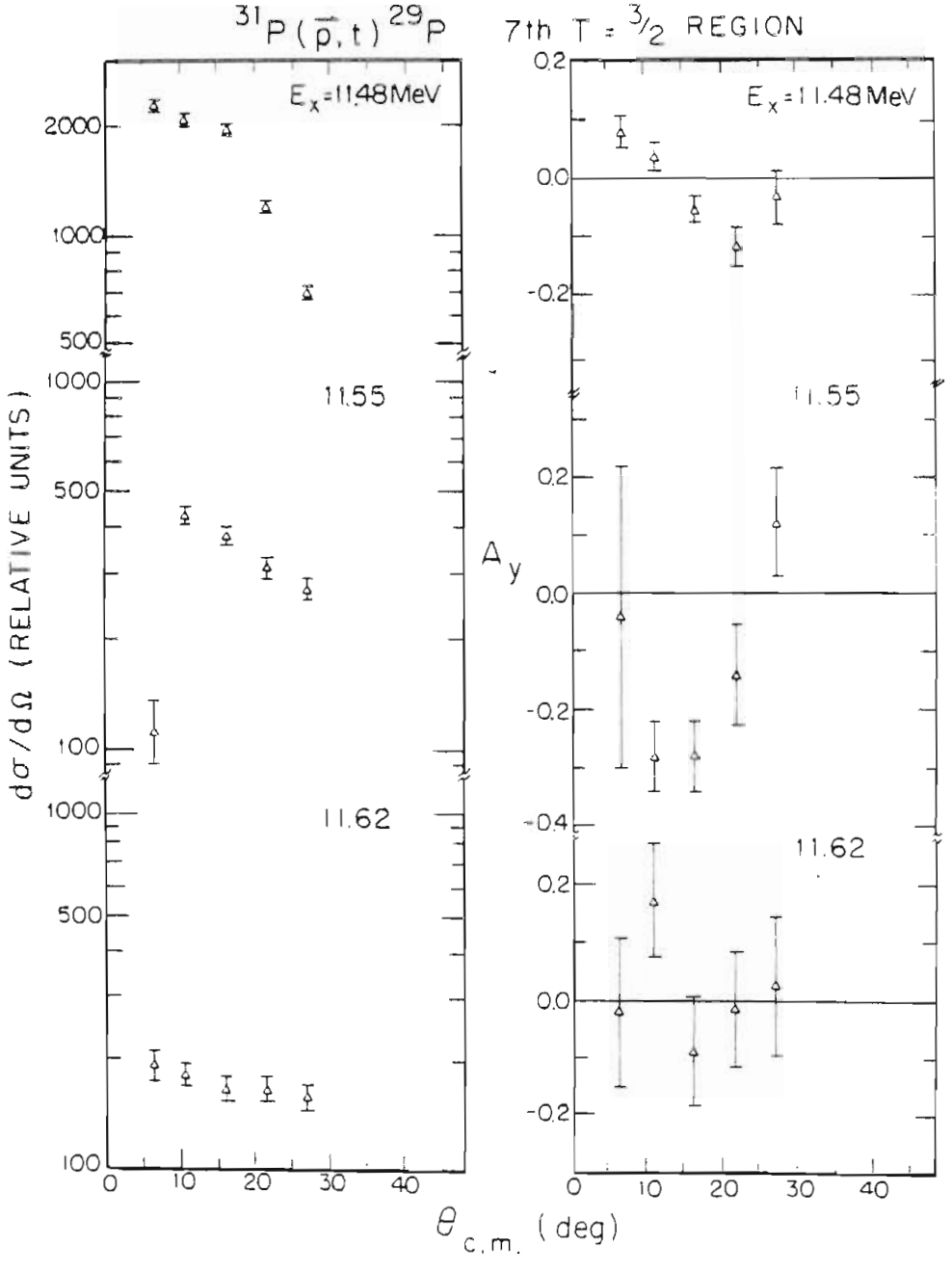

Figure 4-20 The $^{31}P(\vec{p},t)^{29}P$ cross-section and analyzing-power angular distributions for states in the energy region of the seventh T=3/2 state. The 11.48-MeV state has been assigned as the seventh T=3/2 state in ^{29}P. See Fig. 4-17.

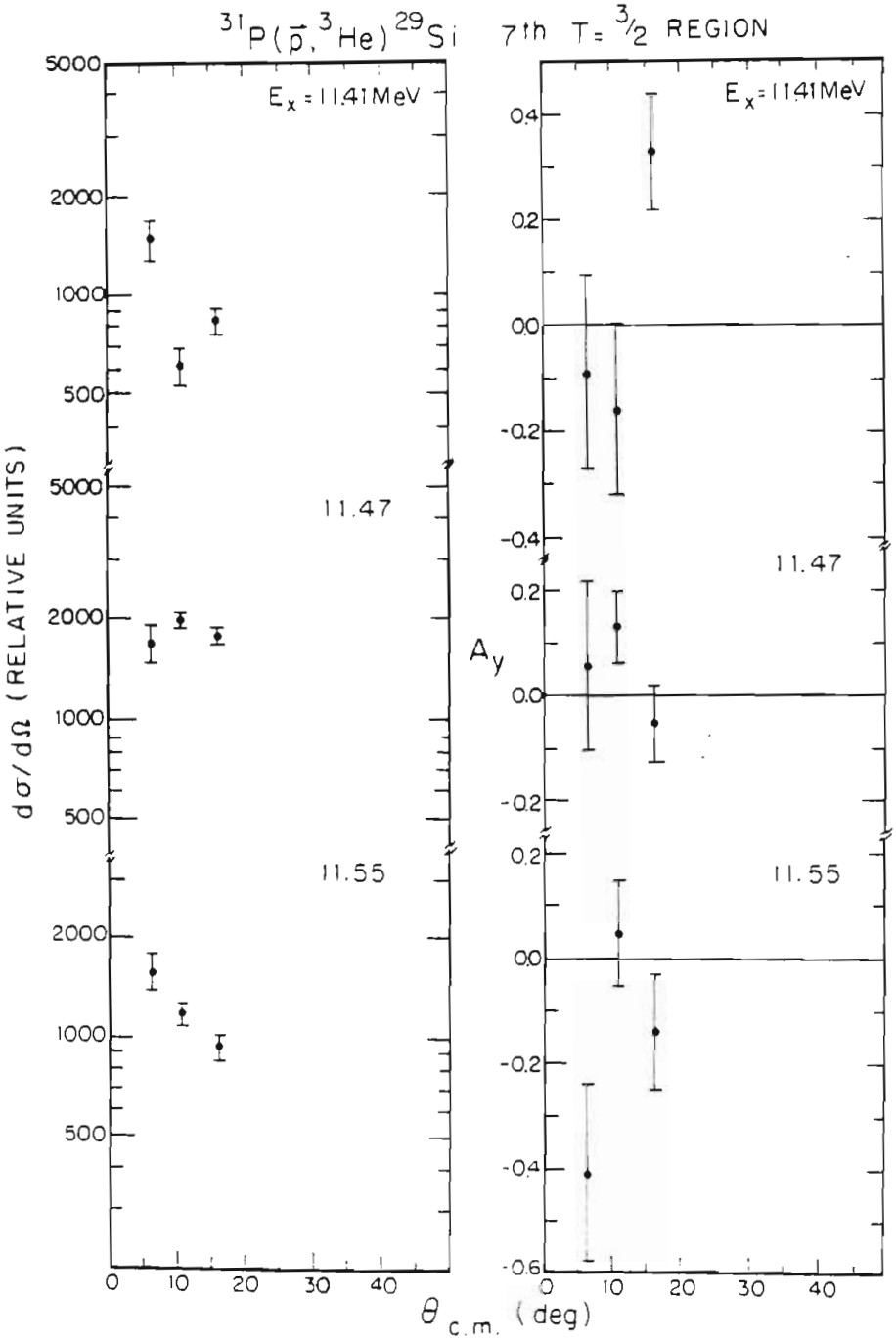

Figure 4-21 The $^{31}P(\vec{p},^{3}He)^{29}Si$ cross-section and analyzing-power angular distributions for states in the energy region of the seventh T=3/2 state. The 11.47-MeV state has been assigned as the seventh T=3/2 state in ^{29}Si. See Fig. 4-17.

identified in the Princeton (p,t) work, as a result of a contaminant peak which obscured this level. The comparison of cross-section and analyzing-power angular distributions is shown in the lower half of Fig. 4-12. The (p,t) and (p,^{3}He) states in the energy regions surrounding these states are shown in Figs. 4-22 and 4-23. The $1/2^+$ character of this state is apparent from the $\ell = 0$ type of angular distribution.

4.6 Summary of IUCF Results. The (p,t) and (p,^{3}He) measurements made at IUCF were very successful in identifying the T=3/2 levels in the $T_z=|1/2|$ A=25 and A=29 nuclei. The excitation energy assignments for these levels are based on the Princeton (p,t) and (p,^{3}He) measurements. The ^{31}P target thickness and resolution problems resulted in poor counting statistics and fewer angles being measured for the $^{31}P(\vec{p},^3He)^{29}Si$ measurements. However, the T=3/2 levels could still be assigned as a result of the analyzing-power measurements. Extracting reliable peak sums from the poorer resolution IUCF data required the high-resolution spectra measured at Princeton.

The final T=3/2 levels identified by the $^{27}Al(p,t)^{25}Al$ and $^{27}Al(p,^3He)^{25}Mg$ cross-section angular distributions are presented in Table 3-3 in conjunction with the Princeton work. The T=3/2 levels observed by $^{31}P(\vec{p},t)^{29}P$ and $^{31}P(\vec{p},^3He)^{29}Si$ cross-section and analyzing-power measurements are listed in Table 3-5. The isospin of the states in Tables 3-3 and 3-5 which were identified by the comparison of the IUCF (p,t) and (p,^{3}He) angular distribution measurements is indicated by a superscript "I" following the energy of the state. The tentative identification of the third T=3/2 state in ^{29}P is labeled by a

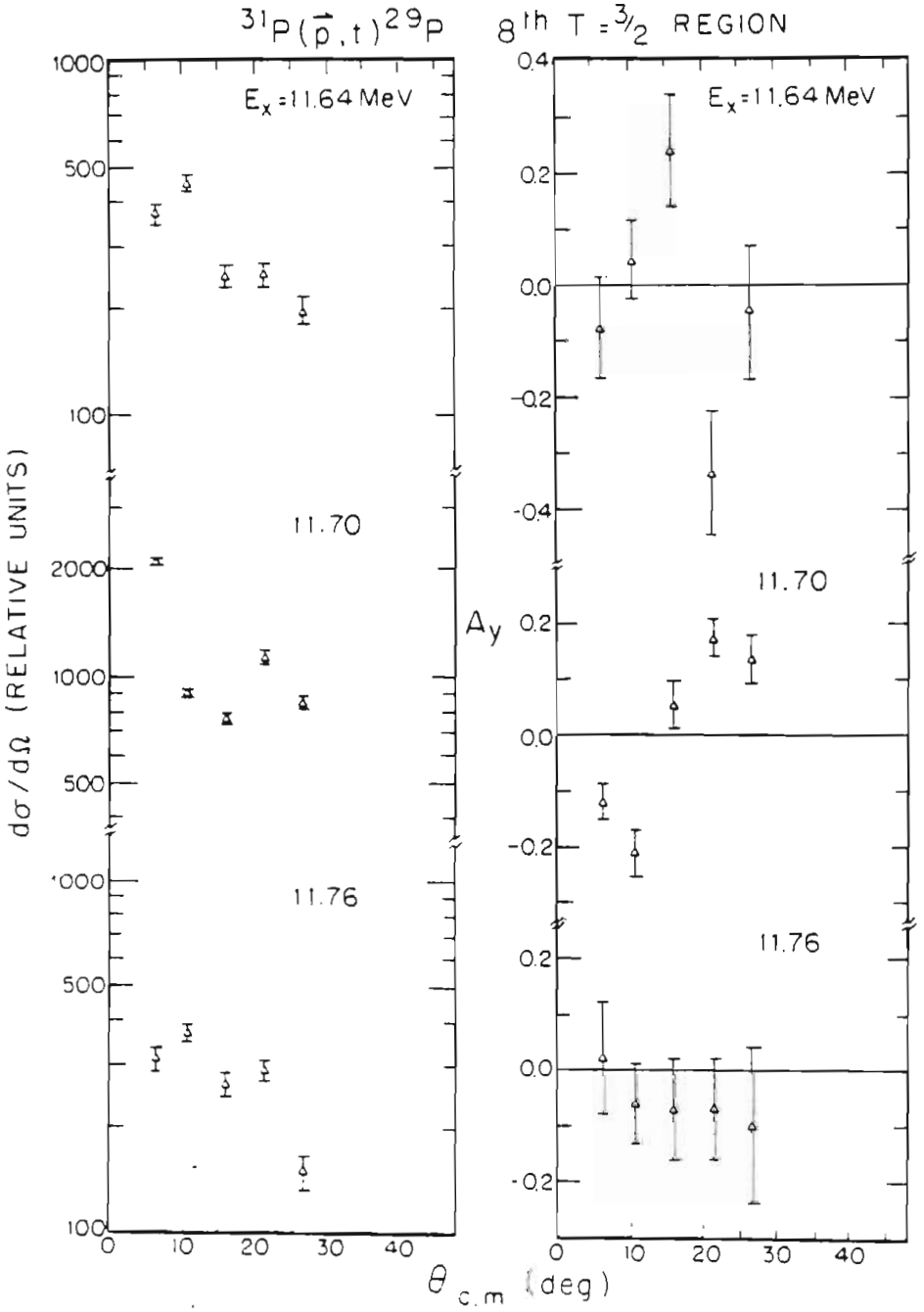

Figure 4-22 The $^{31}P(\vec{p},t)^{29}P$ cross-section and analyzing-power angular distributions for states in the energy region of the eighth T=3/2 state. The 11.70-MeV state has been assigned as the eighth T=3/2 state in ^{29}P. See Fig. 4-12.

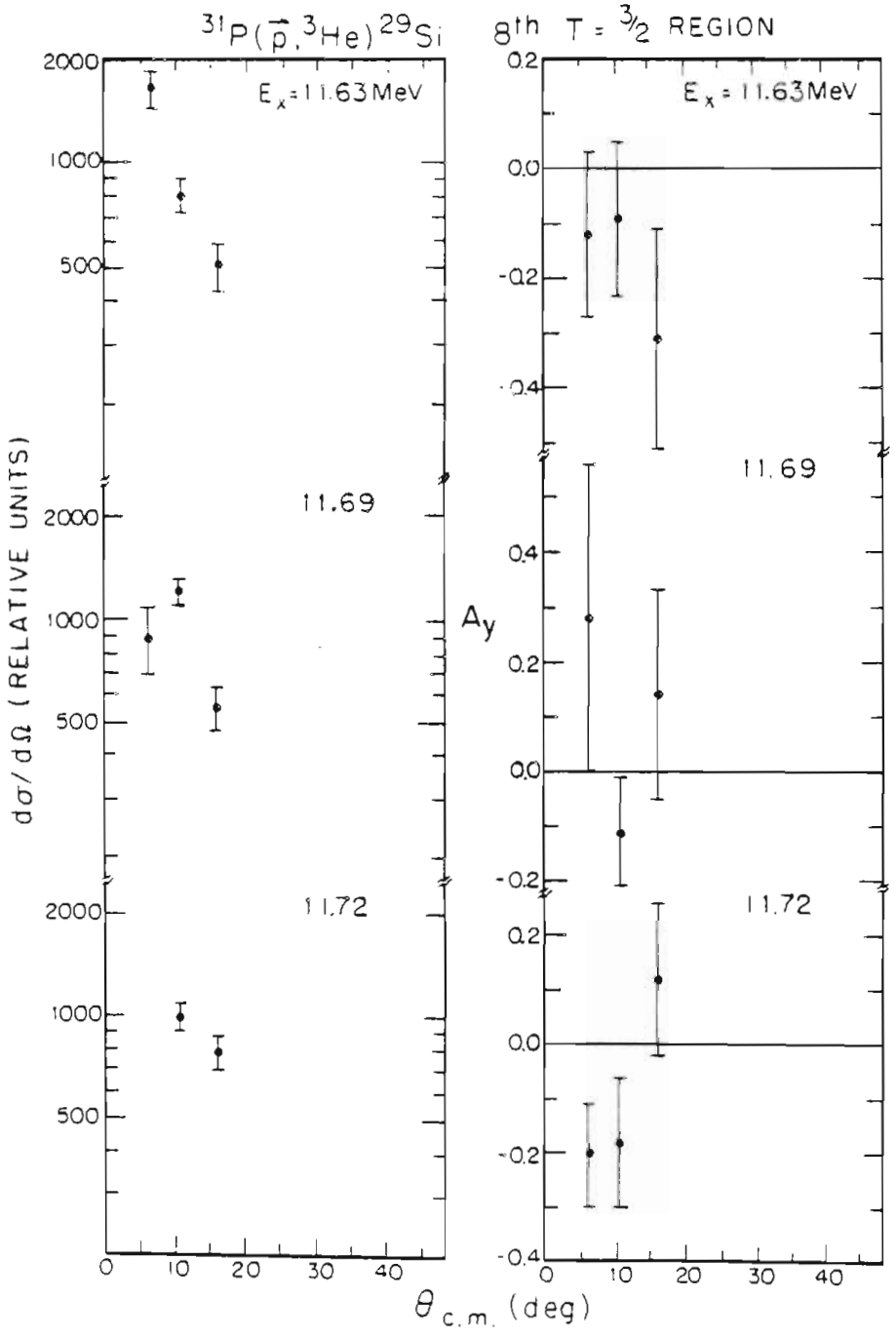

Figure 4-23 The $^{31}P(\vec{p},^{3}He)^{29}Si$ cross-section and analyzing-power angular distributions for states in the energy region of the eighth T=3/2 state. The 11.72-MeV state has been assigned as the eighth T=3/2 state in ^{29}Si. See Fig. 4-12.

superscript "i".

4.7 Summary of (p,t) and (p,^{3}He) Measurements. The success of the (p,t) and (p,^{3}He) measurements performed at Princeton and Indiana resulted in the location and identification of high-lying T=3/2 levels in A=4n+1 $T_z=|1/2|$ nuclei. The IUCF $^{27}Al(p,t)^{25}Al$, $^{27}Al(p,^3He)^{25}Mg$, $^{31}P(\vec{p},t)^{29}P$, and $^{31}P(\vec{p},^3He)^{29}Si$ measurements confirmed the conclusions reached from the corresponding single-angle data taken at Princeton. This confirmation resulted in greater confidence in the single-angle $^{35}Cl(p,t)^{33}Cl$, $^{35}Cl(p,^3He)^{33}S$, $^{39}K(p,t)^{37}K$, and $^{39}K(p,^3He)^{37}Ar$ measurements performed at Princeton.

The accuracy of the excitation energies determined from the Princeton single-angle measurements was much better than hoped. The $(\vec{p},p)$ and (p,p) resonances measured at TUNL were found within 2-10 keV of the resonance energies predicted from the (p,t) measurements. The original expectation was to determine the excitation energies from the (p,t) measurements only to $\pm$ 10-15 keV.

Many of the T=3/2 states located in the A=4n+1 $T_z=-1/2$ nuclei as a result of the (p,t) and (p,^{3}He) measurements were observed at TUNL using $(\vec{p},p)$ scattering. The techniques developed to make these $(\vec{p},p)$ measurements, the $(\vec{p},p)$ measurements, and the resonance parameters extracted from these measurements are discussed in Chapters 5 through 14.

5. Introduction to High-Resolution $(\vec{p},p)$ and (p,p) Investigations

5.1 Description of T=3/2 Isospin-Forbidden Resonance Measurements.

The (p,t) and (p,^{3}He) measurements used to locate the T=3/2 states in the A=4n+1 $T_z=|1/2|$ nuclei are isospin-allowed reactions (discussed in Chapters 3 and 4). These measurements alone do not reveal any information about the isospin mixing that allows the T=3/2 states in the A=4n+1 nuclei to decay through isospin-forbidden channels. One must observe the isospin-forbidden decay of the T=3/2 states in order to measure effects associated with isospin mixing.

5.1.1 Relationship of Resonance Parameters and Isospin Admixtures.

The resonance parameters which reflect the isospin mixing are the total decay width of the T=3/2 state and the partial decay width of the observed decay channel. The total decay width Γ characterizes the overlap of the T=3/2 state wave function with the wave function in the energetically allowed decay channels. If the T=3/2 state and all the energetically available particle decay channels had pure isospin wave functions, the only possible decay of the T=3/2 states in the A=4n+1 nuclei would be limited to γ-decay and isospin-allowed particle decays.

For the lowest T=3/2 states in the A=4n+1 $T_z=-1/2$ nuclei with $A \leq 45$, there are no isospin-allowed particle decays. There are usually no isospin-allowed particle decays for the first five to ten T=3/2 states in the A=4n+1 $T_z=-1/2$ nuclei for $21 \leq A \leq 45$. The locations of

the first T=1 states in the A=4n nuclei, to which the A=4n+1 nuclei could decay by nuclear emission, are presented in Table 5-1. The approximate number of T=3/2 states in those A=4n+1 T_z=-1/2 nuclei which have only isospin forbidden particle decays up to the energy where the decay to the T=1 state is allowed are also listed. The T=1 states in the A=4n nuclei are the first isospin-allowed particle decay channels to become open for the T=3/2 decays. The neutron decay channel for the T=3/2 states in T_z=-1/2 A=4n+1 nuclei becomes possible only at higher excitation energies (see Table 5-1).

The observed total widths of the T=3/2 levels in the T_z=-1/2 A=4n+1 nuclei with isospin-forbidden particle decays range from 40 eV to several keV. The isospin-allowed γ decay widths are only a few eV because of the weakness of the electromagnetic decay. Thus, the observed total widths are dominated by the isospin-forbidden processes. The total and partial decay widths are very sensitive to the isospin admixtures which occur in the T=3/2 states of the A=4n+1 system, the decaying particle internal state, the final state, or any combination of these. From measurement of the partial decay width, the reduced width for a particular decay channel can be obtained. As defined in Chapter 1, the reduced width is the partial width divided by twice the Coulomb penetrability. Dividing by the penetrability removes the kinematic and angular momentum dependences of the reaction from the partial width.

It is not certain what effect the isospin allowed decay channels have on the isospin-forbidden decays once the isospin-allowed particle decays become energetically allowed. The isospin allowed channels are

Table 5-1 Decay Channels for the T=3/2 States in A=4n+1 T_z=-1/2 nuclei [Ajz79, Ajz81, Ajz82, End78].

- o The excitation energy and resonance energy of the first T=3/2 states are listed for reference.
- o The I-F T=3/2 State column is the approximate number of T=3/2 states in the T_z=-1/2 nucleus for which there are only isospin-forbidden particle decays.
- o The energies corresponding the the decay channels are the excitation energies in the compound system where the decays become energetically allowed. The T=1 column refers to proton decay to the lowest T=1 state in the A=4n target.

Compound System						Target System			I-F
A=4n+1	A=4n+p E_b (MeV)	First T=3/2 E_x (MeV)	Decay Channels α (MeV)	n (MeV)	T=1 (MeV)	Target A=4n	First T=1 E_x (MeV)	First T=3/2 E_R (MeV)	T=3/2 States
^{9}B	-.185	14.6550 ± .0025	1.69	18.58	19.85	^{8}Be	17.64	16.695	1
^{13}N	1.9434	15.0645 ± .001	9.49	20.07	16.38	^{12}C	15.11	14.2308 ± .0002	1
^{17}F	0.6004	11.1933 ± .0023	5.82	16.81	13.62	^{16}O	12.80	11.2636 ± .002	4
^{21}Na	2.4318	8.973 ± .003	6.56	17.10	10.79	^{20}Ne	10.27	6.872 ± .005	10
^{25}Al	2.2713	7.901 ± .002	9.15	16.93	9.93	^{24}Mg	9.52	5.966 ± .002	13
^{29}P	2.7471	8.379 ± .002	10.46	17.86	9.66	^{28}Si	9.32	5.835 ± .004	11
^{33}Cl	2.2769	5.544 ± .001	6.48	15.75	7.23	^{32}S	7.00	3.370 ± .001	7
^{37}K	1.8571	5.047 ± .002	6.22	15.45	6.80	^{36}Ar	6.61	3.278 ± .003	4
^{41}Sc	1.0857	5.940 ± .004	6.27	16.19	7.86	^{40}Ca	7.66	4.976 ± .004	21

certainly not energetically favored compared to the isospin-forbidden decays. However, there may be a large overlap of wave functions for the isospin-allowed channel because the T=1 states in the A=4n nuclei are analogs to the ground state of the T=1 parent nuclei, and thus should have simple structure. It is expected that the total widths of the T=3/2 state would increase once an isospin particle decay channel becomes open. The effect on the elastic scattering p_o partial decay width is more subtle. If all the decay channels were independent, then the occurrence of the isospin-allowed decay would not affect the partial width. However, the final state wave function is comprised of all the decay channels and is a quantum mechanical system which is not a set of independent wave functions. Thus, the elastic scattering partial decay width may also increase once the isospin-allowed particle decay channels become available.

5.1.2 Measurement Techniques Used to Extract the Resonance Parameters. All previous analyses performed to extract the total widths and p_o partial widths for the decay of the T=3/2 states in the T_z=-1/2 nuclei required combining data from at least two separate measurements. All but one of the experiments measured (p,p) elastic scattering energy excitation functions in order to obtain part of the necessary data. The exception was the first T=3/2 ^{9}B decay measurement, for which the determination of the widths relied on measurements of decay branching ratios and the ^{9}Be Γ_γ width. The extraction of the total and p_o partial widths was based on relationships between the branching ratios, and on several assumptions [McD76a, Ad171, Ad172, Ber73].

The measurements additional to the (p,p) energy-excitation function data which are needed to deduce the T=3/2 state p_o partial width depend on the analysis method used to extract the widths. One method is to measure and analyze the off-resonance angular distributions. The off-resonance data are parameterized by an optical model analysis. The T=3/2 (p,p) resonance is then analyzed assuming an isolated single-level Breit-Wigner resonance and using phase-shift analysis techniques to determine the mixing of the resonance with the off-resonance cross section [McD69, Skw74, Hin76]. This method, called an optical-model phase-shift analysis, allows extraction of the resonance energy E_R, the spin and parity of the state J^π, and the total width Γ. The p_o partial width Γ_p can be extracted in some cases [Skw74], although there are examples where the branching ratio of Γ_p / Γ must be known [Hin76] to deduce the partial width.

Another method [Iko76] used to extract the resonance widths involves using a model-independent helicity amplitudes analysis. This analysis assumes an isolated Breit-Wigner resonance amplitude mixing with off-resonance amplitudes. The off-resonance cross section and analyzing power must be measured. This analysis method is sensitive to the total width, and thus the branching ratio Γ_p / Γ must be known in order to extract Γ_p. The different resonance analysis methods will be discussed in detail in Chapter 6.

For the first T=3/2 states in A=4n+1 T_z=-1/2 nuclei, the p_o branching ratio is known from β^+-delayed proton decay measurements (see Table 2-1 for references). The results from the (p,p) energy excitation

function measurements combined with the branching ratio Γ_p / Γ yield a value for the partial proton width. Extracting a partial proton width for the higher T=3/2 resonances requires either using a different method to determine the branching ratio or performing the angular distribution measurements and phase-shift analysis. However, the phase-shift analysis method becomes less reliable at higher excitation energies as more T=1/2 states contribute to the off-resonance cross section and as more partial waves and decay channels participate. The phase-shift analysis may not be sensitive to both the total and partial widths for narrow resonances which have a small effect in the cross section.

Measuring the branching ratios of higher T=3/2 states can be accomplished by populating the T=3/2 states through an isospin-allowed reaction [Ade73]. The isospin-forbidden decays of the T=3/2 state can be observed in coincidence with the outgoing reaction products of the isospin-allowed reaction channel. For example, it would have been possible to make our (p,t) measurements in coincidence with the T=3/2 particle decays. However, the experiments would have required a substantial increase in beam time. Although this technique has not been used to measure any of the high lying T=3/2 states branching ratios, it was used in measuring branching ratios for some of the first T=3/2 states [Ade69, Ade73] and for the first T=2 states [Fre79].

There are also instances where the branching ratios are determined by a comparison of the inelastic and elastic cross-section yields [Tei69, Goo67]. Unless only two or three channels are open this is a dubious method. Even with only two channels open it would require

careful angular distribution measurements. In general, comparing cross sections at a few angles is not sufficient to determine the branching ratios.

5.1.3 A Single Measurement Technique to Extract Resonance Parameters. Experimental techniques and an analysis method were developed in the present research to allow the determination of all the resonance parameters (E_R, J^π, Γ, and Γ_p) from a single experiment. The experimental method was to take high-resolution $(\vec{p},p)$ energy excitation functions of cross section and analyzing power. Calculations predicting that the combined cross-section and analyzing-power excitation function data would be sensitive to both the total and partial proton widths provided the motivation for the this technique [Tho79]. Thus, one experimental measurement could be used to acquire all the necessary resonance parameters. A computer program T32GRD was written for the analysis and will be discussed in Chapter 6.

To illustrate the analysis technique, a model-independent, helicity amplitude, analysis method mentioned in the previous section was used to make fits to cross-section excitation function data for the first T=3/2 resonance in ^{13}N. Several calculations were performed using a fixed total width determined from earlier measurements, but used several different branching ratios. The calculated fits for different branching ratios resulted in equally good fits to the cross-section excitation function data. However, the predicted analyzing-power excitation functions were very sensitive to different branching ratios. The results of these calculations are shown in Fig. 5-1. Although the

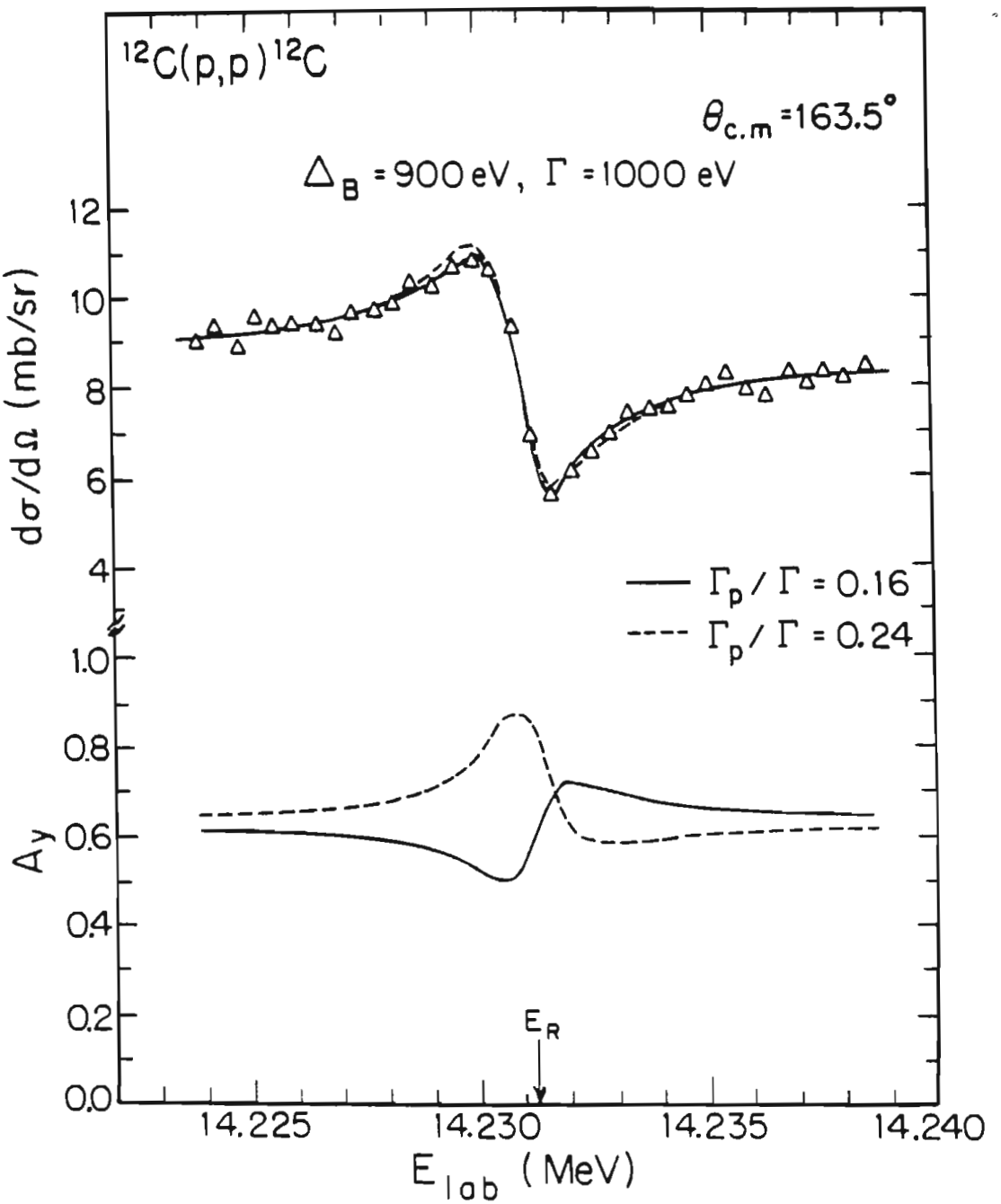

Figure 5-1 Calculated T32GRD cross section fits to first T=3/2 $^{12}C(p,p)^{12}C$ resonance. Fits for two different branching ratios are shown. The predicted analyzing power excitation functions are plotted for the two fits. Although the fits to the cross section excitation function data are not very sensitive to the different branching ratios, the A_y data are sensitive in phase and amplitude to the branching ratios.

most striking features are the phase differences of the analyzing-power predictions, the difference in amplitudes for the two different branching ratios is significant.

5.2 Overview of Present High-Resolution Measurements. A project of developing a system to perform routine high-resolution polarized beam measurements was undertaken. Although polarized beam energy excitation functions have been previously acquired [Ada66], there was no reported high-resolution polarized beam energy excitation function data prior to this work. In addition, this is the first extraction of branching ratios of very narrow resonances by measurement of polarized beam energy excitation functions.

5.3 Outline of High-Resolution Measurements Presentation. The details of the analysis method and development of the computer fitting code T32GRD will be described in Chapter 6. The necessary improvements and changes to the existing high-energy resolution system at TUNL in order to acquire high-resolution polarized beam data are discussed in Chapter 7. A beam energy spread measurement system designed and implemented to make more reliable high-resolution measurements is presented in Chapter 8. Chapter 9 explains the beam energy magnet analysis system calibration which allows the assignment of absolute resonance energies to $\pm$ 2 keV. The data from the measured T=3/2 resonances are presented in Chapters 11, 12, and 13.

5.4 Review of Previous T=3/2 Resonance Measurements. The decay parameters of the first T=3/2 states in A=4n+1 T_z=-1/2 nuclei p_o decays were presented and briefly discussed in Chapter 1. A summary of the

results is presented in Table 1-1 and the reduced widths are plotted in Fig. 1-1. A more complete review will not be presented here but can be found in [Iko75, Iko76, McD76]. Several of the first T=3/2 states were remeasured using the high-resolution polarized beam techniques. These remeasurements were used to check the analysis method by comparing the Γ and Γ_p values extracted from the new analysis of the cross-section and analyzing-power excitation function data with those obtained previously from cross-section measurements and known branching ratios.

The previous measurements of resonance parameters for the high-lying T=3/2 states in these same A=4n+1 T_z=-1/2 nuclei will now be presented. There have been no high-lying states previously measured in A=9, A=37, or A=41 T_z=-1/2 nuclei. No measurements were made in the present study of high-lying T=3/2 levels in the A=9 or A=41 system because of problems in locating and/or measuring their high-lying resonances. The second T=3/2 level in ^{9}B has an isospin-allowed particle decay to the T=1 state in ^{8}Be. The location of high-lying T=3/2 states in ^{9}B and ^{41}Sc have not been determined.

5.4.1 High-lying T=3/2 States in ^{13}N. Two states in ^{13}N possibly corresponding to T=3/2 levels were observed previously in ^{12}C(p,p)^{12}C excitation functions. The resonance parameters were determined using an optical-model phase-shift analysis with an isolated single-level resonance [Lev69]. The resonance parameters used in fits for these states are presented in Table 5-2. As listed in Table 2-1, there are (^{3}He,n) data identifying T=3/2 states in the A=4n+1 nuclei in the same energy regions where the (p,p) resonances were found [Ade69]. These

possible T=3/2 states in the A=4n+1 T_z=-1/2 nuclei cannot be correlated with states in the T_z=|3/2| parent nuclei because the spins and parities of the T_z=|3/2| excited states have not been determined [Ajz81].

The state at 18.352 MeV in ^{13}N has a much greater total and partial widths than the observed widths of any known high-lying T=3/2 states in light nuclei. The state at 18.961 has widths which are more usual and in agreement with values found for other T=3/2 states. Both of these resonances occur at excitation energies which allow the isospin-allowed decay to the first T=1 state in ^{12}C. The opening up of an isospin-allowed channel would certainly increase the total width and would result in a smaller Γ_p / Γ branching ratio. The (p,p) study reported that states with branching ratios less than 0.01 could not be observed [Lev69]. Although the (p,p) data were considered to be measured by state-of-the-art high resolution methods when taken, the resolution is poor by present standards. It is possible that the reported states observed in (p,p) excitation functions may not be the T=3/2 states and that the T=3/2 states suggested by the (^{3}He,n) data were not observed in the (p,p) excitation functions.

No effort to measure high-lying T=3/2 states in ^{13}N was made in the present studies. The high incident proton energies required ($E_p \geq$ 17.8 MeV) are above the nominal upper limit for the TUNL FN tandem accelerator (17.5 MeV). Also, all high-lying T=3/2 states in ^{13}N have isospin-allowed particle decays. The first T=3/2 state was remeasured with polarized beam in the present study.

5.4.2 High-lying T=3/2 States in ^{17}F. The resonance parameters for

Table 5-2 Previously Measured Resonance Parameters of High-Lying T=3/2 States in A=4n+1 T_z=-1/2 nuclei.

A=4n+1	T=3/2 State (MeV)	E_x (MeV)	E_R (MeV)	J^π	Γ (keV)	Γ_p (keV)	REF
^{9}B	2	17.076 ± .004	19.420	$(1/2^-)$	22.0 ± 5.0	------	[Ben74]
^{13}N	-	18.406 ± .005	17.857 ± .005	$3/2^+$	66.0 ± 8.0	16.5	a
	-	18.961 ± .005	18.460 ± .010	b	23.0 ± 5.0	------	a
^{17}F	2	12.5508 ± .0023	12.7077 ± .002	$3/2^-$	2.83 ± 0.12	0.94 ± 0.06	[Hin76]
	3	13.080	13.271 ± .004	$(1/2^+)$	2.0 ± 1.0	0.08 ± 0.04	[Skw74]
	4	13.061	13.250 ± .004	$5/2^-$	2.0 ± 1.0	0.30 ± 0.15	[Skw74]
	5	13.782	14.017 ± .004	$5/2^+$	12.0 ± 5.0	0.24 ± 0.12	[Skw74]
	6	14.310	14.579 ± .010	$7/2^-$	20.0 ± 5.0	2.20 ± 1.10	[Skw74]
		14.3042 ± .0033	14.3040 ± .003		19.3 ± 1.6	1.65 ± 0.12	[Hin76]
	7	14.177	14.4438 ± .006	$3/2^-$	27.0 ± 5.0	1.08 ± 0.50	[Skw74]
^{21}Na	2	9.220 ± .007	7.128 ± .005	$1/2^+$	2.3 ± 0.5	1.10 ± 0.30	[McD69]
^{25}Al	2	7.970 ± .004	5.938 ± .003	$3/2^+$	0.21 ± 0.05	0.10 ± 0.03	[Iko76]
^{29}P	(2)	9.743	(7.248 ± .006)	$1/2^+$	6.3 ± 3.0	----	[Tei69]
^{33}Cl	2	6.985	4.855 ± .003	$3/2^+$	10.0 ± 1.0	7.0 ± 0.07	[Abb73]
	3	7.401	5.284 ± .003	$5/2^+$	11.0 ± 1.1	10.4 ± 1.04	[Abb73]

a) [Ajz81] combination of data from [LeV69] and [Ber76].

b) $J^\pi = 3/2^-$ or $7/2^+$

the second through seventh T=3/2 states in ^{17}F have been reported [Skw74, Hin76]. These states were measured using (p,p) scattering and off-resonance angular distribution measurements. The resonance parameters were extracted using the optical-model phase-shift analysis method. The results of these measurements are summarized in Table 5-2.

The more recent measurements [Hin76] of the 12.71 and 14.57 MeV resonances had good beam resolution and careful consideration of resolution parameters. However, the other measurements [Skw74] were taken with resolution which is poor by present standards, and the large error bars reflect the large uncertainties in the data quality and the fact that at the high excitation energies where the T=3/2 states occur in ^{17}F, the optical-model phase-shift analysis method becomes difficult. The first four T=3/2 resonances have no isospin-allowed particle decays. All the other reported resonances occur at excitation energies which allow isospin-allowed decay to the T=1 state in ^{12}C.

One disturbing feature of the reported T=3/2 states in ^{17}F is their energy location relative to the T_z=+3/2 parent states. As discussed in Chapter 4, the (p,t) and (p,^{3}He) identification of T=3/2 states in T_z=-1/2 nuclei indicated that there was a systematic behavior of the high-lying T=3/2 state excitation energies when compared with the energies of the T=3/2 states in the T_z=3/2 nuclei. The data from other isobaric multiplets indicated that the high-lying states would be found at slightly smaller, or nearly the same, energies as predicted from adding the corresponding T_z=3/2 excited state energy to the excitation energy of the lowest T=3/2 state in the T_z=-1/2 nuclei. However, the ^{17}F

states identified from the [Skw74] (p,p) work do not exhibit this behavior. Based on the poor resolution of this work, the lack of other experimental evidence to verify the isospin of these states, and the lack of systematic behavior of the energy locations, some of these identifications may be incorrect. The present study examined only the first and second T=3/2 states.

5.4.3 High-lying T=3/2 States in ^{21}Na. The second T=3/2 in ^{21}Na was observed previously by ^{20}Ne(p,p)^{20}Ne scattering [McD69]. The location of this state has been confirmed by several other measurements, as shown in Table 2-1 [But68, Ben73a, Ade69, Bea70]. The resonance parameters given in Table 5-2 were extracted using an isolated single-level resonance and phase shift analysis technique. This resonance occurs at a lower excitation energy than the resonances in ^{13}N and ^{17}F. Hence, the phase shift analysis method should be more reliable for extracting the resonance parameters since fewer partial waves and phase shifts are present.

Because neither a windowless differentially pumped gas target nor an ^{20}Ne ion-implanted target was available to perform the high-resolution $(\vec{p},p)$ measurements, no measurements of high-lying T=3/2 levels in ^{21}Na were attempted in the present study.

5.4.4 High-lying T=3/2 States in ^{25}Al. The second T=3/2 resonance in ^{25}Al has been measured using ^{24}Mg(p,p)^{24}Mg scattering [Iko76, Tei69]. For both measurements the data were analyzed by a model-independent method using isolated Breit-Wigner resonance level amplitudes and constant off-resonance amplitudes which described the cross section and

analyzing powers. The data of Ikossi [Iko76] were taken with high-resolution techniques. However, the extraction of the partial proton width is based on a Γ_p / Γ value determined by comparison of inelastic and elastic cross section yields. The resonance parameters are presented in Table 5-2.

The present study measured the first and second T=3/2 states in ^{25}Al by taking polarized beam excitation functions. The third T=3/2 resonance was observed with unpolarized beam.

5.4.5 High-lying T=3/2 States in ^{29}P. The second T=3/2 state in ^{29}P was tentatively identified previously by measuring (p,p) energy excitation functions [Tei69]. However, the location of the T=3/2 state is in disagreement with our current result from ^{31}P(p,t)^{29}P and ^{31}P(p,^{3}He)^{29}Si measurements. The resonance parameters for this state were extracted in [Tei69] using the model independent isolated resonance analysis method and are presented in Table 5-2.

The present study has measured the first, second, fourth, sixth, and seventh T=3/2 states. We have also measured a resonance that has been tentatively identified as the third T=3/2 state. Our identification of the second T=3/2 resonance is in disagreement with the earlier work.

5.4.6 High-lying T=3/2 States in ^{33}Cl. The resonance parameters for two resonances claimed to be the second and third T=3/2 resonances in ^{33}Cl were measured using (p,p) scattering [Abb73]. The resonance parameters extracted for these two resonances are presented in Table 5-2. The identification of these levels as T=3/2 states and much of the

rest of this work is in strong disagreement with the present results.

The present work has measured polarized beam excitation functions for the first, second, and third T=3/2 states. The location of these T=3/2 levels was confirmed from the $^{35}Cl(p,t)^{33}Cl$ and $^{35}Cl(p,^{3}He)^{33}S$ measurements.

5.4.7 High-lying T=3/2 States in ^{37}K. Although no previous studies of high-lying T=3/2 states in ^{37}K had been performed, the first, second and third T=3/2 levels in ^{37}K were studied in the present work. The results from all the $(\vec{p},p)$ measurements will be presented in Chapters 11, 12, and 13.

6. $(\vec{p},p)$ and (p,p) Investigations - Analysis

6.1 Introduction. The effect of very narrow nuclear resonances on (p,p) scattering can be described by a single-level Breit-Wigner resonance amplitude and non-resonant scattering amplitudes. However, correct extraction of the resonance parameters requires more than a description of the nuclear scattering processes. The various experimental resolution effects which modify the observed resonance scattering must also be understood and considered in the calculations. The energy spread of the incident protons, the effect of using a finite-energy-loss target, and the lattice vibrations of the target nuclei are energy-averaging parameters that all smear the observed cross-section and analyzing-power energy excitation functions.

This chapter will present the $(\vec{p},p)$ scattering analysis method used to describe the experimentally observed nuclear scattering. A description of the resolution parameters and the calculation of these resolution effects will also be presented. However, a general review of nuclear scattering theory will not be included. For an introduction to or review of scattering theory, refer to nuclear physics textbooks such as [Jac75] or [Sat80].

6.2 (p,p) Resonance Analysis Methods. Several different analysis methods can be used to describe the proton elastic-scattering resonance cross section and analyzing power. All of these analysis methods assume

that a narrow nuclear resonance described by a single-level Breit-Wigner amplitude is interfering with non-resonant scattering amplitudes. The off-resonance cross section is assumed to be a mixture of broad T=1/2 levels and other continuum states.

One method to describe the non-resonant (off-resonance) amplitudes utilizes a set of constant phase shifts [Lan58, McD69]. The assumption of constant phase shifts is valid if the penetrability and shift functions are constant over the energy region of the resonance. This R matrix model can be formulated exactly if the non-resonant scattering is only from Coulomb scattering. However, the phase-shift method becomes unmanageable and yields ambiguous results as the bombarding energy increases, because of the large number of complex phase shifts required.

An improvement to the above analysis method is the use of an optical-model analysis to describe the off-resonant scattering amplitudes [Tho68]. The resonance scattering can be described again as the collision matrix resulting from the interference of the single-level resonance amplitudes with the non-resonant scattering amplitudes. However, at the excitation energies in the compound nucleus where the high-lying T=3/2 states occur there are many distinct T=1/2 resonances and the optical-model analysis is unsuitable, especially in the light mass, s-d shell nuclei considered here.

A combination of the above phase-shift and optical-model methods has also been used [Skw74, Hin76, McD76]. This analysis method uses an optical-model parameterization of the off-resonance cross sections to determine the non-resonant phase shift amplitudes. This is sometimes

called the optical-model, complex phase shift method. This method is a variation of the optical-model method described above and experiences the same problems at high excitation energies.

6.2.1 Helicity Amplitude Analysis Method. The method we chose to analyze the $(\vec{p},p)$ resonance measurements is a model-independent helicity-amplitude method. This analysis method is practical for resonances which are sufficiently narrow such that the non-resonant scattering amplitudes can be approximated as constant over the energy interval of the resonance excursion.

For scattering of spin-1/2 and spin-0 nuclei at a particular c.m. angle θ, the differential cross section σ and the analyzing power A_y are given by [Cri49]

$$\sigma = |a|^2 + |b|^2, \qquad 6\text{-}1$$

$$\sigma \cdot A_y = 2 \cdot \mathrm{Im}(a^* b). \qquad 6\text{-}2$$

where $\sigma \cdot A_y$ is referred to as the analyzing power cross section. The non-spin flip amplitude "a" and the spin-flip amplitude "b" are described by

$$a = a_{nr}(\theta) + a_R(\theta,E) \qquad 6\text{-}3a$$

$$b = b_{nr}(\theta) + b_R(\theta,E) \qquad 6\text{-}3b$$

with each amplitude represented by the sum of a non-resonant and

resonant amplitude. The non-resonant amplitudes are assumed to depend only weakly on bombarding energy E, and hence are assumed constant over the small energy regions of the T=3/2 resonance. For a single-level Breit-Wigner resonance the resonant amplitudes are

$$a_R(\theta,E) = \frac{J+1/2}{k}\left[\frac{\Gamma_p/2}{E-E_R+i\Gamma/2}\right]P_L(\cos\theta) \qquad 6\text{-}4$$

$$b_R(\theta,E) = \frac{(-1)^{J-L-1/2}}{k}\left[\frac{\Gamma_p/2}{E-E_R+i\Gamma/2}\right]P_L'(\cos\theta) \qquad 6\text{-}5$$

where J and L are the resonance spin and orbital angular momentum, k is the wave number at bombarding energy E, E_R is the resonance energy, and Γ and Γ_p are the total and partial widths for the scattering.

The cross section can then be expressed as [Iko76]

$$\sigma = \sigma_{nr} + |a_R|^2 + |b_R|^2 + 2\cdot Re[\, a_{nr}a_R^* + b_{nr}b_R^* \,] \qquad 6\text{-}6$$

where the non-resonant cross section σ_{nr} is

$$\sigma_{nr} = |a_{nr}|^2 + |b_{nr}|^2. \qquad 6\text{-}7$$

The cross section is a combination of three terms: the off-resonance cross section, the pure resonance cross section (the second and third terms in 6-6), and the interference between the the resonant and non-resonant amplitudes (the last term). The analyzing-power cross section is

$$\sigma \cdot A_y = 2 \cdot \mathrm{Im}\left[a_{nr} b_{nr}^{*} + a_{nr} b_R^{*} + a_R b_{nr}^{*} + a_R b_R^{*} \right] \qquad 6\text{-}8$$

where the first term is simply the off-resonance $(\sigma \cdot A_y)_{nr}$, the second and third terms represent the non-resonant and resonant amplitude interference, while the last term is the pure resonance contribution to $\sigma \cdot A_y$. This contribution vanishes if a_R and b_R are described by 6-4 and 6-5, from which $a_R b_R^{*}$ is purely real.

6.2.2 Inclusion of Energy Resolution Parameters. The resolution effects must be properly included in order to describe the observed energy-averaged cross sections σ_o and analyzing cross sections $(\sigma \cdot A_y)_o$. This can be accomplished by a direct convolution of the energy resolution function $f(E,E')$ with the calculated cross section and analyzing power cross section

$$\sigma_o(E) = \int f(E,E')\sigma(E')dE' \qquad 6\text{-}9a$$

$$(\sigma \cdot A_y)_o(E) = \int f(E,E')\sigma \cdot A_y(E')dE'. \qquad 6\text{-}9b$$

The exact details of the calculation of the resolution function will be discussed in Sections 6.3 and 6.4.

6.2.3 The Grid-Search Calculations. The polarized beam excitation function data were fitted by performing a simultaneous search of the resonance parameters and the non-resonant spin-flip and non-spin-flip amplitudes. As stated earlier, the non-resonant amplitudes were assumed to be constant across the energy region of the resonance excursion.

Because the T=3/2 isospin-forbidden resonances are small effects in the observed cross section, the T=3/2 resonant amplitudes contribute mainly from the interference terms in Eqs. 6-6 and 6-8. Therefore, it is important to determine the off-resonance cross section and analyzing power accurately. The magnitudes of the non-resonant amplitudes a_{nr} and b_{nr} are then constrained by the observed off-resonance cross section and analyzing powers.

The previous unpolarized beam energy excitation function studies using the helicity-amplitude analysis method [Iko76] only calculated fits to the cross section term (Equation 6-6). However, the off-resonance cross section and analyzing power still had to be measured in order to determine σ_{nr} and $(\sigma \cdot A_y)_{nr}$ to constrain the non-resonant amplitudes. In the present analysis both of these terms were determined simply by measuring the energy excitation function over an energy region larger than the resonance excursion. The off-resonance σ and A_y data were determined from a combination of σ and A_y measured at energies below and above the resonance excursion. As long as the measurements extend beyond the resonance excursion energy region, and the non-resonant amplitudes are constant or nearly constant, then in the energy averaging the off-resonance σ_{onr} and $(\sigma \cdot A_y)_{onr}$ will not be affected by the energy averaging resolution function f(E,E'). Thus, the energy averaging off-resonance components will be equivalent to the σ_{nr} and $(\sigma \cdot A_y)_{nr}$ described in Eqs. 6-7 and 6-8.

The off-resonance σ_{onr} and $(\sigma \cdot A_y)_{onr}$ can be expressed in terms of the complex amplitudes, written as $a_{nr} = a_r + ia_i$ and $b_{nr} = b_r + ib_i$

(a_r, a_i, b_r, and b_i real), as follows:

$$\sigma_{onr} = a_r^2 + a_i^2 + b_r^2 + b_i^2 \qquad 6\text{-}10$$

$$(\sigma \cdot A_y)_{onr} = 2(a_i b_r - a_r b_i). \qquad 6\text{-}11$$

These equations are bilinear in b_r and b_i. Hence, two values of each of b_r and b_i are possible for a given a_r and a_i if only σ is used. The allowed values of a_r and a_i are constrained by $a_r^2 + a_i^2 \leq \sigma_{onr}$. The addition of the $(\sigma \cdot A_y)_{onr}$ measurement reduces the number of free non-resonant parameters from three to two, and (by (6-11)) removes the two-fold ambiguity in b_r and b_i.

The fitting procedure uses a grid search of all possible a_r and a_i values for a given set of resonance parameters. The set of resonance parameters searched (expressed in Eqs. 6-4 and 6-5) are the resonance energy E_R, the spin and parity of the resonance J^π, the total width Γ, and the partial width Γ_p. The other free search parameter is a resolution parameter Δ_{BD} described in Sections 6.3 and 6.4.

The grid search of these parameters produces a fit which minimizes χ^2, defined for simultaneous fitting of cross section and analyzing power data as

$$\chi^2 = \sum_{i=1}^{N} \left[\frac{\sigma_{exp}(E_i) - \sigma_o(E_i)}{\Delta\sigma(E_i)} \right]^2 \cdot N^{-1} + \left[\frac{(\sigma \cdot A_y)_{exp}(E_i) - (\sigma \cdot A_y)_o(E_i)}{\Delta\sigma \cdot A_y(E_i)} \right]^2 \cdot N^{-1}. \qquad 6\text{-}12$$

The terms σ_{exp} and $(\sigma \cdot A_y)_{exp}$ are the measured values, $\Delta\sigma$ and $\Delta\sigma \cdot A_y$ are the statistical standard deviations in the measured values, the terms σ_o and $(\sigma \cdot A_y)_o$ are the energy average calculated cross section and analyzing-power cross section, and N is the number of data points. A discussion of the fitting analysis code, the techniques used to fit the data, and the sensitivity of this analysis method to the resonance parameters will be presented in Section 6.4 after discussing the resolution effects.

6.3 Resolution Effects. The energy averaging distribution $f(E,E')$ which affects the observed cross section and analyzing-power data (see Eqs. 6-9a and 6-9b) consists of several different types of resolution distributions combined. The resolution effects are:

(1) A finite incident proton beam energy distribution. This results from two principal processes: energy fluctuations of the acceleration system, and energy straggling of the proton beam in the terminal stripping foil. A detailed discussion of these processes is presented in Chapter 7.

(2) Energy straggling of the incident protons as they pass through the target foil before the nuclear collision.

(3) Doppler broadening from scattering of the incident protons by moving target nuclei.

(4) An increase of the resolution as a result of atomic processes in the atom of the target nucleus.

Figure 6-1 presents the resolution effects of several of the above mentioned processes on the pure nuclear excitation function calculated for the first T=3/2 resonance in ^{13}N. A description of each of these

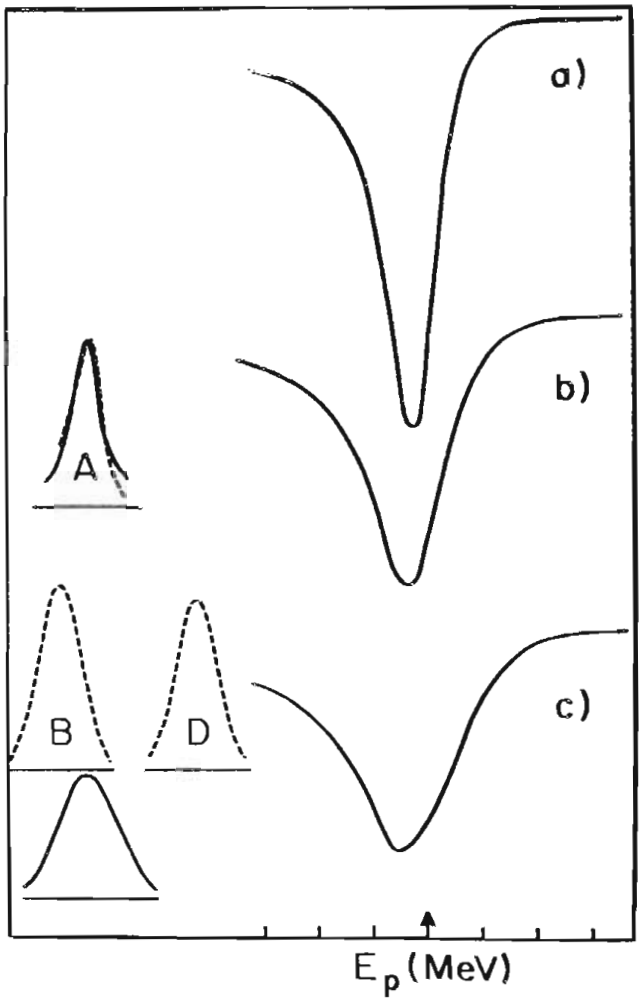

Figure 6-1 Energy resolution effects on $^{12}C(\vec{p},p)^{12}C$ 139° cross section excitation function measurement. (a) is the pure nuclear excitation function. (b) is the convolution of atomic effects (A) (dashed line) approximated by the Lorentzian shape (solid line) with (a). (c) is the final calculated cross section resulting from the convolution of (b) with the total resolution function shown in the lower left hand corner. The resolution distribution includes the beam energy spread distribution (B), Doppler broadening distribution (D), and the target energy straggling distribution (not shown). The tick marks are 1 keV energy steps, with all distributions having the same energy scale. The distribution (c) can be compared with the measured cross section presented in Section 11.2.

resolution effects and the method used to calculate the resulting energy distributions will now be discussed.

6.3.1 Energy Straggling. As a charged particle traverses through matter it undergoes several different types of interactions: elastic and inelastic collisions with atomic electrons, and collisions with nuclei. Inelastic scattering by atomic electrons is the dominant interaction process for MeV energy protons passing through thin (100–1000 atom) targets. Each interaction results in the charged particle losing a small portion of its kinetic energy. An initially mono-energetic beam of particles passing through a thin target will emerge with a distribution of particle energies distributed about an energy equal to the average energy loss of a charged particle passing through the target foil.

A distribution of particle energies occurs because each particle undergoes hundreds of independent interactions, with considerable fluctuations in the number and type of interactions experienced by individual particles. The energy loss process and resulting distribution of energies are described by an energy straggling distribution $f(x,\Delta,E)$, which predicts the probability of a charged particle of energy E going through a material of thickness x losing an amount of energy Δ. Thin targets were used in our high-resolution $(\vec{p},p)$ measurements in order to minimize the target energy straggling (averaging) contribution. However, the energy straggling distribution is very asymmetric for small energy losses and must be accounted for correctly in the total resolution function in order to produce good fitting to the measured data.

A derivation of the equations governing energy loss of charged particles in matter and the resulting energy straggling distributions will not be presented here. There is a large amount of literature, and several review articles are available on these subjects. [Liv37, Lan44, Vav57, Fan63, Shu67].

An exact solution of the energy straggling probability distribution $f(x,\Delta,E)$ is nearly impossible since complete knowledge of the total collision cross sections are known for only a few simple cases. Numerical calculations of the distribution transport equations in a statistical fashion would be very complicated and time consuming [Jar78]. However, when $\Delta E \ll E$ the straggling distribution transport equation can be approximated using a Laplace-transform method [Lan44], or by a slightly modified transform [Vav57]. These distributions can be calculated directly [Cla71], or by more sophisticated methods such as using Fourier analysis [Sch74]. Comparisons of experimental energy straggling measurements for protons with predictions using these methods exhibit good agreement [Goo57, Sel64, Mac68].

The regions where these calculational methods are valid depend on the following factors: the energy E, mass m, and charge q of the incident particle; the target material A and Z; and the target thickness x [Sel64, Jar78, Bic75]. The regions where the calculational methods are valid have been parameterized by comparing the results obtained from the different calculational methods with experimental results and conditions (E, m, q, Z, A, and x) [Sel64, Jar78].

The three mathematical distributions used to calculate the energy straggling distribution are the Landau distribution [Lan44], the Vavilov distribution [Vav57], and a Gaussian distribution [Boh15, Liv37, Sel64]. The conditions under which these distributions accurately describe the straggling process have been parameterized by the ratio [Vav57]

$$k = \xi/\varepsilon_{max}. \qquad 6\text{-}13$$

Here ξ, derived from the electron scattering cross section, is defined as

$$\xi = 2\pi e^4 q^2 ZN\rho x/Amv^2 \qquad 6\text{-}14$$

with electron charge e, particle charge number q, target nuclei charge Z, Avogadro's number N, target density ρ, target thickness x, target atomic weight A, particle mass m, and particle speed v. The ε_{max} term in k is the maximum possible energy transfer for a heavy particle and electron collision. The nonrelativistic expression is

$$\varepsilon_{max} = 2mv^2/(1-\beta^2) \qquad 6\text{-}15$$

where $\beta = v/c$. The expression k then reduces to

$$k = 0.150sq^2Z(1-\beta^2)/A\beta^4 \qquad 6\text{-}16$$

where s is the target thickness expressed in g/cm^2. The approximate limits of k where the different distributions have been shown to be valid by agreement with the experimental data are [Sel64, Mac68, Jar78]

$k < 0.01$	———	Landau
$0.01 \leq k < 10.0$	———	Vavilov
$k > 10.0$	———	Gaussian.

For our high-resolution (p,p) or $(\vec{p},p)$ measurements the typical values for k were less than 0.02, thereby corresponding to straggling distributions which are either Landau or Vavilov.

The effect of these very asymmetric energy loss distributions (with a tail towards large energy losses) on the observed cross section excitation functions is to distort the high-energy side of the resonance excursion because of the energy smearing from the low energy straggling tail. An example of the predicted cross sections for a ^{55}Co resonance is shown in Fig. 6-2 [Iko76]. The predicted cross sections calculated using either a symmetric resolution function or an asymmetric resolution function containing the correct energy straggling distribution are compared to the experimental data [Iko76]. An interactive computer code STRAGL was written on the VAX/11-780 to calculate the correct straggling distribution. The following parameters are input: the incident particle, incident particle energy, the target mass and charge, and the target thickness. The STRAGL code uses the Fourier series routines of [Sch74] to calculate the Landau and Vavilov distributions.

Another interactive computer code CSTRAGL was written to allow the convolution of two energy straggling distributions. This code used the identical calculational routines as STRAGL in calculating the individual straggling distributions. The two straggling distributions were then convoluted numerically to obtain the total straggling distribution. The

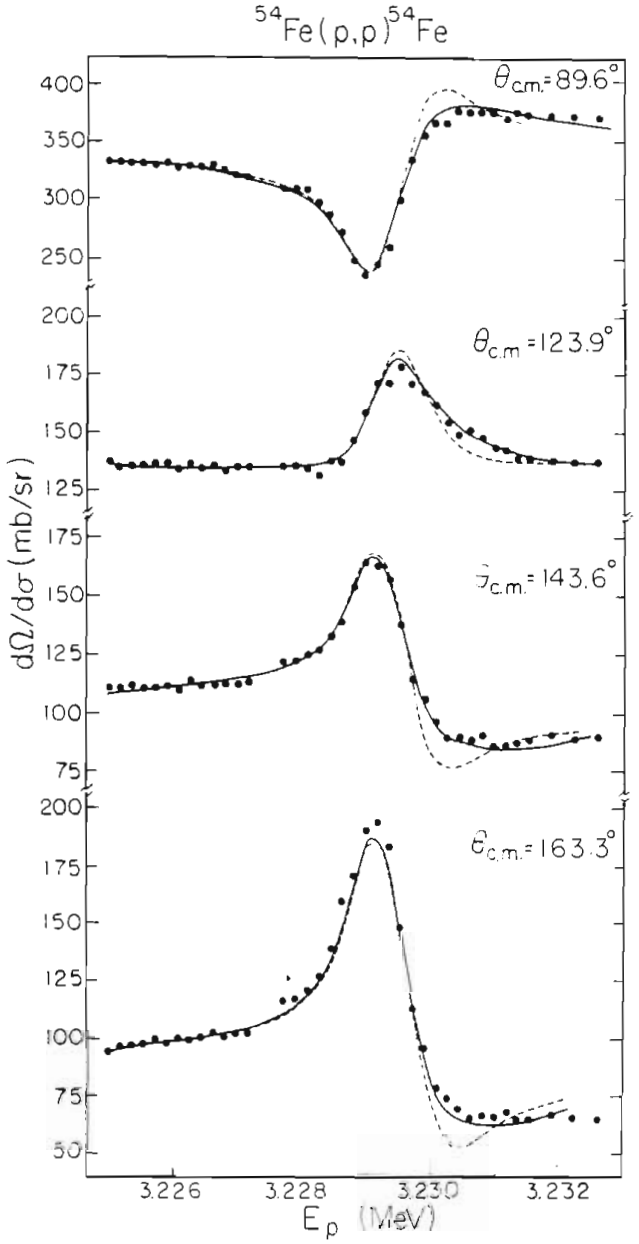

Figure 6-2 Calculated best-fits $^{54}Fe(p,p)^{54}$ cross section are shown compared with the measured values. The resolution distribution used in calculating the solid line included the asymmetric target straggling distribution. The dashed line results from calculations including only a symmetric Gaussian resolution distribution.

convolution of the two distributions can be expressed as

$$f(x_1+x_2,\Delta) = \int_0^{\Delta} f(x_1,\Delta-\Delta')\cdot f(x_2,\Delta')\cdot d\Delta' \qquad 6\text{-}17$$

where x_1, x_2, Δ, and Δ' represent the same terms described earlier for the probability distribution $f(x,\Delta,E)$. In performing the numerical calculations, the convolution of the straggling distributions must be in the proper phase sense to achieve the additive straggling results (instead of smearing the distribution if the wrong convolution order is chosen).

The motivation for writing the CSTRAGL code was that many of the targets used in the $(\vec{p},p)$ experiments are polyatomic bi-elemental compounds and not single-element targets. The assumption was made that the straggling in the compound target was the same as the straggling in two separate single-element targets. The justification for this approximation is based on measurements of energy losses in compounds and energy losses in separate single-element targets. The results of these measurements show that energy losses are additive to within experimental accuracy [Chu78], which is known as Bragg's additivity rule.

The STRAGL code was tested by comparison with published calculations [Sel64]. The convolution code CSTRAGL was tested by calculating the straggling distribution for two single-element targets made of the same material. The straggling distributions for two thicknesses x_1 and x_2 of the same element were calculated and convoluted by CSTRAGL. The resulting straggling distribution from CSTRAGL was

compared with the straggling distribution calculated by STRAGL for the same element target of thickness $x_1 + x_2$.

Both computer codes allowed interactive calculations and display of the distributions. The code CSTRAGL was incorporated directly into the T32GRD resonance analysis code.

6.3.2 Incident Beam Resolution. The incident beam energy spread is the combination of two distinct components: energy fluctuations introduced by the accelerator and the beam energy analyzing system, and beam spread resulting from energy straggling in the terminal stripper. Typical total beam energy spreads are 425-600 eV for unpolarized beams and 550-700 eV for polarized beams. The beam resolution is usually the dominant energy averaging component in the resolution distribution. A complete description of the TUNL high-energy resolution system and the components which contribute to the accelerator beam energy fluctuations is detailed in Chapter 7. The contributions to the beam energy spread from the terminal stripping foil or gas arise from the energy straggling of the beam as it passes through the terminal stripper. The reasons for using a terminal stripper foil or gas, and the straggling calculations showing the magnitude of the stripper energy straggling resolution broadening contribution, are presented in Chapter 7.

The beam energy spread after the beam passes through the magnet analyzing system has been measured for polarized and unpolarized beams (see Section 7.4 and Chapter 8). Unpolarized beams are stripped with gas stripping and have negligible energy straggling at the terminal. The measured distributions reveal a symmetric, Gaussian beam energy spread

distribution. With polarized beams we must use foil stripping, and a significant beam energy spread contribution from the energy straggling in the terminal results. The energy-straggling distributions are known to be asymmetric with a long low-energy tail, as discussed in Section 6.3.1. One might expect that the incident polarized beam on target would reflect this asymmetry in the beam energy spread. However, measurements of the beam energy distribution under accelerator conditions where the energy straggling at the terminal is maximum reveal that the beam energy distribution is only slightly asymmetric and remains essentially Gaussian. See Section 8.6 for a description of these measurements.

The fact that the measured beam distribution is not very asymmetric is explained by considering two properties of the beam and the beam transport system. The beam energy spread is measured after the magnet analyzing system. This energy analyzing system has both a limited energy acceptance and limited beam angular divergence acceptance. See Chapters 7, 8, and 9. Thus, the energy straggling low-energy tail is cut off by the energy analyzing and beam transport system. However, the energy acceptance of the magnet analyzing system in the typical beam transport configuration at TUNL is too large to cut off the entire low energy tail and cannot account for the observed (nearly) symmetric beam energy spread. The rest of the asymmetric tail is eliminated because the beam comprising the low-energy tail of the beam straggling distribution contains those particles which have undergone the most scattering interactions. This small-angle scattering increases the angular divergence (emittance) of this part of the beam. (The emittance of a beam describes the transverse momentum components of the beam, where

transverse is with respect to the beam direction.) Thus, the beam in the low energy straggling distribution tail usually has a higher emittance than the beam transport system angular acceptance, and is therefore probably not transported through the system.

In the present work, the beam energy distribution was assumed to be a symmetric Gaussian distribution in all calculations of resonance parameters. However, with the development of a direct beam energy resolution measurement system (see Chapter 8) it is possible to measure this resolution directly. Thus, in future measurements any asymmetries in the distribution can be accounted for directly in the analysis.

6.3.3 Target Doppler Broadening. The Doppler broadening energy resolution distribution is a consequence of the fluctuations of the center-of-mass energy (E_{cm}) of the nuclear scattering reactions. The variation of the center-of-mass energy is a result of lattice vibrations of the target nuclei. This resolution effect was first observed in slow neutron scattering [Lam39]. The exact calculation of the resolution distribution is often difficult or impossible because it requires full knowledge of the solid-state structure and lattice binding of the target atoms.

One's first reaction when considering the effect of the solid-state lattice vibrations on the observed resolution of a nuclear scattering process is probably to assume that it is completely negligible. The average quantal energy $\bar{\varepsilon}_N$ (mean energy/degree of freedom) which describes the kinetic energy of a nucleus bound in a solid is only on the order of ~ meV (10^{-3} eV), which is exceedingly

small when compared to the incident proton beam energies of ~ MeV and to the energy resolution $\lesssim 1$ keV. The vibrational motions of the nuclei occur as a result of the zero-point and thermal motions of the nuclei about the Bravais lattice binding sites. (A review of lattice dynamics, quantum theory of solids, and statistical mechanics governing this behavior can be found in most graduate level solid-state textbooks. A recommended presentation is in Chapters 20-24 of [Ash76].

For a simple estimate of Doppler broadening, consider a single-element solid whose atoms are vibrating in one dimension along the x-axis with average speed v_N. The center-of-mass energy for a proton moving with velocity v_p along the x axis and scattering from one of the target nuclei can then be described for the two average velocity cases ($+v_N$ for a nucleus moving toward the proton, and $-v_N$ for a nucleus moving away from the beam) as

$$E_{cm}^{\pm} = \frac{1}{2}\frac{m_p \cdot M}{m_p + M}(v_p \pm v_N)^2 \qquad 6\text{-}18$$

The term $\frac{m_p \cdot M}{m_p + M}$ is just the reduced mass m_r. The width of the energy resolution distribution in one-dimension, Δ_{D1}, is proportional to $E_{cm}^{+} - E_{cm}^{-}$ so that

$$\Delta_{D1} \propto 2m_r \cdot v_p v_N = 4m_r\left[\frac{E_p \cdot E_N}{m_p \cdot M}\right]^{1/2} \qquad 6\text{-}19$$

where E_N is the energy of the target nucleus in the lab frame. The width is proportional to the product of velocities and hence can result in the Doppler broadening process significantly adding to the observed total

resolution.

The three-dimensional Doppler broadening distribution is a Gaussian distribution with a FWHM width of [Lyn68]

$$\Delta_D = \left[16 \ln 2 \cdot \frac{m_p}{M} \cdot E_p \bar{\varepsilon}_N \right]^{1/2} \qquad 6\text{-}20$$

where $\bar{\varepsilon}_N$ is the average quantal energy of vibration. All the terms in Eq. 6-20 necessary to calculate the Doppler broadening distribution are known, except for the parameter, $\bar{\varepsilon}_N$ which is discussed in detail below.

The size of the Doppler broadening energy averaging contribution can be significant. The 14.231 MeV $^{12}C(p,p)^{12}C$ resonance is an example where all the conditions which contribute to a large Doppler broadening width are present: high beam energy, low target mass, and very high average quantal lattice energy (66 meV). With these parameters, Δ_D equals 940 eV, which is the dominant energy averaging term. Calculations of the observed cross section both including and excluding the Doppler broadening contribution are shown along with the data for this resonance in Fig. 6-3. Although the $^{12}C(p,p)^{12}C$ resonance is an extreme case, the Doppler broadening distribution is usually one of the dominant contributions to the total resolution distribution.

The calculation of the average quantal energy $\bar{\varepsilon}_N$ is straightforward for mono-atomic solids, but very difficult for compounds. For a mono-atomic solid an exact calculation of $\bar{\varepsilon}_N$ can be made by using quantum theory and the harmonic crystal approximation [Ash76]. The average quantal energy is

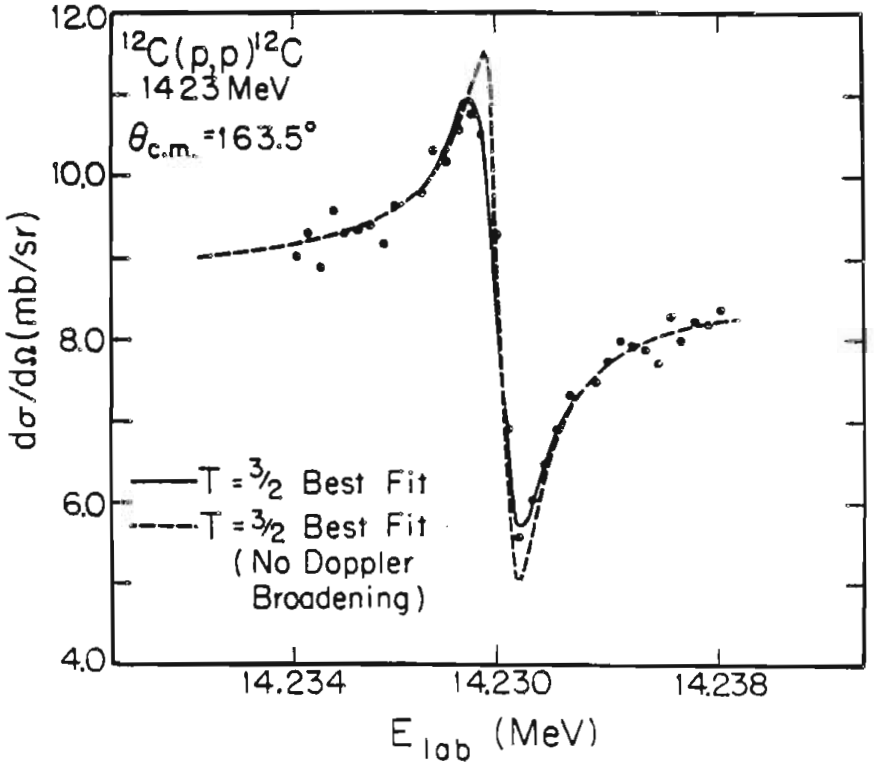

Figure 6-3 The best-fit calculation (solid line) for the first T=3/2 resonance in ^{13}N which includes energy averaging of a Doppler broadening distribution of 940 eV. The dashed line represents the resonance shape if no Doppler broadening were present. The resonance parameters used in the calculation are listed in Table 11-2.

$$\bar{\varepsilon}_N = \int_0^\infty g(\gamma) \cdot h\gamma/2 \cdot \coth[h\gamma/2kT] \cdot d\gamma \qquad 6\text{-}21$$

where k is Boltzmann's constant, T is the temperature of the solid in Kelvin, h is Planck's constant, $g(\gamma)$ is the density of normal modes per unit volume, and γ is the frequency of the normal modes in Hz. The integral can be numerically integrated and solved when $g(\gamma)$ is available.

The calculation of $g(\gamma)$ requires knowledge of the Bravais reciprocal lattice structure of the solid, and measurements of the phonon dispersion of the solid. The phonon dispersion can be measured using several techniques such as neutron scattering, electromagnetic inelastic scattering of x-rays, or visible-light scattering as discussed in [Ash76] Chapter 24. The normal modes per volume $g(\gamma)$ has been determined for many mono-atomic solids.

However, if $g(\gamma)$ is not known, the Debye model of lattice vibrations can be used to estimate the average quantal energy. This model approximates the entire vibrational spectrum by three branches which have a linear dispersion with frequency [Ash76]. This yields for the number of normal modes per unit volume

$$g_D(\gamma) = 3(\gamma/\gamma_{max})^2 \cdot d\gamma/\gamma_{max}, \qquad 6\text{-}22$$

where $\gamma_{max}=k\Theta/h$ and Θ is the Debye temperature. Substitution of this quantity into Eq. 6-21 yields an expression for the average quantal energy

$$\bar{\varepsilon}_{DN} = \frac{3}{8}k\Theta + (kT)\cdot 3\left(\frac{T}{\Theta}\right)\int_0^{\frac{\Theta}{T}}\left[\frac{x^3}{e^x-1}\right]\cdot dx \qquad 6\text{-}23$$

where T is the temperature of the solid in Kelvin and the integral is a Debye function which has been tabulated [Abr64]. The Debye approximation for $\bar{\varepsilon}_N$ is good if the Debye temperature is derived from measurements (of the specific heat at constant pressure) near the temperature of the nuclear scattering experiment.

A comparison of the two methods of calculating the average quantal energy was made for the Doppler broadening distribution of the 14.231-MeV $^{12}C(\vec{p},p)^{12}C$ resonance. The target foil was amorphous carbon [ARI01] which has a graphite like crystalline structure. The $g(\gamma)$ determination was available in the literature [Nic72] and direct numerical evaluation of the integral in Eq. 6-21 yielded $\bar{\varepsilon}_N$ = 66.1 meV. The Debye calculation used two Debye temperatures [Kru53] to account for the transverse and longitudinal vibrations resulting from the elastic anisotropy of the graphite lattice bindings and yielded $\bar{\varepsilon}_{DN}$ = 66.9 meV. The excellent agreement between the two methods results in part because both methods used data appropriate for the same temperature regime. It also shows that the Debye model is a reasonable method to estimate the average quantal energy.

Because most of the (p,p) measurements are performed at room temperature or slightly higher, it is very important to select room temperature data (either Debye temperatures or $g(\gamma)$) when calculating $\bar{\varepsilon}_N$ and not low temperature data. It should also be pointed out that the Einstein model can be used for representing the vibrational spectrum at

temperatures $T \geq \Theta_E \simeq \Theta$, where $\Theta_E = \hbar\omega_E/k_B$ and ω_E is optical branch frequency derived from the specific heat [Ash76]. However, it is not valid in the typical target temperature region of our (p,p) or $(\vec{p},p)$ measurements. (The Einstein method was used by [Iko76] for the Δ_D determinations.)

The temperature dependence of the quantal energy is exhibited in the Debye representation of Eq. 6-23. It is clear that reducing the temperature will lower the quantal energy, and thus reduce the energy averaging contribution to the resonance measurement. However, for many solids the zero-point motions (represented by the Debye temperature) dominate the average quantal energy for temperatures ~ 300° K. Therefore, for many targets cooling will not significantly reduce the Doppler broadening contribution.

The temperature of the target should be considered when making the (p,p) and $(\vec{p},p)$ measurements and calculating the Doppler broadening. A thin target under bombardment by a charged particle beam has an energy deposited proportional to the energy loss of each particle multiplied by the number of particles incident on the target

$$E_{dep} = \bar{E}_1 \cdot I \cdot 10^{-6} \text{ W} \qquad 6\text{-}24$$

where I is the beam current in μA and $\bar{E}_1$ is the average energy loss in the target in eV. If the thin target is assumed to have very low thermal conductivity, then the effective temperature of the thin target in a vacuum can be estimated by considering only blackbody radiative energy

losses. Then the Stefan-Boltzmann Law results in

$$E_{dep} = A \cdot \sigma \cdot (\Theta_T^4 - \Theta_S^4) \qquad 6\text{-}25$$

where Θ_T is the target temperature, Θ_S is the surrounding temperature, σ is Stefan's constant, and A is the area of the target irradiated. For the present polarized beam intensities and beam spot sizes, this formula estimates a target temperature only a few degrees higher than the surroundings. However, unpolarized beam intensities can result in target temperatures 30-50% above room temperature, thereby contributing to increased Doppler broadening. Thus, an effort should be made to maximize the beam spot area on the target in order to minimize the target temperature.

The above discussion on determination of the average quantal energy, and thus the Doppler broadening, has been only for mono-atomic solids. The $\bar{\varepsilon}_N$ can be determined for polyatomic solids, although it is much more difficult. The principal difficulty in estimating the average quantal energy is determining what fraction of the vibrational spectrum results from vibrations of the nuclei under study. The measured vibrational spectrum usually yields only a sum of the vibrations for all the elements in the compound. Likewise, a determination of the Debye temperature of the compound includes the contributions for all the compound members. However, if the exact lattice structure of the polyatomic solid is determined, then the normal modes of vibration resulting from each element can be predicted [Mor76]. Analysis of several compounds has been performed with very good results [Mor79,

Mor76]. A computer code to perform the calculations is also available [Mor82].

Both the crystalline structure and the frequency spectrum of the solid must be known to perform these calculations. Unfortunately, a search of the literature for our two compound targets of SiO and Sb_2S_3 did not reveal the information necessary to perform the calculations. Thus, for compound targets the resolution contribution from Doppler broadening was a fitting parameter.

6.3.4 Atomic-Excitation Effects. Atomic excitation processes can contribute to the total energy averaging resolution distribution [Tho80, Fea79]. If the electrons of the target atom are excited during the nuclear scattering, some of the energy available to the center-of-mass system is removed. This results in fluctuations of the center-of-mass energy depending on the probability distribution for exciting the atomic states. This resolution effect is similar to the Doppler broadening in that it is essentially a kinematical effect of center-of-mass energy fluctuations. However, the processes of the interactions are entirely different. In the present work, only the first T=3/2 resonance in ^{13}N was analyzed including atomic-excitation effects. This $^{12}C(\vec{p},p)^{12}C$ resonance was a good case to analyze because the conditions to excite the atomic processes are quite favorable. A description of these processes has been presented elsewhere [Tho80]. There is currently some discussion of the validity of these results [Bri81].

6.4 Analysis Codes and Method. A group of data analysis codes was developed to strip and analyze the (p,p) and $(\vec{p},p)$ resonance data. The

development of the analysis codes was based on the philosophy of writing codes to perform specific tasks. This provides the ability to review the results of each calculation at each step of the analysis process. This method of analysis allows a large amount of feedback and control, unlike the method of developing a super code which allows one to input the initial raw data and return the final results. However, the codes were developed to minimize user handling of the data. Each code was written to produce disk file or magnetic tape output directly compatible with the input of the next analysis code. The general outline of input/output and procedures performed by the analysis codes are presented in Fig. 6-4.

Because of the large amount of data generated, it was necessary to develop a file name convention to distinguish between the different experimental data and between the various files generated in analyzing the data. A summary of the naming convention in presented is Appendix B. A discussion of the analysis codes will now be presented.

6.4.1 Preliminary Data Analysis. The energy excitation function spectra were analyzed using the TUNL Honeywell DDP-224 computer with the analysis code HPOPAY. The details of the data acquisition code HPOP are presented in Section 10.5. The basic functions of HPOPAY were to sum the peaks of interest in the spectra and to calculate the asymmetries for each run of an energy excitation function. The code allowed continuous execution of a sequence of commands to read data, sum channels, calculate asymmetries, then to store the resulting excitation functions in arrays. There was also the ability for the user to easily interrupt

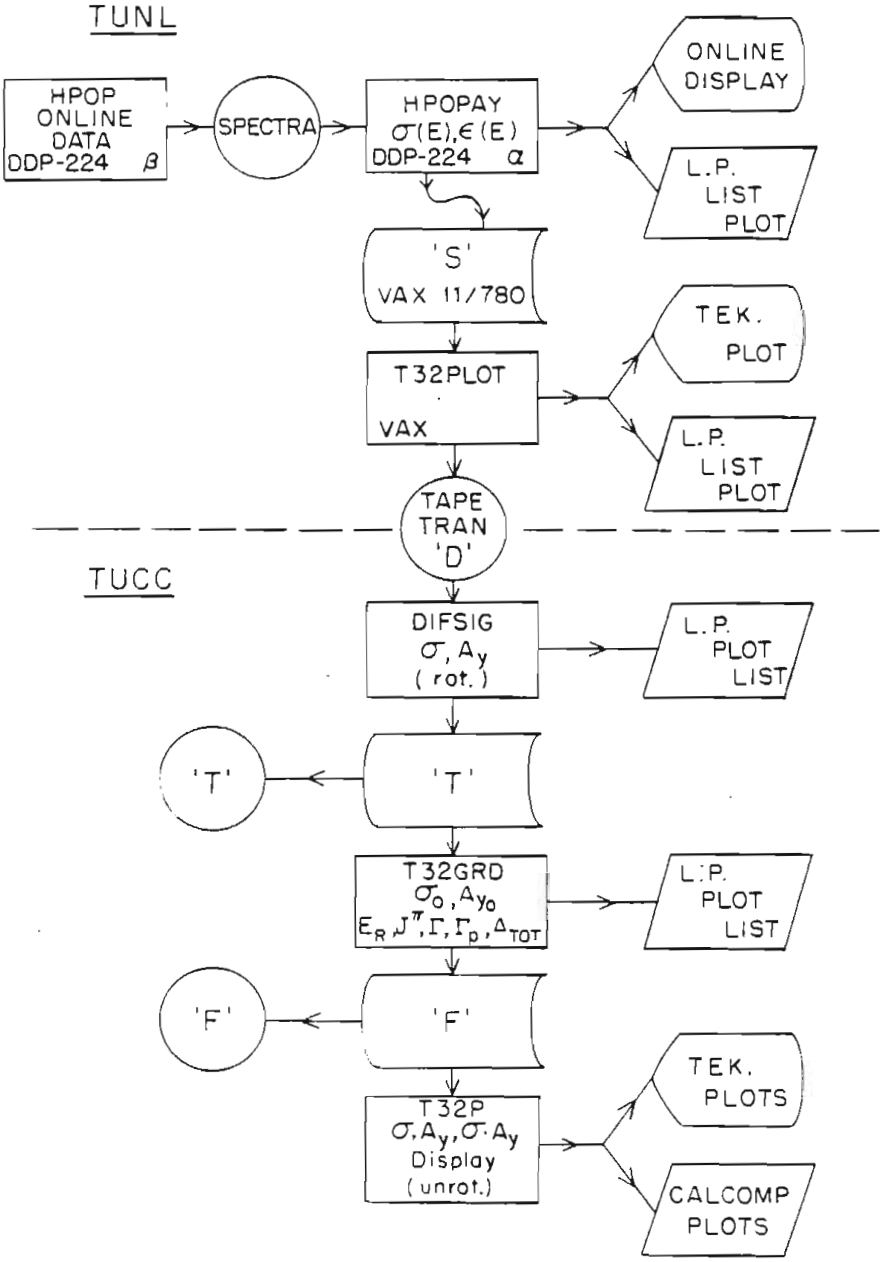

Figure 6-4 Computer program structure used to analyze $(\vec{p},p)$ resonance data using standard flowchart symbols. Abbreviations and symbols used: line-printer output - L.P., Tek. plots - Tektronix terminal on-line plots, circles represent magnetic tape storage, the capital letters in single quotes are the letters used to distinguish different file types.

the automatic stripping of the data to check the summing gates and make necessary changes before resuming the auto-summing mode. Data transfer of the energy excitation functions or of individual spectra to the TUNL DEC VAX/11-780 computer was accomplished using a data transfer line connecting the two computers. Once the excitation function data were on the VAX, the code T32PLOT was used to produce sophisticated compact line printer or CRT (Tektronix) plots of the data by using the Bell Laboratory GRZ plotting routine package [BEL01]. Tables of the yield and asymmetry excitation functions were also printed for reference. Finally, T32PLOT generated output files in compatible format for input to the DIFSIG code.

The VAX format DIFSIG input files were transferred by tape to the Triangle Universities Computation Center (TUCC) where they were translated and copied onto disk. The more complicated part of the analysis was performed at TUCC because of the superior Fortran compiler, larger CPU memory, and faster turn-around time on jobs.

The code DIFSIG calculates differential cross sections and analyzing powers for the 4 or 5 sets of angles measured. The cross sections and analyzing powers are output to disk files in a compatible input for the helicity-amplitude analysis program T32GRD. DIFSIG also produces line-printer tables and plots of the cross-section and analyzing-power excitation functions. One further capability of DIFSIG is to rotate either the cross section, analyzing power, or both of the excitation functions. The purpose of this rotation was to produce a constant off-resonance cross section and/or analyzing power. The

rotation was performed by selecting data points on both ends of the resonance excursion and performing a linear least squares fit to these data. The data were then rotated about some pivot point selected to occur as close as possible to the resonance energy. A discussion of the validity of this analysis method is in Section 6.5.

6.4.2 Resolution Calculations. The computer codes STRAGL and CSTRAGL used to calculate the energy straggling distributions have already been discussed in Section 6.3.1. A third code RESDIS was developed to convolute Gaussian and energy straggling distributions. This code allows interactive calculation and optional display of the energy distribution resulting from a Gaussian and a one- or two-element target. The code incorporates the CSTRAGL subroutines to calculate the straggling distribution. It is a useful code to use before or during an experiment when deciding on the stripper foil thickness or target thickness necessary to obtain a certain total resolution.

6.4.3 Helicity Amplitudes Analysis Code - T32GRD. The helicity-amplitude code T32GRD is written based on the equations presented in Sections 6.2.1-6.2.3. This code searches the non-resonant amplitudes and the resonance parameters of resonance energy E_R, spin and parity J^π, total width Γ, and reduced width Γ_p. The total resolution function is calculated for an energy straggling distribution Δ_{ST} and a Gaussian resolution distribution Δ_{BD} including both the Doppler broadening and incident beam energy spread distributions. In general, the straggling contribution is well known from target thickness measurements, and thus the straggling distribution width is not

searched. However, due to ambiguities of knowing the beam resolution and the Doppler broadening, the parameter Δ_{BD} is considered a search parameter. The analysis code is valid for spin-1/2 and spin-0 particle scattering on spin-0 targets.

A code by the name of T32GRD was originally developed by Ikossi to analyze the unpolarized beam excitation functions using the helicity-amplitude analysis method [Iko75]. There were several inefficient sections of code, no subroutine structure, and several serious unchecked array overflow problems in the original code. As part of the present research a new T32GRD code was written in conjunction with Thompson, with several fundamental changes in the calculation algorithms.

The chief increase in efficiency of T32GRD was achieved by convoluting the resonant quantities, not the calculated cross sections. Thereby when non-resonant amplitudes were changed the resolution convolutions were not recalculated. The computational time required by the new code to perform a search of the non-resonant amplitudes was decreased compared to the old code time by a two orders of magnitude. After several other modifications, another factor of 10 in speed was obtained. Thus, the new code can perform over 1000 variations of non-resonant amplitudes in the time it took the old code to perform one such search. This increase in computing speed allowed complete and thorough searches to be made. For example, a typical resonance excitation function was analyzed using a total of 10^5 parameter values. After the basic code was developed, the ability to calculate $(\vec{p},p)$

analyzing power excitation functions and to include these in the parameter search was added.

Within T32GRD, the subroutine FINITE used to calculate the resolution function and to select optimum internal energy step sizes was also completely rewritten. An analytical selection of the optimum internal energy step size used in calculating the various resolution functions and the theoretical cross sections and analyzing powers was developed using the code RESDIS. The selection of the optimum internal energy step size for resolution-function calculations is evaluated in terms of the total width of the resonance, the different resolution effect widths, and the experimental energy step size. With certain combinations of these parameters and depending on the energy region measured, the optimum step size will be too small and require a number of steps across the resonance energy region which is too large for the array sizes. When this overflow problem arises the step size is increased until the total number of energy steps necessary to cover the data will be within the allowed array space limit. However, the user is warned with a message, and the optimum step size and actual step size are output.

The calculated resolution function within FINITE includes the CSTRAGL subroutines, and can thus include straggling for single elements or two-member compounds. The use of CSTRAGL also allows the calculation of the proper Landau, Vavilov, or Gaussian straggling distribution. The total resolution function is calculated by convoluting the straggling distribution with a Gaussian distribution which includes both the

Gaussian contributions of Doppler broadening and the incident-beam Gaussian energy spread. Another feature of FINITE is that the total resolution function is peaked at the correct energy relative to the mean energy loss of the incident beam in the target. This energy compensation allows the extraction of the true nuclear resonance energy. Finally, a plotting routine was added to FINITE to allow optional output of the total resolution function distribution, the straggling distribution, and the beam-plus-Doppler Gaussian distribution, along with their FWHM widths.

A summary of several of the major capabilities of T32GRD is:

(1) The code can perform χ^2 non-resonant amplitude searches to cross- section and analyzing-power data, only cross-section data, or only analyzing-power data.

(2) Either a search of Γ_p or Γ_p / Γ can be performed, depending on the user's preference.

(3) Line-printer plots (GRZ routines) of experimental data and calculated fits are available, allowing quick and easy analysis of the search results.

(4) A χ^2 non-resonant amplitude search grid is printed, allowing easy assessment of convergence amplitude searches.

(5) A χ^2 contour-type grid for the resonance parameters Γ and the beam-Doppler Gaussian width is produced as a function of either Γ_p or Γ_p / Γ.

(6) An extensive four-level debug input option is included to allow easy debugging of problems during calculations. This facility, included during the initial writing of the code, was instrumental in

developing a reliable and error-free code.

(7) T32GRD can write the data and the results from single-shot calculations to disk, allowing permanent storage. This disk output is used by the code T32P to allow the production of Calcomp incremental plots for the cross section, analyzing power, and analyzing-power cross-section energy excitation functions. In addition, T32P can be used to reverse the rotation of any data which were rotated by DIFSIG.

Additional program options can be found in the T32GRD program listing and documentation [Wil82]. The program has over 3500 lines of source code.

6.5 T32GRD Fitting Analysis Procedures. Several general procedures were followed when running the grid-search code T32GRD and extracting the resonance and resolution parameters. For each measurement angle the resonance parameters mentioned in Section 6.2.3 were determined independently for the excitation-function data. The initial searches of the data covered the entire non-resonant amplitude space allowed by the off-resonance cross section and analyzing power data. The starting resonance parameter search mode searched the branching ratio Γ_p/Γ and Γ. The full range of physically acceptable branching ratios were covered from 0.1 to 0.9 in 0.2 steps. The total width Γ was initially searched in large steps centered about a width estimated from an examination of the resonance data. An estimation of the incident beam resolution from observations of system performance during the measurements, and calculations or estimations of the Doppler broadening

width, were used to determine the starting values of the beam-plus-Doppler resolution-parameter search.

For most of the $(\vec{p},p)$ resonances analyzed, a solution to the best branching ratio converged very quickly. After localizing the value of Γ_p/Γ, the resonance parameter search mode was changed to search Γ_p and Γ. This is a much easier mode, because the two parameters are no longer coupled. As the search started to converge, the non resonant amplitudes and resonance-parameter values were searched in finer grid steps.

The expected J^π value for the T=3/2 resonance as predicted from the parent analog state was used as the starting J^π value. In several cases, different J^π values were tried in order to check the sensitivity to the spin and parity. The measurement of data at 4 or 5 different angles provided sufficient sensitivity to J^π. The resonance energy was estimated from the resonance excursion in the data and searched by changing the value and seeing the resulting changes in the χ^2 values.

The $(\vec{p},p)$ excitation function measurements allowed an unambiguous determination of the parameters of E_R, J^π, and Γ_p. However, in a few cases there was less sensitivity to determining the total width Γ and the beam-Doppler width Δ_{BD}, because there were similar effects produced in the calculations by the two parameters. This is one of the reasons why it would be useful to know the incident beam resolution and the target Doppler broadening. This insensitivity to Γ and Δ_{BD} was especially prevalent for the forward-angle data.

Excitation function data with non-constant off-resonance cross section and/or analyzing power values were initially searched with no manipulation of the data. If no reasonable fits could be obtained, the data were adjusted by rotation to have constant off-resonance parameters. The majority of the data were not treated in this fashion. The analyses using rotated data are explicitly indicated when presented in Chapters 11, 12, and 13. After the resonance parameters had been determined using the rotated data, the same search parameters were searched with the original unrotated data in order to estimate the rotation's relationship to the extracted resonance parameters.

6.6 Determination of Resonance Parameters and Estimation of Errors. The final resonance parameters were determined from the best-fit resonance parameters extracted from the 4 or 5 measured angles. The final extracted parameters for Γ, Γ_p, and Δ_{BD} were determined using the weighted average of the parameters determined independently at 4 or 5 angles. The weights for each individual angle's parameters were determined from the relative sensitivity to the χ^2 searches. Thus, an arbitrary change in χ^2 of between 10-25% was chosen to determine the relative errors of the resonance parameters. The procedure to determine these relative errors for each angle's data was to keep two of the three search parameters Γ, Γ_p, and Δ_{BD} fixed at their best fit values. The value of the third parameter was then searched a sufficient amount both above and below the best fit value to extract the searched parameters' values at a χ^2 value 10-25% worse than the best-fit χ^2 value. Half the difference of the parameters above and below the best-fit value was then

used as the relative error. This method gave more weight to data which were most sensitive to the χ^2 searches. In cases were the data showed very little sensitivity to the resonance parameters, the fits to the angle were not included in calculating the average resolution parameters.

The weighted mean best fits were calculated for the search parameters Γ, Γ_p, and Δ_{BD}. The weighted mean resonance energy was determined by taking a weighted average of the individual resonance energies using the weights obtained from combining the relative errors from the three χ^2 searched parameters.

The uncertainty of the mean resonance values Γ, Γ_p, and $\Delta_{B_0 D}$ was determined from the calculation of the average variance. These are the errors listed with the data presented in Chapters 11, 12, and 13. The uncertainty of the resonance energy was determined from the uncertainty of the magnet energy calibration rather than from the variances between different angle best-fit values. The variances between different angle energies were usually less than 400 eV.

The curves shown with the measured excitation functions in Chapters 11, 12, and 13 were calculated using the mean resonance values and not the individual angle best-fit values. The latter usually produced excellent fits to the data.

6.7 Test and Assessment of Analysis Methods. Six of the first T=3/2 resonances which had been previously measured by using different techniques were remeasured using the new $(\vec{p},p)$ measurement method and

the helicity-analysis technique. As mentioned earlier, the previous measurements had relied on β^+-delayed proton measurements to determine the branching ratio Γ_p / Γ. Comparing our extracted values with these values allowed us to test our measurement and analysis method. The results presented in Table 6-1 indicate the reliability of our measurements. The branching-ratio determinations are in excellent agreement with those from the β^+-delayed proton decay of the T=3/2 states.

Thus, one measurement technique can yield all the necessary information to determine the resonance parameters. With the verification of our analysis method, $(\vec{p},p)$ energy excitation functions were measured on 11 high-lying T=3/2 states, and resonance parameters were extracted for nine of these resonances. Although the $(\vec{p},p)$ measurements were made with poorer beam resolution than the (p,p) measurements, these measurements are still much more sensitive and better able to determine the resonance parameters than the very good resolution (p,p) measurements. This should be apparent when one considers the fact that the unpolarized-beam analyses are not at all constrained by the resonance analyzing-power excitation functions. The lack of sensitivity of the (p,p) measurements becomes very clear after performing resonance parameters searches for both (p,p) and $(\vec{p},p)$ data.

The reliability of the $(\vec{p},p)$ measurements is usually quite good for reasonable beam resolution, smooth excitation-function data, and constant off-resonance cross sections and analyzing power. However, in cases of very poor beam resolution and a very weak resonance effect in

Table 6-1 Comparison of First T=3/2 Resonance Parameters Determined by Previous Measurements and Present Results.

[o] The references for previous results list the (p,p) reference first, followed by the reference which determined the branching ratio.

Compound Nucleus	Previous Measurement Results				Present Measurement Results $(\vec{p},p)$				
	E_R (MeV)	Γ (eV)	Γ_p (eV)	$\frac{\Gamma_p}{\Gamma}$	E_R (MeV)	J^π	Γ (eV)	Γ_p (eV)	$\frac{\Gamma_p}{\Gamma}$
^{13}N	14.2308 ± .0002	1100 ± 90	210 ± 11	0.19 [a]	14.2308 ± .002	$3/2^-$	1010 ± 30	261 ± 15	0.268
^{17}F	11.2636 ± .002	200 ± 40	19 ± 3	0.09 [b]	11.2642 ± .002	$1/2^-$	183 ± 13	23 ± 2	0.126
^{25}Mg	5.866 ± .003	155 ± 50	26 ± 9	0.17 [c]	5.8671 ± .002	$5/2^+$	105 ± 18	17.6 ± 4	----
^{29}P	5.834 ± .002	360 ± 50	300 ± 40	0.83 [d]	5.8392 ± .002	$5/2^+$	271 ± 10	216 ± 5	0.80
^{33}Cl	3.370 ± .001	115 ± 15	115 ± 15	1.00 [e]	3.3745 ± .002	$1/2^+$	100 ± 9	98 ± 9	0.98
^{37}K	3.278 ± .003	40 ± 20	40 ± 20	1.00 [f]	3.2840 ± .002	$3/2^+$	38 ± 6	34 ± 5	0.90

a) [Hin75a], [Ade73]; b) [Hin76], [Ade73]; c) [Iko76], [Sex73]

d) [Iko76], [Har64]; e) [Iko76], [Har71]; f) [Goo67]

the excitation functions the analysis may become ambiguous. The measurement of the first T=3/2 resonance in ^{25}Al is an example of this. The overall resolution was poor (1200 eV) and the resonance itself has a total width of 100 eV and a proton partial width of 18 eV. The $(\vec{p},p)$ data were not sufficient to extract both the total width and proton partial width. However, using the branching ratio obtained from previous measurements resulted in determining a total width in good agreement with an unpolarized beam of very good energy resolution.

The most questionable resonance-parameter extractions occur for the analysis of resonances which have non-constant off-resonance cross sections and analyzing powers. The method of rotating the data is somewhat questionable. Comparisons of results for measurements which had data at some angles not rotated and data at some angles rotated, indicated that for small rotations, there was very still good agreement between the rotated and unrotated data. However, extracting resonance parameters for very weak resonances on rapidly changing cross sections or analyzing powers may not be possible by searching on the rotated data using the helicity-amplitude method. Thus, the determination of the resonance parameters for these cases may be inaccurate.

7. $(\vec{p},p)$ and (p,p) Investigations - High-Resolution Beams

7.1 Introduction. The observation of narrow nuclear resonances with total widths of $\Gamma \simeq 100$–1000 eV by measuring energy excitation functions demands the availability of incident particle beams which have energy resolution comparable to, or less than, the resonance widths. The incident beam width is determined by three effects: the energy spread from the ion-source, energy fluctuations of the accelerator, and straggling from beam interacting with stripping foils or gas. Calculations indicate that straggling from interaction with residual gas in the beam tube is relatively negligible ≤ 20 eV. However, the voltage fluctuations of the accelerator normally dominate the beam energy width. This width is characterized by its full width at half maximum (FWHM), ΔE_B, sometimes expressed in terms of the ratio $\Delta E_B/E$.

The isospin-forbidden (p,p) resonances of interest occur at incident proton energies of 3 MeV and higher and can be ideally measured with electrostatic tandem Van de Graaff accelerators. The typical energy resolution of a tandem Van de Graaff using conventional energy regulation techniques is $\Delta E_B/E \simeq 1*10^{-4}$; thus, a factor of 3 to 5 improvement is needed to reduce the beam resolution to the $\Delta E_B \simeq 500$ eV needed for a total resonance width of this order. A low-noise, fast, slit-feedback system has been developed at TUNL to achieve this necessary resolution [Wes82, Ble78]. Considerable work by people from

all three universities has gone into making this high-resolution system a reliable and useful research tool. This system has undergone continuous refinement in an effort to achieve a state-of-the-art beam resolution.

A description of the high-resolution beam transport system will be presented in Section 7.2 followed by an overview of the high-resolution energy control system in Section 7.3 . Problems associated with obtaining high-resolution polarized beams will be discussed in Section 7.4, followed by a review in Section 7.5 of the diagnostics developed to determine the energy spread of the beam. A description of a direct beam energy spread measurement system will be presented Chapter 8.

7.2 TUNL High-Resolution Beam Transport. The unpolarized proton beam was obtained from a direct extraction ion source [Law65], DENIS I, while the polarized beam was obtained from a Lamb-shift polarized ion source [Cle74]. Both of these sources have very well regulated acceleration voltage power supplies and exhibit beam energy spreads of 3-6 eV [Pre73] and $\leq$ 12 eV [How82], respectively. The negative ion beams are accelerated by a High Voltage Engineering Corporation model F.N. tandem accelerator. At the center of the accelerator the negative ions are stripped by either gas or foils to produce the positive ions which are accelerated to the high-energy end of the tandem where they are momentum analyzed by a dual-90° magnet system. The magnet analyzing system will be described in Chapter 9.

Following this momentum analyzing system, a switching magnet bends the beam 60° into a beam line where all high-resolution measurements

were performed. Figure 7-1 is a diagram of the high-energy beam transport system. This beam transport system, which has both a high-transmission and a high-resolution operating mode, was always run in the high-resolution operating mode for the experiments described here. In this mode, the quadrupole singlets before the first 90° magnet and after the second 90° magnet are used to increase the horizontal size of the beam going through the analyzing system in order to achieve maximum resolving power of the magnets. However, this feature is only important for obtaining good resolution cyclograaff beams. Cyclotron beams have a large, instantaneous energy spread, but a tandem beam has an instantaneous energy spread due simply to straggling. With gas terminal stripping this means that the tandem beam is essentially a mono-energetic beam. Thus, the resolving power of the analyzing system is not critical to obtaining the high energy resolution. For example, with the dual-90° magnet system set to object and image slit openings of 2 mm, a 4 MeV proton beam with a beam energy spread of 960 eV will be accepted by the analyzing system.

The sextupole magnets before the first and after the second analyzing magnet make second-order corrections to the main analyzing magnet fields. For a review of the overall lab capabilities, see [New74].

7.3 High-Resolution Beam Energy Regulation. In a tandem accelerator using a belt charging system, the energy spread of the beam is due primarily to instantaneous voltage fluctuations at the terminal caused by uneven charging of the terminal by the belt or charging

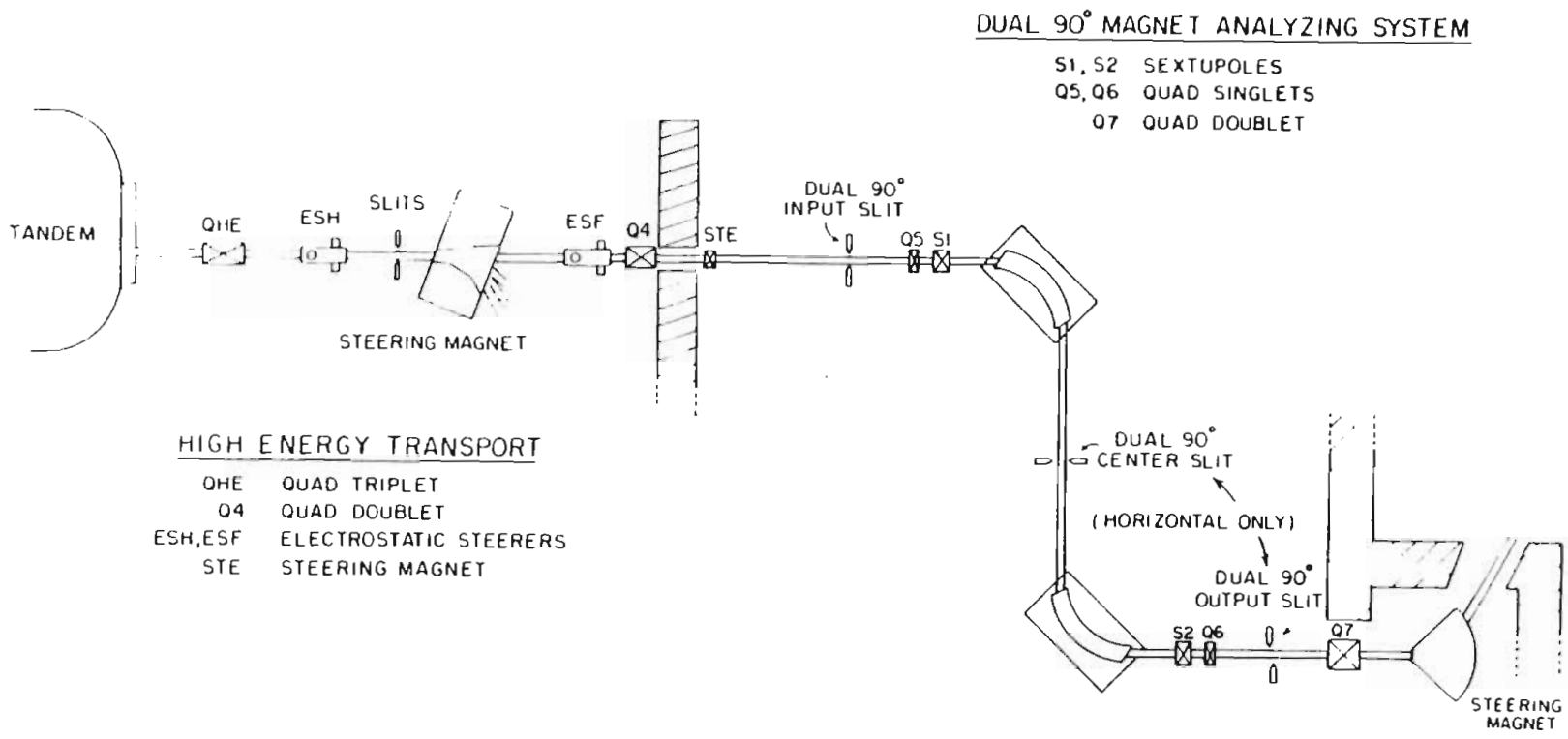

Figure 7-1 TUNL high-energy end, dual-90° magnet analyzing system, and experimental beam line.

system. Many different methods of terminal energy regulation have been developed and there are extensive discussions of energy control systems available [Thi74, Ver75, Tak72, Dzu72, Rot74, Cai74].

For many experiments, regulation of the fluctuations by corona feedback to the terminal yields sufficient resolution. This feedback loop uses metal plates mounted on opposite walls of the tandem pressure vessel to pick up terminal voltage fluctuations through capacitive coupling (CPU channel). The signal from these plates is used to control the grid voltage of a corona tube whose anode is connected to a set of sharp needles which draw current from the terminal, and hence regulate the amount of charge on the terminal [Thi74, Ver75]. The CPU feedback is only sensitive to a.c. fluctuations and is not sufficient to control the d.c. terminal voltage level. The d.c. terminal voltage is controlled by either a generating voltmeter mounted on the pressure vessel wall, or the voltage is controlled by a slit-difference signal generated when beam strikes the output slits of an analyzing magnet system. The slit-difference signal is used together with the CPU feedback to control the corona feedback. This feedback loop is rather slow because of the slow transit time of electrons in the insulating gas. It is limited to correcting 1-10 Hz fluctuations and generally results in beam energy spreads of 2.0-6.0 keV. However, to achieve beam energy spreads on the order of 500 eV it is necessary to correct fluctuations in the kHz region.

A direct fast-feedback energy regulation loop has been implemented at TUNL [Wes82, Ble78]. It uses feedback from analyzing magnet output

slits connected via a light link to a high-voltage $\pm$ 8 kV amplifier located in the tandem terminal which applies an energy correction signal to the stripper canal inside of the terminal. The slit-difference signal is also used to control the terminal d.c. level and to correct slow fluctuations by feedback to the corona tube in place of, or in conjunction with, the capacitive pick-up plates (CPU) signal. When the slit feedback system is running, the generating voltmeter (GVM) feedback is automatically switched out of the loop.

The horizontal analyzing slits which are located at a beam focus after the second 90^{o} magnet are sensitive to the beam energy. If the beam energy is greater than the energy set by the magnet analyzing system, then more beam will intercept the right high-energy slit. A lower energy beam will intercept the low-energy slit on the left side of the beam. Hence, the difference of the currents measured on these slits can be used to develop a feedback signal containing information about energy fluctuations of the beam. This feedback signal is used to correct the 1-10 Hz accelerator terminal voltage fluctuations through the corona correction. Faster fluctuations, from 5 Hz to 5.0 kHz, are corrected by sending the signal from a LED mounted against a glass port outside the pressure tank through a Lucite light pipe inside the machine column to a photomultiplier tube located in the terminal. The phototube output then controls the high-voltage amplifier, which applies a correction signal to the stripping canal (and foils) inside the terminal. Without the fast terminal amplifier feedback, the overall beam resolution is limited to around 2.0-6.0 keV. Figure 7-2 is a schematic of the entire feedback loop system. Details on the design and implementation of these

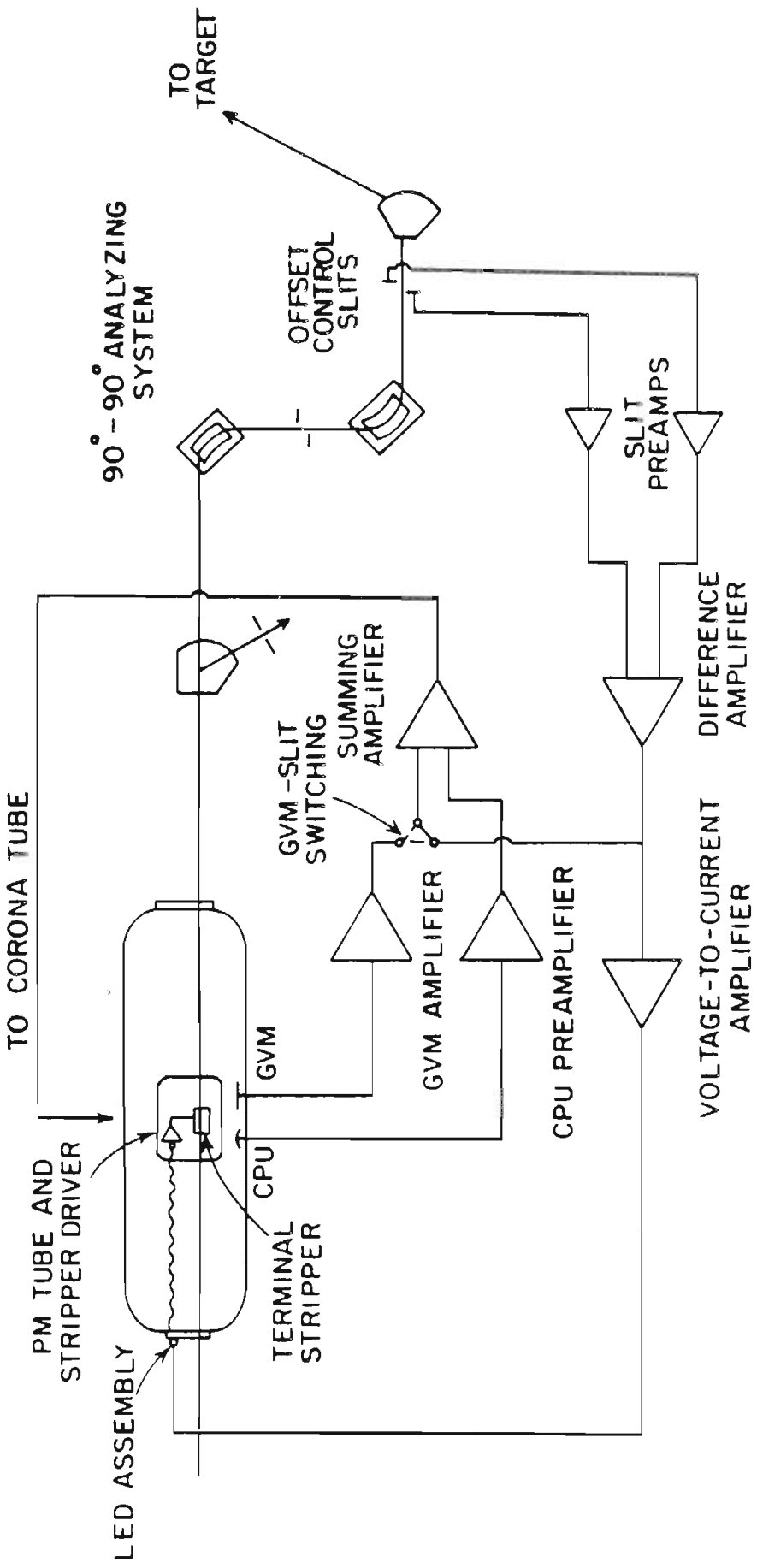

Figure 7-2 Schematic diagram of TUNL high-resolution fast feedback system.

amplifiers is given in [Wes82]. For details of the theory behind the feedback network, see [Ble78].

For a stable feedback system and high-resolution beams, the difference fluctuations generated from the feedback slits should be entirely due to true energy fluctuations. Hence, the slits are oil-cooled to eliminate electrical noise and are offset from each other to prohibit electrons knocked off one slit from introducing cross-talk to the other slit channel. The most difficult sources of non-energy fluctuations to correct are position instabilities in the beam, which generate slit-difference error signals identical to true energy fluctuations. These instabilities can be generated anywhere along the beam transport system: for example, changing plasma or extraction conditions in the ion-source; charging up of insulated slits, beam stops, or beam monitors by stray beam; instabilities due to line-voltage fluctuations; sections of accelerator tubes with unstable resistances. It is nearly impossible to eliminate all sources of position instabilities.

However, the slit-difference signals from the dual-90^{o} magnet analyzing system <u>input</u> slits can be used as feedback to a set of horizontal and vertical electrostatic steerers, ESF in Fig. 7-1, located between the high-energy end of the accelerator but before these input slits. This allows the beam incident into the analyzing system to be kept centered at the analyzing system input. This beam will follow the same path through the analyzing system to the output slits. This relies on correct beam transport such that beam energy changes affect beam

position to only second order.

One other consideration is that, since the energy resolution feedback network depends on the slit-difference signal, it is necessary for the analyzing magnets to have negligible current fluctuations. To insure that this was true, we monitored the analyzing magnet currents by looking at the voltage across a shunt resistor in the analyzing magnet current supply. This signal was observed with a differential voltmeter, because we were looking for changes in the current of one part in 10^4 to 10^5. The magnet currents typically had 10-50 eV noise. The analyzing magnet current supply control system was upgraded to achieve these noise levels. The calibration of current (Amps) to energy (eV) was accomplished by stepping the magnetic field a known energy as measured by a field measuring device calibrated to energy, as described in detail in Chapter 9.

Operating under optimum conditions and with gas (oxygen) stripping, the best incident proton beam resolution is ΔE_B = 425 eV. Under typical operating conditions, and for most tandem energies with proton beam intensities of ~ 1-5 μA, the energy resolution is ΔE_B = 500-600 eV. Measurements to determine the beam resolution will be discussed in Section 7.5 and Chapter 8.

7.4 High-Resolution Polarized Beams. Experiments using polarized high-resolution beams typically have slightly poorer resolution than unpolarized experiments and are much more difficult experiments to perform. Part of the difficulty is that two complicated systems, the polarized ion source and the high-resolution energy regulation system,

must run well simultaneously. The typical polarized proton beam intensity on target is ~ 100 nA while the unpolarized beam is typically 1–5 μA. Thus, the control beam on the analyzing system output slits is only 1–10 nA for the polarized beam while the unpolarized beam intercepting these slits is 0.1–1.0 μA. The two to three orders of magnitude less control beam, and hence lower signal–to–noise ratio of the polarized beam, results in a less stable feedback system and poorer resolution.

Another reason for the poorer beam resolution is that using polarized beams requires foil stripping in the terminal so that the beam does not become depolarized [Hae65]. Gas stripping minimizes the contribution of straggling to the beam resolution (see Table 7–1). However, in a gas stripper the H^- ion has time between the removal of its first electron and its second for the nuclear spin of the proton to precess about the magnetic field of the unpaired electron. The time between the two electrons being stripped varies randomly for different particles in the beam so that the beam of particles will become depolarized. However, in a stripping foil, the second electron is stripped with a much smaller time delay, and the nuclei do not have time to become depolarized. Thus, the necessary use of a self–supporting foil (which is thicker than the gas) introduces poorer resolution from the corresponding increase in beam straggling. As discussed in Chapter 6, the straggling decreases with increasing energy so the effect on the total incident beam resolution goes down with increasing incident energy.

Table 7-1 Beam Resolution Dependence on Terminal Stripping.

A comparison of observed incident beam resolution as a function of beam energy and terminal stripping parameters assuming a 500 eV FWHM Gaussian energy fluctuation distribution.

The total resolution distribution is calculated by numerically folding the 500 eV Gaussian distribution together with the calculated straggling distribution.

Beam Energy	Terminal Voltage	Total Observed Beam Width (FWHM)					
		(Gas Stripping)		(Carbon Foil Stripping (g/cm^2))			
		1 mT	3 mT	1.8	3.6	10.0	20.0
(MeV)	(MV)	(eV)	(eV)	(eV)	(eV)	(eV)	(eV)
2.0	1.0	504	531	626	789	1562	2705
		26	78	260	518	1441	2662
4.0	2.0	501	510	558	626	939	1561
		13	39	130	262	721	1441
6.0	3.0	500	504	535	581	764	1136
		–	26	87	175	482	963
8.0	4.0	500	502	524	558	686	941
		–	20	66	131	362	723
12.0	6.0	500	500	512	536	617	766
		–	–	44	88	242	484
16.0	8.0	500	500	507	524	585	688
		–	–	33	66	182	364

Calculations were performed to evaluate the effect of different terminal stripping conditions. The contributions to the total incident beam resolution were assumed to be a Gaussian distribution representing all energy fluctuations, and the appropriate straggling distribution calculated for the stripping conditions. The total resolution was calculated by numerically folding the two resolution components together. Table 7-1 presents the results of the calculations for various gas (oxygen) and foil (carbon) stripping conditions and machine energies. The energy fluctuations were kept fixed at 500 eV FWHM. The total gas thickness due to gas stripping is hard to estimate, since during experiments the terminal stripper pressure is monitored indirectly by a gauge at the high-energy end of the machine and not by a gauge at the stripper itself. Simultaneous measurements of the pressure in the stripper box and at the high energy end were made in an attempt to calibrate the high energy end measurements [Wes76]. The measurements in the terminal stripper box were not made directly in the stripper canal. However, these measurements yield an absolute lower limit for the pressures in the stripping canal and allow estimates of the pressure in the canal to be made based on the geometry of the stripping canal and box. Under normal gas stripping operating conditions, a high energy end vacuum of 6-10 μTorr, the stripper canal pressure is ~ 0.2-3.0 mTorr. Table 7-1 presents straggling calculations for both reasonable and upper limit pressures of gas stripping.

It is clear from the results presented in Table 7-1 that when using polarized beams it is necessary to use thin foils to minimize the

straggling. The results also show that calculating the total resolution by adding the two resolution contributions in quadrature underestimates the actual resolution distribution. Because of the importance of the straggling resolution contribution, an interactive computer code RESDIS was written for the TUNL DEC/VAX computer. It allows interactive calculation of the total incident beam resolution function (with input of stripping foil material, foil thickness, energy fluctuation conditions, and machine energy).

In order to minimize the straggling, carbon foils 1.0-5.0 $\mu g/cm^2$ thick were tested in the machine for their stripping properties. Carbon foils, ~ 10 $\mu g/cm^2$, are generally used for stripping because of their long lifetimes in the beams. Foils $\geq$ 1.8 $\mu g/cm^2$ were usable, meaning that on the average they would survive > 8 hours exposure to the beam, the minimum time needed to take an energy excitation function. The thin foils also have the property that they cause less of an increase in beam emittance from scattering, and therefore allow better transport of the initially poorer emittance polarized beam.

Several tests were performed on resonances at low energies of 3.374, 3.930, and 5.275 MeV where straggling in the terminal stripper contributes a maximum amount to the beam resolution. The tests measured the same resonance with gas stripping, a thin 1.8-4.0 $\mu g/cm^2$ carbon foil, and a 10.0 $\mu g/cm^2$ foil. The results for measuring the 3.374 MeV $^{32}S(p,p)^{32}S$ resonance, which has a total width of 100 eV, are shown in Fig. 7-3 for the three different stripping conditions. At 3.374 MeV the straggling width for the gas stripping is 10-60 FWHM. The 10 $\mu g/cm^2$

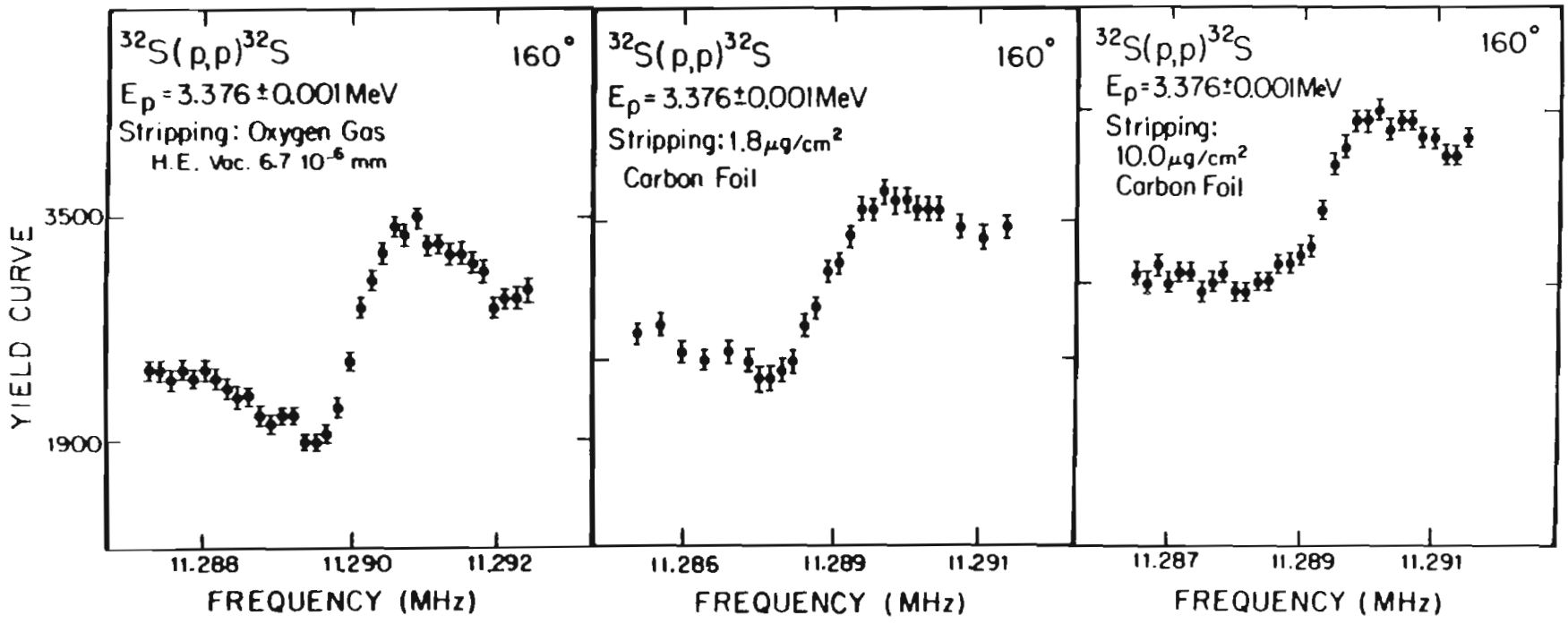

Figure 7-3 Terminal stripping resolution test. Excitation functions over lowest T=3/2 resonance in ^{33}Cl for three different stripping conditions.

carbon foil has a straggling width of 860 eV FWHM, and for a 1.8 $\mu g/cm^2$ foil the width is 155 eV. The observed resolution for the 1.8 $\mu g/cm^2$ foil is about 15–20% worse than gas stripping, but for the $^{32}S(p,p)^{32}S$ resonance measured at 5.275 MeV the 1.8 $\mu g/cm^2$ foil contributed to only 10–12% worse observed resolution.

Separate measurements with polarized and unpolarized beams were made on a 50 eV total width $^{50}Cr(p,p)^{50}Cr$ resonance located at 3.930 MeV. This width had been previously determined by [Sal77]. The measurements were performed in succession to insure similar energy fluctuations and machine conditions. The total resolution for the energy excitation functions were extracted using the R-matrix analysis code MULTI [Sel69]. Pertinent resolution parameters for the polarized and unpolarized data are compared in Table 7-2. The contributions of energy fluctuations have been separated from the total resolution distribution by using the code RESDIS. One would expect the energy fluctuations for both beams to be comparable. The results from RESDIS agree with these expectations.

Thus, for measuring polarized beam excitation functions, thin carbon foils can be used with only 10–20% decrease in incident beam resolution at low energies. However, carbon foils greater than 10 $\mu g/cm^2$ will not produce acceptable resolutions at any tandem energies. Approximately 20 of the 80 foil stripper positions were reserved for the thin high-resolution foils.

One additional problem associated with using foils to obtain high-resolution polarized beams was discovered after taking some of the

Table 7-2 Polarized and Unpolarized Beam Resolution Parameters.

A comparison of incident beam resolution parameters determined by measuring a 50 eV FWHM total width $3/2^-$ $^{50}Cr(p,p)^{50}Cr$ resonance located at an energy of 3.930 MeV.

The incident beam resolution was extracted by fitting the data using the R-matrix code MULTI [Sel69].

The Resolution - Straggling Column is the Gaussian resolution distribution width necessary to obtain the total observed resolution. It is numerically calculated by folding the two distributions together to obtain the total resolution distribution.

$^{50}Cr(p,p)^{50}Cr$			
Type of beam		unpol.	pol.
Feedback Control Slits		output	output
Beam Resolution	(eV)	465.0	600.0
Resolution - Straggling	(eV)	> 450.0	490.0
Stripping : gas H.E.	(μT)	10.0	
foil	(g/cm^2)		3.2
Straggling at Terminal	(eV)	< 50.0	230.0
Slit Settings : input	(mm)	2.00	2.50
center	(mm)	1.00	1.00
output	(mm)	2.00	2.00
Control Slit I	(μA)	$5.0*10^{-7}$	$0.9*10^{-7}$
Control Slit Diff.	(V)	< 0.5	< 0.2
Terminal Ripple	(kV)	< 2.5	< 2.5
Average Beam on Target	(μA)	1.4	0.065

resonance data. To transport and mount the thin carbon foils a layer of Formvar is first put on the stripping frame to give the foil extra strength. The Formvar will burn off the frame when bombarded with an intense enough beam. However, it was discovered that the Formvar was not burning off with the lower intensity and larger diameter polarized beam. Thus, some of the data were taken with the Formvar backing still in place. From comparisons of (p,p) elastic scattering measurements taken with carbon foils having a Formvar backing and without a Formvar backing, it was estimated that the Formvar is ~ 15–25 $\mu g/cm^2$ thick, and hence can severely degrade the beam resolution (see Table 7–1). After this problem was discovered, the thin stripping foils were always prepared before taking excitation functions by bombarding them with more than 1 μA of beam for several minutes until the Formvar was gone. (The intensity of the accelerated beam measured on the high-energy cup would increase suddenly when the Formvar was burned through).

In summary, the accelerated polarized proton beam has poorer resolution than the unpolarized beam. At the lower energies, where the machine runs more stably, straggling in the stripper foils contributes to poorer resolution. At the higher energies where the straggling becomes less important, the energy fluctuations are greater, and there is less feedback slit signal to control the terminal fluctuations. Even with these limitations, polarized high-resolution proton beams of 550–700 eV FWHM are now routinely obtained, which gives TUNL a unique research tool.

7.5 Monitoring High-Resolution Performance. There are several methods to evaluate the beam energy spread. A direct method is to measure an extremely narrow resonance of known width (~ 10 eV FWHM). Usually the widths of these states, which occur below or near the Coulomb barrier, have been determined from R-matrix fitting of many resonances (~ 100) over a small energy range (~ 500 keV). The analysis of many resonances which occur over a region where the incident beam resolution is essentially constant can improve the accuracy with which the widths and resolution effects are extracted. However, very narrow resonances with known total widths occur at energies below ~ 4 MeV, whereas most of the isolated isospin-forbidden resonances under study lie above 4 MeV. Because of the lack of a direct way to determine absolutely the beam resolution at higher energies, a direct beam energy resolution measurement was developed and will be discussed in Chapter 8. However, there are several diagnostics used to estimate the stability and resolution of the beam indirectly.

The signal generated from the capacitive pick-up (CPU) plates and the feedback control slit-difference signals are continuously monitored on an oscilloscope. The capacitive pick-up plate signal measures the 1-30 Hz terminal voltage ripple while the control slit-difference signal shows 1 Hz to ~ ~ 5.0 kHz energy fluctuations of the incident beam.

The CPU signal with no energy regulation feedback indicates the general condition of the machine charging system. If the machine is running poorly from problems with the charging current supply, or because the belt is transporting charge in an inhomogeneous manner

because of deterioration of the belt, or because the belt is hitting somewhere and scraping off charge, then the terminal ripple will reflect this. Under good charging system conditions the typical free-running terminal fluctuations, with generating voltmeter control of the machine, are 5-10 kV, depending on the machine energy. Generally, an increase in energy also produces an increase in beam energy spread. With the corona feedback system turned on (input from the CPU, the slits or both), the CPU signal shows the controlled terminal fluctuations to be 2-4 kV when the charging system is operating well. We periodically calibrated the CPU signal to a known voltage fluctuation by connecting a variable frequency high-voltage power supply directly to the terminal (with the machine not running) and measuring the response of the pick-up signal.

Another diagnostic available on-line while running is the control slit-difference signal. However, evaluating this signal is much more difficult because of the dependence of this signal's magnitude to beam optics, since a larger beam results in more current on the slits. In theory, the beam size at the output slit can be kept constant with energy. However, in practice the higher the energy the smaller or more rigid the beam. This results partially from a smaller beam emittance, angular divergence of the beam or transverse beam momentum component, at higher energy. The polarized beams have a greater emittance than the unpolarized beams due to source characteristics. Also, the emittance is increased by the terminal strippings which vary with the energy of the beam and the individual foil or gas stripping properties.

If the beam transport system is run correctly and consistently with prescribed slit settings and Q5-Q6 quadrupole currents, then for unpolarized beams, which have a small emittance and use gas-stripping (which contributes very little to beam emittance), the slit-difference diagnostic can indicate the beam resolution to within a factor ~ 2. At low energies the magnitude of the slit-difference signal has been related to beam energy spread using measurements of a narrow resonance of known width. For measurements all made within ~ 1-2 MeV of each other the diagnostic would be even more useful.

However, for polarized beams which are very dependent upon the beam emittance, and thus the beam energy and the quality of the particular stripping foil, only gross information is available. However, intimate knowledge of transport characteristics such as input slit currents, slit size dependences, and beam energy dependences coupled with a day-to-day knowledge of machine operating characteristics may in conjunction with the slit-difference signal allow an estimate of the beam resolution to a factor of ~ 1.5-2. The system used to log the machine parameters is discussed in Chapter 10. Values for a few of these diagnostics for polarized and unpolarized beams are presented in Table 7-2 for measurements made on the same narrow resonance.

Finally, a third diagnostic, which is not yet fully explored nor put in continuous use, is monitoring of the slit-difference signal with a frequency spectrum analyzer. This reveals the frequencies involved in the beam energy fluctuations. In Figs. 7-4 and 7-5 the spectrum for a 3.2 MeV unpolarized proton beam is shown for the terminal amplifier on

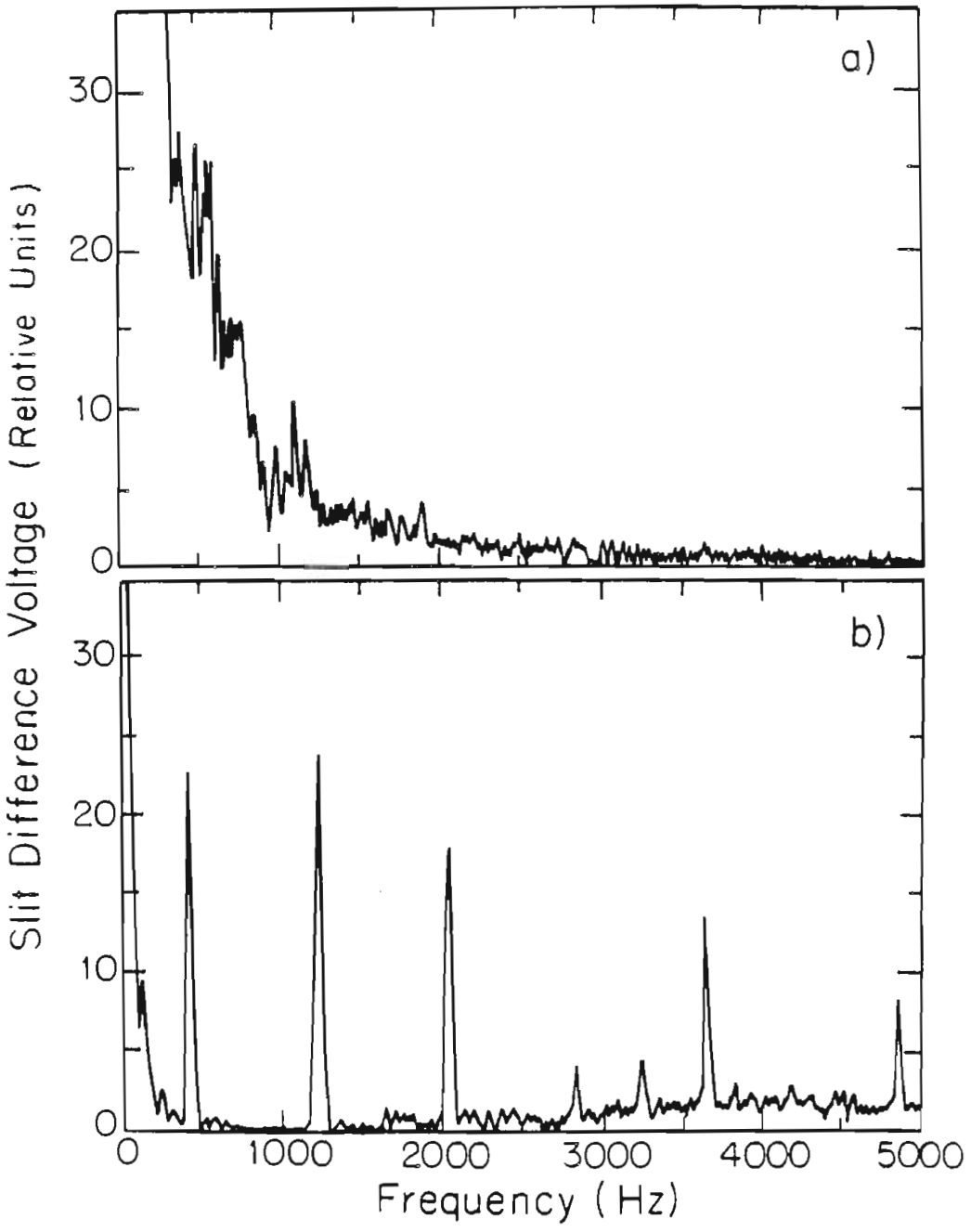

Figure 7-4 Frequency spectrum of slit-difference signal.

a) Terminal amplifier off, only CPU feedback from slits.
b) Terminal amplifier on, slit feedback to CPU and terminal amplifier.

Notice the large amount of d.c. to 1 kHz signal in a). The spikes in b) are due to constructive feedback of noise by the terminal amplifier.

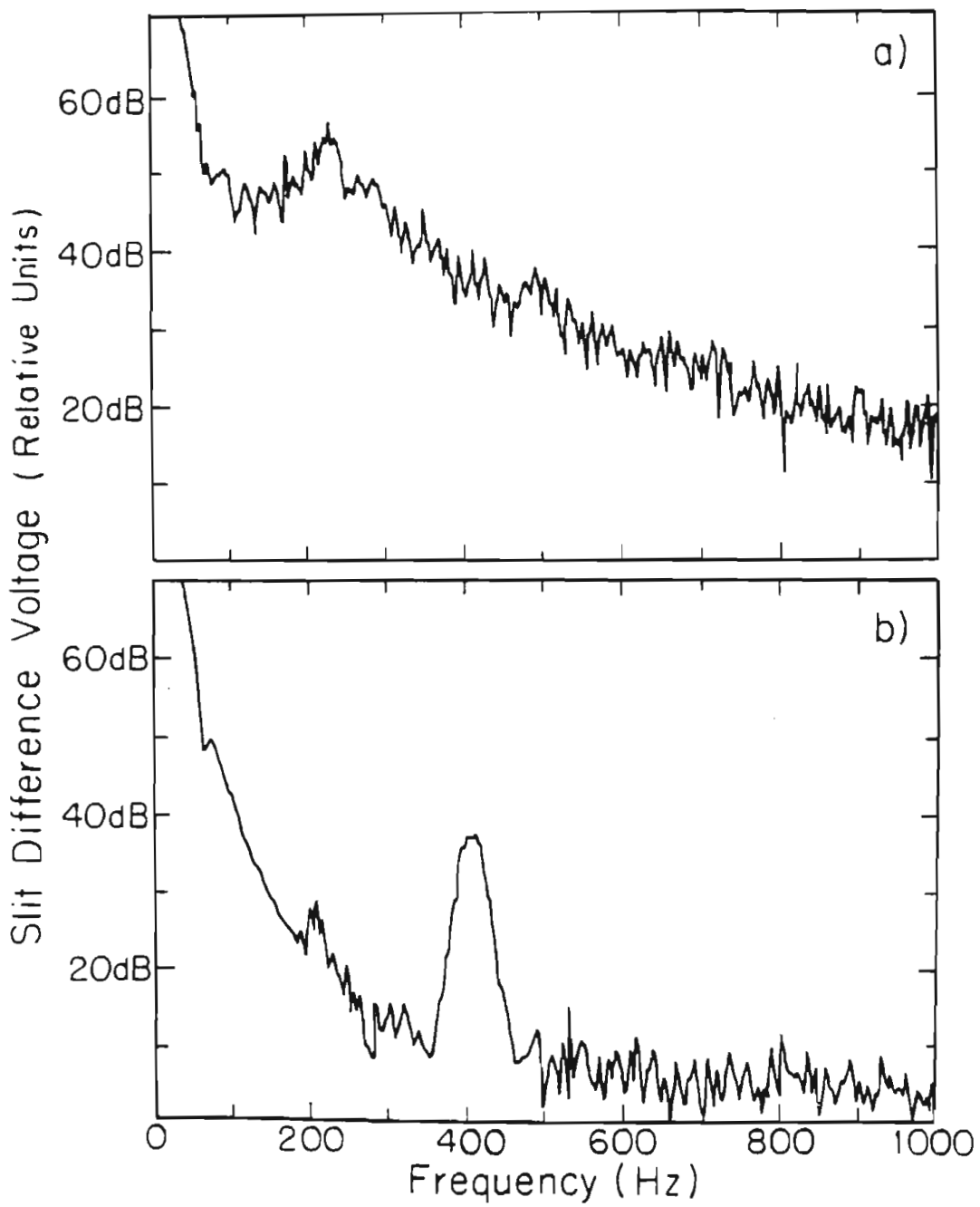

Figure 7-5 Slit-difference log frequency spectrum (d.c. to 1 kHz).

a) Terminal amplifier off, only CPU feedback from slits.

b) Terminal amplifier on, slit feedback to CPU and terminal amplifier.

Principal frequency region which contributes to beam energy spread.

and off. The effect of the terminal amplifier fast feedback on the frequency spectrum is dramatic. The initial use of this diagnostic indicated components in the feedback system which needed more filtering. Noise at 400 Hz and 800 Hz from the terminal amplifier was found to limit feedback gain. The use of the analyzer also revealed a serious problem of high-frequency noise in a new design slit-preamplifier which was not at all obvious from observing just the oscilloscope slit-difference signal.

7.6 Summary. High-resolution polarized proton beams of 550-700 eV FWHM and unpolarized proton beams of 425-600 eV FWHM are available from the TUNL accelerator system for the proton energy range 2 to 16 MeV. The routine use of high-resolution polarized beams makes TUNL a unique facility. The beam resolution is most likely limited by a combination of factors: charging system stability, the analyzing magnet stability, slit preamplifier noise, and, for polarized beams, straggling in the terminal stripper. However, the magnitude of the resolution for the accelerated beam is approaching that contributed by other effects such as Doppler broadening, as discussed in Chapter 6.

Modest improvements in resolution could be made to reduce contributions from magnet instability and amplifier noise at reasonable cost. However, it would require considerable effort. Reducing the resolution below 350 eV by improving the charging system would require major expense and time.

8. $(\vec{p},p)$ and (p,p) Investigations - Direct Beam Resolution Measurements

8.1 Introduction. Accurate measurement or calculation of parameters contributing to the observed experimental resolution are necessary to extract reliable resonance data. As discussed in Chapter 6, the incident beam resolution is one of the dominant contributions to the observed resolution for most (p,p) measurements. However, all previous measurements at TUNL (and most other labs as well) have relied only on indirect measurements of the beam resolution. In cases where there are many resonances studied within a small range of bombarding energies at or below the Coulomb barrier, this lack of knowledge is not critical to the extraction of resonance parameters. But for measuring the T=3/2 isospin-forbidden resonances, which are isolated and usually above the Coulomb barrier, an independent measurement of the beam resolution is essential for best results.

The present and earlier [Iko76] resonance experiments relied on performing the resonance analysis while using the beam resolution as one of the search parameters (as detailed in Chapter 5). In an attempt to improve the reliability of the extracted resonance parameters, a system to make direct measurements of the beam energy spread was developed and implemented. A further advantage to such a measurement system is that one can determine before making the difficult excitation function measurements whether the beam spread from the accelerator is acceptable.

The necessary resolution is determined by the total width and strength of the resonance which is being measured.

The energy resolution measurement scheme was inspired by a system [Hin75] of similar principle developed at the Institut fur Strahlen- und Kernphysik at Bonn. The method of measurement will be outlined followed by details on the design. The implementation of the system and the results of measurements taken at TUNL will then be presented.

8.2 Measurement Principle. The incident beam resolution is measured by using a bending magnet which transforms an energy distribution of the beam into a position distribution. The general idea, shown schematically in Fig. 8-1, is to use the dispersion of a point-to-point imaging magnet to separate particles of different energies to different positions on the x-axis of the image plane. Here the trajectories are plotted in the magnetic midplane. The coordinate system for a trajectory of a charged particle moving in a static magnetic field is shown in Fig. 8-2. This coordinate notation is used throughout this chapter and is from [Bro67]. A charged particle moving through a uniform field bending magnet with magnetic field B_o (in kilogauss) will follow a radial trajectory with radius of curvature ρ_o (in cm) determined by

$$B_o\rho_o = \frac{1}{0.3q}\left[E^2 + 2EE_r \right]^{1/2} \qquad 8\text{-}1$$

where E is the particle energy, E_r is the particle rest energy (both in MeV), and q is the particle charge. A particle having a given mass and

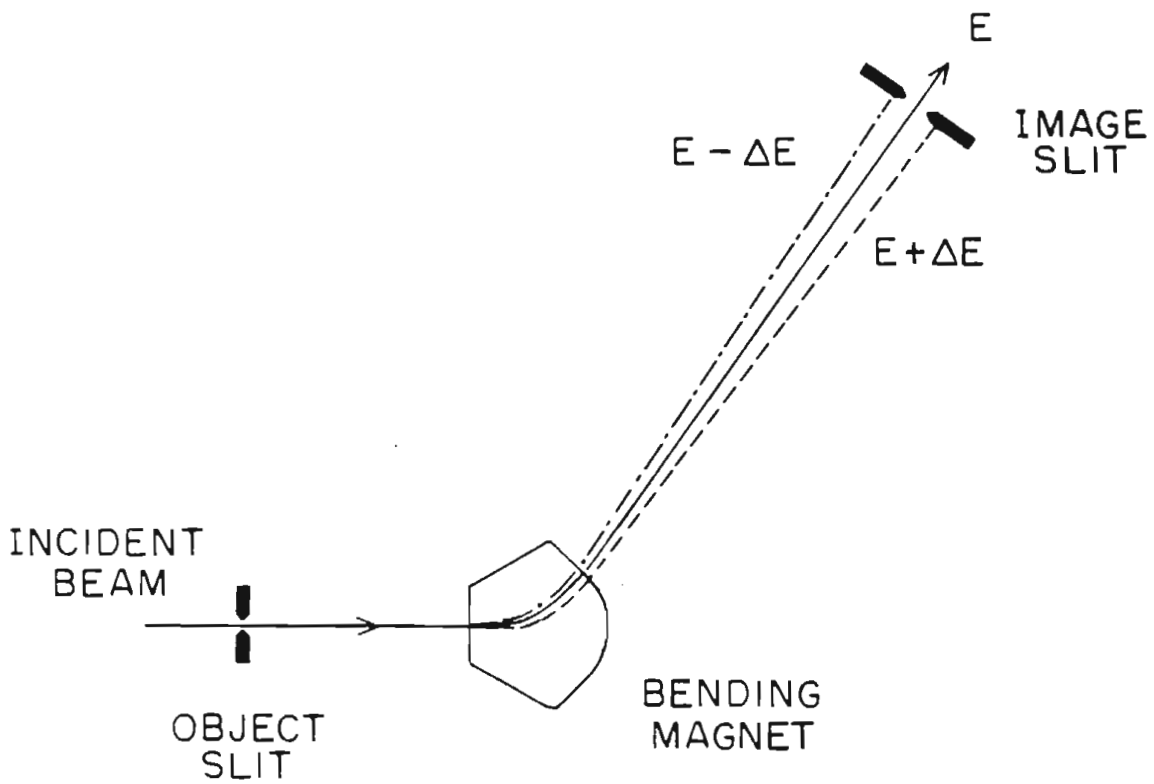

Figure 8-1 Beam energy spread measurement principle.

A simple bending magnet's dispersion can be used to translate energy information into position information. The diagram is shown for the magnetic midplane.

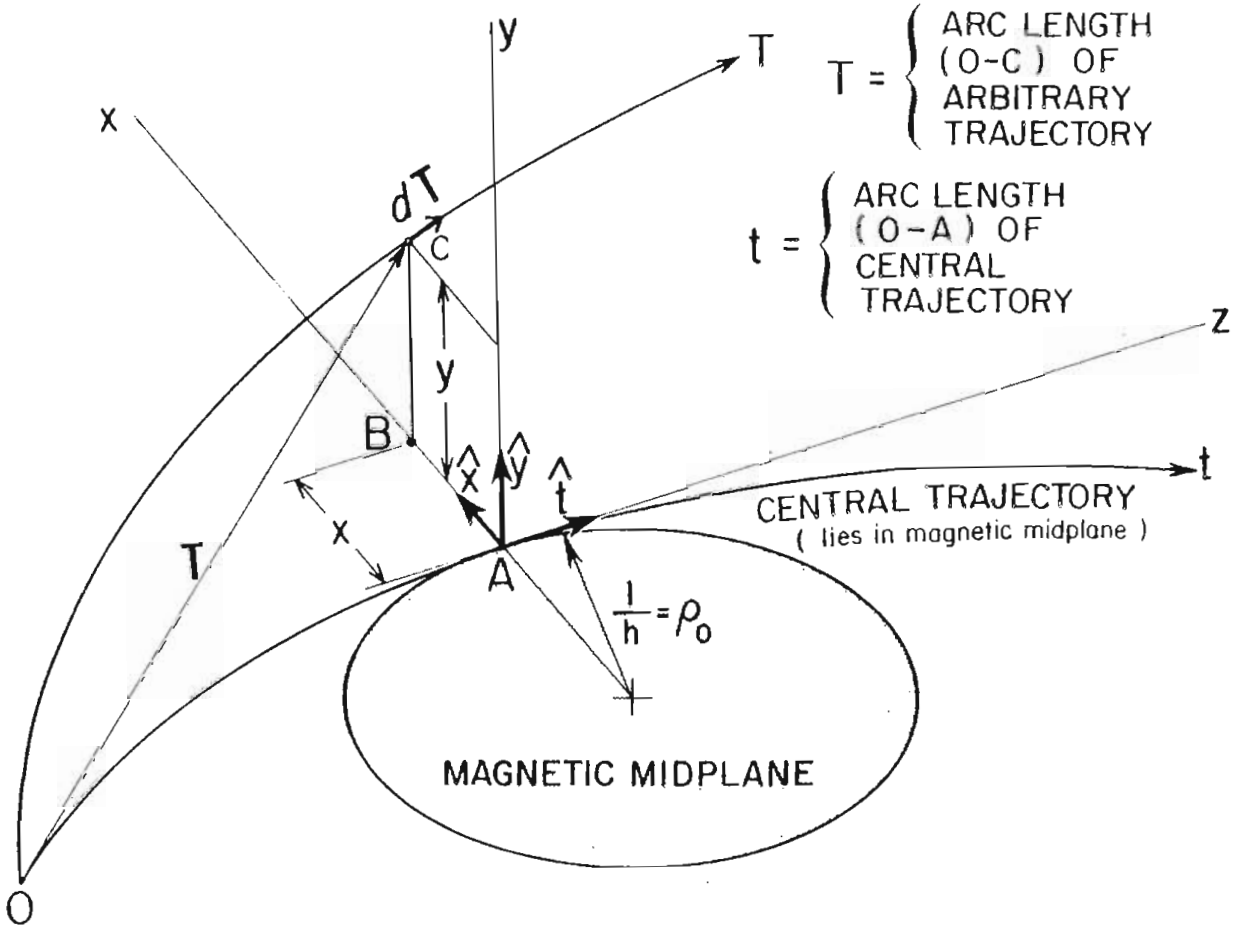

Figure 8-2 The standard beam transport coordinate system from [Bro67].

charge, but with more energy, $E + \Delta E$, traverses a longer radius of curvature and will be bent a smaller angle than a particle of energy E and will appear at the image to the right of the particle of energy E. Conversely, a lower energy particle, $E - \Delta E$, will traverse a shorter radius of curvature and will be bent a greater angle, appearing at the image to the left of the particle of energy E. Therefore, to determine the beam resolution it is only necessary to know the momentum dispersion and magnification of the analyzing magnet system and to measure the spatial distribution of the beam in the x-plane at the image slits.

To first order, the displacement in position at the image relative to the incident particle energy (or momentum) is

$$\frac{\Delta E}{E} \simeq 2\frac{\Delta p}{p} = \frac{w_i}{2D} \qquad 8-2$$

where p is the particle momentum along the t-axis (the beam trajectory direction), D is the momentum dispersion of the magnet, and w_i is the horizontal size of the beam at the image. The size of this beam at the image is determined by the horizontal size of the object beam w_o (usually defined by slits) and the analyzing magnet magnification to be

$$w_i = M_x w_o \qquad 8-3$$

where M_x is the magnification. Hence, a modest dispersion of ~ 2000 mm, a magnification of 1, and image and object slit gaps of 10 μm will yield a system with a resolution of $1 * 10^{-5}$. A 5 MeV proton beam with an energy spread of 500 eV (FWHM) would in this hypothetical situation have

a x-plane size at the image slits of 100 μm. Since most steering magnets have a dispersion of this size, and because the position distribution can be measured accurately, this is a feasible measurement to determine the beam resolution. An alternative method of determining the incident beam energy spread by detecting the energy of the beam would require an energy detector with better resolution than that of the incident beam. This is very difficult to accomplish. The best resolution for a charged particle detector and electronics is 15-20 keV. A very expensive high-resolution spectrograph may have 1-2 keV resolution.

In designing an analyzing-magnet resolution measurement system several important factors should be considered. The measurement should be made after the point where the final energy spread of the beam has been determined, i.e. after the analyzing magnet system. The measurement should also be made upstream of the target. At TUNL this requires that the system be located after the dual-90^{o} magnet analyzing system. Also, the entire beam phase space must be completely sampled to determine the true beam resolution. The narrow object slit has a very limited acceptance and sees only a very small portion of the beam. In addition, the beam after the dual-90^{o} magnet analyzing system clearly has a strong position-energy correlation introduced by the analyzing magnets. In order to sample the entire beam phase space and remove all position-energy dependences, it is necessary to sweep the beam across the object slit, such that over a period of time the entire phase space is uniformly sampled. This sweeping needs to sample evenly the beam phase space and reflect the average beam energy resolution.

Finally, one must consider the actual measurement of the beam distribution itself. This involves measuring the beam intensity at the image slit as a function of position in the x-plane. Because the slits are so narrow, the current intensity is too small to measure directly. However, measurements can be made conveniently using a solid state particle detector located behind the image slit. For example, a current of $1.6 * 10^{-17}$ A would yield a detector count rate of 6000 counts per minute. Although it is conceivable that one could try and step the image slit and detector horizontally across the beam distribution, it is much easier to sweep the beam itself across a fixed image slit. The x-plane deflection of the beam could be accomplished by sweeping the ΔE analyzing magnet, but it is not easy to sweep continuously a large iron magnet. Instead, the beam is swept in the x-plane by using an electrostatic steerer located just after the magnet. This steerer voltage can be ramped conveniently at several Hz.

Thus, the problem of measuring the beam resolution distribution becomes a problem of measuring the beam intensity versus a ramping voltage applied to the electrostatic steerer. The calibration of ramping voltage versus energy can be accomplished by changing the ΔE analyzing magnet field and observing the shift of the beam intensity centroid. Chapter 9 details the calibration of the analyzing magnet's magnetic field to energy.

8.3 System Design. The existing beam transport system at TUNL severely constrained the design of the beam energy resolution system. The physical locations as well as the beam transport characteristics of

the steering magnet used as the ΔE analyzing magnet and the dual-90° magnet analyzing system were fixed. The locations of all focusing elements were also fixed. Another consideration was the need to design a system with components that could be inserted accurately and reproducibly and then removed from the normal beam transport system by remote control. Thus, one could directly measure the beam resolution before and after taking each excitation function in a reasonable time, with minimum adjustment of the beam transport system. The basic ΔE measurement and beam transport components are shown in Fig. 8-3. A drawing of the beam line components is presented in Fig. 8-4. These figures also define the component terminology which will be used in the chapter. Details of the components and design of the system will be now be presented.

8.3.1 Analyzing Magnet. For the measurement system to be feasible it is necessary that the beam size at the image be 5 to 10 times greater than the image slit opening in order to achieve reasonable spatial resolution. Since the smallest slit opening that the instrument shop can accurately produce is ~ 10 μm, the beam spot from a typical high-resolution beam (500 eV (FWHM)) needs to be ~ 100 μm so that the position resolution, as determined by the image slit, is sufficient. As explained in Section 8-2, this requires that the magnet have a dispersion divided by magnification of ~ 2000 mm. First-order calculations for the 70-70 magnet, which assume a point-to-point bending magnet with a bending angle of 60°, yield a dispersion of 1875 mm and a magnification of 0.735, or D/M = 2551 μm. See [Bro67, Pen61, and Law77] for details on beam transport of charged particle beams. The bending

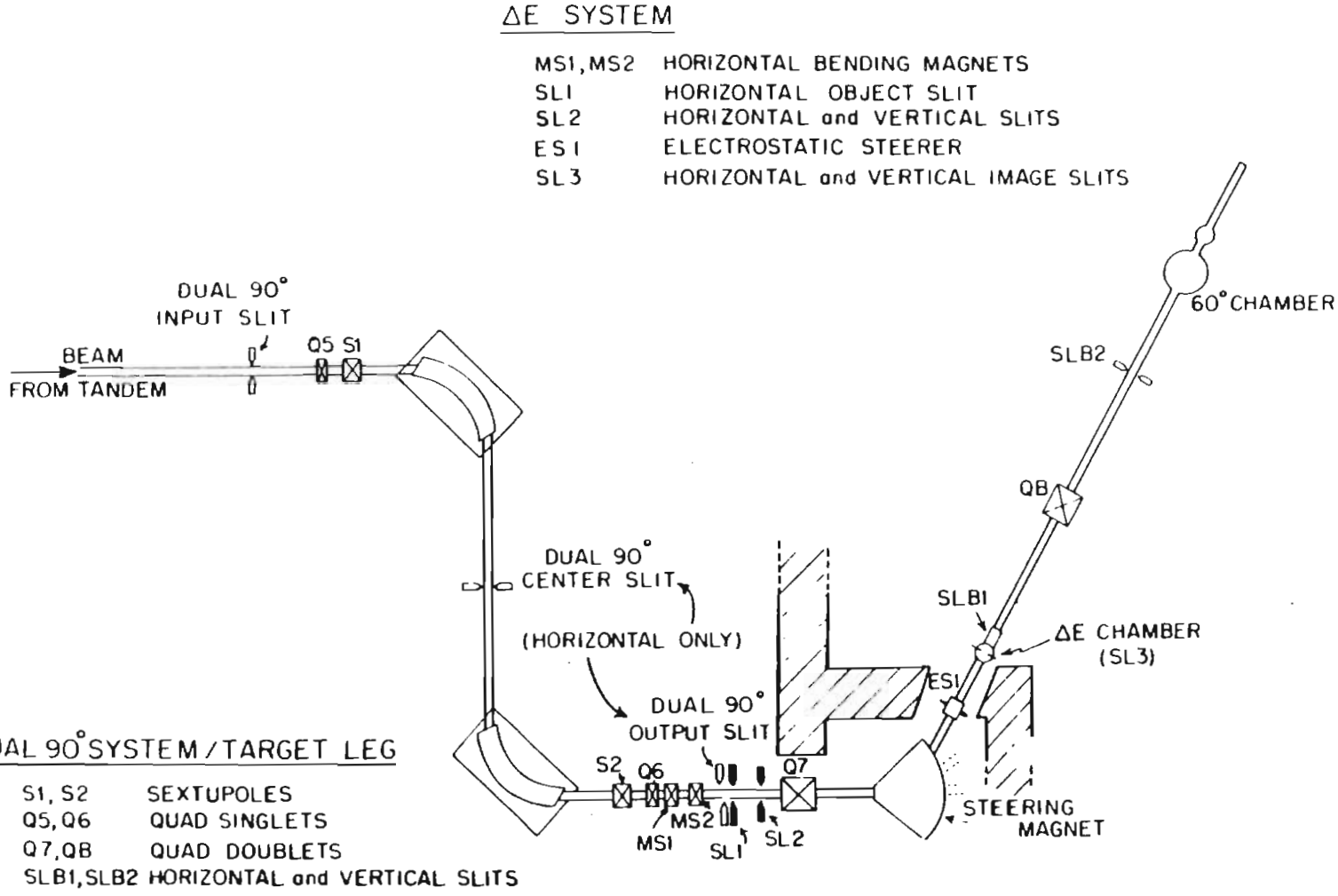

Figure 8-3 The ΔE beam transport and measurement system.

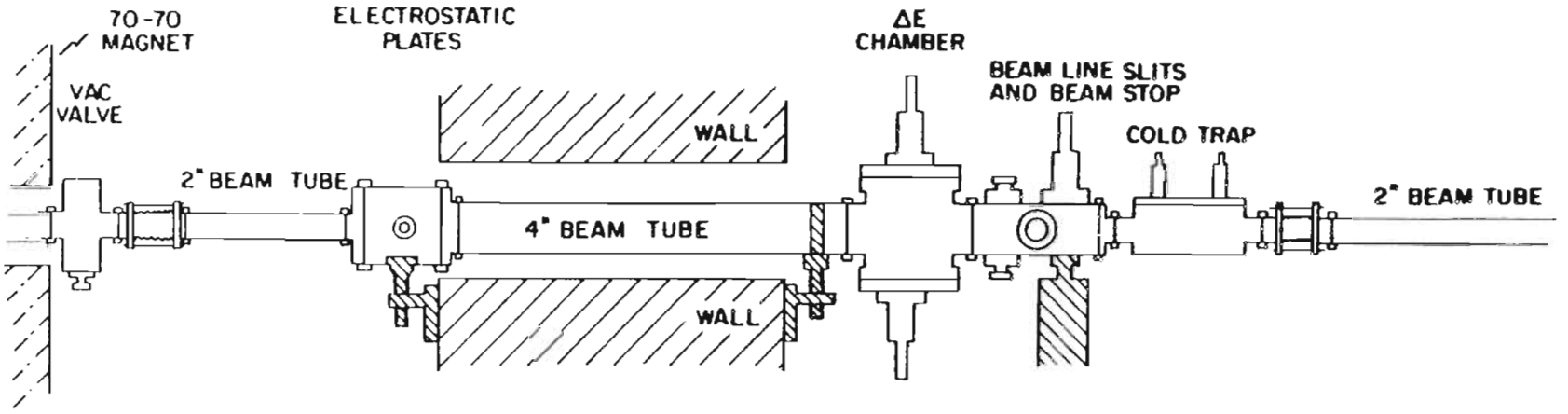

Figure 8-4 A side view of the 60^{o} beam line ΔE components.

angle of 60° was used for the ΔE measurements and all the excitation function measurements. It should be mentioned that for the 60° left beam line, the 70–70 magnet inverts the image relative to the object. One can see that with normal beam optics this feature is desirable because the 70–70 bending magnet cancels the beam position–energy correlation introduced by the dual-90° magnet analyzing system. Thus, a beam is produced at the 70–70 magnet image slits and on target with little or no position–energy dependence. This beam optics feature of the dual-90° and 70–70 magnets has no effect on the resolution measurement since the beam at the object slit is swept in a random fashion, thus removing the position–energy dependence.

The TUNL 70–70 steering magnet is not a point–to–point bending magnet as would be desired in the ideal system. Instead it is a semicircular bending magnet with horizontal and vertical focusing. However, a point–to–point focus can be achieved by using the quadrupole doublet Q7 which is located just before the analyzing magnet. Beam transport calculations were performed using the code TRANSPORT [Bro70]. The calculations were made for three separate conditions: (a) Q7 quadrupole doublet off, (b) using the first Q7 doublet with a required horizontal focus at the actual image slit location, and (c) using Q7 with a required point–to–point focus at the image slit. The complete beam characteristics for the three solutions are given in Table 8–1 for a 3–MeV and 8–MeV proton beam with an energy spread of 500 eV (FWHM) and 10 μm object slits. The notation of the table is based on the coordinate system presented in Fig. 8–2, where x is the beam distribution size related to the energy spread. The calculated dispersion for the

Table 8-1 Beam Properties at Image of ΔE System.

The beam radial size (x and y), angular divergence (x' and y'), magnification (M_x and M_y), and momentum dispersion as calculated using TRANSPORT for 3 and 8 MeV beams with beam energy spreads of 500 eV (FWHM). See Fig. 8-2 for coordinate system.

Solution a) Q7 quadrupole doublet off.

Solution b) Radial focus solution required at image slit.

Solution c) Point-to-point solution required at image slit.

Energy (MeV) and Solution	Q7 Doublet (kG)	(kG)	x (mm)	x' (mr)	y (mm)	y' (mr)	M_x	M_y	D (mm)
3 a	0.00	0.00	2970	20.60	5.83	12.61	1.06	0.56	2810
b	1.03	0.00	336	4.39	59.62	65.85	5.47	4.33	3994
c	-1.65	1.72	332	15.16	23.18	36.00	1.58	2.32	3994
8 a	0.00	0.00	11080	21.21	15.76	5.74	0.58	0.05	1744
b	0.12	0.00	88	19.93	5.15	13.61	1.21	0.44	2802
c	-0.89	0.48	88	26.04	9.93	7.39	0.92	1.00	2802

point-to-point solution is in reasonable agreement with the first-order calculations. The point-to-point solution is the preferred beam optics solution used during excitation function measurements. Calculations for several other incident beam energies for different object slit sizes are shown in Table 8-2. The results for beam resolutions of 500 eV and 1000 eV are presented. In addition to giving an indication of how large the image size is as a function of energy, the calculations also were used to determine how sensitive the output beam size would be to the object-slit size. One would like for the object-slit size to be small enough so that the image size would be dominated by the energy dispersion of the magnet. Then the measured intensity distribution would be caused only by the beam dispersion and not also by the slit size. The results for this calculation, as shown in the table, indicate that for slit sizes $\leq$ 20 μm this will be the case.

Finally, the magnet current and the 70-70 magnet potentiometer (pot) increments for the ΔE analyzing magnet were calibrated to energy by measuring the change in magnetic field at energies of 3, 5, and 8 MeV. This was accomplished by first using the dual-90° magnet analyzing system to determine the energy of the incident particle beam, as described in Chapter 9. With the beam energy known, the beam then was put through the ΔE analyzing magnet and centered on the beam line slits. Then the magnetic field of the analyzing magnet was measured with a nuclear-magnetic-resonance gaussmeter. Since the beam energy was known, the magnet calibration constant could be extracted. The magnetic field was incremented and calibrated to the pot increments. This calibration method was necessary because there is only one NMR gaussmeter in the

Table 8-2 Beam Size at the Image of the ΔE System.

The beam radial size for beam energy resolutions of 500 eV and 1000 eV (FWHM) are presented as a function of energy and object slit sizes.

E (MeV)	ΔE/E *10^4	ΔP/P *10^4	ΔE = 500 eV (FWHM) Object Slit Size (μm)				ΔE = 1000 eV (FWHM) Object Slit Size (μm)			
			1	10	20	50	1	10	20	50
3	1.66	0.83	332	332	332	340	662	664	664	668
5	1.00	0.50	170	170	172	178	340	340	342	344
8	0.63	0.31	88	88	90	98	176	176	176	182
10	0.50	0.25	64	64	68	86	126	126	128	138
14	0.36	0.18	38	40	48	82	76	78	82	106

lab. However, after measuring three different energies there was an apparent linear dependence of energy-change-to-pot-increment value. Then, a linear-least-squares fit to these points yielded

$$\left[\text{eV/pot. inc.}\right](E) = -27.47 + E_{Beam} * 79.554 \qquad 8\text{-}4$$

where E_{Beam} is the beam energy in MeV.

8.3.2 Object Slit SL1 and Acceptance Slit SL2. The horizontal object slit SL1 made of 30-mil tantalum was placed as close as possible to the focus which occurs at the dual-90° output slits. The slit is at the end of an oil-cooled rod attached to an air-throw plunger. This allows its easy remote insertion and removal from the beam path. A beam stop to measure the current through this slit was also included in its design. The slit was originally set to an opening of 25 μm, although a setting of 12 μm has also been used. During ΔE measurements most of the beam is stopped on this slit and the dual-90° slits. Thus, these slits are used to monitor the total incident beam by integrating the sum of currents from both. The slit SL2 is used to limit the acceptance of the analyzing magnet system.

Accurate resolution measurements require that each particle incident to the analyzing system follow the same input trajectory. One slit will not determine a unique trajectory into the magnets. Therefore, horizontal and vertical slits were added between the object slits and the analyzing magnet. The location of these slits was determined completely by the physical limitations of the system. The only available

place to install these slits was at a beam line cross which was already in use as a beam stripper. Thus, a design was made for a new beam stripper which would also allow room for mounting the SL2 slits. These slits were mounted at the end of a water-cooled rod attached to an air-throw plunger for automatic control, in a similar fashion to the SL1 slit. The 30-mil-thick tantalum slits were set to a vertical opening of 16 mils and a horizontal opening of 2 mils. The choice of 30-mil tantalum was based on using as thin a material as possible to minimize slit-edge scattering, while also insuring that proton beams with energy up to 16 MeV would be entirely stopped.

Accurate alignment of the slits SL1, SL2, the dual-90° image slits, and the analyzing magnet is very critical for making the energy spread measurements. If these slits are not all on a line with the magnet, then it is almost impossible to get any non-scattered beam through the system. The alignment of this part of the system proceeds as follows: A telescope is placed at 0° relative to the analyzing magnet between the output beam line quadrupole and the 0° beam line chamber (which requires disassembly of the 0° beam line). Then this telescope is set to a line defined by the 70-70 magnet and the second 90° magnet. The horizontal and vertical point in the 70-70 magnet is defined by the optical sight rod designed for the magnet. Establishing the second 90° magnet point is more difficult because the horizontal and vertical alignment points are defined by brass plates mounted on the top and side of the magnet. These alignment points must be transferred to the telescope line of sight. Beam ports at 0° relative to both the magnet entrance and exit ports extend out of the magnet opposite the entrance

and exit ports. Hence, a sight glass can be mounted on the port opposite the magnet exit port and can be seen from the telescope. The line defined by the two brass plates on top of the magnet can be used to determine a vertical line which intersects a sight glass port. This is accomplished by using a plumb-bob line suspended above the floor and bent 90^{o} to pass over the two plates. The horizontal line must be established by using a telescope set to the horizontal line of the 90^{o} magnet indicated by a brass plate mounted on one of the magnet faces. Then the line can be transferred using the telescope to the sight glass mounted on the beam port. With these two points established, the slits can be aligned.

8.3.3 Total Beam Phase Space Sampling. The elimination of the position-energy dependence of the beam at the object slit SL1 and the scanning of the total beam phase space were accomplished using steering magnets MS1 and MS2 located before the object slits. The magnets only steered the horizontal x-plane components of the beam because the beam incident on SL1 had just been momentum analyzed by the dual-90^{o} magnet system. For completeness the beam should be swept both horizontally and vertically. However, for the initial measurements we decided that the horizontal ramping would be sufficient.

Again, the existing beam transport and beam line equipment severely limited the placement of these magnets. In an ideal situation the magnets would be located after the dual-90^{o} analyzing system so the sweeping magnets would not affect the beam on these control slits. However, there was not enough room between the dual-90^{o} and 70-70

magnets for the system to be implemented in this fashion. The most serious deficiency of the implemented ΔE analyzing system is that the slit-feedback energy-regulation control system must use the dual-90° center slits for feedback instead of the output slits. There should be sufficient gain in the feedback system so that the resolution of the beam will not be degraded by this change. At lower energies where the energy fluctuations are smaller and the spatial size of the beam is bigger, the center slit feedback yields comparable resolution.

Excitation functions over a narrow resonance in $^{50}Cr(p,p)^{50}Cr$ with total width of 50 eV [Sal77] were measured with slit control at the center slits and the output slits, with no statistically significant difference in the observed resolution between the measurements. A summary of the results of these measurements is given in Table 8-3. The resonance widths were extracted using the R-matrix fitting code MULTI [Sel69]. Two air-core bending magnets were designed to sweep the beam horizontally across the object slit SL1. If only one magnet was used, there would be an angular dependence to the sampled beam. Thus, two magnets were used and were swept at two asynchronous frequencies. The magnetic field needed to deflect the beam over its entire phase space at SL1 was calculated by assuming that the steering magnets would be simple circular bending magnets. The magnetic fields necessary to sweep beams of various sizes and energies were then calculated based on the possible magnet locations. The results of these calculations are presented in Table 8-4.

Table 8-3 Beam Resolution Tests - Measuring a Narrow Nuclear Resonance.

The incident beam resolution determined by measuring a 50 eV (FWHM) total width $3/2^-$ $^{50}Cr(p,p)^{50}Cr$ resonance located at an energy of 3.930 MeV.

The incident beam resolution was extracted by fitting the data using the R-matrix code MULTI [Sel69].

The Resolution + Straggling Row is the Gaussian resolution distribution width necessary to obtain the total observed resolution. This is calculated by numerically folding the Gaussian and straggling distributions together to obtain the total resolution distribution.

$^{50}Cr(p,p)^{50}Cr$					
Type of beam		unpol.	unpol.	unpol.	pol.
Feedback Control Slits		center	center	output	output
Beam Resolution	(eV)	475.0	475.0	465.0	600.0
Resolution + Straggling	(eV)	> 460.0	> 460.0	> 450.0	490.0
Stripping : gas H.E.	(μT)	9.6	9.6	10.0	
foil	(g/cm^2)				3.2
Straggling at Terminal	(eV)	< 50.0	< 50.0	< 50.0	230.0
Slit Settings : input	(mm)	2.00	2.00	2.00	2.50
center	(mm)	0.50	1.00	1.00	1.00
output	(mm)	2.00	2.00	2.00	2.00
Control Slit I	(μA)	$2.0*10^{-7}$	$1.3*10^{-7}$	$5.0*10^{-7}$	$0.9*10^{-7}$
Control Slit Diff.	(V)	< 0.15	< 0.2	< 0.5	< 0.2
Terminal Ripple	(kV)	< 2.5	< 2.5	< 2.5	< 2.5
Average Beam on Target	(μA)	1.4	1.4	1.4	0.065

Table 8-4 ΔE Beam Deflection by Sweeping Magnet Field Versus Beam Energy.

The necessary magnetic field for the sweeping magnets MS1 and MS2 to deflect beams in the x-plane 0.5, 1.0, or 2.0 mm at the SL1 object slit versus the incident beam energy.

The beam momentum is listed in column 2.

Beam Energy	Beam p	--- Beam Spot Size at SL1 ---					
		0.5 mm		1.0 mm		2.0 mm	
		MS1	MS2	MS1	MS2	MS1	MS2
(MeV)	(MeV/c)	(gauss)	(gauss)	(gauss)	(gauss)	(gauss)	(gauss)
3.0	75.1	14	26	28	52	55	104
6.0	106.3	19	37	39	73	78	147
9.0	130.3	24	45	48	90	95	180
12.0	150.5	28	52	55	104	110	208
15.0	168.4	31	58	62	116	123	233

After determining the necessary fields, the actual coils were designed by assuming that they were Helmholtz coils. For simplicity, the coils were built on Plexiglass frames, with the idea that after initial testing a revised design might be necessary. The steering magnets consisted of two sets of 18 gauge copper wire coils wound 220 turns around a 4.125-inch-diameter Plexiglass frame and extended to an outer diameter of 5.625 inches.

The coils were powered with either a Kepco model BOP 36-5M bipolar operational amplifier [KEP01] or an OPAMP model 440C [OPA01] audio amplifier using two dc 30 Volt/5 Amp power supplies. These amplifiers were driven by variable voltage triangle waves generated by standard waveform generators. The magnetic fields of both steering magnets were mapped with a Hall-effect gaussmeter and calibrated to coil input current (voltage). The maximum undistorted triangle waveform magnetic field was measured as a function of frequency. For frequencies below 40 Hz, the steering magnets can produce undistorted peak-to-peak magnetic fields up to 65 Gauss and acceptable waveforms up to 90 Gauss. For higher frequencies or fields the coils overheat because their air cooling is insufficient. Thus, these coils cannot produce the fields required for complete phase space coverage of the beam for energies above ~ 9MeV.

The asynchronous frequencies of 39.2 Hz and 21.8 Hz were selected by using an oscilloscope with one of the signals as input to the x amplifier and the other connected to the y amplifier. This allowed selection of frequencies with a minimum of overlapping harmonics. A time

lapse photo of the oscilloscope pattern was taken to measure this effect quantitatively by looking for possible intense patterns caused by overlapping harmonics between the sweeping frequencies. The frequencies were continuously monitored for possible drifts.

8.3.4 The Image Slit. A special ΔE chamber was designed to contain the SL3 slit and the solid state detector. The design criteria were: 1) A compact chamber allowing good alignment. 2) The ability to control remotely the placement of the detector and the image slit SL3 in and out of the beam. 3) A beam intensity detection system to insure that the incident beam into the chamber would not destroy the solid state detector. 4) The ability to access quickly the ΔE vacuum chamber and remove either the detector or slits without disturbing the alignment. 5) The option of having several sets of slits to use depending on the beam energy being measured.

Following these design criteria, a 6-inch inner diameter and 8-inch outer diameter chamber was built by the TUNL instrument shop. The small size of the chamber allows it to be kept very near the normal beam line image slits and beam stop. Thus, there is only a small change in focus between the SL3 slit and the beam line slits. The chamber was located before the beam line slits so these slits would not have to be removed or adjusted during the ΔE measurements.

The detector holder and image slit were mounted on an air-throw plunger similar to the SL1 and SL2 arrangements. The horizontal and vertical SL3 slits were placed in separate housings which can easily be removed from the front of the plunger rod with no need for realignment.

There is easy access at the back of the plunger to the solid state detector which is mounted in an insulated sleeve. The plunger assembly is mounted on the beam axis on the chamber top plate. Both the top and bottom plates of the chamber could be removed and transported to a nearby work table without having to disconnect any air pressure lines.

The beam intensity may be great enough to damage the solid state detector, but too small to detect reliably with available electrometers. However, this beam intensity detection problem was solved by detecting nuclear scattering from a gold foil mounted on an air-plunger target rod. Like the slit mounts, this target rod could be quickly placed into, or removed from, the beam. Another solid state detector was mounted in the chamber wall at an angle of 35° to the target rod. The target rod plunger is mounted off-center on the chamber bottom plate to obtain the minimum scattering angle possible for the gold foil and hence the maximum sensitivity to the beam intensity. Another consideration was to prevent the SL3 and detector plunger from hitting the target rod plunger. A schematic of the chamber geometry is presented in Fig. 8-5 and a side view of the chamber is presented in Fig. 8-4. A glass port was included on the side of the chamber to allow a visual check of conditions.

The alignment of the SL3 slits was accomplished with the same procedure used to align the 60° beam line. A telescope was placed at the end of the beam line on a vertical line established by a marker which can be inserted within the 70-70 steering magnet and a point obtained by suspending a string and plumb-bob centered to a brass marker located in

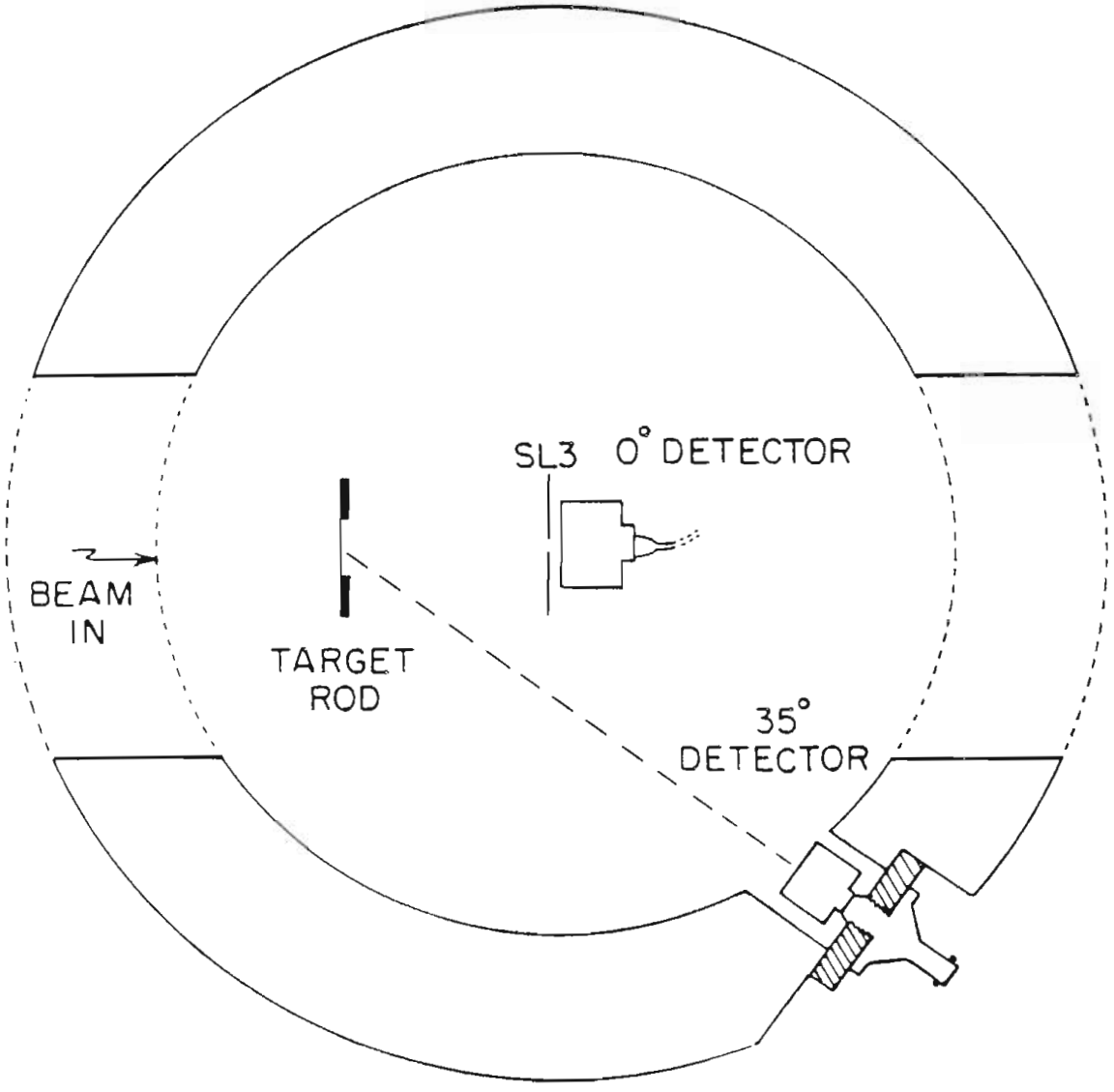

Figure 8-5 Schematic view of the ΔE chamber.

The geometry of the SL3 slits, 0° detector, target rod, and 35° detector are shown.

the floor. The telescope height was determined by the marker within the 70–70 magnet and by using a level vertical sight.

8.3.5 Beam Position Scanning at the Image Slit. The final component of the ΔE measurement scheme is the x-plane horizontal electrostatic steerer ES1 located after the 70–70 bending magnet (see Fig. 8–4). An available steerer was used which had 5-inch long plates with 1.5-inch separation. Calculations of beam deflection were performed for several possible ES1 steerer and SL3 slit separations. The necessary voltages for beams of various sizes and energies are presented in Table 8–5. Note that the decrease in beam size with energy results in a slow decrease of necessary sweeping voltage. The electrostatic steerer voltage was obtained using a Kepco high voltage model OPS 5000 operational amplifier [KEP01]. The amplifier is driven with a triangle waveform at 1–15 Hz. The operational amplifier is a unipolar supply which can swing a maximum voltage of 5 kV.

8.4 Ideal Experimental Measurement Procedures. General procedures were developed and followed to make energy spread measurements. The incident beam was tuned to the beam line slits and beam stop in the normal high-resolution tuning manner. The beam spread feedback control was then switched from the output dual-90° slits to the center slits and the beam was again peaked at the beam line beam stop. The object slit SL1 was then inserted and the beam passing through this slit was measured on the beam stop located directly after this slit. If possible, this beam intensity was also measured on a beam stop located in the beam line after the 70–70 magnet. Next the acceptance limiting

Table 8-5 ΔE Beam Displacement by Electrostatic Sweeping Versus Beam Energy.

The voltage applied to the electrostatic steerer ES1 necessary to deflect beams 100 μm in the x-plane at the SL3 image slit versus the incident beam energy.

The voltage needed to deflect a fixed beam energy spread versus energy is also presented. These voltages are based on the beam transport calculations of beam spot size and energy given in Table 8-2.

Beam Energy	- Beam Size at SL3 Image Slit -		
	100 μm	500 eV	
(MeV)	ES1 (Volts)	ES1 (Volts)	Size (μm)
3.0	324	1073	332
5.0	540	918	170
8.0	864	760	88
10.0	1080	691	64
14.0	1512	605	40

slit SL2 was put into the beam and the beam intensity was measured at the ΔE chamber by counting the protons scattered off the gold foil into the 35^{o} solid state detector. The sweeping magnets were then set to the magnetic fields necessary to sample the entire beam phase space. If a small counting rate of less than a few hundred counts per minute was observed with the scattering detector, then the target rod was removed and the image slits and 0^{o} detector were inserted into the beam path. The output of the detector preamp was always monitored with an oscilloscope to make sure that the detector was not being destroyed by an excessive count rate. If the counting rate was safe, then SL3 was kept in the beam and the electrostatic sweeping was started.

The data were acquired using the VAX 11/780 computer and the XSYS [Gou81] data acquisition system. The two-parameter data consisted of the 0^{o}-particle energy spectra and the corresponding electrostatic sweeping voltage spectrum. The ADC conversion of the electrostatic sweeping voltage was triggered by the same pulse used to gate the ADC particle spectrum. Individual software gates could be set around limited regions of the particle or voltage spectra in order to study the different 0^{o}-spectrum and electrostatic-voltage-spectrum dependences.

8.5 Actual Measurement Procedures. The actual measurement procedures were never quite as simple as the ideal situation described in the above section. With SL1 and SL2 in place it was sometimes difficult to find the beam because of transport misalignment problems. Often the difficulty seemed to be caused by y-axis misalignment of the beam. Once the beam was found and its intensity maximized, the situation

was reversed, and generally there was excess beam. Reducing the intensity required that the beam be detuned with focusing elements and/or be limited by tightening various slits which occur before the ΔE measurement system. Usually several hours of tuning the system were required before measurements could be taken. Reducing the slit sizes of the dual-90° system also had the undesirable effect of increasing the resolving power of this analyzing system and perhaps producing a better resolution beam than would be observed when operating under normal conditions.

The other principal difficulty in the measurement was the severe problem with slit scattering. The typical ΔE slit parameters are listed in Table 8-6. The small slit-gap area to slit-edge area ratio indicates that there will be substantial slit scattering. The difficulty in making these measurements is understandable when one considers the slit sizes and slit alignment accuracies necessary. Several different sets of slit-gap parameters were tested. Large SL1 and SL2 slit scattering yielded a broad, featureless electrostatic voltage spectrum with no apparent distribution peak. The percentage of slit scattering could be altered by changing the beam transport. With proper alignment the slit scattering form SL1 and SL2 should not be a problem.

The slit scattering which occurs at SL3 is the hardest to discriminate against because, unlike the SL1 and SL2 scattering, the particles which scatter here enter the 0° detector directly without being dispersed by the analyzing magnet. To understand the 0° spectrum better, special SL3 slits were constructed with double slits. The slits

Table 8-6 ΔE Experiment Typical Slit Gaps and Thickness.

The slit gaps and thicknesses for the SL1, SL2, and SL3 slits are presented.

The slit gaps are presented in mils and thicknesses in inches.

The slit gap area to slit edge area ratio is also listed.

Slit Designation	Gap Defined by Slit	Slit Gap		Slit Edge		Gap / Edge %
		(mils)	(μm)	(mils)	(μm)	
SL1 (object)	horizontal	0.5	12.7	30.0	762.	0.84
SL2	horizontal	4.0	102.0	30.0	762.	6.7
	vertical	16.0	406.0	30.0	762.	26.7
SL3 (image)	horiz.-thin	0.4	10.0	3.0	76.	6.7
	horiz.-thick	0.8	20.0	20.0	508.	----
	vertical	3.5	89.0	20.0	508.	17.5

consisted of thin 0.003-inch stainless steel slits set to the desired 10 μm gap. These slits were not thick enough to stop beams above ~ 3.5 MeV. Behind these slits were a set of 0.020-inch tantalum slits set to approximately 20 μm as shown in Fig. 8-6.

The beam which passed through the thin slits was then observed in the 0° particle spectrum as a broad low-energy peak. The slit-scattered particles occur at energies above this peak while the highest energy peak corresponds to particles that have passed directly through the 10 μm gap. The 0° particle spectra are shown for several different incident beam energies in Fig. 8-7. The spectra do not have identical energy gains. Setting these slit gaps is extremely difficult because the thin slits are not very rigid. We discovered that one set of SL3 slits did not define a plane perpendicular to the incident beam. Thus, when the slits were mounted flush on the mounting rod no unscattered beam reached the 0° detector, resulting in a spectrum with no high energy peak and a large scattered peak. When the slits were rotated slightly by tilting the slits relative to the mount, the beam was able to pass through and a good ratio of unscattered-to-slit-scattered counts resulted, as shown in Fig. 8-8.

8.6 Measurement Results. Measurements of the beam energy spread were made during several experiments at energies of 3, 3.9, 5, 7.6, and 8.9 MeV. The observed beam sizes and resolutions were within limits expected from the calculations and measurements of narrow resonances.

Figure 8-9(a) displays the 0° spectrum for a measurement performed with an unpolarized 5 MeV incident beam. The figure also shows the

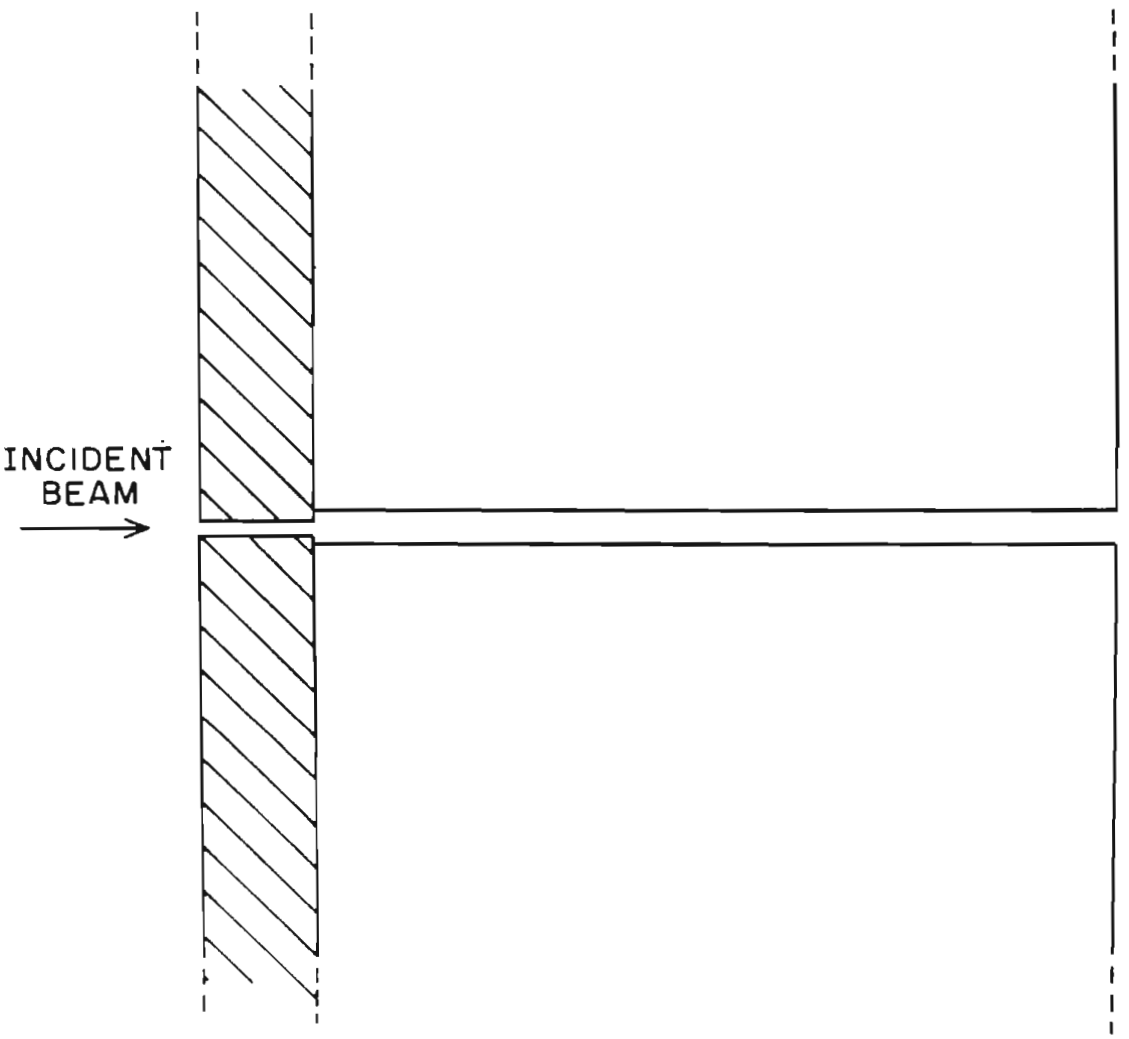

Figure 8-6 Scale view of the ΔE SL3 horizontal image slit design as viewed in the non-bending plane. Notice the slit gap-to-edge ratio.

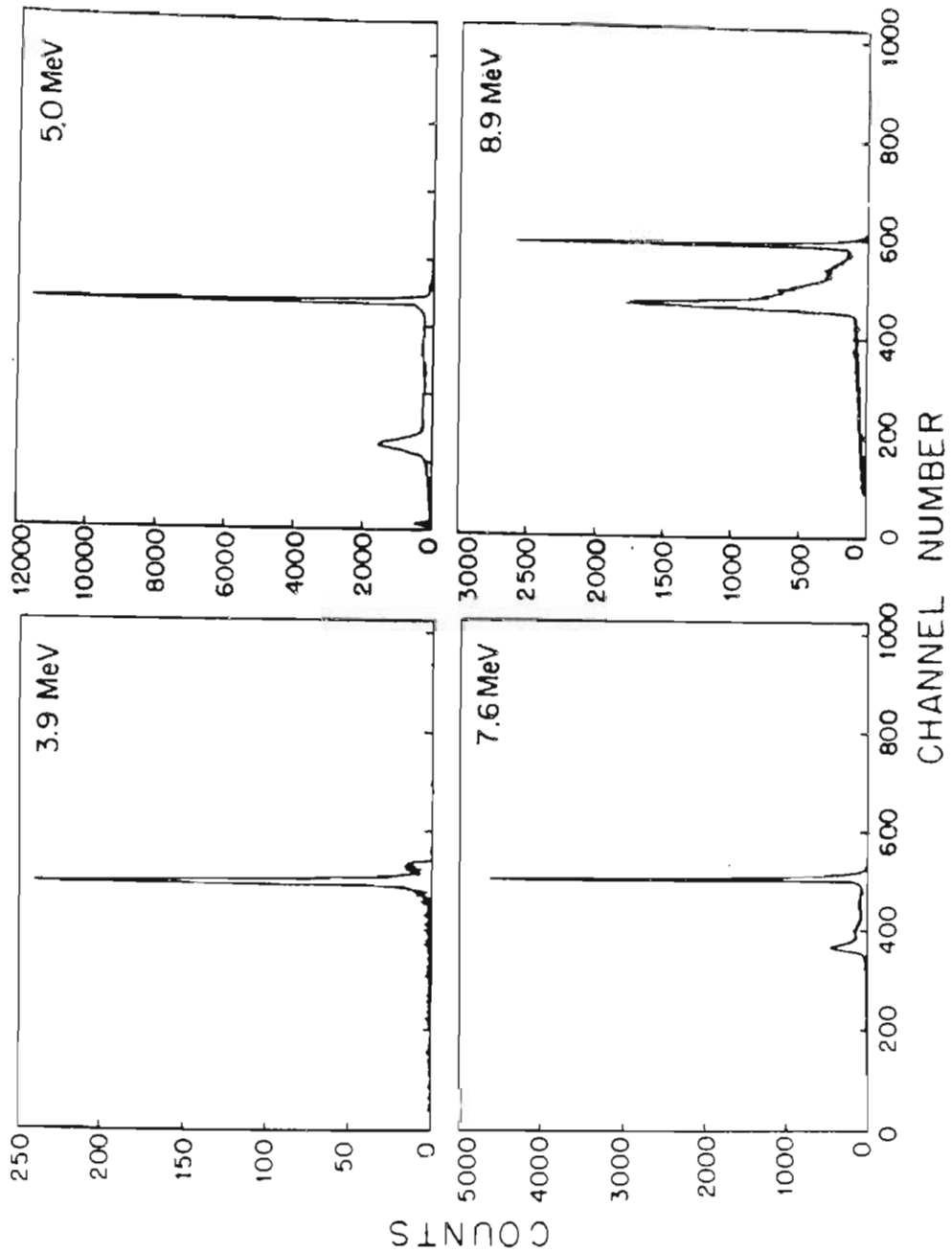

Figure 8-7 Particle spectra from ΔE 0^{o}-detector. The 0^{o} spectra for 3.9, 5.0, 7.6, and 8.9 MeV proton beams. The unscattered peak is at the extreme right or high energy end of the spectrum. The low energy peak is from the beam which passes through the thin slits. The counts between the peaks are from slit scattering.

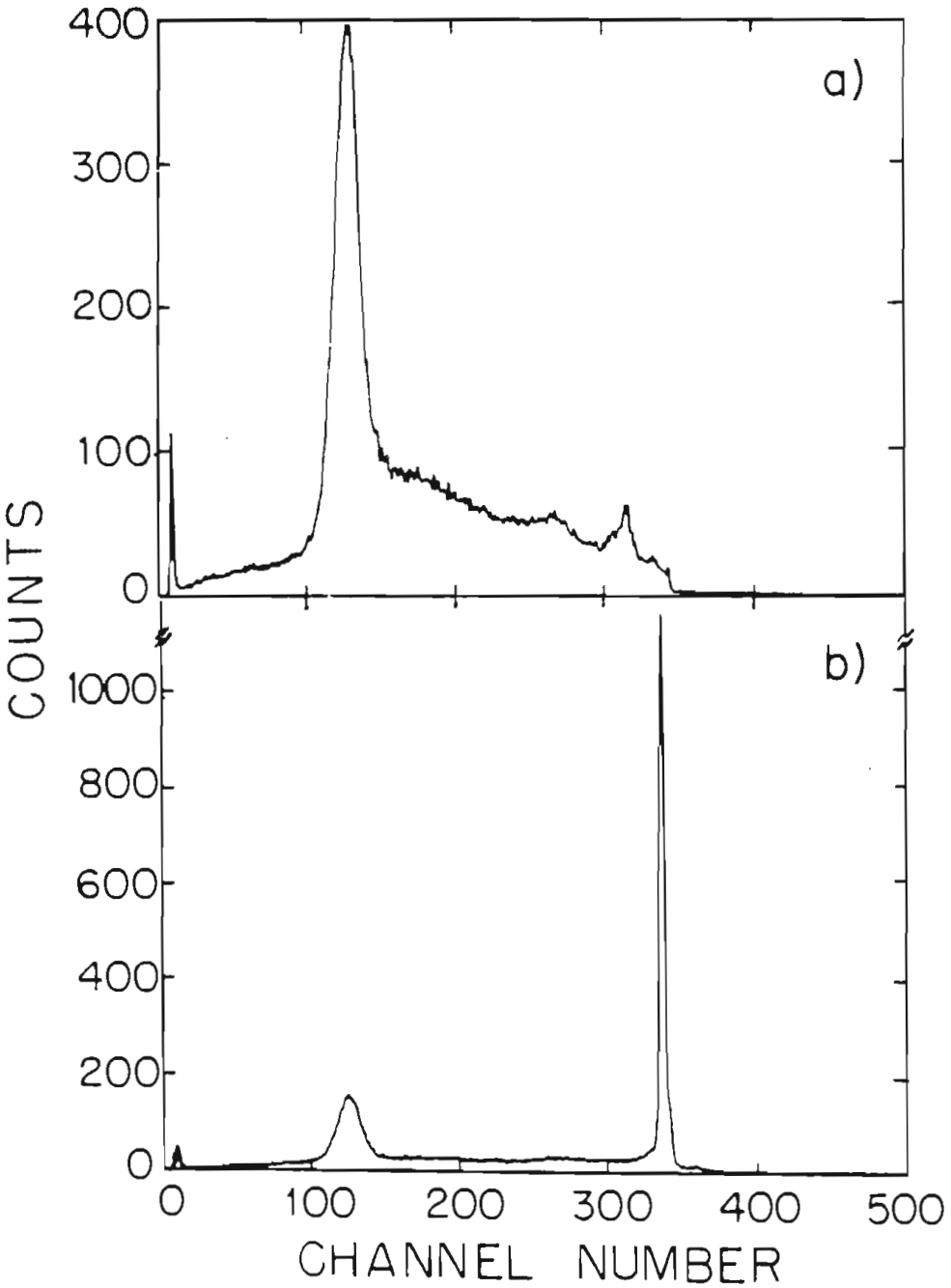

Figure 8-8 The 0° spectra taken with a 5-MeV proton beam.

a) Spectra taken with the SL3 slit mounted flush to the slit mount. The SL3 gap is not open to the incident beam which results in no unscattered peak.

b) Spectra taken with the SL3 slit tilted and no longer flush to the mount. Here the SL3 gap is open to the incident beam yielding a large unscattered peak.

resulting electrostatic steerer voltage spectrum for two cases. The upper spectrum, Fig. 8-9(b), shows the total voltage distribution obtained from all the events observed by the particle detector. The lower spectrum, Fig. 8-9(c), shows the distribution of voltages which results only from the particles in the high energy peak of the particle detector. This fact was determined by setting a gate around the high energy peak and then storing ramp voltages pertaining to events within that gate. The calibration of voltage spectrum channels to absolute energy (as described earlier in Section 8.2) yields an energy width for the peak of 450 eV, which is in good agreement with the value expected from measuring the narrow resonance. The measurement of the polarized beam resolution was made directly after measuring the narrow $^{50}Cr(p,p)^{50}Cr$ resonance. The distribution shown in Fig. 8-10 has a total width of 588 eV which is in excellent agreement with the value of 600 eV extracted from the resonance data.

Another interesting result from the measurements was the effect of line voltage shifts on beam energy. We know from monitoring the dual-90° analyzing magnet current that line-voltage changes produce shifts in the magnet current which the NMR gaussmeter does not correct. We have suspected that these shifts result in beam energy shifts. The energy distribution measured during one of these line voltage shifts is shown in Fig. 8-11. The two distinct peaks are separated by 870 eV. This indicates that the magnet currents should always be carefully monitored and recorded while taking energy excitation functions.

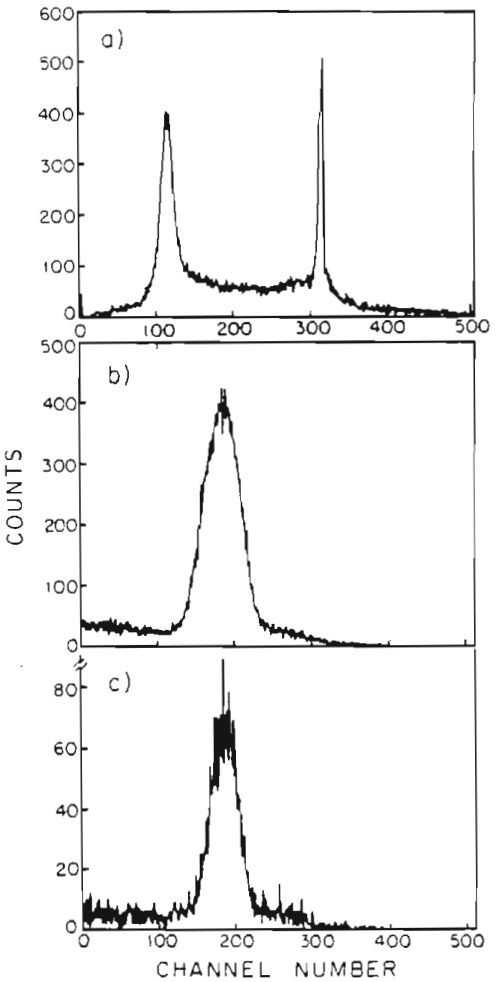

Figure 8-9 Beam energy spread measurement of a 5-MeV unpolarized proton beam.

a) 0° spectra showing the unscattered beam, which is the high energy peak, along with slit scattered beam.

b) Electrostatic sweeping voltage applied to ES1, gated by pulses from all the 0° detector pulses.

c) Beam energy spread represented by the intensity distribution obtained from the voltage applied to ES1, gated by pulses from only unscattered particles in the 0° detector. The FWHM of this distribution is 450 eV.

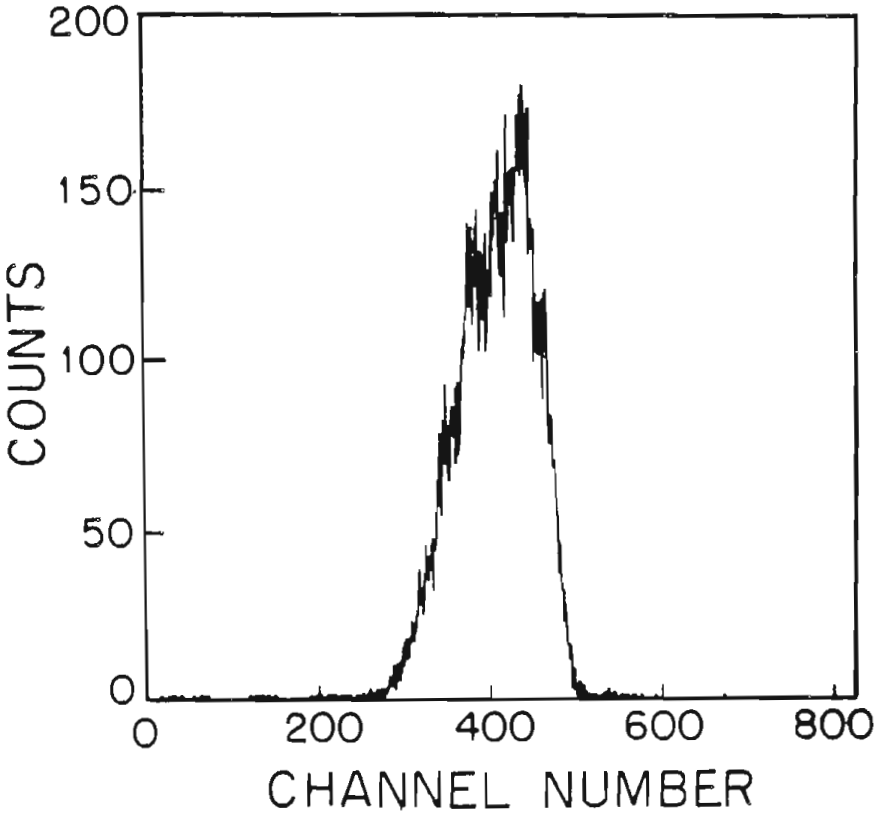

Figure 8-10 Polarized beam energy spread distribution taken for a 3.9 MeV incident beam and a 3.2 $\mu g/cm^2$ carbon stripping foil. The observed FWHM is 588 MeV.

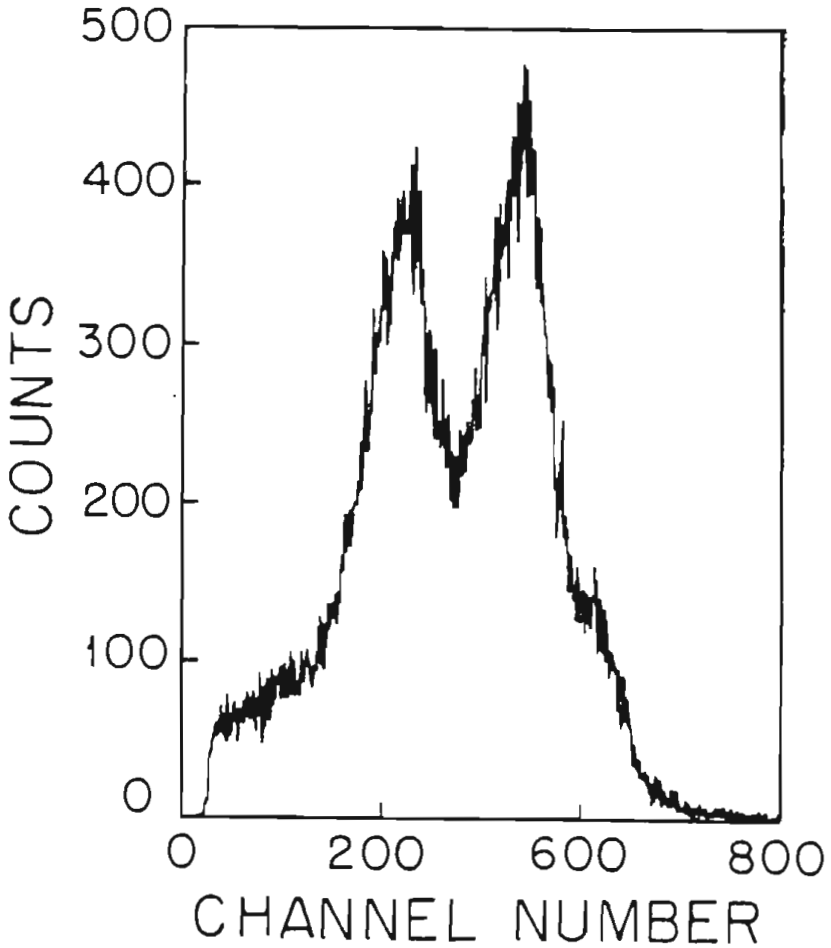

Figure 8-11 A double peaked beam energy spread distribution resulting from a line voltage shift and corresponding beam energy shift. The two distinct peaks are separated by 870 eV. The beam energy is 5 MeV.

8.7 Summary and Recommendations. A conceptually very simple direct measurement of the beam spread has been designed and implemented at TUNL. Measurements of the beam energy spread have been made with the system. They are in good agreement with the results obtained by measuring narrow resonances. The system as currently implemented will probably not be able to make routine measurements of the beam resolution before and after taking energy excitation functions. However, there are several improvements which should be made to the current system, and several other changes which might make routine measurements possible if this ability is required.

Many components in the original system were designed to be functional but not extremely complicated or difficult for the instrument shop to build. Even with this design, the current system required over three months of shop time. Now that the system has been shown to work the following improvements should be implemented: 1) The beam optics should be calculated for both polarized and unpolarized beams originating from the ion sources; the original calculations were based on parameters for unpolarized beams starting at the high-resolution system. 2) New sweeping magnets should be designed and built to cover all tandem energies after performing the total beam optics calculations. 3) Work should be done to improve the SL1, SL2, and SL3 slits and make the slits adjustable. This would be a challenging design project. 4) A NMR gaussmeter for the 70-70 magnet should be acquired and installed. 5) The entire machine and beam transport system alignment should be checked and fixed. Slight shifts and movements which do not affect

normal beam transport may be the cause of some of the steering problems. These improvements would make the measurements much easier and more reliable.

In order to make routine measurements with this measurement scheme, it may be necessary to redesign the SL1 and SL2 slits so that their gaps and their absolute positions can be adjusted externally. This is an extremely difficult design task. Also, a better and more automatic beam alignment system needs to be used. Finally, other possible resolution measurement systems, such as laser monitoring of the neutral beam [Tem81], should be considered if routine measurements are desired.

9. $(\vec{p},p)$ and (p,p) Investigations - Magnet Analyzing System Calibration

9.1 Introduction. An energy calibration of the Triangle Universities Nuclear Laboratory's dual-90° magnet momentum-analyzing system was performed for proton beams in the energy range from 1.88 to 14.23 MeV. The motivation behind the calibration was twofold: First, to facilitate searches for the narrow T=3/2 isospin-forbidden nuclear resonances; and secondly, to measure the energies of these T=3/2 states to an accuracy better than other methods. These methods of locating the T=3/2 states using isospin-allowed reactions, as discussed in Chapter 2, normally can assign energies with an accuracy between ±10 and ±50 keV. The original TUNL magnet system calibration [Pur71] was based on only one calibration point, and since the (p,p) resonances of interest occur at energies throughout the specified energy range, a new and complete calibration of the energy analyzing system was needed. Previous studies performed at TUNL measuring the first T=3/2 (p,p) resonances did not assign the resonance energies [Iko76].

Another goal of our measurements was to determine the reproducibility of the calibration values, in order to estimate the precision with which we can assign energies. After measuring several of the calibration reactions numerous times during different experimental runs performed over a period of about 1-1/2 years, we determined that the dual-90° magnet analyzing system allows reproducible measurement of

beam energies to a precision of ± 2 keV.

The magnet system calibration was performed using energy calibration points selected by the following criteria: (1) The energy must have been determined previously by absolute energy measurement techniques. (2) The energy must be within a range accessible with the TUNL F.N. tandem accelerator. (3) The measurement of the calibration point must be feasible with available detectors. A list of the calibration reactions used is given in Table 9-1. Originally, calibrant reactions spaced evenly over the tandem energy range were selected. However, when initial measurements showed that the magnet calibration constant changed with energy in the region of low magnetic fields, several additional reactions were measured at lower beam energies in order to determine this change more accurately. Absolute-energy (p,n) and (p,p) reactions and a non-absolute-energy (p,p) reaction were measured during several runs in order to determine the long term reproducibility of the magnet calibration.

A description of the magnet analyzing system will be presented, followed by the experimental measurement techniques used. Then the analysis and results of the calibration will be given, along with a brief discussion and summary.

9.2 Experimental Setup. The proton beam was obtained from the direct extraction ion source, DENIS I, and accelerated by the tandem accelerator before being momentum analyzed by the dual-90° magnet system shown in detail in Fig. 9-1. Following this momentum analyzing system, a switching magnet bent the beam 60° into the beam line where all energy

Table 9-1 Magnet Analyzing Calibration Reactions.

Reaction	Target	E ± ΔE (keV)	Measurement Method	Reference
$^{7}Li(p,n)^{7}Be$	Li	1880.41 ± 0.08	absolute	[Bar81]
$^{13}C(p,n)^{13}N$	^{13}C (99.99%)	3235.7 ± 0.07	absolute	[Mar66]
$^{19}F(p,n)^{19}Ne$	CaF_2	4234.3 ± 0.80	absolute	[Mar66]
$^{27}Al(p,n)^{27}Si$	Al	5803.3 ± 0.26	absolute	[Nay77]
$^{58}Ni(p,n)^{58}Cu$	^{58}Ni (99.76%)	9514.1 ± 2.70	absolute	[Fre76]
$^{16}O(p,p)^{16}O$	SiO	12707.7 ± 2.00	non-absolute	[Hin76]
$^{12}C(p,p)^{12}C$	C	14230.75 ± 0.20	absolute	[Hue74]

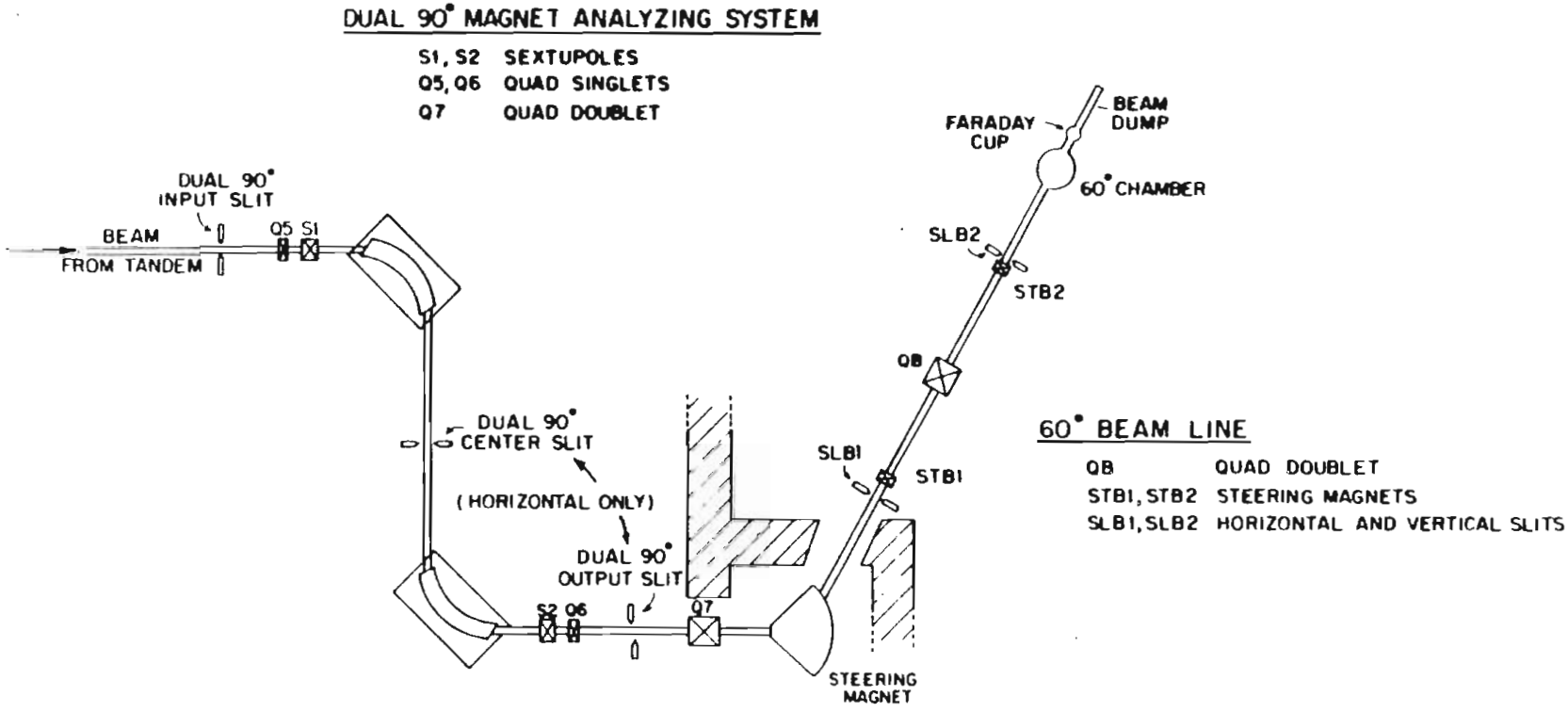

Figure 9-1 The TUNL dual-90° magnet analyzing system and experimental beam line.

calibration measurements were performed. The calibration reaction runs were made using the high-resolution operating mode described in Chapter 7. The dual-90° magnet momentum analyzing system consists of two almost identical 90° magnets powered in series from one supply. To compensate for slight differences in the magnets, the second magnet has an additional trim current power supply. The magnetic field is measured and controlled by a nuclear magnetic resonance (NMR) gaussmeter [VAR01] using a probe located in the pole gap of the first magnet. The relationship of measured NMR frequency to the energy of a particle passing through this bending magnet should be a constant, expressed as

$$K=(ME/Q^2 f^2)(1+E/(2Mc^2)) \qquad 9-1$$

where M is the mass of the particle in amu, E is the energy of the beam in keV, Q is the charge of the particle in units of e, f is the NMR frequency in MHz, and Mc^2 is the rest energy of the particle in keV.

9.3 Experimental Techniques. The measurement of the calibration (p,n) threshold or (p,p) resonance reactions required taking energy excitation functions over the energy region of interest. For an accurate and reproducible magnet calibration, it was necessary to develop and follow a consistent set of beam transport procedures and to monitor carefully all energy dependent machine parameters while acquiring the excitation function data.

9.3.1 Consistent Beam Transport Procedures. For each measurement several basic procedures were followed. First, the dual-90° magnet

analyzing system was recycled to eliminate hysteresis effects. This was accomplished by running the magnets at maximum current for two minutes, reducing the current to zero for two minutes, and then slowly raising the current to the proper magnetic field as determined by the NMR probe signal. If by mistake the desired magnetic field was exceeded, then the recycling procedure was repeated. Following the recycle, the magnet current was set to be adjusted automatically by the NMR magnetic field sampling device.

Several steps were consistently repeated in obtaining a tuned beam. The beam was stopped at the center of the dual-90^{o} magnet system after passing only through the first 90^{o} magnet while the machine energy was controlled using a signal from the generating voltmeter. Directly in front of this beam stop were 1 mm wide horizontal slits. The accelerated beam energy was adjusted to peak the beam passing through these slits on the beam stop. After two slit preamps became available, the energy regulation system was at this point switched to slit feedback using the center dual-90^{o} slits for control. Next the beam was allowed to pass through the second 90^{o} magnet where it was stopped at another beam stop following the 2 mm wide output slits. The beam was centered at these slits using the trim power supply connected to the second 90^{o} magnet coils. Only after these steps had been completed was the control of the machine energy switched from the generating voltmeter and capacitive plate pickup feedback to the output slit control feedback mode. The center slits were then opened to 5 mm to allow normal beam transport. The calibration threshold or resonance excitation function measurement was then begun, with care taken not to tune the beam transport

parameters located before the analyzing magnet system.

9.3.2 Monitoring Procedures. During the measurements the analyzing magnet current, the line voltage, and the overall machine and beam stability were monitored carefully. The magnet current was monitored using a sensitive differential voltmeter across the magnet power-supply shunt resistor. It was found that line voltage changes of 2 to 3% would cause magnet current shifts corresponding to 200-500 eV in beam energy. In an attempt to reduce these effects, we operated the NMR gaussmeter on a line-voltage regulator. There was potential for improvement since the magnet current was controlled by a correction signal from this gaussmeter. However, no improvement was seen. After extensive investigation we have concluded that the observed current shifts, although not within the specifications of the magnet power supply, could not be eliminated without major effort and/or expense. Thus when these fluctuations occurred, typically during times of power load changes (e.g. 6:30 - 8:30), they were documented for later analyses to determine possible effects on the energy excitation functions.

In addition to careful magnet current and line voltage monitoring, detailed logs were kept of the beam transport system operating parameters and vacua for each excitation function. Since several energy excitation passes were made for each calibration reaction, comparisons of these logs helped in evaluating the resulting set of threshold or resonance energies.

9.3.3 Data Acquisition Methods. Energy excitation functions were acquired using data acquisition codes which allowed automatic stepping

of the incident beam energy by changing the necessary beam transport power supplies and incrementing the NMR gaussmeter frequency via an external programmable frequency synthesizer [FLU02]. The ability to acquire the excitation functions automatically reduced the chance of error and also insured very consistent data acquisition procedures for the many separate energy passes.

Both (p,n) thresholds and (p,p) resonance measurements were required to provide sufficient calibration points over the energy range of the accelerator. This necessitated using several different data acquisition methods and particle detection techniques. The (p,p) resonance reactions used four solid-state detectors placed at various angles inside of the scattering chamber. Excitation functions were then taken in 250–1000 eV steps over the resonances. Beam current integration was obtained with a suppressed Faraday cup located behind the chamber.

For the (p,n) thresholds at energies below and including the $^{27}Al(p,n)^{27}Si$ threshold, a BF_3 long counter placed at 0^{o} was used to detect slow neutrons. The targets were mounted on a tantalum beam dump at the end of the experimental beam line with the detector located ~ 20 cm from the target. The energy excitation functions were started below the expected threshold and data were taken with energy step increments of 300–2000 eV. These excitation functions were continued until well above the threshold energy. The collimation of the beam in the beam line was adjusted to minimize neutron background. The beam current on a suppressed beam stop was integrated to obtain the beam incident charge for each data point.

For the $^{58}Ni(p,n)^{58}Cu$ threshold measurement the high neutron background made using the long counter not feasible. For this experiment a NE-102 plastic scintillator was placed 7.2 cm from the target, which was mounted in the center of the scattering chamber. This scintillator, which was at a lab angle of 60^{o}, was then used to detect β^{+} decay. The beam was mechanically chopped after the machine control slits and before the last switching magnet, allowing the target to be irradiated for a given number of incident particles. Then the β^{+} decay was detected for several half-lives while the beam was off. Chopping of the beam before the switching magnet eliminated most beam-related background counts in the scintillator. Beam integration was obtained using the suppressed Faraday cup located after the chamber. Energy excitation functions were again continued well above the threshold energy region. The program CHOPBS was written to automatically chop the beam and acquire data.

9.3.4 Target Preparation. The targets used for the calibration measurements were prepared or obtained by several methods. Both the natural carbon, ~ 10 $\mu g/cm^2$ thick, and the ^{13}C, ~ 300 $\mu g/cm^2$ thick, targets were obtained commercially, [ARI01] and [PEN01] respectively. The Al target was a 100 mg/cm^2 thick piece of aluminum metal. The lithium was prepared by rolling natural lithium to a ~ 150 mg/cm^2 thick target. The fluorine target was made by a vacuum evaporation of 450 $\mu g/cm^2$ of CaF_2 onto a 5 mil tantalum plate by using standard resistive heating techniques [Mug79] with a tantalum boat. The target was a 460 $\mu g/cm^2$ self-supporting 99.76% isotopically enriched ^{58}Ni foil mounted on a standard target ring. The ^{58}Ni was evaporated onto $BaCl_2$

coated glass slides, using an Al_2O_3 coated tungsten boat, by resistive heating techniques. The oxygen target was a ~ 10 $\mu g/cm^2$ thick SiO sample evaporated onto a carbon backing using an electron-gun vacuum evaporation technique with a tungsten crucible [Mug79].

9.4 Results of Calibration Measurements. Data were acquired during seven separate runs over a period of almost 1-1/2 years. Some absolute and secondary calibration reactions were measured during separate runs in order to estimate better the error from non-reproducibility of beam transport parameters. After discovering from initial measurements that the magnet calibration constant (K in Eq. 9-1) seemed to be changing at low magnetic fields, several additional low-energy calibration reactions were measured. Table 9-2 presents a summary of the results, including the number of passes made during each run, the average magnet calibration constant K for each reaction, and the energy reproducibility error. A representative sample of data for the different threshold excitation functions can be seen in Figs. 9-2 through 9-6.

9.4.1 Analysis of (p,n) Threshold Data. The (p,n) threshold reactions were analyzed using the thick-target relation for s-wave neutrons emerging just above threshold energy, where the energy integrated yield varies as the 3/2 power of E_n, the outgoing neutron energy [Mar66]. Thus, the basic analysis method was to fit the neutron yield below the threshold region with a linear least-squares fit to obtain the background neutron yield. Then this calculated background was subtracted from the original yield to obtain the true counts. The true

Table 9-2 Dual-90° Magnet Calibration Results.

Reaction	Number of runs	Time elapsed (years)	Number of passes	K ± ΔK ($k\ eV*amu/MHz^2$)	Energy reproducibility error for protons (eV)
$^{7}Li(p,n)^{7}Be$	1		4	26.716039 ± 0.0018	
$^{13}C(p,n)^{13}N$	1		2	26.723098 ± 0.0003	
$^{19}F(p,n)^{19}Ne$	2	0.2	7	26.732486 ± 0.0028	450.
$^{27}Al(p,n)^{27}Si$	1		3	26.738591 ± 0.0016	
$^{58}Ni(p,n)^{58}Cu$	1		3	26.742349 ± 0.0024	
$^{16}O(p,p)^{16}O$	4	0.6	7	* ± 0.0019	900.
$^{12}C(p,p)^{12}C$	3	1.2	5	26.74030 ± 0.0040	2100.

* $^{16}O(p,p)^{16}O$ reaction, a non-absolute energy reference, was used only in magnet reproducibility measurements.

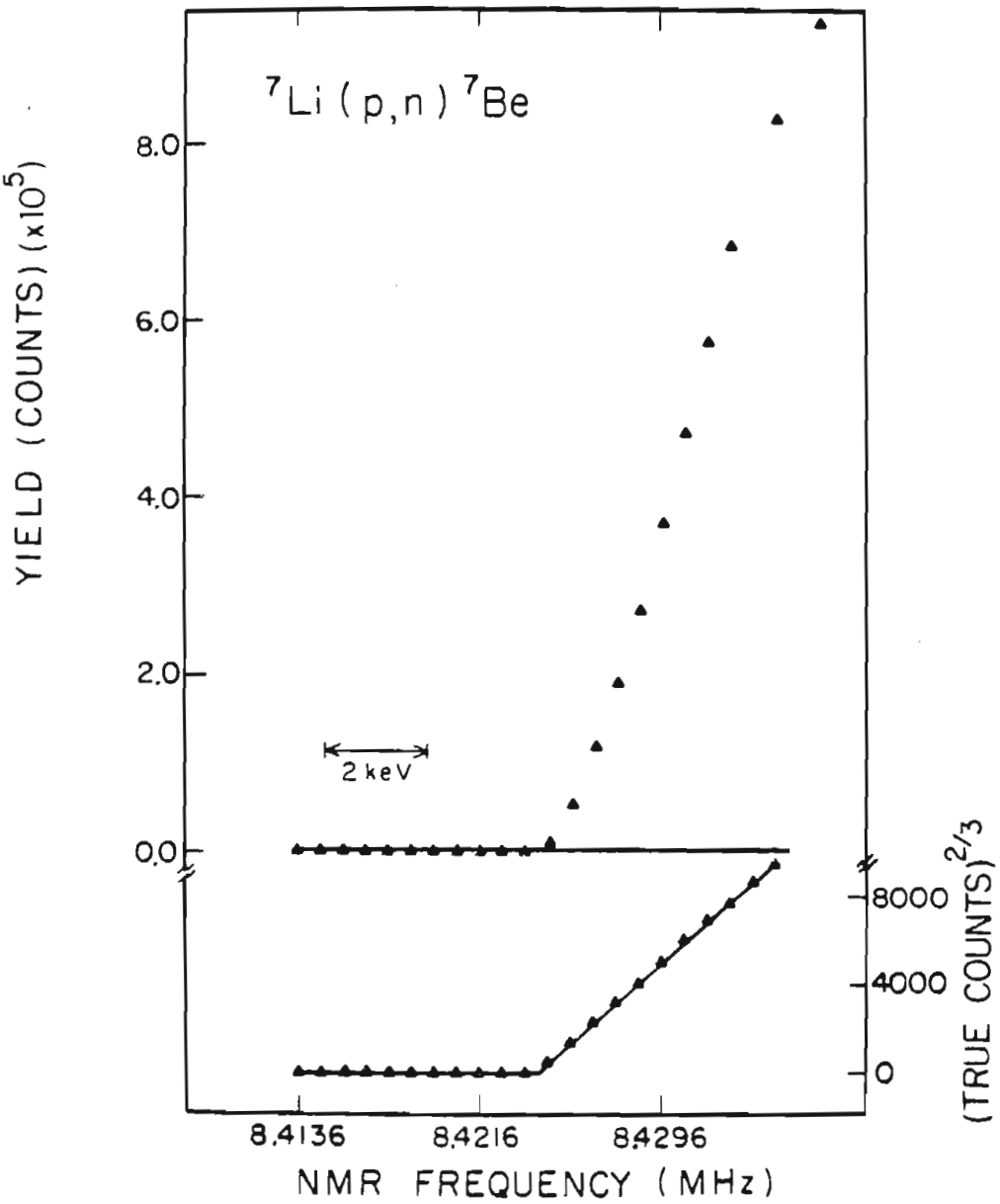

Figure 9-2 ^{7}Li(p,n)^{7}Be threshold excitation function. The neutron yield from the BF_3 counter is shown in the upper plot along with the calculated background obtained by fitting the data below threshold. The lower plot is the (true counts)$^{2/3}$ data with the best-fit shown. The energy steps are 445 eV.

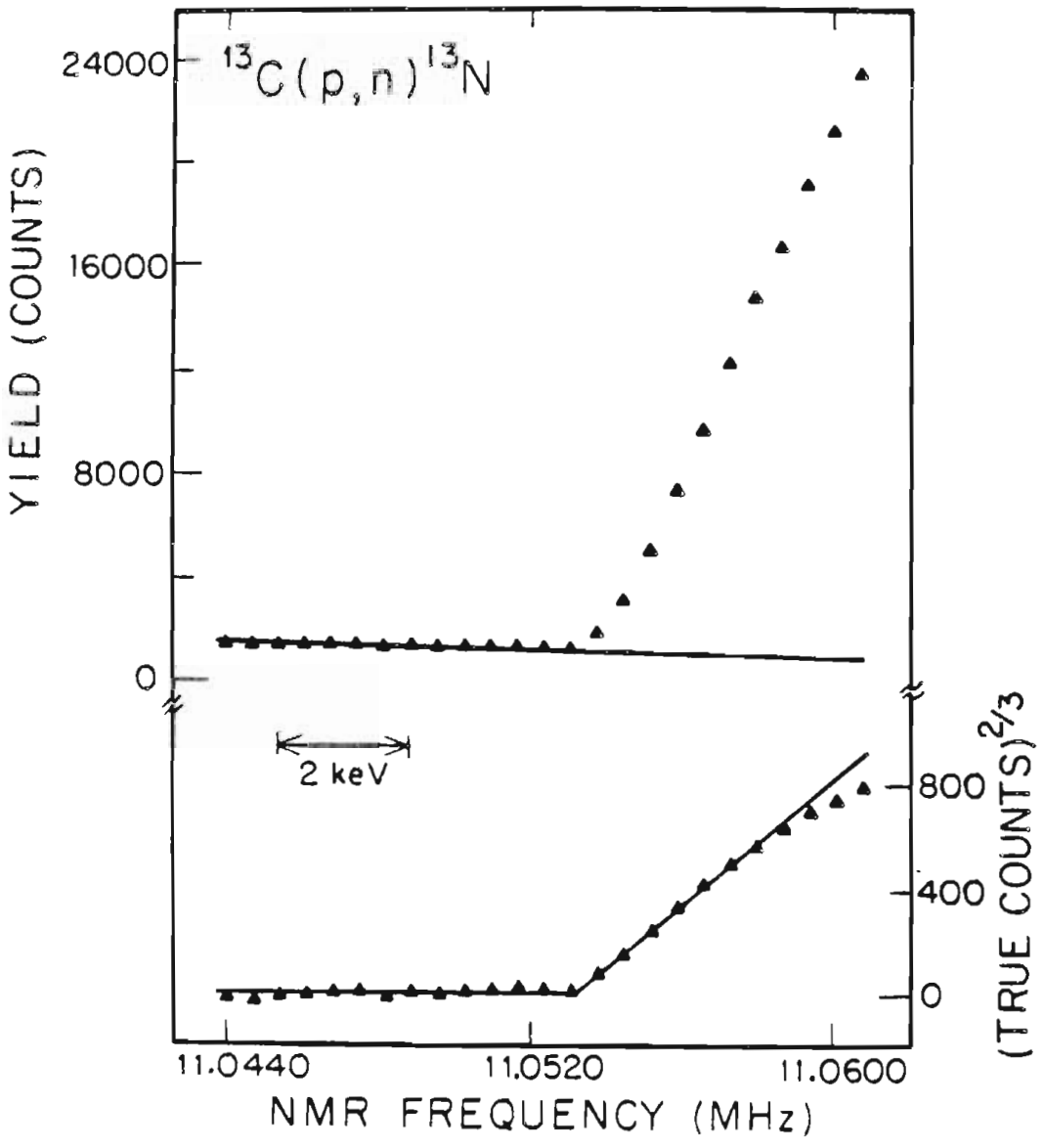

Figure 9-3 $^{13}C(p,n)^{13}N$ excitation function. The neutron yield and calculated (true counts)$^{2/3}$ are shown versus NMR frequency. Fits to the data are also indicated. The energy step size is 410 eV. See Section 9.4.1 of text for explanation.

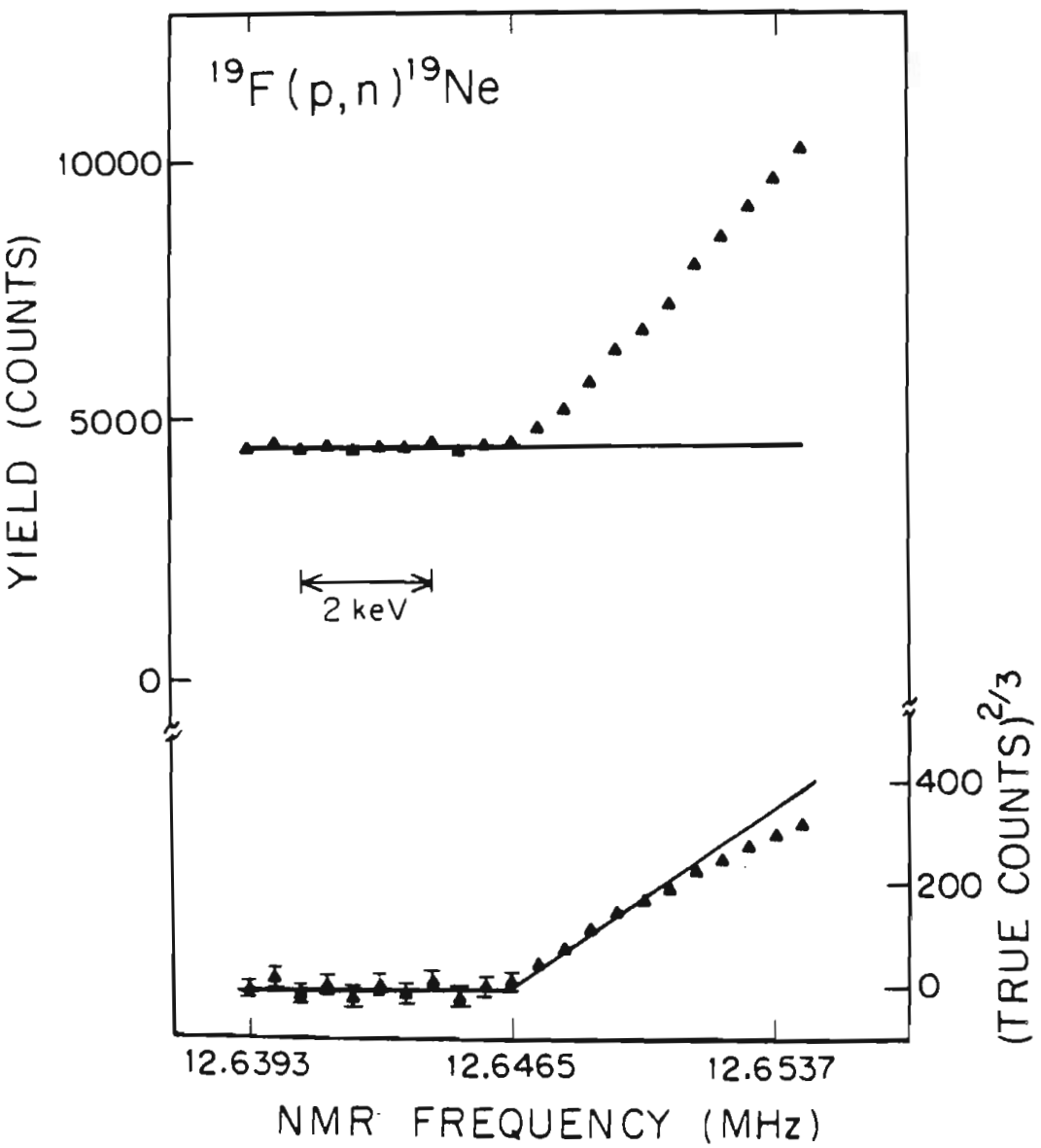

Figure 9-4 $^{19}F(p,n)^{19}Ne$ excitation function. The neutron yield and calculated (true counts)$^{2/3}$ are shown versus NMR frequency. The energy step size is 400 eV. See Section 9.4.1 of text for explanation.

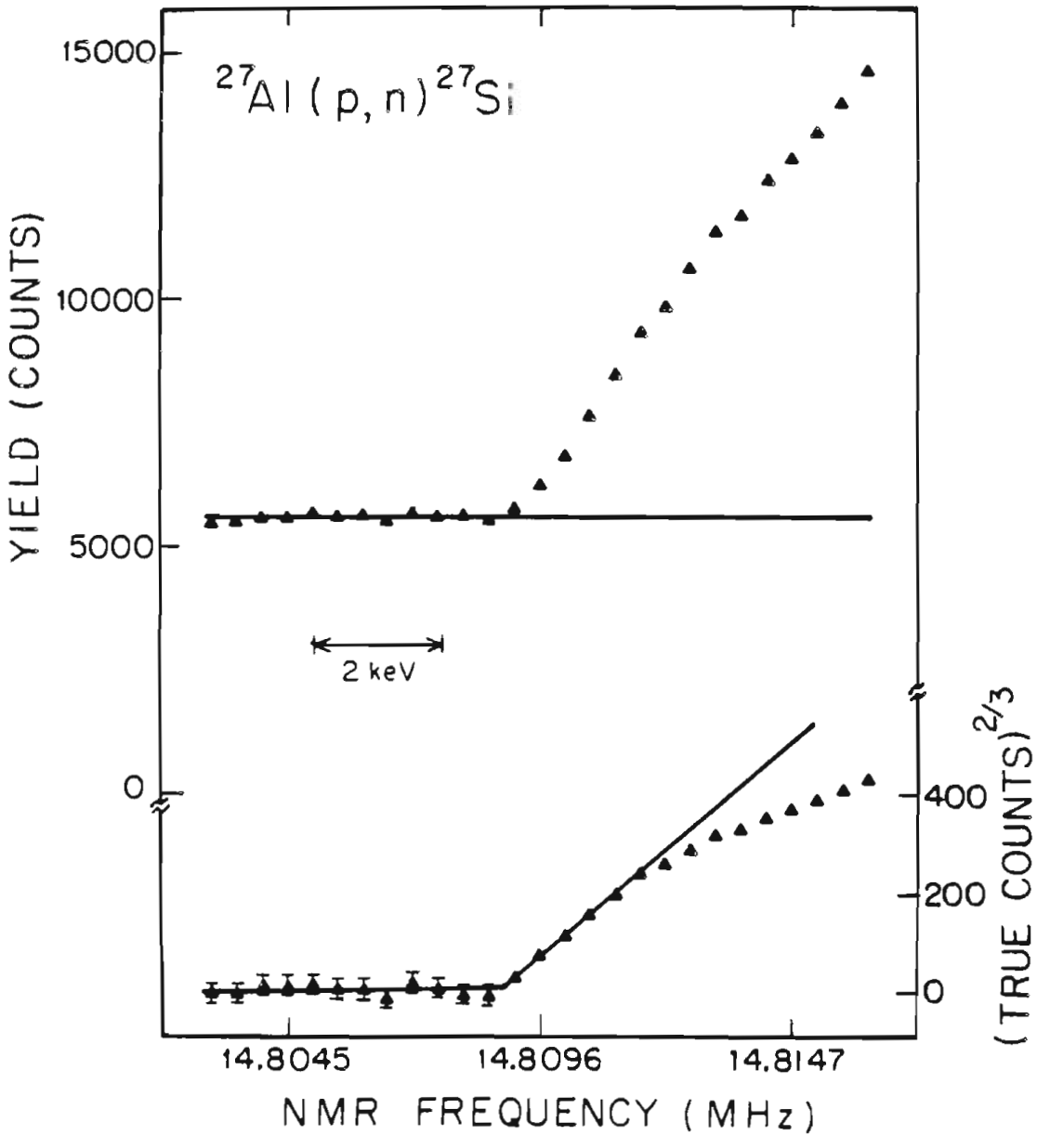

Figure 9-5 $^{27}Al(p,n)^{27}Si$ excitation function. Notice the divergence of the (true counts)$^{2/3}$ data from the calculated fit due to the increase of the outgoing neutron cone angle. The energy step size is 390 eV. See Section 9.4.1 of text for explanation.

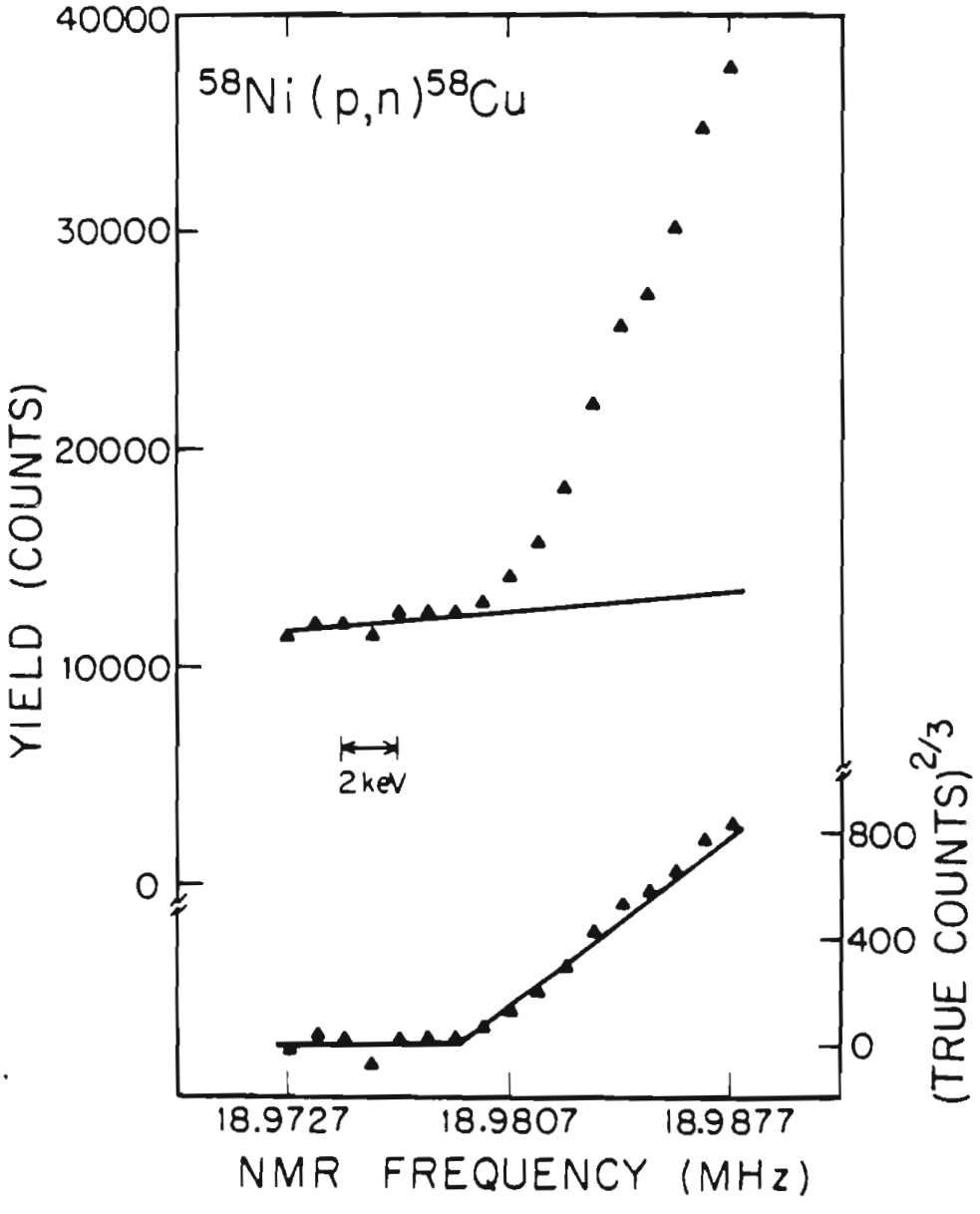

Figure 9-6 $^{58}Ni(p,n)^{58}Cu$ excitation function. The neutron yield from the scintillator is shown with calculated background obtained from fitting the data below threshold. The lower plot is the (true counts)$^{2/3}$ data with the best-fit shown. Unlike data from the BF_3 detector, these data do not have the divergence of (true counts)$^{2/3}$ from the calculated fit. The energy step size is 1000 eV.

counts were raised to the 2/3 power. For an accurate power-law relationship, this leaves a linear increase of (true counts)$^{2/3}$ versus E_n. These resulting data were then fitted by linear least-squares to obtain the zero intercept of the line and hence the threshold energy. Several background fits and (true counts)$^{2/3}$ fits were made for various choices of range of data in the excitation region in order to estimate possible errors caused by the analysis. Best-fits were determined by minimizing the chi-square value of the fit. The fits to the background and the (true counts)$^{2/3}$ data can be seen in Figs. 9-2 through 9-6. The program THRESH was written on the VAX 11/780 using the above analysis method to interactively analyze all (p,n) threshold data.

It was discovered for many of the (p,n) passes that the expected 3/2 power-law relationship of neutron yield to outgoing neutron energy did not hold. Here the theoretical fit diverged upward from the data at higher neutron energies. This effect can result when the solid angle subtended by the long counter does not include the entire neutron cone, where the cone angle opens with increasing neutron energy. Calculations for this solid angle indicated that the detector should have subtended the entire neutron cone for energies < 20 keV above threshold for all of the calibration reactions.

The effective detector solid angle was investigated by locating the detector at different distances from the target while comparing the rate of divergence of the fit to the (true counts)$^{2/3}$ as a function of position. These tests indicated that the detector did not perform as a perfect long counter, but in fact lost counting efficiency much sooner

than expected - a few keV above threshold. The effect of moving the detector position can be seen in Fig. 9-7. The data taken with the long counter were still usable because the excitation function step sizes were generally small, less than 1 keV, and the fitting program and resulting chi-square values were very sensitive to the exact E_n value at which the power-law no longer held. Hence, excitation function data of energy above this point were not included in our determination of the zero intercept and the neutron threshold. This effect is clear in the plots of (true counts)$^{2/3}$ vs NMR frequency, as shown in Figs. 9-3 through 9-5 for data taken with the BF_3 detector. Here the excitation functions always have fewer counts than the calculated fits at higher excitation energies. Notice that as the target mass increases, the divergence of (true counts)$^{2/3}$ from the calculated values also increases as expected from the kinematic relationship of reaction product masses to the outgoing neutron cone size. It should be pointed out that the divergence of the data from the true power law will also be observed if the targets used are too thin. This occurs when the incident beam energy minus the threshold energy is greater than the energy loss in the target. However, the calibration targets used for the (p,n) threshold reactions were always greater than 25 keV thick.

9.4.2 The (p,p) Resonance Analysis. Our absolute $^{12}C(p,p)^{12}C$ resonance calibration value was based on the Munich absolute energy assignment [Hue74] where the calibration energy was determined by taking the apparent resonance center for data at $\theta_{lab} = 160^{\circ}$. Although this provides an absolute energy calibration point, this is not necessarily the actual resonance energy.

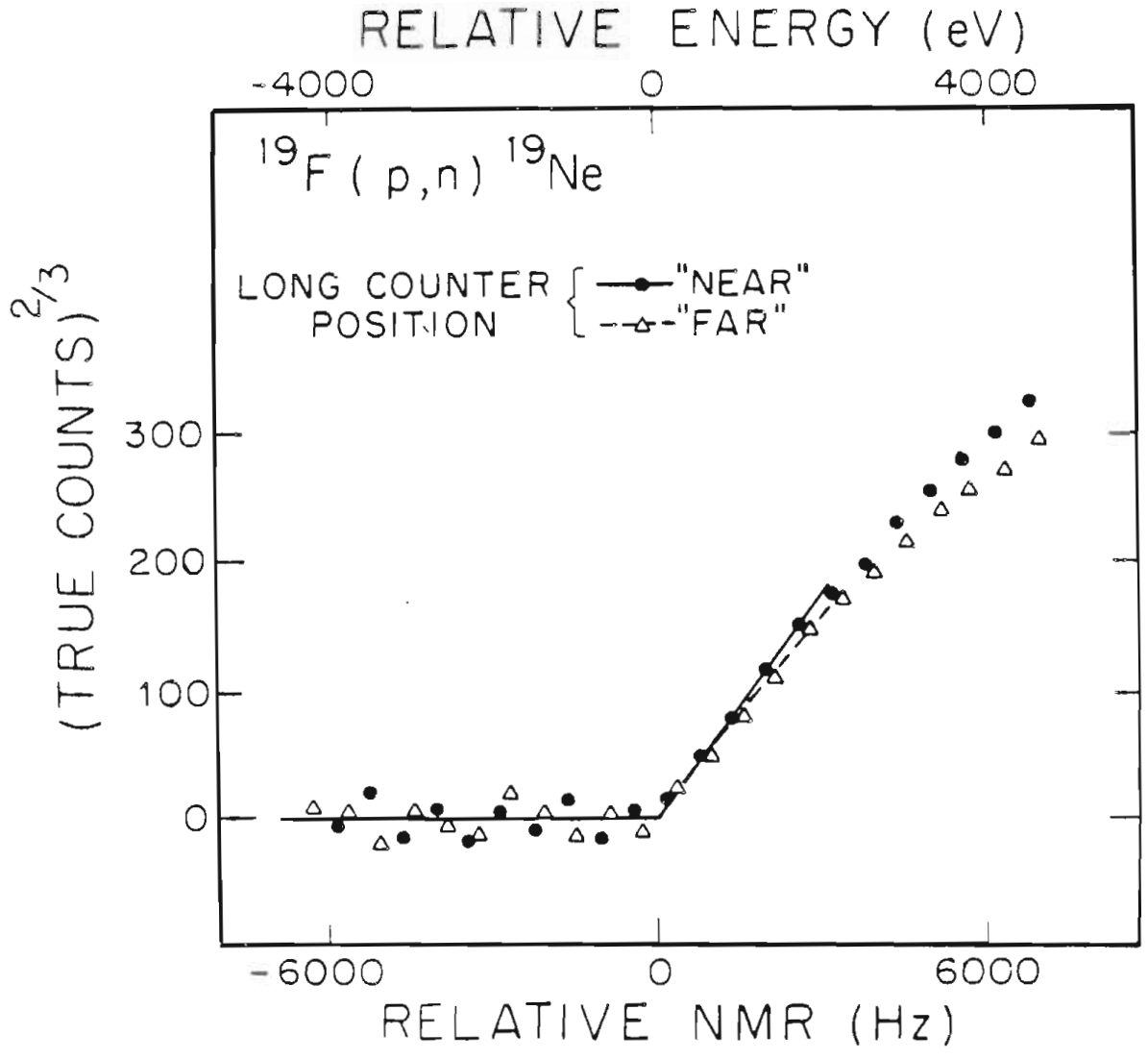

Figure 9-7 $^{19}F(p,n)^{19}Ne$ excitation functions $(true\ counts)^{2/3}$ data with the best-fits shown for two different detector positions. The data from the "far" position exhibits faster divergence from the expected linear dependence than the "near" position data.

For our $^{12}C(p,p)^{12}C$ excitation functions acquired with a detector at $\theta_{lab} = 162^{\circ}$, the calibration energy was determined by assuming a linear energy relationship from the maximum to the minimum in the excitation function yield and then using a linear interpolation to determine the midpoint. Thin targets of 5-10 $\mu g/cm^2$ thickness were used in the (p,p) resonance work to insure the necessary good resolution. A representative $^{12}C(p,p)^{12}C$ excitation function is shown in Fig. 9-8.

9.4.3 Error Estimation. There are three principal factors which can contribute to possible error in our measurement of the different magnet calibration reactions: statistical errors, fitting errors, and reproducibility from pass to pass and experimental run to run. The statistical error was negligible in determining the threshold or resonance energy in all cases. The error in fitting the background counts and determining the true counts was also found to be unimportant. However, in determining the threshold energies from the fits there is a possibility of systematic errors. To study this error, the data were fitted using various combinations of the data points in the linear region above threshold, excluding only a few points at threshold. In all cases the threshold value corresponding to the lowest chi-square was used. The total deviation of this value from that with the greatest chi-square was always less than 200 eV. Furthermore, a grid-search method was employed to change systematically the linear least-square parameters while observing the resulting chi-square and energy threshold value, thereby estimating the sensitivity of the threshold energy to the chi-square value. This provided another demonstration that systematic

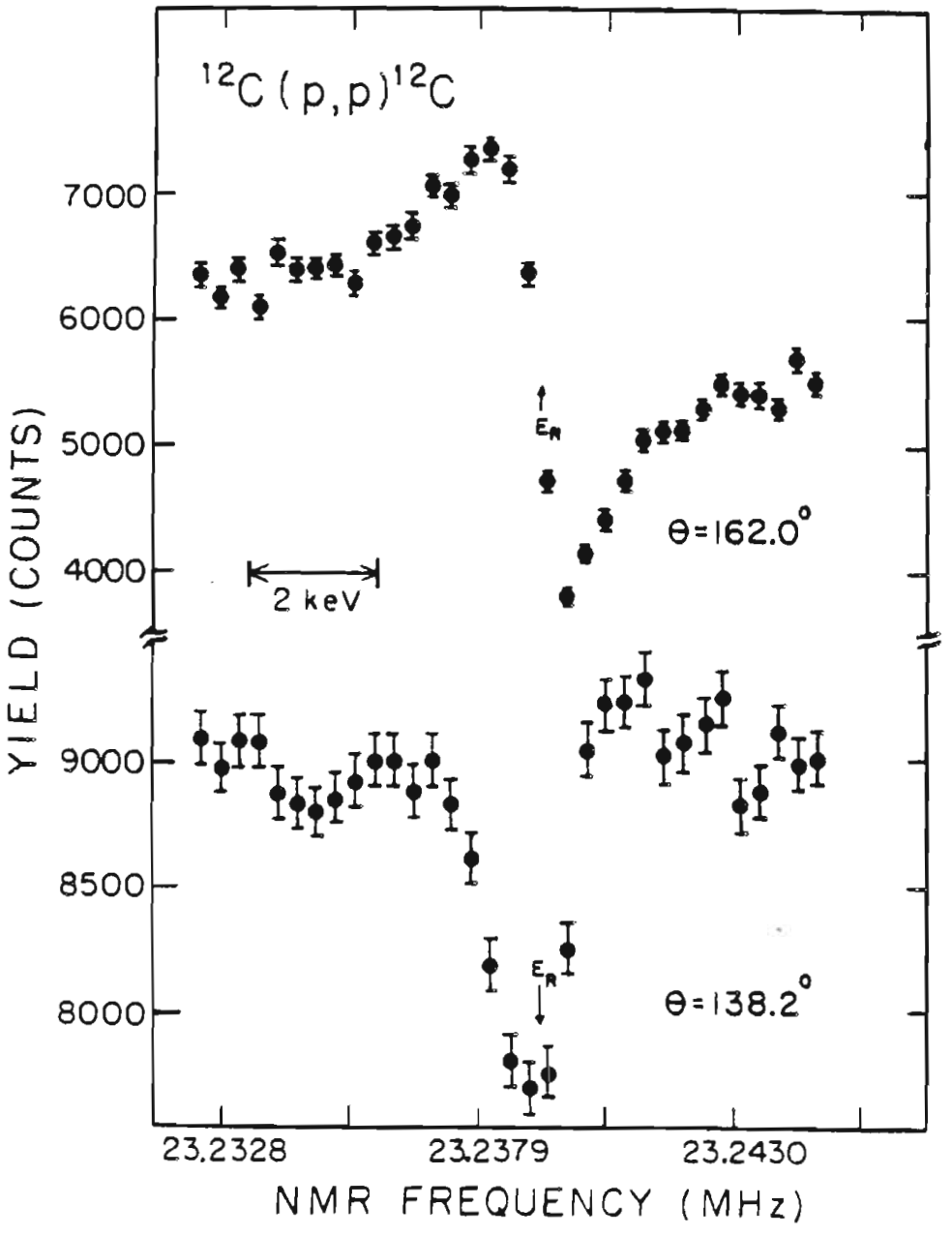

Figure 9-8 $^{12}C(p,p)^{12}C$ excitation function. The excitation functions for two solid state detectors at lab angles of 162° and 138° are shown. The calibration energy is indicated by the arrows. The energy step size is 300 eV.

errors were negligible.

The limiting error of the magnet calibration is in fact the reproducibility error resulting from variations in threshold or resonance energies extracted from separate excitation passes. For each calibration reaction, several passes were always made (see Table 9-2). However, for a true estimate of the reproducibility error we scheduled several experimental runs over a fairly long time period and measured some of the same reactions on separate runs. This was done for three different reactions: $^{19}F(p,n)^{19}Ne$ and $^{12}C(p,p)^{12}C$ reactions which provide absolute energy values, and the $^{16}O(p,p)^{16}O$ second T=3/2 resonance reaction where the resonance energy has not been absolutely determined. The reproducibility errors for these three reactions, expressed in equivalent proton energy, are presented in Table 9-2. It was found that a proper magnet recycle, as outlined earlier, was critical to obtaining consistently reproducible results. The results of these measurements show that the magnet calibration, with proper recycle and beam tuning, is precise to $\pm$ 2 keV.

9.4.4 Magnet Analysis System Calibration. The results from the calibration reactions showed that the magnet calibration "constant", K, was in fact not constant with beam energy. Thus, the calibration reaction data were divided into two regions, one for the constant region and one for the non-constant region.

A fit in the non-constant region was obtained by including the $^{7}Li(p,n)^{7}Be$, $^{13}C(p,n)^{13}N$, and $^{19}F(p,n)^{19}Ne$ calibration points in a linear least-squares fit of calculated K versus NMR frequency. These

data were weighted by adding in quadrature the error of the absolute calibration energy from the literature with our error from the measurement, always taken as the 2 keV reproducibility error.

For the constant region the weighted mean K-values from the $^{27}Al(p,n)^{27}Si$, $^{58}Ni(p,n)^{58}Cu$, and $^{12}C(p,p)^{12}C$ reactions were used, with their weighted error being determined the same way as in the non-constant region. The transition from the non-constant to the constant region was simply taken at their intercept. The calibration data and fit are displayed in Fig. 9-9. The previous magnet calibration [Pur71], based on only the carbon resonance, is also shown. Also plotted are two dashed lines which represent the change in K for a ± 2 keV shift in the measured energy relative to the measured frequency. Clearly the estimation of a 2 keV reproducibility error is generous in the lower energy region.

The origin of the non-linearity of the magnet analyzing system is not understood. However, a similar effect has been observed in the analyzing systems of several other laboratories [Ove69, Dav69].

9.5 Discussion and Summary. The calibration of the TUNL dual-90° magnet analyzing system was completed for proton beam energies spanning the energy range 1.9 to 14.2 MeV. Both threshold and resonance absolute reactions, coupled with various nuclear measurement techniques, yielded a new calibration of the magnet analyzing system with a minimum of systematic errors. The careful studies of possible errors, involving the repetition of these measurements over a period of 1-1/2 years, allowed a determination of the analyzing system's long-term energy

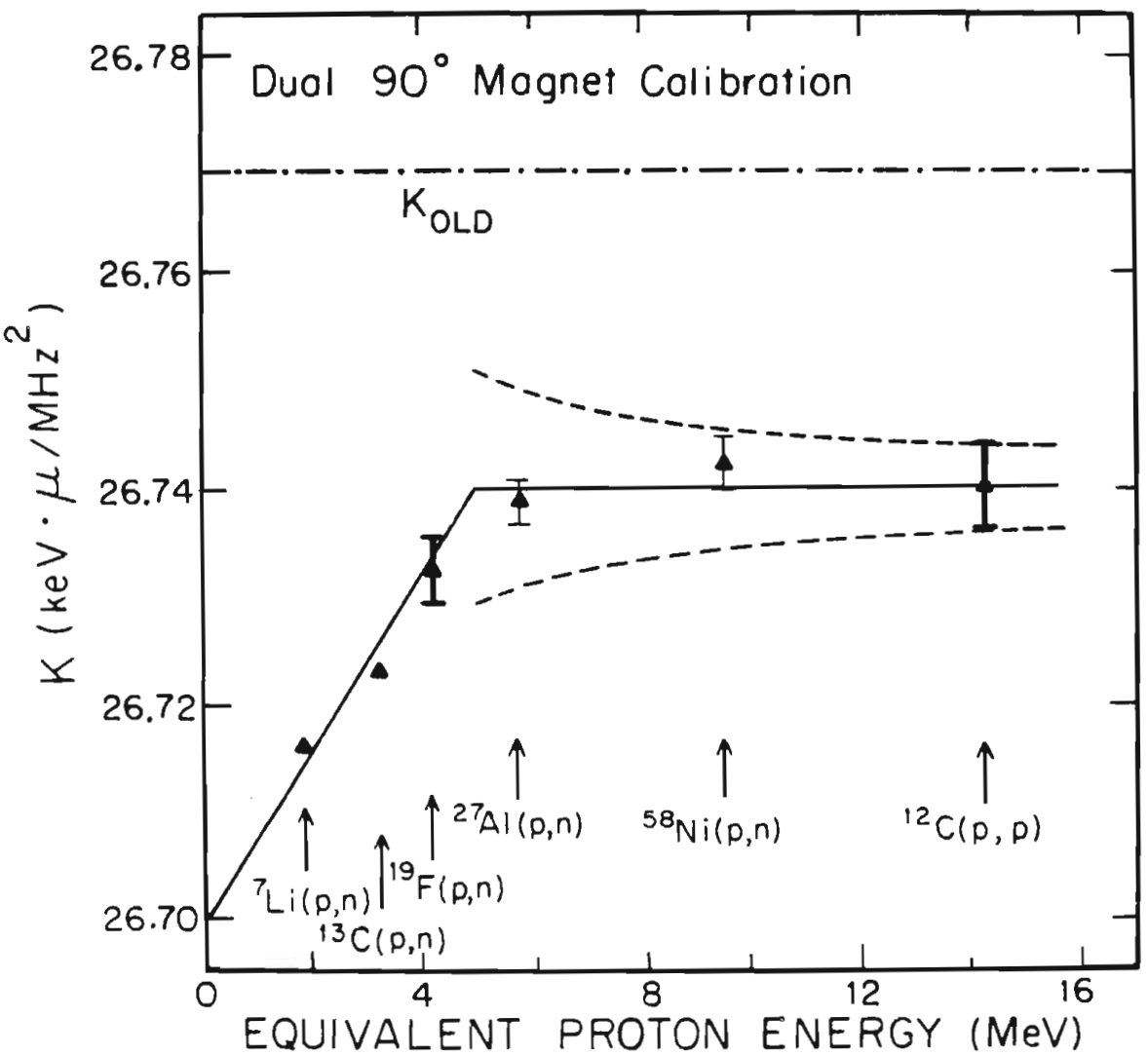

Figure 9-9 Magnet calibration constant K versus equivalent proton energy for the magnet analyzing system. The solid line is the new fit to the calibration data. The previous calibration [Pur71] is the dash-dot line. The error bars for $^{12}C(p,p)^{12}C$ and $^{19}F(p,n)^{19}Ne$ are measurements of the long-term reproducibility error between different accelerator runs. The dashed lines represent the effect of a 2 keV error in the measured energy on the calibration constant K, which shows the calibration accurate to pm2sp(1)keV. Note the suppressed zero for K.

reproducibility. Thus, we were able to use the calibration results to facilitate the searches for the narrow (p,p) resonances and to assign energies reliably to the corresponding states. We feel that we can now confidently assign the resonance energies of these states to $\pm$ 2 keV.

10. $(\vec{p},p)$ and (p,p) Investigations - Experiments

10.1 Introduction. Polarized and unpolarized high-resolution beam excitation function data were taken using the TUNL high-resolution system described in Chapter 7 and the 60^{o} beam line and chamber. The polarization data were acquired during runs spanning a two-year period. However, most of the same procedures were followed and similar conditions existed for all of these runs. This chapter will present a summary of the procedures used to prepare the targets for the high resolution (p,p) experiments. Also, the the beam line setup, chamber setup, general run procedures, and the data acquisition codes will be discussed. Emphasis will be given to some of the special procedures required for taking polarized high-resolution data.

10.2 Targets and Target Preparation. The UNC target making facilities were used for making the high-resolution targets. The targets were made to an optimum thickness as determined by two competing factors, count rate and straggling in the target. For the best possible experimental resolution one would like targets made as thin as possible in order to minimize straggling of the incident protons (see Chapter 6). However, for counting purposes the targets should be thick enough so that sufficient counting statistics (1-3%) can be acquired in a reasonable amount of time. This count rate factor is more important for taking polarized data than unpolarized data because there is an order of

magnitude less polarized beam intensity. For most of the isospin-forbidden resonances, the energy excitation functions were first taken with very thin targets using unpolarized beam. Based on the width and the cross section of the resonance, an optimum target thickness was selected for making the polarized beam measurements. High-resolution polarized or unpolarized beam excitation functions required targets that were too thin to be self-supporting. As a result, all targets were evaporated onto carbon backings ~ 3-10 $\mu g/cm^2$ thick. These backings were mounted on the target rings prior to being used in an evaporation.

Several general target making procedures were always followed. The evaporations were monitored using a vibrating crystal deposition meter [SL001] which indicated the rate and amount of evaporation. The absolute thickness values produced using the vibrating crystal technique were not always accurate for evaporations of the thin 2-12 $\mu g/cm^2$ targets. However, the relative precision of the vibrating crystal from evaporation to evaporation was found to be excellent. For many of the experiments the initial targets were evaporated to a thickness indicated by the vibrating crystal. The evaporator was then left set up and ready for more evaporations. If the thicknesses of the initial targets were not correct, new targets could be evaporated to given thicknesses relative to the original batch.

The evaporated material was usually only a few hundred atom layers thick, which required taking precautions before, during, and after the evaporation. The carbon foils mounted on the target rings were never left in the evaporator without liquid nitrogen cooling of the diffusion

pump cold trap. This prevented buildup of diffusion pump oil or byproducts on surfaces within the system. The desiccators were roughed down to forepump vacuum using pumps equipped with molecular sieves. Finally, both the top and bottom carbon foil surfaces were shielded until the actual evaporation had started. This prevented outgassed material from depositing on the foils.

After completing an evaporation, the evaporator bell-jar was brought up to atmospheric pressure with a dry N_2, He, or Ar gas, depending on the evaporated material. The target rings were immediately transferred to a desiccator and pumped down to vacuum. One advantage to keeping the targets under vacuum is that the foils can be transported with less chance of breakage. The foils and backings are so thin that they can break from casual air movement. Another reason for keeping the foils under vacuum is to limit possible absorption of material by the target. Such absorption can degrade the resolution of the spectra and introduce contaminant peaks. It was apparent that targets not kept under vacuum had poorer resolution. This was especially true of hygroscopic and oxidizing targets.

One important consideration when using the high-resolution targets was the target age and treatment. Old targets which had been subjected to beam bombardment for a long length of time usually had degraded resolution. This is due to the buildup of pump oil, pump oil byproducts, and vacuum sealing greases. The buildup of material and degrading of the resolution were directly dependent on the length of time the target had been used, the amount of beam that had bombarded the target, and the

general vacuum conditions during the bombardment. Care was taken to have as good a vacuum as possible. A liquid nitrogen cold trap was installed and used in the beam line to stop any backstreaming of material from any pumps located before the beam line. There was no cold trap on the chamber turbopump. The data-taking procedure was to use new targets whenever possible, especially when measuring a very narrow resonance.

The methods used to prepare the C, ^{24}Mg, SiO, Sb_2S_3, and Ar targets will now be discussed. Several different methods were tested in making Mg, SiO, and Sb_2S_3 targets. However, only a summary of the most successful method for each target will be presented.

The carbon foils used in measuring the ^{13}N isospin-forbidden resonance and as backings for all other targets were commercially obtained [ARI01] amorphous carbon foils, which have a graphite crystalline structure. The thickness of these foils was determined by optical methods to an accuracy of 10 % [ARI01].

The ^{24}Mg targets were prepared by resistive heating vacuum evaporation of 99.96 % isotopically enriched ^{24}MgO powder obtained from Oak Ridge National Laboratory, Isotope Sales Division [OAK01]. The MgO was reduced to Mg during the evaporation by mixing a 1:6 ratio of the MgO with zirconium powder [Tak66]. This mixture was then placed in a closed tantalum boat and, to produce good thermal contact, wet with ethanol. Once under vacuum, the boat was heated to reduce the MgO while leaving the target rings shielded. After the reduction process was complete, the Mg evaporation was started. Although a few uniform thickness 2-15 $\mu g/cm^2$ ^{24}Mg targets were obtained, consistent results

from evaporation to evaporation were never obtained. Various techniques such as different base vacuum pressures (10^{-4}–10^{-7} Torr) and different substrate temperatures were tried. In many of the evaporations there would be a layer of Mg powder settled onto the surfaces. Also, sometimes the Mg would stick to one target foil and not to those surrounding it. Once the Mg started sticking, it would continue to do so. The conclusion based on these tests and others [Fau82, Wes77] is that the Mg does not consistently stick to the carbon foil substrate, especially when making very thin foils. One solution to this problem would be either to evaporate the Mg onto a different backing, such as a higher-A metal foil, or to evaporate a very thin 5–15 atom layer of Au or some other metal onto the carbon substrate before the Mg evaporation. These techniques might work because the Mg seemed to adhere very well to metal surfaces. Another possible method would be to use a glow discharge to clean the carbon foils [Hol61] before evaporating the Mg. Preliminary work [Nel82] indicates that this may yield consistent Mg evaporations.

The ^{16}O and ^{28}Si experiments used SiO targets. The most reliable and consistent method to prepare the targets was by vacuum evaporation of natural SiO using an electron-gun technique [Mug79] with a tungsten crucible. Targets of 2–50 $\mu g/cm^2$ were evaporated under a typical vacuum of 10^{-6}–10^{-7} Torr. The electron-gun evaporation produces targets of SiO, whereas the resistive heating evaporation produces composite targets of SiO, SiO_2, and Si_2O_3 with a composition dependent upon the base vacuum [Cac71]. The SiO targets prepared by the electron-gun method were found to have almost no water absorption, while the targets prepared by resistive heating were hygroscopic [Cac71]. The electron-gun

evaporations allowed routine SiO target production with excellent results. The resolution of these electron-gun prepared targets was better and did not seem to degrade as quickly as the targets made by resistive heating.

The ^{32}S targets were prepared using natural Sb_2S_3 powder. The compound was selected based on its stability under proton beam bombardment and the simplicity of the target preparation. Tests with CdS and AgS compounds were also performed, but the Sb_2S_3 was found to be the best under our circumstances. The vacuum evaporation was performed using resistive heating and a closed tantalum boat. Reliable and uniform targets 3-50 $\mu g/cm^2$ thick were prepared in a routine fashion using this method.

The ^{36}Ar targets were prepared using ion-implantation of ^{36}Ar ions into a carbon foil backing [Bur81]. These foils were prepared at a commercial facility [SPI01]. It was hoped that targets of 1-3 $\mu g/cm^2$ thickness of ^{36}Ar could be made with an implant energy of 5-10 keV. These thicknesses are below the saturation limits imposed by the implant energy. The low energy of the ^{36}Ar ions would have minimized the depth of the ^{36}Ar distribution in the host carbon foil and also minimized the straggling. Unfortunately, the ^{36}Ar was implanted at both 10 keV and 50 keV, yielding targets which produced much worse resolution than desired. In addition, the double injection energy resulted in a very complicated double peaked ^{36}Ar distribution in the carbon foil. The resulting targets were found to have 1.5-2.1 $\mu g/cm^2$ of ^{36}Ar implanted into a maximum depth of 13 $\mu g/cm^2$ (660 $\AA$ in the 91 $\mu g/cm^2$ carbon backing

foil.

The thicknesses of the Mg, SiO, Sb_2S_3, and Ar foils were determined by Rutherford scattering of 1.3822 MeV protons. These measurements were made using the TUNL K.N. Van de Graaff accelerator, with four detectors set to lab angles of 90^o, 105^o, 135^o, and 160^o. Either the foil used in taking the resonance excitation function data was measured, or a foil was measured that had been directly cross-calibrated to the foil used in the excitation measurement. These thicknesses were then used to calculate the absolute cross sections for the energy excitation measurements. These cross sections were in good agreement with the available published results. The ^{36}Ar thickness was also checked by normalizing the results of an optical model calculation [Tho81] to forward angle data taken at 3.28 MeV.

10.3 Beamline and Chamber Setup and Geometry. All polarized and unpolarized beam excitation functions were measured in the 60^o scattering chamber. The high-resolution beam was obtained as explained in Chapters 7 and 9. The beam line transport components are shown in Fig. 10-1.

During unpolarized beam measurements the beam was kept centered on the target by using feedback information from the SLB2 slits and a special split Faraday cup located behind the chamber. The slit-difference signals from the left-right and up-down SLB2 slits were used as feedback to the first magnetic steerer STB1. A split Faraday cup with four isolated triangular leaves was built to integrate the current and to produce left-right and up-down feedback to the steering magnet

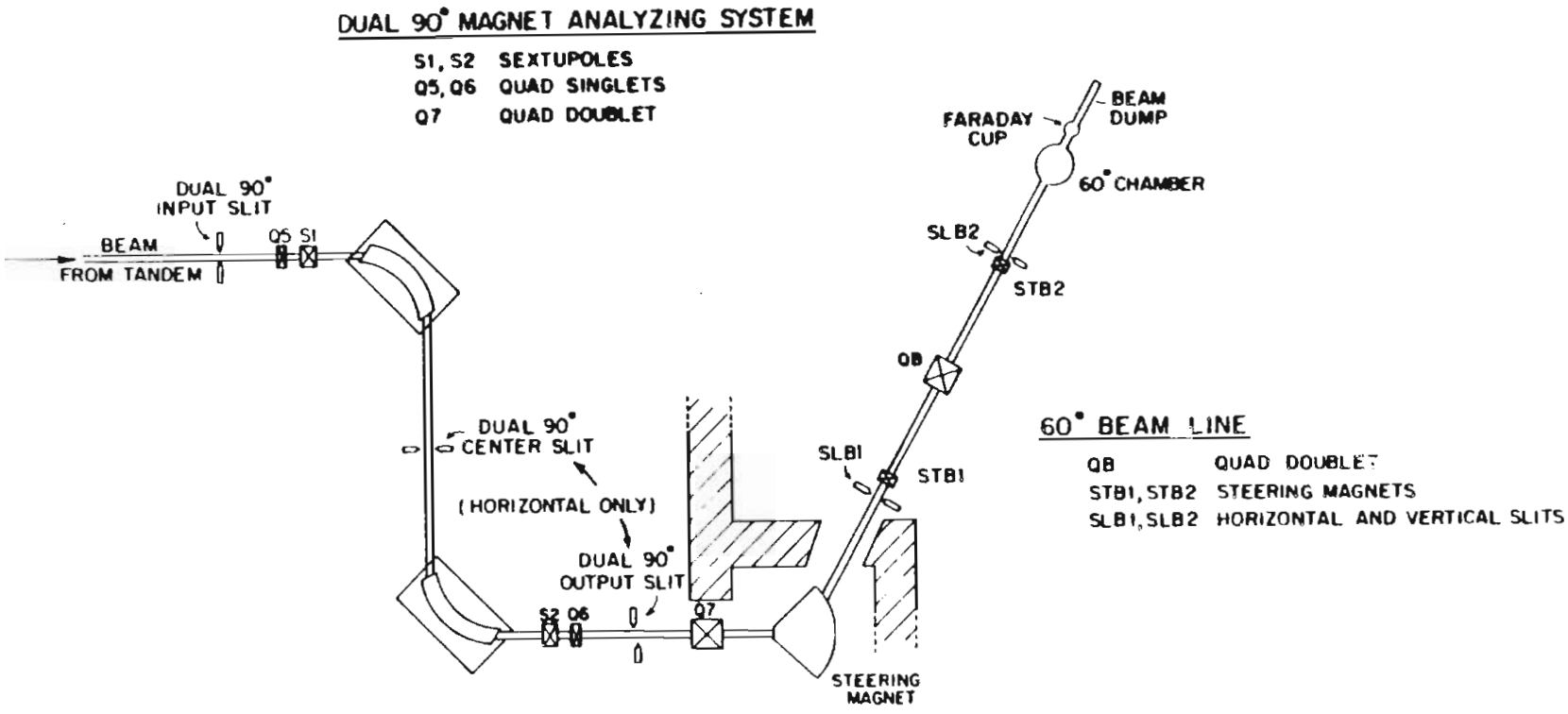

Figure 10-1 The 60^{o} experimental beam line and TUNL dual-90^{o} magnet analyzing system.

STB2 located right after the SLB2 slits. The location of the steering magnet STB2 directly after the first set of feedback slits SLB2 minimized any cross talk between feedback channels. The two feedback systems kept the beam fixed on the same flight path. This eliminated beam wander on the target and the corresponding problems of yield changes due to target thickness nonuniformity. The polarized beam measurements used a proton polarization monitor in place of the split Faraday cup. During these measurements the chamber snout slits located just inside the chamber were used as feedback to the second steering magnet STB2.

In the unpolarized experiments the beam current was integrated by summing the currents from the individual split Faraday cup leaves. A special current-to-voltage summing amplifier was built both to extract feedback information for the steering magnets and to sum the currents from the four leaves. This circuit was based on an earlier one of similar design explained in [Ton80]. Electron suppression of the split Faraday cup was accomplished using a ~ 10 cm long cylindrical suppressor located in front of the cup biased from -50 to -75 volts.

Most of the polarized beam excitation function data were taken using a $^4He(\vec{p},p)^4He$ proton polarization monitor [Har72]. The beam polarization was extracted from the monitor using measured $^4He(\vec{p},p)^4He$ analyzing powers [Sch71]. Several polarization measurements relied on the quench ratio method [Onl71] to determine the beam polarization. Because the polarization monitor was used in place of the split Faraday cup, the total beam current was integrated from the electrically

isolated monitor. The electron suppression of the monitor was accomplished using a -45 Volt battery attached in series to the monitor. From use of the split Faraday cup or the polarization monitor, an absolute error in current integration of $\leq$ 10% resulted.

The unpolarized beam experiments used four to six detectors set to angles determined by the ℓ-value of the resonance being studied. The polarized beam measurements used four sets of left-right detector pairs. In general, one pair of detectors was set to the maximum backward angle of detectors in the chamber which is 163°. The other three pairs were set to angles determined by the ℓ-value of the resonance and the chamber geometry. The chamber, detector holders, and target rod geometries would not allow acquisition of both 90° data and data at three other detector angles. Thus, no polarization data were taken at 90°.

Because of the counting rate problems associated with using thin targets and polarized beams, 150 mm^2 solid state detectors were purchased. These detectors allowed an increase of the total solid angle without a significant increase of angular acceptance. Detectors were placed 4.0-5.0 inches from the target rod with 0.125" collimator widths and 0.500" collimator heights. This yielded solid angles of 5.0-7.4 msr and angular acceptances of $\pm$ 0.9° in the θ-scattering plane and $\pm$ 3.6° in the ϕ-scattering plane. For measurements below 9 MeV, 500 micron thick solid state detectors were used. For measurements above 9 MeV, 1000-2000 micron detectors were used.

10.4 Measurement Procedures. Before taking final excitation function data, the dual-90° magnet system was properly recycled and the

beam tuned as explained in Chapter 9. This was done to allow the extraction of accurate resonance energies. The magnet monitoring procedures discussed in Chapter 9 were also followed while taking the energy excitation functions.

Special machine logs and run summary logs were developed to keep track of the large number of excitation functions measured and the number of important machine-resolution parameters which needed to be monitored. Information was recorded on these sheets during and after each excitation function measurement. They were an enormous help in knowing the machine and experimental conditions during later analysis. Examples of these log sheets are shown in Figs. 10-2 and 10-3.

The polarized beam data were acquired by taking both spin-up and spin-down data for each excitation function point. In conjunction with the use of left-right detector pairs this data-taking sequence provides analyzing power data without first-order spin misalignment and current integration errors.

10.5 Data Acquisition. Data were acquired for each detector using standard nuclear charged-particle counting electronics consisting of a preamplifier, spectroscopy amplifier, and a linear gated stretcher triggered by an overlap coincidence module. The overlap coincidence unit was triggered by a single channel analyzer (SCA) used to discriminate out low-voltage signals. There was an additional SCA which could be used as an anti-coincidence input to discriminate out the strong carbon ground-state peak from the backing foil [Iko75].

Figure 10-2 High-Resolution Machine Log Sheet.

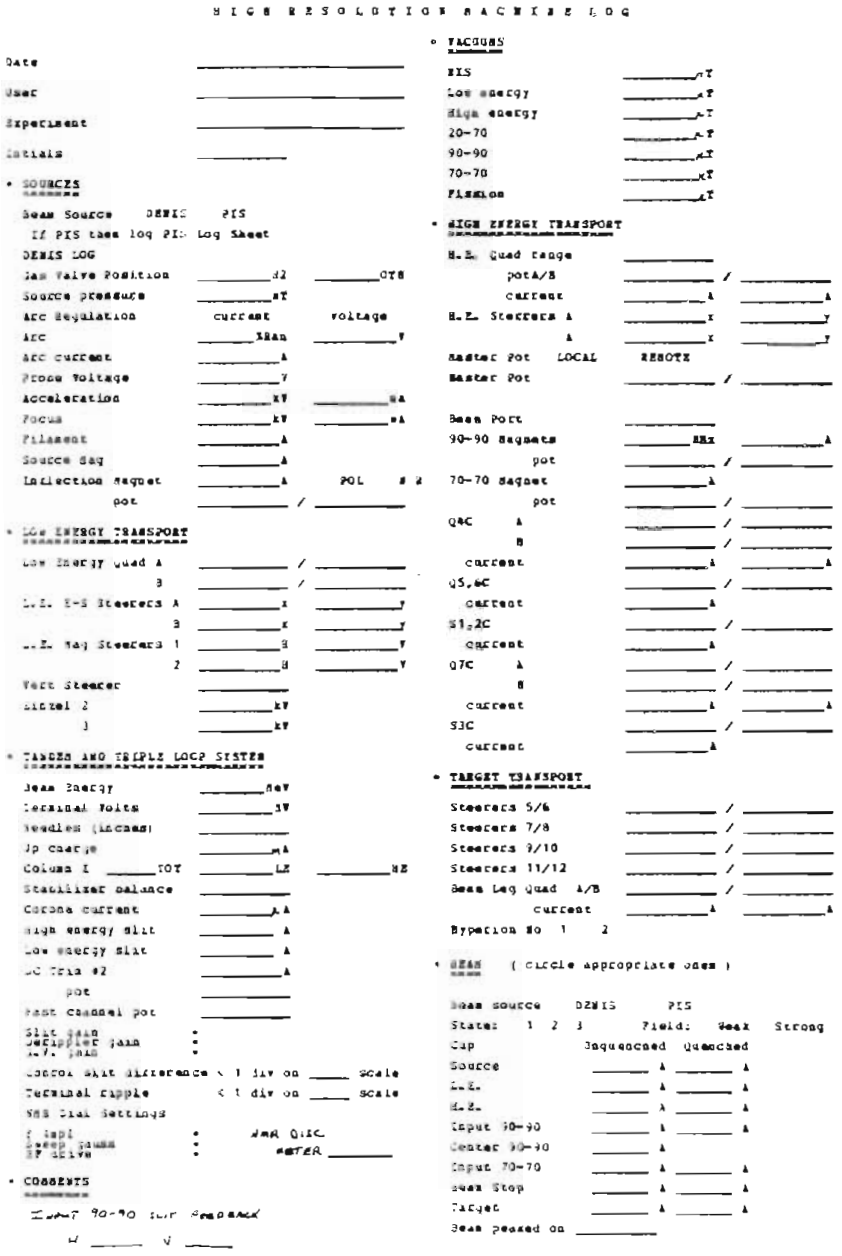

HIGH RESOLUTION MACHINE LOG

Date _____

User _____

Experiment _____

Initials _____

• SOURCES

Beam Source DENIS PIS

If PIS then log PIS Log Sheet

DENIS LOG

Gas Valve Position _____ #2 _____ OTS

Source pressure _____ mT

Arc Regulation current voltage

Arc _____ XRay _____ V

Arc current _____ A

Probe Voltage _____ V

Acceleration _____ kV _____ uA

Focus _____ kV _____ uA

Filament _____ A

Source Sag _____ A

Inflection Magnet _____ A POL # 2

pot _____ / _____

• LOW ENERGY TRANSPORT

Low Energy Quad A _____ / _____

B _____ / _____

L.E. X-Y Steerers A _____ x _____ y

B _____ x _____ y

L.E. Mag Steerers 1 _____ x _____ y

2 _____ x _____ y

Vert Steerer _____

Einzel 2 _____ kV

3 _____ kV

• TANDEM AND TRIPLE LOOP SYSTEM

Beam Energy _____ MeV

Terminal Volts _____ kV

Needles (inches) _____

Gp Charge _____ uA

Column I _____ TOT _____ LE _____ HE

Stabilizer Balance _____

Corona Current _____ uA

High energy slit _____

Low energy slit _____

LC Trim #2 _____ A

pot _____

Post Channel Pot _____

Slit Jaws

Switching Jaws

A.V. Jaws

Source Slit Difference < 1 div on _____ Scale

Terminal Ripple < 1 div on _____ Scale

SNS Dial Settings

f Appl

Sweep Gauss

RF Drive

NMR Qtrc

METER _____

• COMMENTS

Insert 90-90 slit Readback

H _____ V _____

• VACUUMS

PIS _____ mT

Low energy _____ uT

High energy _____ uT

20-70 _____ uT

90-90 _____ uT

70-70 _____ uT

Fission _____ uT

• HIGH ENERGY TRANSPORT

H.E. Quad range _____

pot A/B _____ / _____

current _____ A _____ A

H.E. Steerers A _____ x _____ y

A _____ x _____ y

Master Pot LOCAL REMOTE

Master Pot _____ / _____

Beam Port _____

90-90 Magnets _____ kHz _____ A

pot _____ / _____

70-70 Magnet _____ A

pot _____ / _____

Q4C A _____ / _____

B _____ / _____

current _____ A _____ A

Q5,6C _____ / _____

current _____ A

S1,2C _____ / _____

current _____ A

Q7C A _____ / _____

B _____ / _____

current _____ A _____ A

S3C _____ / _____

current _____ A

• TARGET TRANSPORT

Steerers 5/6 _____ / _____

Steerers 7/8 _____ / _____

Steerers 9/10 _____ / _____

Steerers 11/12 _____ / _____

Beam Leg Quad A/B _____ / _____

current _____ A _____ A

Bypation No 1 2

• BEAM (circle appropriate ones)

Beam Source DENIS PIS

State: 1 2 3 Field: Weak Strong

Cup Unquenched Quenched

Source _____ A _____ A

L.E. _____ A _____ A

H.E. _____ A _____ A

Input 90-90 _____ A _____ A

Center 90-90 _____ A

Input 70-70 _____ A _____ A

Beam Stop _____ A _____ A

Target _____ A _____ A

Beam peaked on _____

Figure 10-3 High-Resolution Excitation Function Summary Log Sheet.

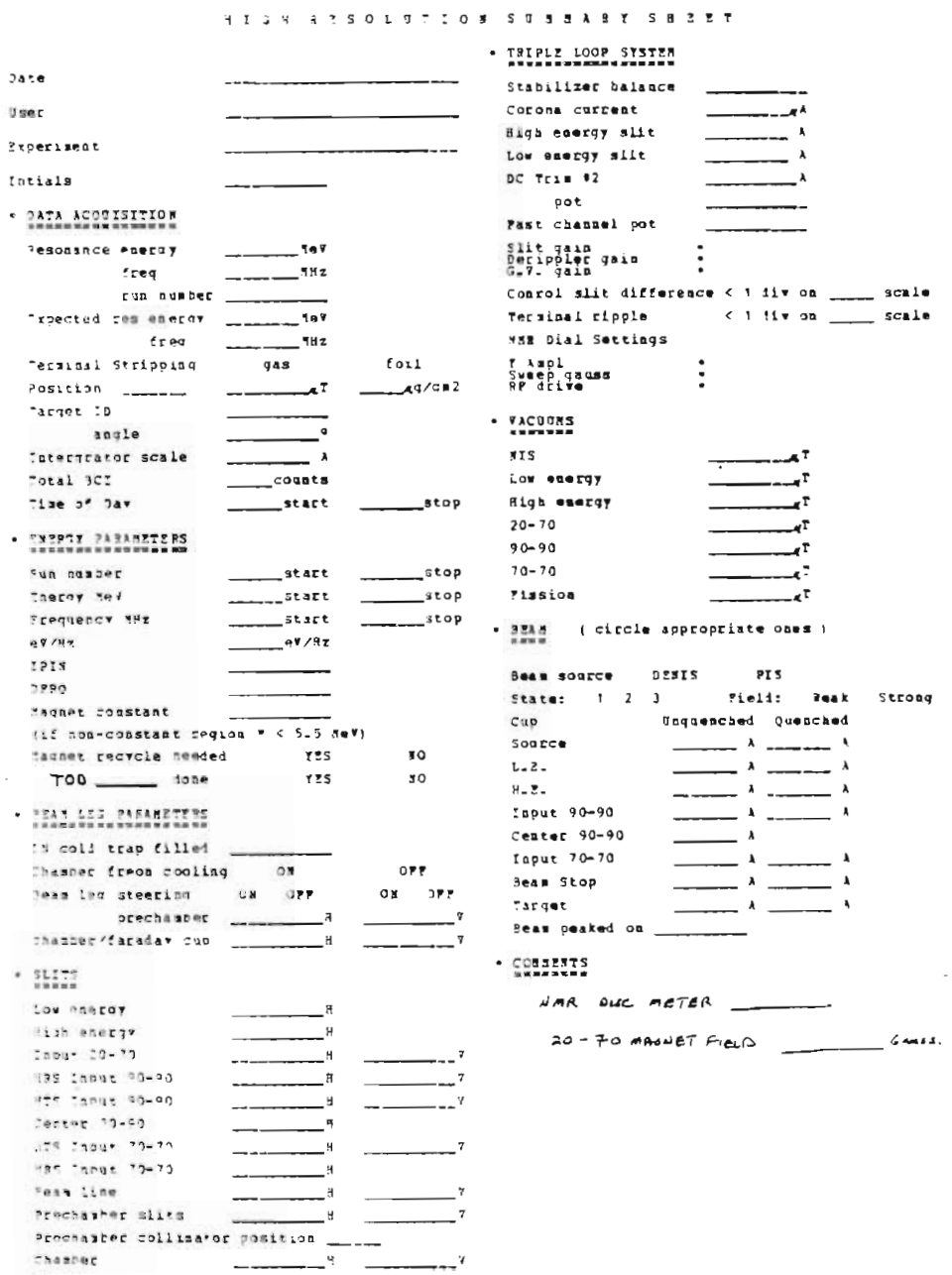

HIGH RESOLUTION SUMMARY SHEET

Date _____

User _____

Experiment _____

Initials _____

• DATA ACQUISITION

Resonance energy _____keV
freq _____MHz
run number _____
Expected res energy _____keV
freq _____MHz
Terminal Stripping gas foil
Position _____ _____T _____ug/cm2
Target ID _____
angle _____°
Integrator scale _____ A
Total BCI _____counts
Time of Day _____start _____stop

• ENERGY PARAMETERS

Run number _____start _____stop
Energy keV _____start _____stop
Frequency MHz _____start _____stop
eV/Hz _____eV/Hz
IPIN _____
DPPO _____
Magnet constant _____
(if non-constant region * < 5.5 keV)
Magnet recycle needed YES NO
TOO _____ done YES NO

• BEAM LEG PARAMETERS

LN coil trap filled _____
Chamber freon cooling ON OFF
Beam leg steering ON OFF ON OFF
prechamber _____H _____V
Chamber/faraday cup _____H _____V

• SLITS

Low energy _____H
High energy _____H
Input 20-70 _____H _____V
HES Input 90-90 _____H _____V
HES Input 90-90 _____H _____V
Center 90-90 _____H
HES Input 70-70 _____H _____V
HES Input 70-70 _____H
Beam line _____H _____V
Prechamber slits _____H _____V
Prechamber collimator position _____
Chamber _____H _____V

• TRIPLE LOOP SYSTEM

Stabilizer balance _____
Corona current _____uA
High energy slit _____ A
Low energy slit _____ A
DC Trim #2 _____A
pot _____
Fast channel pot _____
Slit gain :
Decippler gain :
G.V. gain :
Control slit difference < 1 div on _____ scale
Terminal ripple < 1 div on _____ scale
NMR Dial Settings
F Ampl :
Sweep gauss :
RF drive :

• VACUUMS

MIS _____uT
Low energy _____uT
High energy _____uT
20-70 _____uT
90-90 _____uT
70-70 _____uT
Fission _____uT

• BEAM (circle appropriate ones)

Beam source DENIS PIS
State: 1 2 3 Field: Weak Strong
Cup Unquenched Quenched
Source _____ A _____ A
L.E. _____ A _____ A
H.E. _____ A _____ A
Input 90-90 _____ A _____ A
Center 90-90 _____ A
Input 70-70 _____ A _____ A
Beam Stop _____ A _____ A
Target _____ A _____ A
Beam peaked on _____

• COMMENTS

NMR DEC METER _____

20-70 MAGNET FIELD _____ Gauss.

A Honeywell DDP-224 computer was used to control the experiment. The computer code HPOP was written with the following features:
1) Storage of data from 10 detectors using three ADCs and corresponding routers to acquire the first and second detector pair data, the third and fourth detector pair data, and the polarimeter detector pair data. 2) Calculations of sums and asymmetries for the four detector pairs and polarization monitor pair. 3) On-line displays of the yield curve and analyzing power energy excitation functions for the four detector pairs. 4) Automatic stepping of the beam energy and beam transport parameters (Q4, Q5, Q6, and Q7 quadrupoles; S1, S2, and S3 sextupoles; the dual-90° magnet analyzing system; the dual-90° NMR control frequency; and the 70-70 bending magnet).

11. $(\vec{p},p)$ and (p,p) Data I. - A = 13, 17, 25

11.1 Introduction. The high resolution $(\vec{p},p)$ elastic scattering data will be presented by mass number in this chapter and in Chapters 12 and 13. Important parameters or features of each measured excitation function will be described in the individual sections. For cases where the resonance parameters had been measured previously by different experimental methods, the new parameters will be compared with the results from the earlier work. In addition, a table summarizing the resonance and measurement parameters along with a figure of the excitation function data and fits are included for each resonance. Several of the lowest T=3/2 states which had been measured by a combination of methods (as described in Chapter 5) were remeasured and fitted as a test of the polarized beam excitation function analysis method (as presented in Chapter 6). The tables and figures necessary to present the data will now be discussed.

A summary of each resonance's measurement conditions and extracted or calculated resonance parameters are presented in a concise tabular form. The resonance parameters: resonance energy E_R, spin and parity J^π, total width Γ, proton elastic width Γ_p, elastic branching ratio Γ_p/Γ, and the combined beam energy spread and Doppler broadening resolution term Δ_{BD} are listed in each table. These parameters were extracted from the data using the analysis code T32GRD, as discussed in Chapter 6. The

proton reduced width γ_p^2 calculated from the proton partial width and Coulomb penetrability is also shown. The contribution for target straggling width Δ_{ST} calculated and used in the T32GRD analysis code is also listed.

Several additional parameters are presented for cases where it was possible to calculate or extract them from the data. The Doppler broadening distribution width Δ_D, and the terminal stripper straggling contribution Δ_{SS} (calculated from knowing the terminal stripper foil thickness), are given when known. For cases where the Doppler broadening could be calculated, the beam energy spread Δ_B could be extracted from the Δ_{BD} term. Also, if the terminal stripper straggling contribution was known, the beam energy spread due to energy fluctuations of the accelerator system Δ_E could be extracted. The particular instances where these resolution distributions could be extracted will be discussed on an individual basis. The determination of error was performed as described in Chapter 6.

The second and third parts of the summary tables present a few relevant measurement conditions and geometries. Most of these parameters are self-explanatory. Table 11-1 presents a summary of definitions for the symbols and nomenclature necessary to understand the data summary tables.

The figures show the $(\vec{p},p)$ elastic cross section (the left column) and analyzing power (the right column) data plotted versus incident proton energy (lab frame). Each column presents the data from the four (or five) different detector pairs. The detector pair angles are shown

Table 11-1 Resonance and Resolution Symbols and Definitions.

A. Nuclear Resonance Parameters.

E_R [a] : Resonance energy as measured in the lab frame.

J^π [a] : Spin and parity of the resonance.

Γ [a] : Total resonance decay width (center of mass frame).

Γ_p [a] : Elastic proton partial decay width (center of mass frame).

γ_p^2 : Reduced proton elastic width $\left[\frac{\Gamma_p}{2P_c}\right]$ (where P_c is the Coulomb penetrability).

B. Resolution Parameters.

Δ_{ST} [a] : Target straggling distribution width FWHM (Landau or Vavilov).

Δ_{BD} [a] : The combined beam energy spread and Doppler broadening resolution distribution width FWHM (Gaussian).

Δ_D : Doppler broadening distribution width (Gaussian).

Δ_B : Beam spread resolution distribution FWHM. The combined distribution resulting from energy fluctuations and stripper straggling. (See Chapter 6.)

Δ_{SS} : Stripper straggling distribution width FWHM (Landau or Vavilov).

Δ_E : Energy fluctuations distribution width FWHM (Gaussian).

Δ_{ED} : Combination of Δ_E and Δ_D.

C. Measurement Parameter Definitions.

Total Dis. : The distance from the target to the back collimator.

Coll. Hi. and Coll. Wi. : The height and width of the back collimator which defines the detector solid angle. This back collimator is located just in front of the detector.

a) Resonance parameters calculated or extracted from the resonance data using the analysis code T32GRD.

in the center-of-mass frame unless the summary paragraph states differently. The error bars for both the cross section and analyzing power include only the statistical errors. The T32GRD program calculated fits to the data using the average resonance parameters are shown in all figures unless the summary paragraph states differently. It is important to distinguish the average fits shown, curves obtained with parameters optimized from fits to data at all angles, from the best-fits at individual angles (i.e. fits obtained by optimizing the fitting parameters at each angle). Earlier work [Iko76] presented the data with the individual best-fits. However, plotting the average fits gives a better indication of the overall goodness of fit. Angles with fits that are plotted as dashed lines indicate that these data were not included in obtaining the average resonance parameters, as discussed in Chapter 6.

11.2 First T=3/2 Resonance in ^{13}N. Our results from the polarized high resolution measurements of $^{12}C(\vec{p},p)^{12}C$ have been discussed in detail elsewhere [Tho80]. The summary of resonance parameters is given in Table 11-2. The data and T32GRD calculated fits are shown in Fig. 11-1. The angles shown in the figure are the lab frame angles. This analysis included consideration of atomic-excitation processes, as discussed in Chapter 6. The light mass target and high excitation energy make this an ideal case with which to study the possible atomic effects to the observed resolution and measured resonance parameters. A Doppler broadening width of 940 eV was calculated as described in detail in Section 6.3.3. Unlike most of the other measurements, the beam polarization for this experiment was determined by the quench ratio

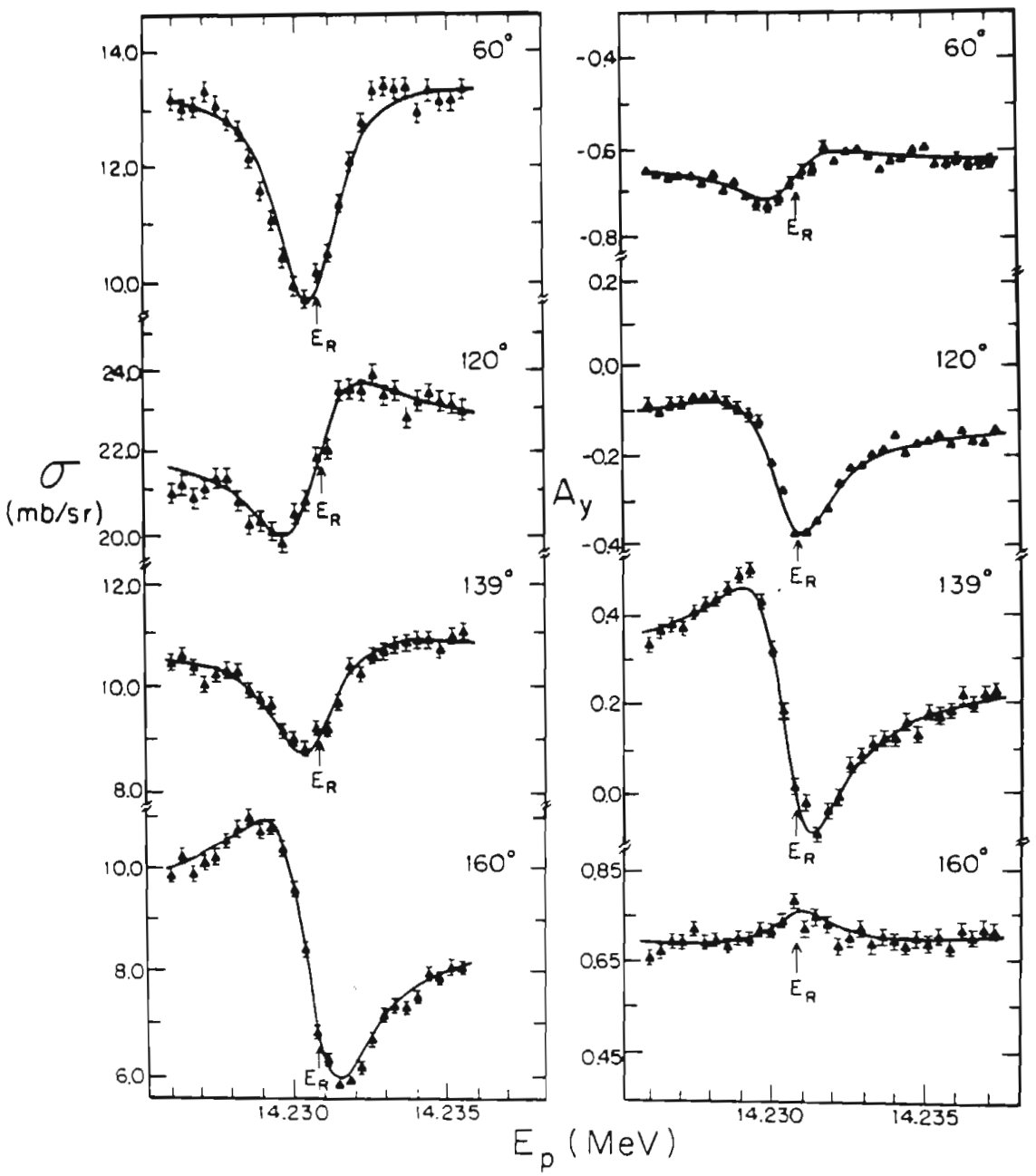

Figure 11-1 $^{12}C(\vec{p},p)^{12}C$ first T=3/2 isospin-forbidden resonance in ^{13}N. Cross-section and analyzing-power excitation functions are shown at four angles. See text and Table 11-2 for details.

Table 11-2 1st T=3/2 State in ^{13}N Resonance Parameters.

$^{12}C(\vec{p},p)^{12}C$ first T=3/2 isospin-forbidden resonance parameters and measurement conditions.

1. Resonance Parameters.[1]

$E_R = 14.2308 \pm .002$ MeV $\quad J^\pi = 3/2^- \quad \gamma_p^2 = 71.0 \pm 4.1$ eV

$\Gamma = 1010 \pm 30$ eV $\quad \Gamma_p = 261 \pm 15$ eV $\quad \Gamma_p / \Gamma = 0.280 \pm .017$

$\Delta_{BD} = 1275 \pm 50$ eV $\quad \Delta_{ST} = 105 \pm 10$ eV $\quad \Delta_D{}^a = 940 \pm 50$ eV

$\Delta_B{}^* = 860 \pm 50$ eV $\quad \Delta_E{}^* = 840 \pm 40$ eV $\quad \Delta_{SS}{}^* = 80 \pm 8$ eV

Angles used in analysis : 64.0°, 124.1°, 142.1°, 161.6°

1) This analysis included atomic effects calculations.
a) Based on best estimate of lattice vibrations.
*) See text and Table 11-1 for explanation of these parameters.

2. Excitation Function Measurement Parameters.

Energy Region Covered = 11.66 keV
Energy Step Size = 365.0 eV
Average Beam Intensity = 50 nA
Average Beam Pol. = 0.88

Target : H-91 10.1 $\mu g/cm^2$ C

Target Nuclei = $50.687 \cdot 10^{16}$ /cm^2
Incident Particles = $2.996 \cdot 10^{14}$

3. Chamber Geometry.

Det. Pair	θ_{lab} (deg)	θ_{cm} (deg)	Total Dis. (inches)	Coll. Hi. (inches)	Coll. Wi. (inches)	Solid Angle (msr)
1L-R	60.0	64.1	4.5	0.25	0.125	2.777
2L-R	120.0	124.1	4.5	0.25	0.125	2.734
3L-R	139.0	142.1	4.0	0.25	0.125	3.488
4L-R	160.0	161.6	4.0	0.25	0.125	3.485

method [Ohl71].

11.3 First T=3/2 Resonance in ^{17}F. The results for the $^{16}O(\vec{p},p)^{16}O$ measurement over the lowest T=3/2 state in ^{17}F are given in Table 11-3. The data are shown in Fig. 11-2. Unfortunately this resonance was measured without having burned off the Formvar backing of the terminal stripping foil, as discussed in Chapter 7. Thus, this resonance was not measured with the optimum resolution. However, several resonances were measured with the same foil in ^{17}F, ^{25}Al, and ^{29}P. The combined data from several different measurements allowed the determination of the thickness of the stripping foil and Formvar. Knowing the thickness of the foil allowed the extraction of the energy fluctuations and Doppler broadening parameter Δ_{ED} by using the code RESDIS. The straggling distribution and the energy fluctuation distribution are folded together using RESDIS. The Doppler broadening for the O atoms in the SiO polyatomic molecule was not calculated because information on the exact lattice structure was not known.

The nuclear resonance parameters are in agreement with an earlier unpolarized-beam measurement by [Hin76]. See Table 11-6 for a comparison of the resonance parameters. However, the extraction of the Doppler broadening parameter in [Hin76] is in error. Their Doppler calculation used an integration of the calculated frequency spectrum for SiO_2. However, this yields the average quantal energy for the SiO_2 molecule, not the energy for the O molecule. Thus, their calculation most likely gives only an estimate of the general magnitude of the effect. Also, their targets were a combination of SiO and SiO_2 [Hin76].

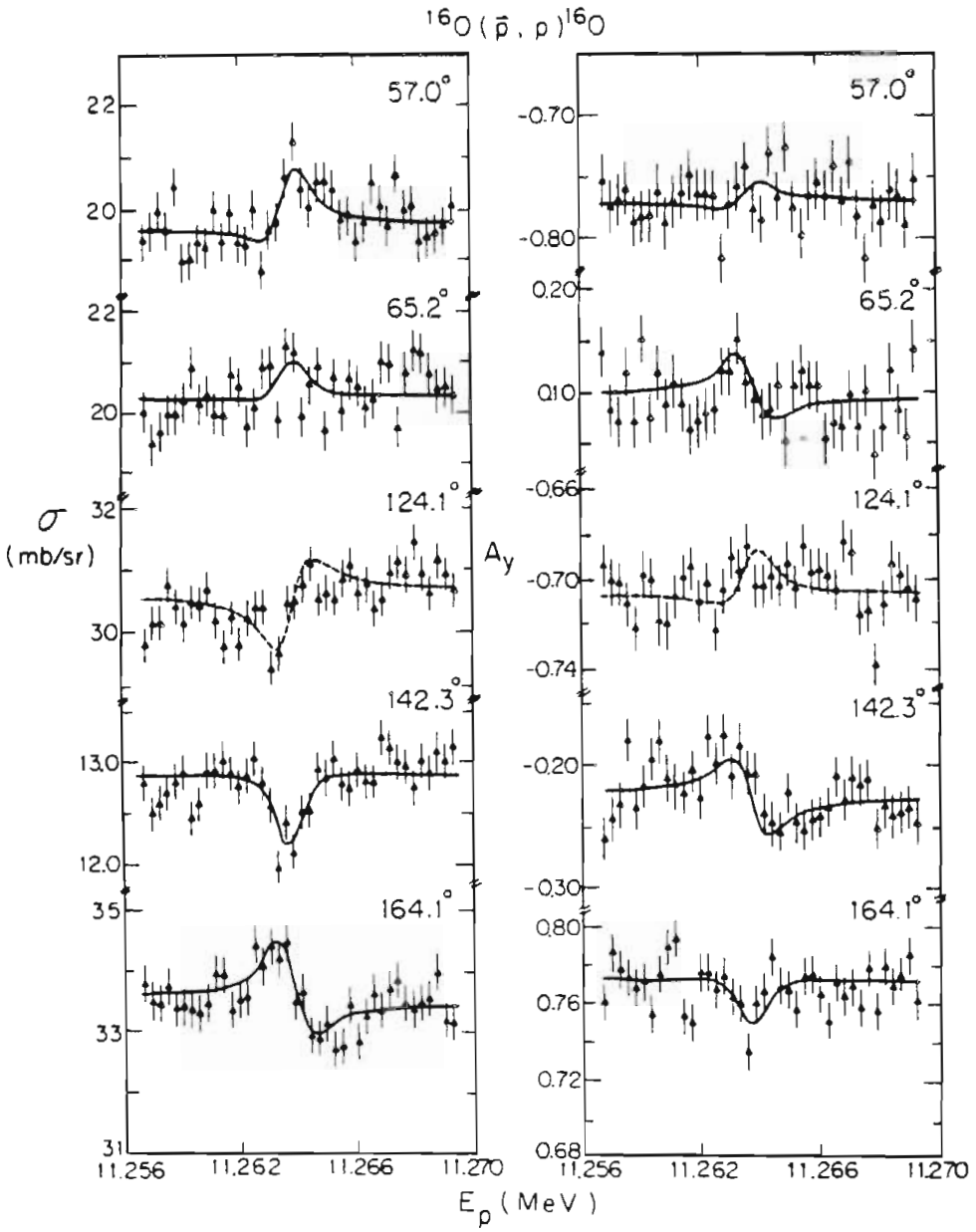

Figure 11-2 $^{16}O(\vec{p},p)^{16}O$ first T=3/2 isospin-forbidden resonance in ^{17}F. Cross-section and analyzing-power excitation functions are shown at five angles. See text and Table 11-3 for details.

Table 11-3 1^{st} T=3/2 State in ^{17}F Resonance Parameters.

$^{16}O(\vec{p},p)^{16}O$ first T=3/2 isospin-forbidden resonance parameters and measurement conditions.

1. Resonance Parameters.

E_R = 11.2642 ± .002 MeV $J^\pi = 1/2^-$ γ_p^2 = 6.77 ± 0.56 eV

Γ = 183 ± 13 eV Γ_p = 23 ± 1.9 eV Γ_p/Γ = 0.126 ± .013

Δ_{BD} = 952 ± 35 eV Δ_{ST} = 181 ± 18 eV Δ_{SS}^* = 530 ± 100 eV

Δ_{ED}^* = 680 ± 100 eV

Angles used in analysis : 57.0°, 65.2°, 142.3°, 164.1°

*) See text and Table 11-1 for explanation of these parameters.

2. Excitation Function Measurement Parameters.

Energy Region Covered = 10.57 keV
Energy Step Size = 270.9 eV
Average Beam Intensity = 90 nA
Average Beam Pol. = 0.78

Target : X-60 13.8 μg/cm^2 SiO / 6.1 μg/cm^2 C

Target Nuclei = $20.287 \cdot 10^{16}$ /cm^2
Incident Particles = $2.996 \cdot 10^{14}$

3. Chamber Geometry.

Det. Pair	θ_{lab} (deg)	θ_{cm} (deg)	Total Dis. (inches)	Coll. Hi. (inches)	Coll. Wi. (inches)	Solid Angle (msr)
1L	54.0	57.0	4.0	0.50	0.0625	1.901
1R	62.0	65.2	4.0	0.50	0.0625	1.901
2L-R	121.0	124.1	4.3	0.50	0.125	6.398
3L-R	140.0	142.3	4.0	0.50	0.125	7.393
4L-R	163.0	164.1	4.0	0.50	0.125	7.393

11.4 Second T=3/2 Resonance in ^{17}F. The data and T32GRD fits from the $^{16}O(\vec{p},p)^{16}O$ measurement over the second T=3/2 state in ^{17}F are shown in Fig. 11-3, with a summary of the resonance parameters given in Table 11-4. This resonance was also measured without having burned off the Formvar backing of the terminal stripping foil. The resolution conditions and Doppler broadening comments presented for the first T=3/2 resonance also apply here. The nuclear resonance parameters are in agreement with an earlier unpolarized measurement by [Hin76]. See Table 11-6 for a comparison of the resonance parameters.

11.5 First T=3/2 Resonance in ^{25}Mg. The first T=3/2 state in ^{25}Mg studied by [Iko76] was remeasured with polarized protons. Figure 11-4 displays the cross section and analyzing power excitation functions. This resonance was measured during the same run and with the same stripping foil and Formvar as the $^{16}O(\vec{p},p)^{16}O$ data. The resonance parameters are presented in Table 11-5. Because of the poor incident beam resolution and the narrow total resonance width, the quality of these data was not sufficient for a normal search of both the total width and the proton partial width. Thus, the previously measured branching ratio [Sex73] was used as an input to T32GRD. The T32GRD fits to these data are shown in the figure as dotted lines to reflect the difference in analysis. The beam-plus-Doppler resolution distribution obtained from the measurement of the second T=3/2 state in ^{25}Al was used in the T32GRD analysis and thus was not a T32GRD searched parameter. The use of the Δ_{BD} from the 5.941 MeV resonance is valid since there is only a 63 keV separation between these two resonances. Also, the measurements

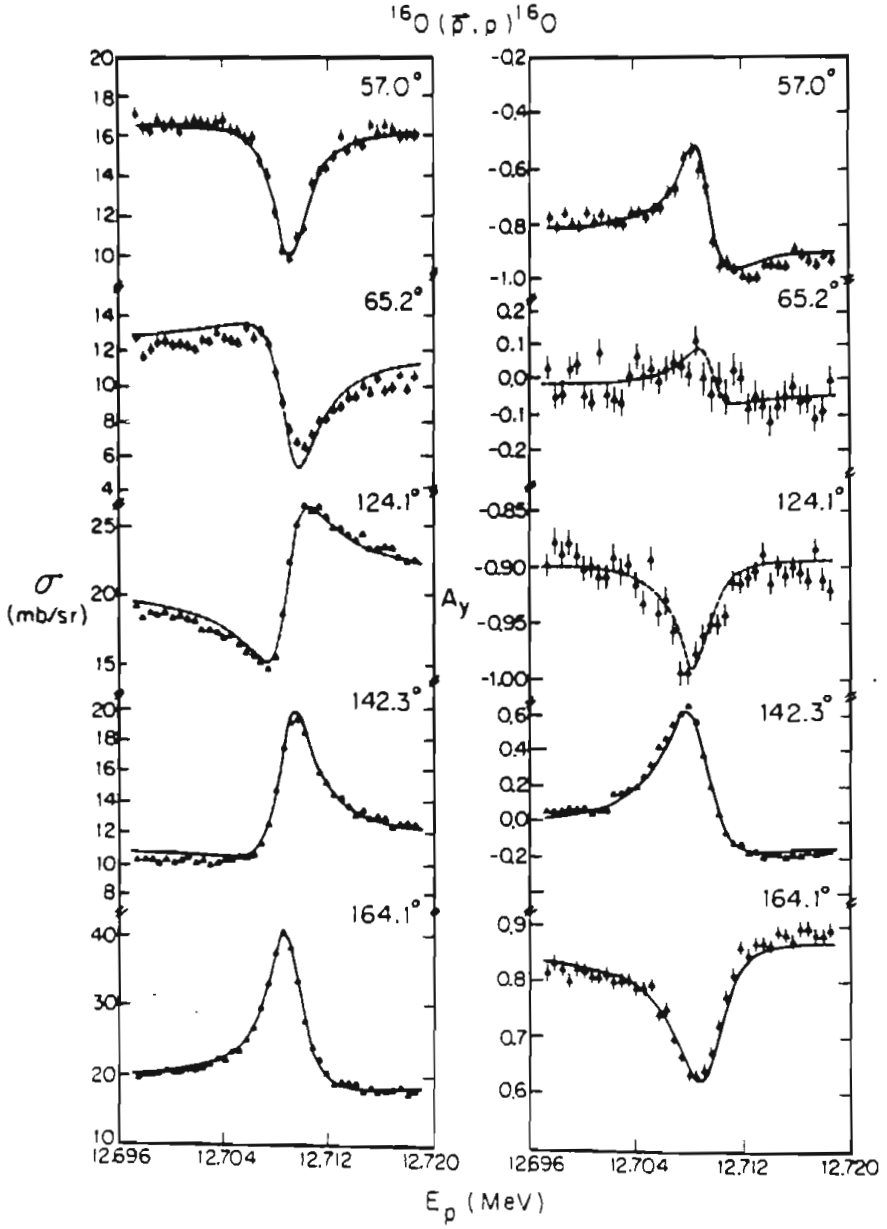

Figure 11-3 $^{16}O(\vec{p},p)^{16}O$ second T=3/2 isospin-forbidden resonance in ^{17}F. Cross-section and analyzing-power excitation functions are shown at five angles. See text and Table 11-4 for details.

Table 11-4 2^{nd} T=3/2 State in ^{17}F Resonance Parameters.

$^{16}O(\vec{p},p)^{16}O$ second T=3/2 isospin-forbidden resonance parameters and measurement conditions.

1. Resonance Parameters.

E_R = 12.7097 ± .002 MeV $J^\pi = 3/2^-$ γ_p^2 = 203.0 ± 6.0 eV

Γ = 2600 ± 200 eV Γ_p = 766 ± 24 eV Γ_p/Γ = 0.295 ± .014

Δ_{BD} = 1130 ± 67 eV Δ_{ST} = 162 ± 16 eV Δ_{SS}^* = 468 ± 100 eV

Δ_{ED}^* = 900 ± 100 eV

Angles used in analysis : 57.0°, 142.3°, 164.1°

*) See text and Table 11-1 for explanation of these parameters.

2. Excitation Function Measurement Parameters.

Energy Region Covered = 12.47 keV
Energy Step Size = 575.0 eV
Average Beam Intensity = 75 nA
Average Beam Pol. = 0.76

Target : X-60 13.8 μg/cm^2 SiO / 6.1 μg/cm^2 C

Target Nuclei = $20.287 \cdot 10^{16}$ /cm^2
Incident Particles = $2.996 \cdot 10^{14}$

3. Chamber Geometry.

Det. Pair	θ_{lab} (deg)	θ_{cm} (deg)	Total Dis. (inches)	Coll. Hi. (inches)	Coll. Wi. (inches)	Solid Angle (msr)
1L	54.0	57.0	4.0	0.50	0.0625	1.901
1R	62.0	65.2	4.0	0.50	0.0625	1.901
2L-R	121.0	124.1	4.3	0.50	0.125	6.398
3L-R	140.0	142.3	4.0	0.50	0.125	7.393
4L-R	163.0	164.1	4.0	0.50	0.125	7.393

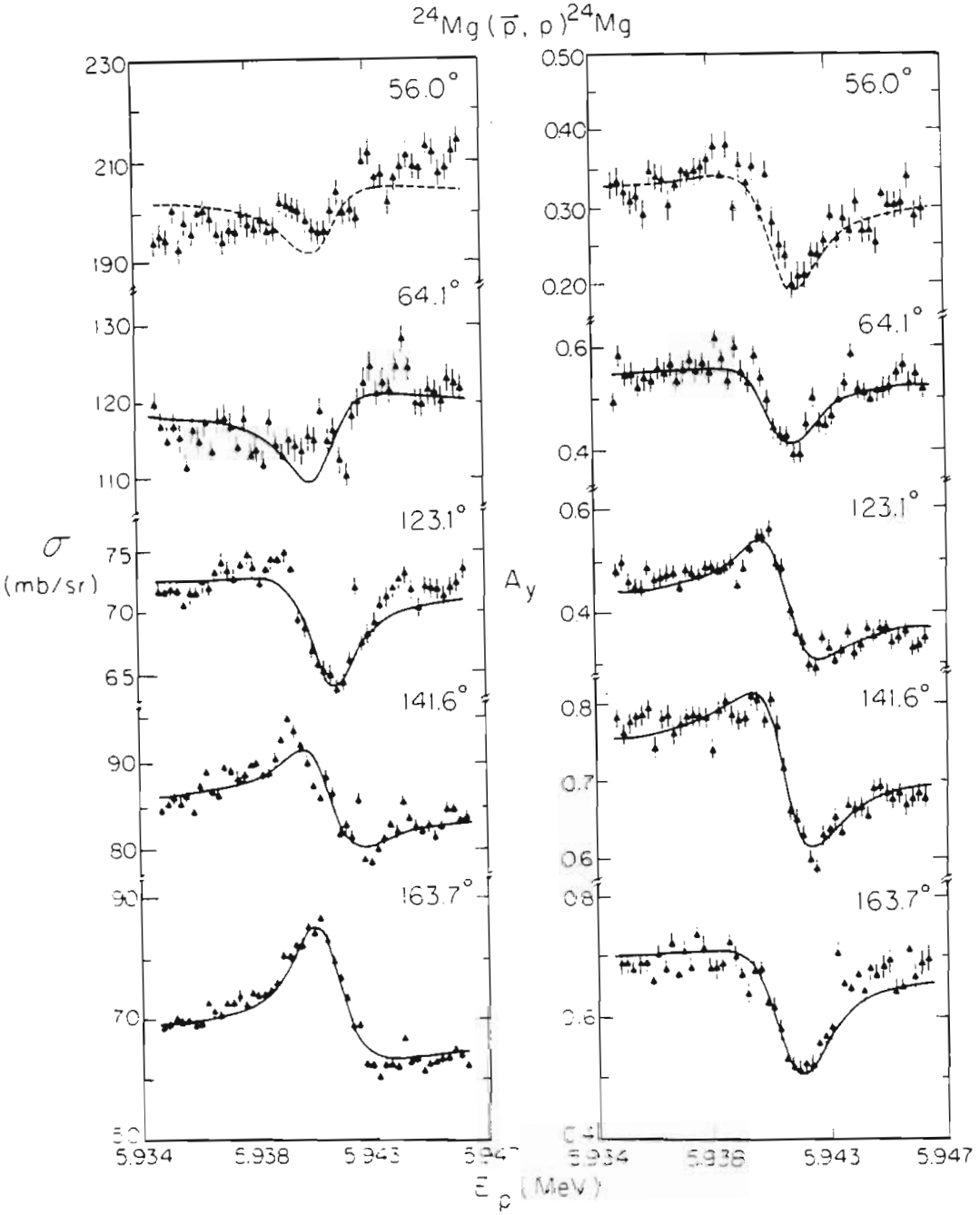

Figure 11-4 $^{24}Mg(\vec{p},p)^{24}Mg$ first T=3/2 isospin-forbidden resonance in ^{25}Al. Cross-section and analyzing-power excitation functions are shown at five angles. See text and Table 11-5 for details.

Table 11-5 1^{st} T=3/2 State in ^{25}Al Resonance Parameters.

$^{24}Mg(\vec{p},p)^{24}Mg$ first T=3/2 isospin-forbidden resonance parameters and measurement conditions.

1. Resonance Parameters.

E_R = 5.8671 ± .002 MeV $J^\pi = 5/2^+$ γ_p^2 = 25.8 ± 4.9 eV

Γ = 105 ± 18 eV Γ_p = 17.6 ± 3.3 eV Γ_p / Γ [a] = 0.168

Δ_{BD} = 1200 ± 100 eV Δ_{ST} = 92 ± 9 eV Δ_D [b] = 270 ± 30 eV

Δ_B * = 550 ± 100 eV Δ_E * = 475 ± 50 eV Δ_{SS} * = 1000 ± 100 eV

Angles used in analysis : 56.0°, 123.1°, 141.6°, 163.7°

a) Did not perform search on this parameter, used [Sex73].
b) Based on best estimate of lattice vibrations.
*) See text and Table 11-1 for explanation of these parameters.

2. Excitation Function Measurement Parameters.

Energy Region Covered = 8.01 keV
Energy Step Size = 235.7 eV
Average Beam Intensity = 70 nA
Average Beam Pol. = 0.74

Target : P-88 2.67 μg/cm^2 ^{24}Mg / 4.5 μg/cm^2 C

Target Nuclei = $2.509 \cdot 10^{16}$ /cm^2
Incident Particles = $2.497 \cdot 10^{14}$

3. Chamber Geometry.

Det. Pair	θ_{lab} (deg)	θ_{cm} (deg)	Total Dis. (inches)	Coll. Hi. (inches)	Coll. Wi. (inches)	Solid Angle (msr)
1L	54.0	56.0	4.0	0.50	0.0625	1.901
1R	62.0	64.1	4.0	0.50	0.0625	1.901
2L-R	121.0	123.1	4.3	0.50	0.125	6.398
3L-R	140.0	141.6	4.0	0.50	0.125	7.393
4L-R	163.0	163.7	4.0	0.50	0.125	7.393

were made in consecutive order with very similar machine conditions and the same stripping foil. The extracted reduced width is in excellent agreement with the [Iko76] data. It should be pointed out that, even though the resolution for the polarized data was much poorer than the unpolarized beam excitation function measurement, the total width could still be extracted reliably because of the additional information provided by the analyzing power measurement. The extraction of the resolution parameters which are discussed in the next section also apply to the measurement of this resonance.

11.6 Second T=3/2 Resonance in ^{25}Mg. The ^{24}Mg($\vec{p}$,p)^{24}Mg second T=3/2 isospin forbidden resonance parameters are presented in Table 11-6. These data yield the first reliable extraction of the second-state resonance parameters. These extracted parameters are in substantial disagreement with earlier results. An earlier study of this state [Iko76] used a proton partial-width-to-total-width branching ratio based on very weak assumptions of the inelastic and elastic proton yields [Tei69]. The analysis of the polarized beam excitation function data, which yields both the total width and the proton partial width, results in a branching ratio almost 3 times smaller and a total width 3.5 times greater than the earlier values. However, the proton partial width is only about 1.3 times greater than the previous result. The data and T32GRD fits are shown in Fig. 11-5.

This measurement was made using the same carbon foil with Formvar backing for terminal stripping as was used for the ^{16}O($\vec{p}$,p)^{16}O measurements. The Doppler broadening for the monoatomic Mg molecule can

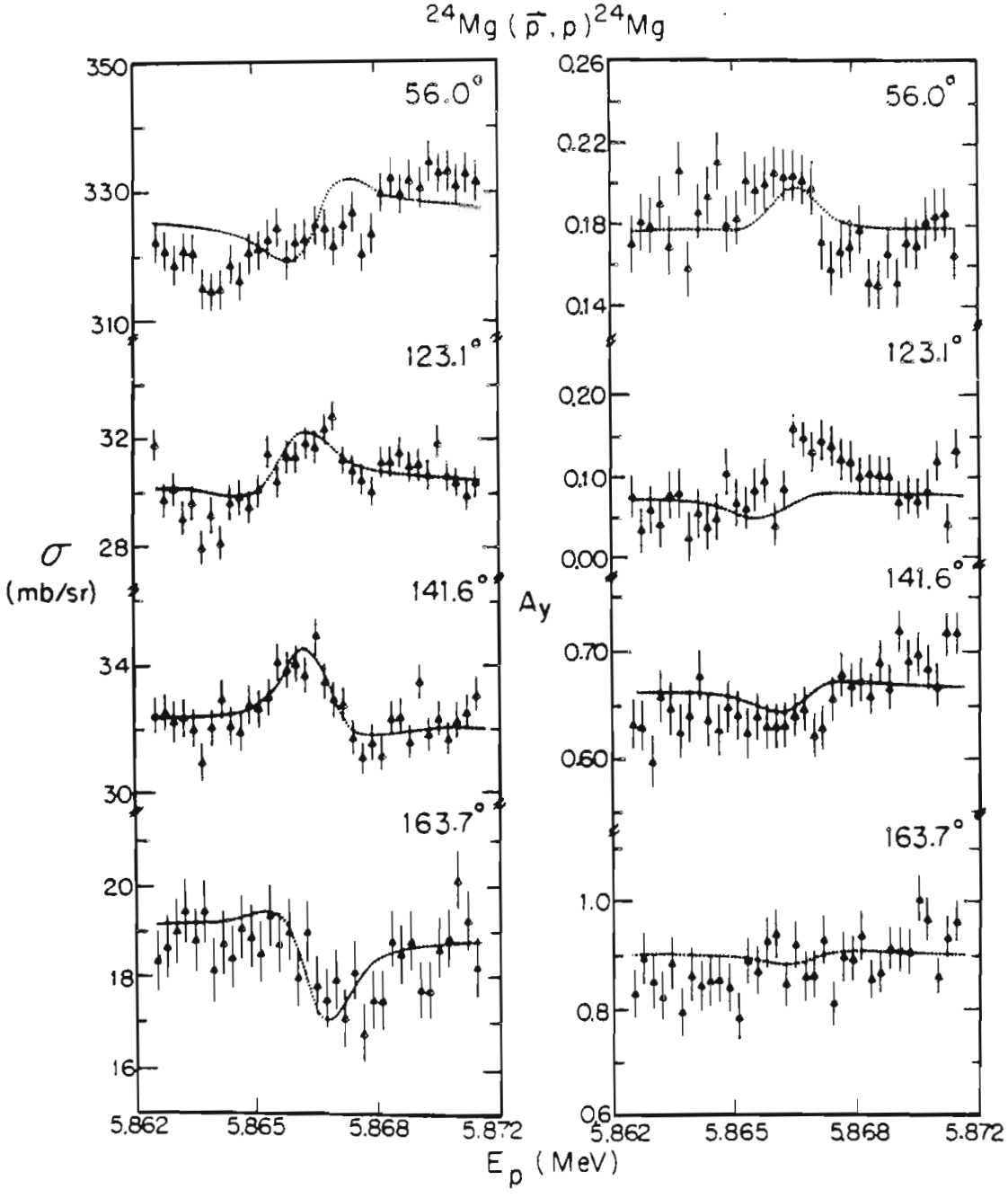

Figure 11-5 $^{24}Mg(\vec{p},p)^{24}Mg$ second T=3/2 isospin-forbidden resonance in ^{25}Al. Cross-section and analyzing-power excitation functions are shown at five angles. See text and Table 11-6 for details.

Table 11-6 2^{nd} T=3/2 State in ^{25}Al Resonance Parameters.

$^{24}Mg(\vec{p},p)^{24}Mg$ second T=3/2 isospin-forbidden resonance parameters and measurement conditions.

1. Resonance Parameters.

E_R = 5.9410 ± .002 MeV $J^\pi = 3/2^+$ γ_p^2 = 330 ± 17 eV

Γ = 1302 ± 135 eV Γ_p = 232 ± 12 eV Γ_p/Γ = 0.178 ± .02

Δ_{BD} = 1200 ± 100 eV Δ_{ST} = 90 ± 9 eV Δ_D[a] = 270 ± 30 eV

Δ_B* = 550 ± 100 eV Δ_E* = 475 ± 50 eV Δ_{SS}* = 1000 ± 100 eV

Angles used in analysis : 64.1°, 123.1°, 141.6°, 163.7°

a) Based on best estimate of lattice vibrations.
*) See text and Table 11-1 for explanation of these parameters.

2. Excitation Function Measurement Parameters.

Energy Region Covered = 12.57 keV
Energy Step Size = 237.1 eV
Average Beam Intensity = 95 nA
Average Beam Pol. = 0.71

Target : P-88 2.67 $\mu g/cm^2$ ^{24}Mg / 4.5 $\mu g/cm^2$ C

Target Nuclei = $2.509 \cdot 10^{16}$ /cm^2
Incident Particles = $2.497 \cdot 10^{14}$

3. Chamber Geometry.

Det. Pair	θ_{lab} (deg)	θ_{cm} (deg)	Total Dis. (inches)	Coll. Hi. (inches)	Coll. Wi. (inches)	Solid Angle (msr)
1L	54.0	56.0	4.0	0.50	0.0625	1.901
1R	62.0	64.1	4.0	0.50	0.0625	1.901
2L-R	121.0	123.1	4.3	0.50	0.125	6.398
3L-R	140.0	141.6	4.0	0.50	0.125	7.393
4L-R	163.0	163.7	4.0	0.50	0.125	7.393

be calculated with confidence using the measured Debye temperature [Lau56] and the techniques outlined in Section 6.3.3. This allows the extraction of the beam-resolution distribution width. The measurement of several resonances at various energies allows the reliable extraction of the terminal stripping straggling distribution. Thus, the actual machine energy fluctuations could be derived.

11.7 Higher T=3/2 Resonances in ^{25}Mg. The (p,t) and (p,^{3}He) cross section data were used to identify the third T=3/2 state in ^{25}Al. Initially, the strong ^{25}Al state observed at 9.135 MeV in the single-angle (p,t) data taken at Princeton was a strong candidate to be the third T=3/2 state in ^{25}Al. However, unpolarized ^{24}Mg(p,p)^{24}Mg data taken over this energy region exhibited no resonance structures. The ^{24}Mg(p,p)^{24}Mg data taken over the 8.858 ^{25}Al state energy region did exhibit a narrow resonance within 5 keV of the predicted resonance energy. The angular distributions taken later at IUCF confirmed that the 9.135-MeV state could not be a T=3/2 state and indicated that the state at 8.858 MeV was the T=3/2 state. The unpolarized yield curves (not absolute cross sections) are plotted in Fig. 11-6. Data from four detector angles are shown, with the detector angles indicated in the lab frame. No attempt was made to extract resonance parameters from these unpolarized data. The resonance is located at an energy of 6.856 MeV.

The ^{27}Al(p,t)^{25}Al and ^{27}Al(p,^{3}He)^{25}Mg angular distribution data have been taken at higher energies and there are several higher-lying T=3/2 state candidate states present. However, no ^{24}Mg(p,p)^{24}Mg data has been taken over these energy regions.

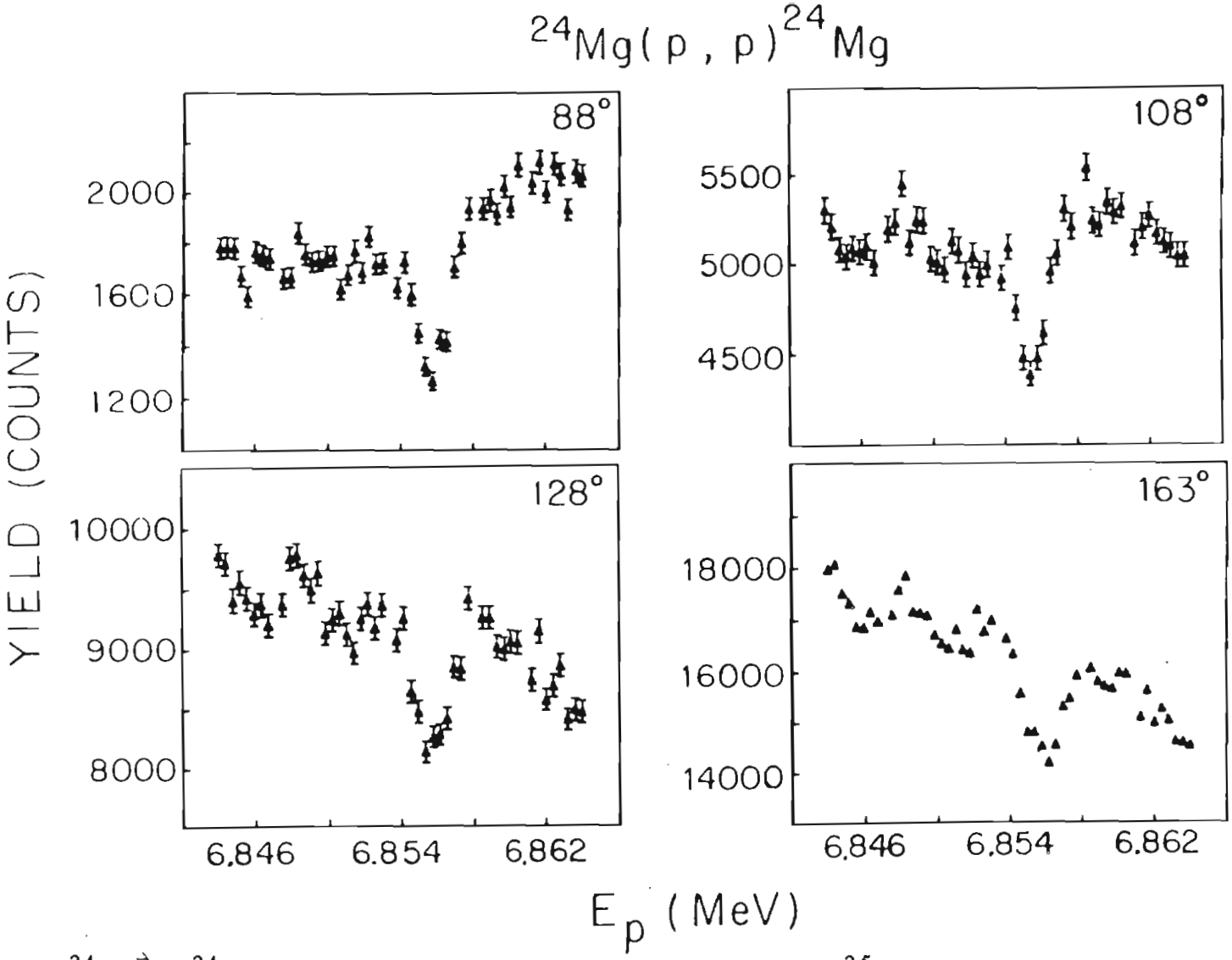

Figure 11-6 $^{24}Mg(\vec{p},p)^{24}Mg$ third T=3/2 isospin-forbidden resonance in ^{25}Al. Yield curve energy excitation functions are shown at four different angles. See Section 11.7 for details.

Table 11-7 T=3/2 ^{13}N and ^{17}F Resonance Parameters.

Measurement of T=3/2 resonance parameters by $^{12}C(\vec{p},p)^{12}C$ and $^{16}O(\vec{p},p)^{16}O$.

Compound Nucleus	T=3/2 State	Previous Measurement Results			Present Measurement Results $(\vec{p},p)$			
		E_R (MeV)	Γ (eV)	Γ_p (eV)	E_R (MeV)	J^π	Γ (eV)	Γ_p (eV)
^{13}N	1	14.2308 ± .0002[a]	1100 ± 90 [b]	210 ± 11 [b]	14.2308 ± .002	$3/2^-$	1010 ± 30	261 ± 15
^{17}F	1	11.2636 ± .002 [c]	200 ± 40 [d]	19 ± 3 [c]	11.2642 ± .002	$1/2^-$	183 ± 13	23 ± 2
^{17}F	2	12.7077 ± .002 [c]	2830 ± 120[c]	940 ± 60 [c]	12.7097 ± .002	$3/2^-$	2600 ± 200	766 ± 24

a) [Hue73] absolute energy determination.

b) [Hin75a] using (p,p) scattering.

c) [Hin76] using (p,p) scattering.

d) [Har71] and [Ade73] branching ratios were used by [Hin76] to determine the resonance parameters.

Table 11-8 T=3/2 ^{25}Al Resonance Parameters.

Measurement of T=3/2 resonance parameters by $^{24}Mg(\vec{p},p)^{24}Mg$.

- The E_x in column 9 is the predicted excitation energy in ^{25}Al from the $(\vec{p},p)$ or (p,p) measurements.
- The E_x in column 10 is the excitation energy in ^{25}Al measured from the (p,t) experiments.

T=3/2 State	Previous Measurement Results [Iko76]			Present Measurement Results					
				$(\vec{p},p)$ and (p,p)				^{25}Al	(p,t)
	E_R (MeV)	Γ (eV)	Γ_p (eV)	E_R (MeV)	J^π	Γ (eV)	Γ_p (eV)	E_x (MeV)	E_x (MeV)
1	5.866 ± .003	155 ± 50	26 ± 9	5.8671 ± .002	$5/2^+$	105 ± 18	17.6 ± 4	7.904	7.898
2	5.938 ± .003	211 ± 50	105 ± 25	5.9410 ± .002	$3/2^+$	1302 ± 135	232 ± 12	7.975	7.968
3	-----	-----	-----	6.856 ± .002	$1/2^+$	——	----	8.853	8.858

11.8 Summary of A=13, 17, and 25. The remeasurement of the previously studied isospin forbidden resonances by measuring cross section and analyzing power excitation functions with polarized beams yields resonance parameters which are in good agreement with the values obtained by other methods. A comparison of the new results and earlier work is presented in Table 11-7. The agreement of the branching ratios with the values obtained from the β^+-delayed proton decay measurements indicates the reliability of the polarized beam excitation function analysis method. The fact that all the resonance parameters can be determined in a single experiment is another advantage of this measurement scheme.

The study of the second T=3/2 state in ^{25}Al utilizing the polarized beam excitation function measurement and analysis allowed the first reliable extraction of this resonance's parameters. The third T=3/2 resonance in ^{25}Al located by using the (p,t) and (p,^{3}He) data was also observed by ^{24}Mg(p,p)^{24}Mg. The conclusions based on these measurements will be presented in Chapter 14.

12. $(\vec{p},p)$ and (p,p) Data II. - A = 29

12.1 Introduction. One of the goals of our study of isospin mixing was to concentrate on locating and determining the resonance parameters of as many T=3/2 states in a given nucleus as possible. The ^{29}P nucleus was chosen for this study based on the results from the $^{31}P(p,t)^{29}P$ and $^{31}P(p,^{3}He)^{29}Si$ data and from the (p,p) excitation functions taken over the energy regions corresponding to the energies of the $^{31}P(p,t)^{29}P$ candidate states. This chapter presents the $^{28}Si(\vec{p},p)^{28}Si$ study of five T=3/2 states which have been identified as T=3/2 states by the (p,t)-(p,^{3}He) cross section and analyzing power angular distribution comparisons. Data are also presented for another state in ^{29}P which could not be definitively assigned as having T=3/2 by the (p,t)-(p,^{3}He) comparison method. The identification of this state as a probable T=3/2 state is based on the resonance measurements coupled with the $^{31}P(p,t)^{29}P$ angular distribution measurements. Although these states were all observed initially by $^{28}Si(p,p)^{28}Si$ unpolarized beam measurements, only the polarized beam results will be presented.

12.2 First T=3/2 Resonance in ^{29}P. The first T=3/2 state in ^{29}P was observed by $^{28}Si(\vec{p},p)^{28}Si$ as a check of our measurement and analysis methods. The results from the polarized beam measurement shown in Table 12-1 were in good agreement with the earlier unpolarized beam work [Iko76]. See Table 12-7 for a comparison of the measurement results. The

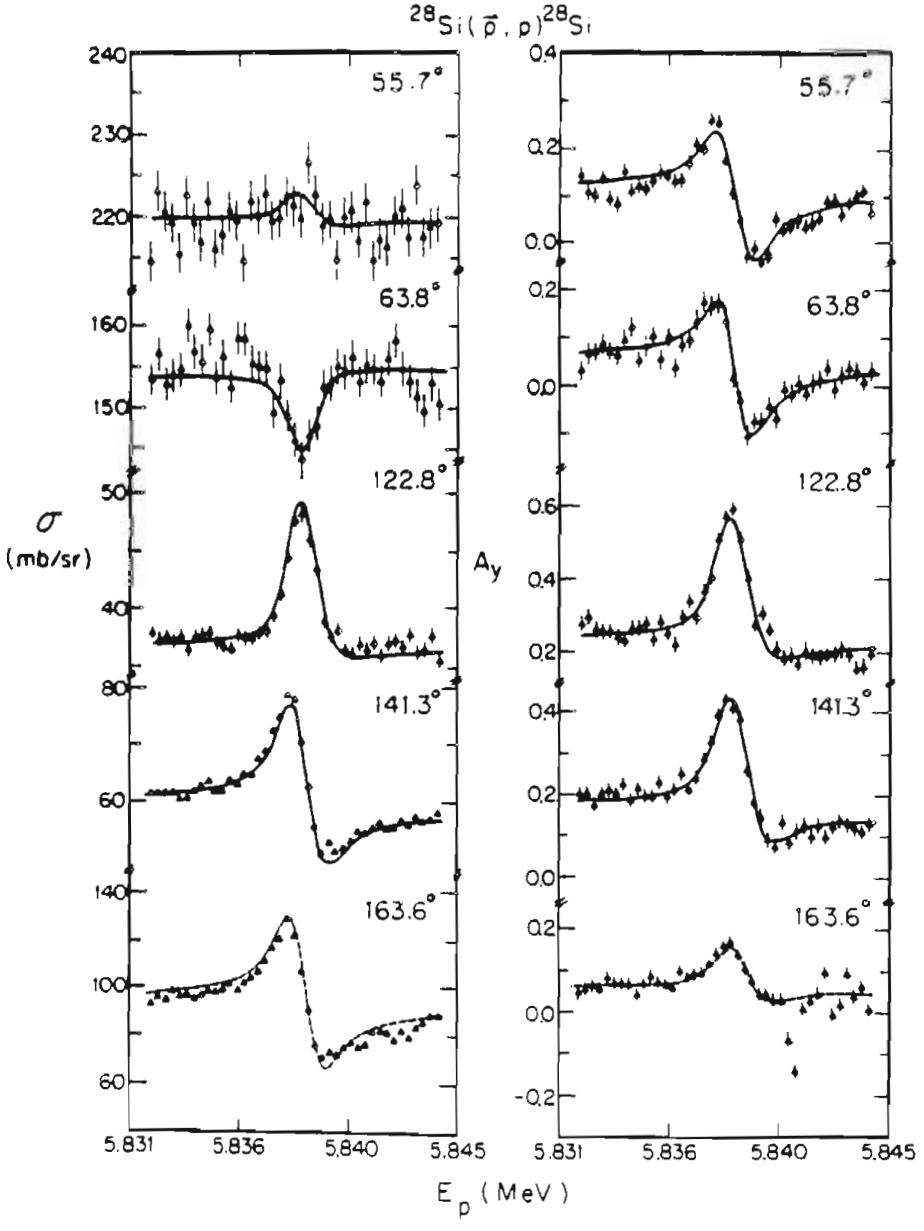

Figure 12-1 $^{28}Si(\vec{p},p)^{28}Si$ first T=3/2 isospin-forbidden resonance in ^{29}P. Cross-section and analyzing-power excitation functions are shown at five angles. See text and Table 12-1 for details.

Table 12-1 1^{st} T=3/2 State in ^{29}P Resonance Parameters.

$^{28}Si(\vec{p},p)^{28}Si$ first T=3/2 isospin-forbidden resonance parameters and measurement conditions.

1. Resonance Parameters.

E_R = 5.8392 ± .002 MeV $J^\pi = 5/2^+$ γ_p^2 = 319 ± 6 eV

Γ = 271 ± 9.9 eV Γ_p = 216 ± 4.4 eV Γ_p/Γ = 0.80 ± .032

Δ_{BD} = 1230 ± 40 eV Δ_{ST} = 347 ± 35 eV Δ_D^* = 330 ± 100 eV

Δ_B^* = 560 ± 100 eV Δ_E^* = 475 ± 50 eV Δ_{SS}^* = 1010 ± 110 eV

Angles used in analysis : 55.7°, 63.8°, 122.8°, 141.3°

*) See text and Table 11-1 for explanation of these parameters.

2. Excitation Function Measurement Parameters.

Energy Region Covered = 12.54 keV
Energy Step Size = 313.5 eV
Average Beam Intensity = 60 nA
Average Beam Pol. = 0.72

Target : P-88 13.8 μg/cm^2 SiO / 6.1 μg/cm^2 C

Target Nuclei = 18.131 · 10^{16} /cm^2
Incident Particles = 0.999 · 10^{14}

3. Chamber Geometry.

Det. Pair	θ_{lab} (deg)	θ_{cm} (deg)	Total Dis. (inches)	Coll. Hi. (inches)	Coll. Wi. (inches)	Solid Angle (msr)
1L	54.0	55.7	4.0	0.50	0.0625	1.901
1R	62.0	63.8	4.0	0.50	0.0625	1.901
2L-R	121.0	122.8	4.3	0.50	0.125	6.398
3L-R	140.0	141.3	4.0	0.50	0.125	7.393
4L-R	163.0	163.6	4.0	0.50	0.125	7.393

data and T32GRD calculated fits are shown in Fig. 12-1. This resonance was measured during the same experiment as the ^{16}O and ^{24}Mg measurements. Poor terminal stripping conditions existed during this measurement since the Formvar was not burned off the terminal stripping foil. The Doppler broadening distribution could not be calculated because of the lack of information on the solid-state structure of the SiO target, as discussed in Chapter 11 for the ^{16}O measurement. However, the proton energy of this resonance at 5.839 MeV is within 100 keV of the proton resonance energy of the second T=3/2 state in ^{25}Mg. The measurements were made under similar machine conditions using the same terminal stripping foil. Thus, the resolution parameters could be extracted for the ^{29}P first T=3/2 resonance based on the ^{25}Mg results. Also, the Doppler broadening contribution could be extracted because all other resolution parameters had been determined.

12.3 Second T=3/2 Resonance in ^{29}P. The second T=3/2 state in ^{29}P identified from the (p,t)-(p,^{3}He) angular distribution comparisons was observed by $^{28}Si(\vec{p},p)^{28}Si$ scattering within 4 keV of the predicted energy. This location does not agree with the previous identification [Tei69]. The data and T32GRD fits are presented in Fig. 12-2. Table 12-2 summarizes the resonance parameters. Because of the uncertainty of the beam energy resolution, the terminal stripping, and the Doppler broadening, no additional resolution parameters could be extracted. The resolution parameters were reasonable considering the fairly large total width of this $1/2^+$ resonance.

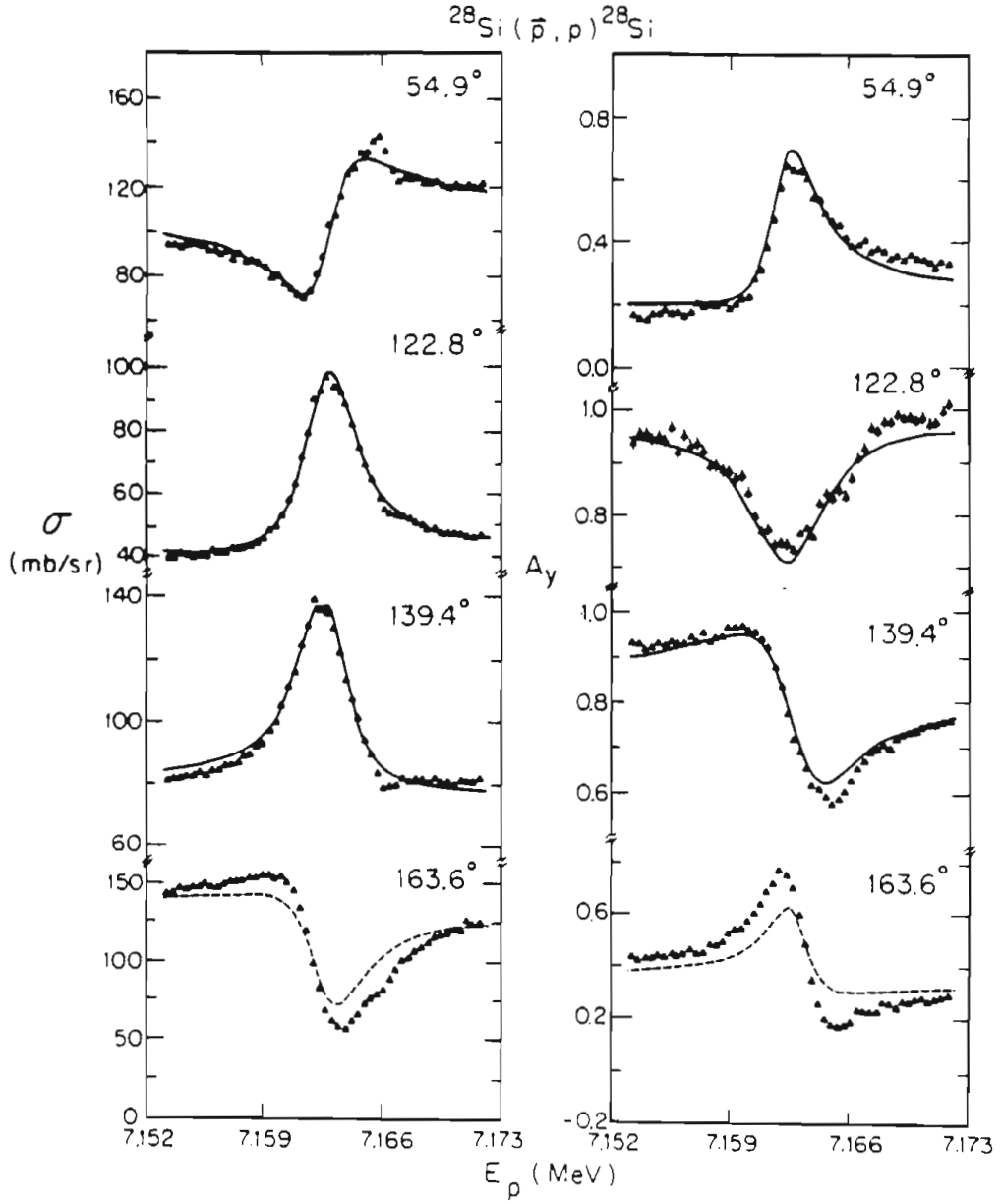

Figure 12-2 $^{28}Si(\vec{p},p)^{28}Si$ second T=3/2 isospin-forbidden resonance in ^{29}P. Cross-section and analyzing-power excitation functions are shown at four angles. See text and Table 12-2 for details.

Table 12-2 2^{nd} T=3/2 State in ^{29}P Resonance Parameters.

$^{28}Si(\vec{p},p)^{28}Si$ second T=3/2 isospin-forbidden resonance parameters and measurement conditions.

1. Resonance Parameters.

$E_R = 7.1632 \pm .002$ MeV $J^\pi = 1/2^+$ $\gamma_p^2 = 789 \pm 13$ eV

$\Gamma = 3066 \pm 54$ eV $\Gamma_p = 2431 \pm 41$ eV $\Gamma_p / \Gamma = 0.793 \pm .02$

$\Delta_{BD}^{*} = 1165 \pm 34$ eV $\Delta_{ST} = 254 \pm 25$ eV

Angles used in analysis : 54.9°, 122.7°, 139.4°

*) See text and Table 11-1 for explanation of these parameters.

2. Excitation Function Measurement Parameters.

Energy Region Covered = 19.10 keV
Energy Step Size = 390.2 eV
Average Beam Intensity = 50 nA
Average Beam Pol. = 0.77

Target : AA17 12.4 $\mu g/cm^2$ SiO / 6.1 $\mu g/cm^2$ C

Target Nuclei = $16.970 \cdot 10^{16}$ $/cm^2$
Incident Particles = $1.748 \cdot 10^{14}$

3. Chamber Geometry.

Det. Pair	θ_{lab} (deg)	θ_{cm} (deg)	Total Dis. (inches)	Coll. Hi. (inches)	Coll. Wi. (inches)	Solid Angle (msr)
1L-R	53.3	54.9	4.0	0.50	0.0625	3.801
2L-R	121.0	122.7	4.75	0.50	0.125	5.243
3L-R	138.0	139.4	4.1	0.50	0.125	7.037
4L-R	163.0	163.6	4.0	0.50	0.125	7.393

This resonance is located between two very broad T=1/2 states. The off-resonance cross sections and analyzing powers at 54.9°, 122.8°, and 139.4° are smooth and only gradually changing, but at 163.6° the T=1/2 resonance lying above the T=3/2 resonance is rapidly changing. See [Tei69] for energy excitation function taken above and below the T=3/2 resonance. The calculations at 163.6° were never able to achieve reasonable simultaneous fits to both the cross section and analyzing power data, and for this reason the extracted parameters from this angle were not included in calculating the average resonance parameters. The calculations using the average resonance parameters shown in Fig. 12-2 also did not produce very good calculated values for the 163.6° data.

12.4 Search for the Third T=3/2 Resonance in ^{29}P. The third T=3/2 state in ^{29}P is a $7/2^+$ state which makes it difficult to observe in the ^{31}P(p,t)^{29}P data and in the (p,p) data. Although two weak candidate states were observed in the ^{31}P(p,t)^{29}P data, the strong T=1/2 states in the corresponding ^{31}P(p,^{3}He)^{29}Si energy region of interest obscured the observation of any existing weak states, as discussed in Chapters 3 and 4. The two ^{31}P(p,t)^{29}P candidate states were observed with unpolarized ^{28}Si(p,p)^{28}Si scattering both at TUNL and at Seattle [Iko80]. An energy excitation function taken by [Iko80] over a 300 keV region including both of these (p,t) candidate states is shown in Fig. 12-3. The search by [Iko80] over this energy region was based on the location of the first T=3/2 state in ^{29}P and the expected excitation energy of higher T=3/2 states based on the known excitation energies of states in the parent nucleus. This method was discussed in detail in Chapter 2. Figure

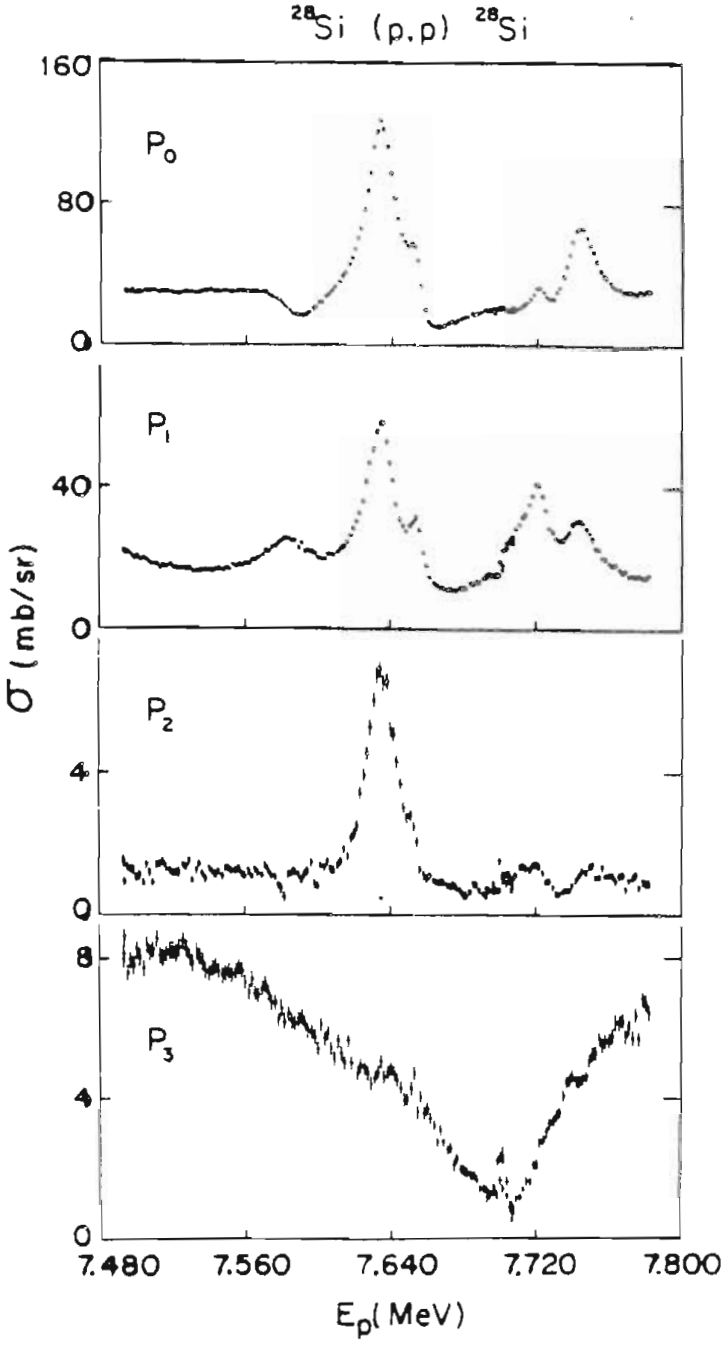

Figure 12-3 Cross-section energy-excitation function data covering an energy region where the third T=3/2 isospin-forbidden resonance in ^{29}P should occur [Iko80]. Data for the elastic and first three inelastic cross sections at a lab angle of 138^{o} are shown. See text for details.

12-3 shows the elastic and first three inelastic (p,p) scattering cross sections for a lab angle of 138°. Small resonance effects in the cross section can be seen in this figure at 7.654 MeV (a bump on the right side of the large resonance in the p_0 and p_1 data) and at 7.701 MeV (the very strong state in the valley of the p_3 data). Both of these resonances are within 3 keV of the energy predicted for the T=3/2 states from our $^{31}P(p,t)^{29}P$ measurements. Based on these $^{31}P(p,t)^{29}P$ measurements, unpolarized $^{28}Si(p,p)^{28}Si$ measurements were taken over the two candidate T=3/2 state energy regions. The resonance at 7.654 MeV was also observed by $^{28}Si(\vec{p},p)^{28}Si$ scattering as shown in Fig. 12-4. The measurement parameters are presented in Table 12-3. No attempt was made to extract resonance parameters because of the rapidly changing off-resonance cross section and analyzing power. The 7.701-MeV resonance was observed by unpolarized beam $^{28}Si(p,p)^{28}Si$ scattering in small energy steps both here and by [Iko80]. The $^{28}Si(p,p)^{28}Si$ data from [Iko80] is shown for this resonance in Fig. 12-5 for lab angles of 138° and 153°.

As discussed in Chapter 4, the state at 7.654 MeV is thought to be the third T=3/2 state. This is based on the (p,t) angular distributions measurements over these two candidate states and the predicted angular distributions from DWBA calculations. The DWBA calculations used the spectroscopic amplitudes for the T=3/2 states predicted from shell-model wave function calculations [Nan82a]. A further argument in favor of this identification can be made based on the decay of the 7.701-MeV resonance to the excited states in ^{28}Si. The third excited state in ^{28}Si is a 0^+ state. The large resonance effect exhibited here in the decay of the

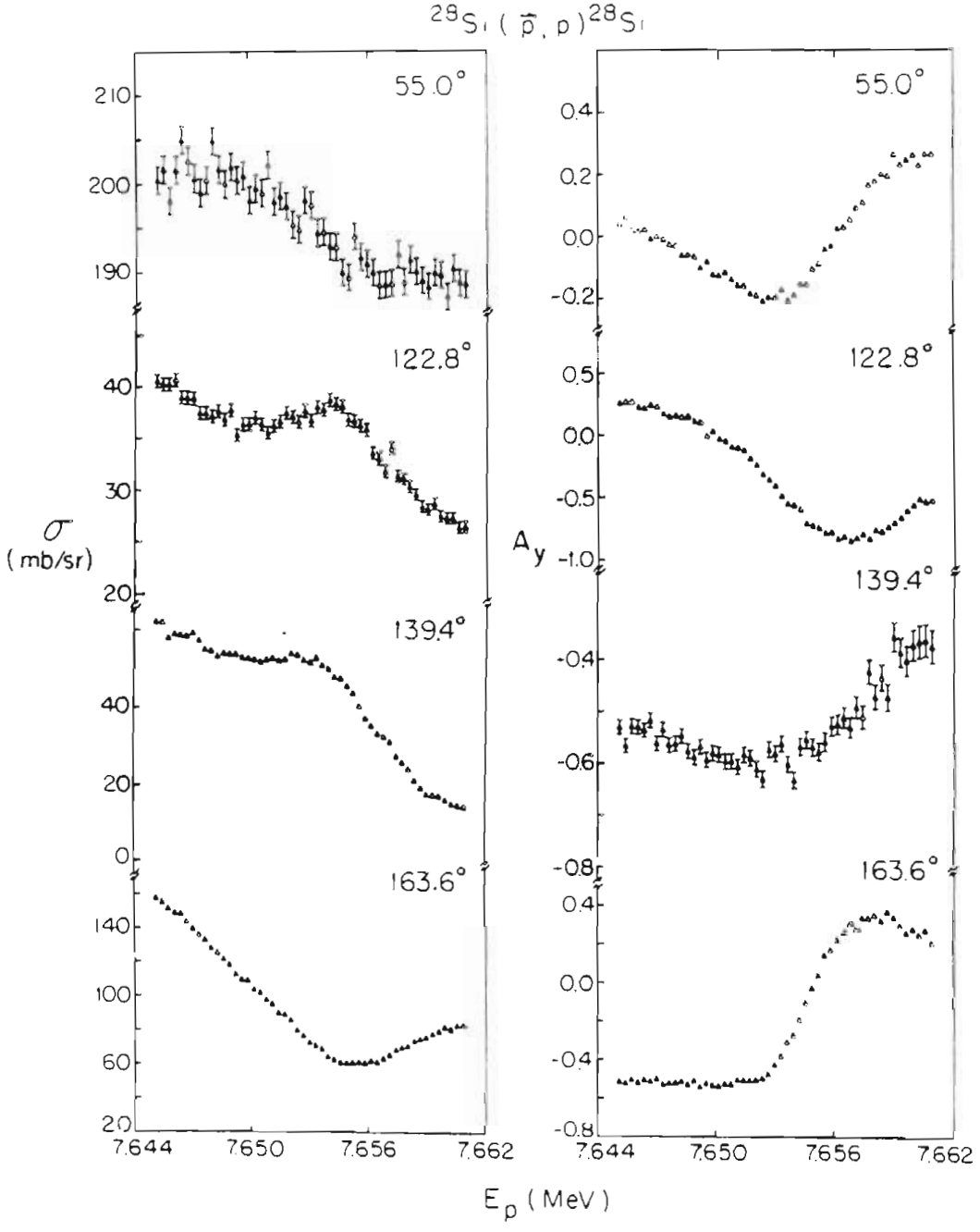

Figure 12-4 Most likely candidate for the third T=3/2 isospin-forbidden resonance in ^{29}P. Cross-section and analyzing-power excitation functions are shown at four angles. See text and Table 12-3 for details.

Table 12-3 Tentative 3rd T=3/2 State in ^{29}P.

Measurement parameters for the $^{28}Si(\vec{p},p)^{28}Si$ excitation functions over the region of the state suspected to be the third T=3/2 ($7/2^+$) state in ^{29}P.

1. Excitation Function Measurement Parameters.

E_R = 7.654 ± .002 MeV

Energy Region Covered = 15.68 keV
Energy Step Size = 313.6 eV
Average Beam Intensity = 140 nA
Average Beam Pol. = 0.72

Target : M-24 4.63 μg/cm^2 SiO / 6.1 μg/cm^2 C

Target Nuclei = $5.850 \cdot 10^{16}$ /cm^2
Incident Particles = $3.745 \cdot 10^{14}$

2. Chamber Geometry.

Det. Pair	θ_{lab} (deg)	θ_{cm} (deg)	Total Dis. (inches)	Coll. Hi. (inches)	Coll. Wi. (inches)	Solid Angle (msr)
1L-R	53.3	54.9	4.0	0.50	0.0625	3.801
2L-R	121.0	122.7	4.75	0.50	0.125	5.243
3L-R	138.0	139.4	4.1	0.50	0.125	7.037
4L-R	163.0	163.6	4.0	0.50	0.125	7.393

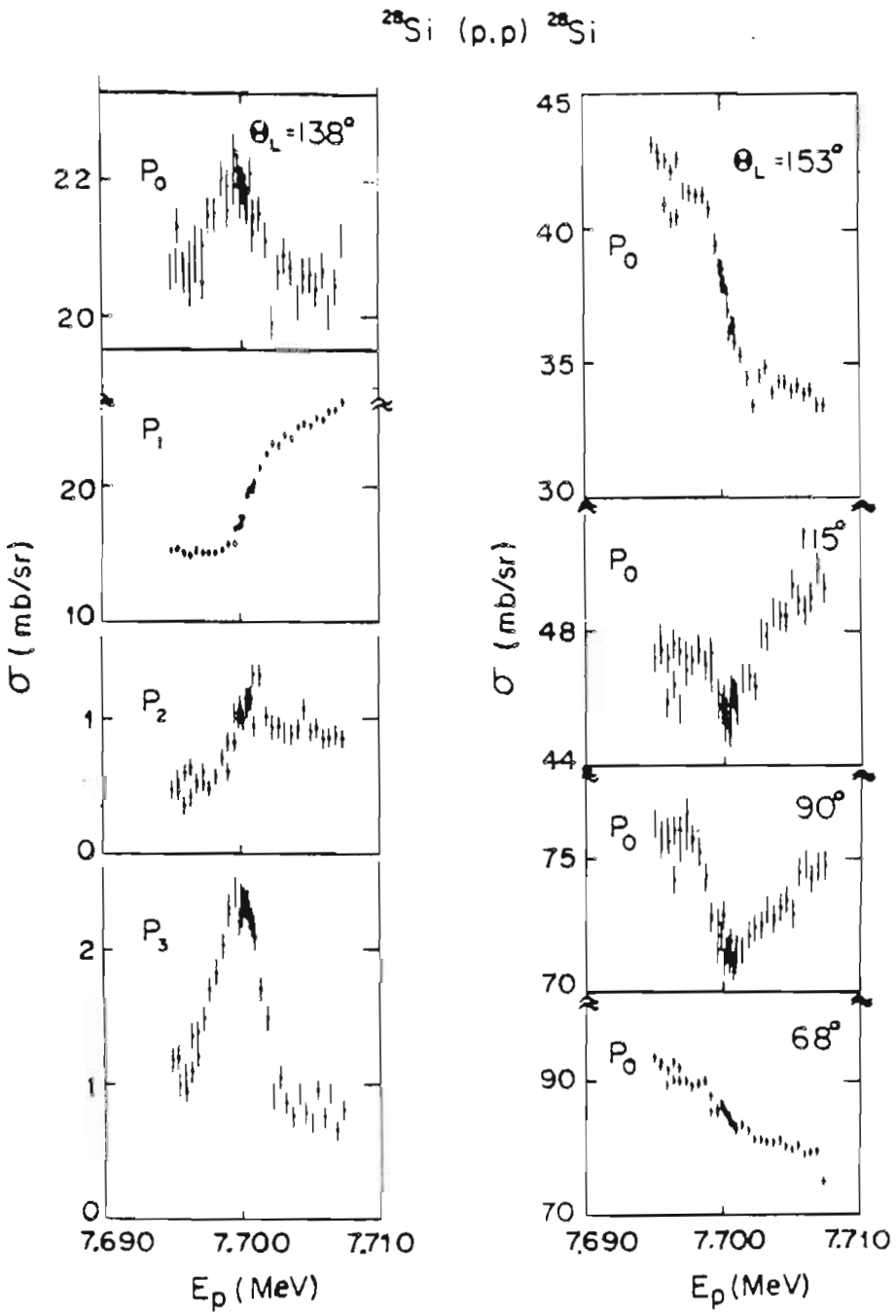

Figure 12-5 Cross-section excitation function data for the 7.701 MeV resonance in ^{29}p [Iko80]. The elastic and first three inelastic cross-sections at a lab angle of 138° and 153° are shown. See text for details.

7.701-MeV state to the 0^+ state would not be expected for this $\ell=4$ transition. However, the strength of the decay of the 7.654-MeV state to the various inelastic states is consistent with a $7/2^+$ compound state decay. The J^π for the ^{28}Si excited states are: p_1, a 2^+ state; p_2, a 4^+ state; and p_3, a 0^+ state. Thus, based on the combined $^{31}P(p,t)^{29}P$ and $^{28}Si(p,p)^{28}Si$ measurements, the third T=3/2 state in ^{29}P is the resonance observed at an energy of 7.654 MeV corresponding to an excitation energy in ^{29}P of 10.137 MeV. No analysis of the polarized beam measurements of the 7.654-MeV state was performed.

12.5 Fourth T=3/2 Resonance in ^{29}P. The fourth T=3/2 state in ^{29}P identified by the (p,t)-(p,^{3}He) measurements was observed by $^{28}Si(\vec{p},p)^{28}Si$ within 9 keV of the resonance energy predicted from $^{31}P(p,t)^{29}P$. Figure 12-6 presents the resonance data and T32GRD fits to the data. This resonance is extremely narrow considering that it lies at an energy of 10.49 MeV in ^{29}P. The resonance parameters are given in Table 12-4. Only the beam-plus-Doppler resolution parameter is given because of uncertainties in the thickness of the terminal stripper foil and because the Doppler broadening distribution cannot be reliably calculated. However, it is clear from the magnitude of the Δ_{BD} that the machine resolution was very good and that most of the Formvar backing was burned off.

12.6 Sixth T=3/2 Resonance in ^{29}P. The sixth T=3/2 state in ^{29}P identified by the (p,t)-(p,^{3}He) comparisons was observed by $^{28}Si(\vec{p},p)^{28}Si$ measurements within 4 keV of its predicted resonance energy. The resonance data and preliminary T32GRD fits to the data are

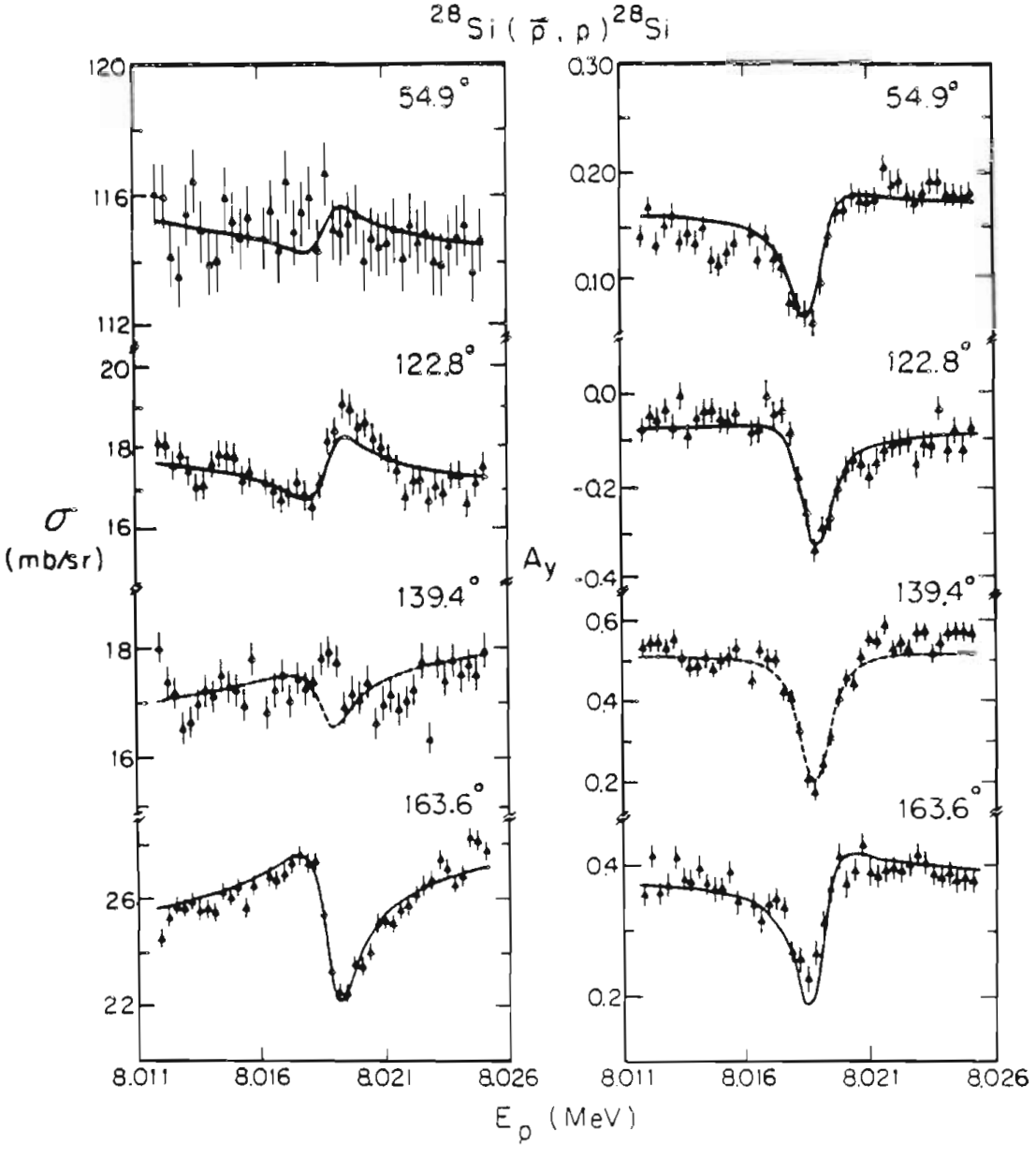

Figure 12-6 $^{28}Si(\vec{p},p)^{28}Si$ fourth T=3/2 isospin-forbidden resonance in ^{29}P. Cross-section and analyzing-power excitation functions are shown at four angles. See text and Table 12-4 for details.

Table 12-4 4^{th} T=3/2 State in ^{29}P Resonance Parameters.

$^{28}Si(\vec{p},p)^{28}Si$ fourth T=3/2 isospin-forbidden resonance parameters and measurement conditions.

1. Resonance Parameters.

$E_R = 8.0192 \pm .002$ MeV $\quad J^\pi = 3/2^+ \quad \gamma_p^2 = 67 \pm 7$ eV

$\Gamma = 884 \pm 170$ eV $\quad \Gamma_p = 99 \pm 11$ eV $\quad \Gamma_p / \Gamma = 0.112 \pm .024$

$\Delta_{BD}^{*} = 860 \pm 106$ eV $\quad \Delta_{ST} = 94 \pm 10$ eV

Angles used in analysis : 54.9^o, 122.7^o, 163.6^o

*) See text and Table 11-1 for explanation of these parameters.

2. Excitation Function Measurement Parameters.

Energy Region Covered = 13.48 keV
Energy Step Size = 320.9 eV
Average Beam Intensity = 110 nA
Average Beam Pol. = 0.72

Target : A-87 5.16 $\mu g/cm^2$ SiO / 4.7 $\mu g/cm^2$ C

Target Nuclei = $6.775 \cdot 10^{16}$ $/cm^2$
Incident Particles = $4.494 \cdot 10^{14}$

3. Chamber Geometry.

Det. Pair	θ_{lab} (deg)	θ_{cm} (deg)	Total Dis. (inches)	Coll. Hi. (inches)	Coll. Wi. (inches)	Solid Angle (msr)
1L-R	53.3	54.9	4.0	0.50	0.0625	3.801
2L-R	121.0	122.7	4.75	0.50	0.125	5.243
3L-R	138.0	139.4	4.1	0.50	0.125	7.037
4L-R	163.0	163.6	4.0	0.50	0.125	7.393

shown in Fig. 12-7. As is clear from the figure, this resonance is not in a region of constant off-resonance cross section and analyzing power as is required by the T32GRD analysis method. The data were rotated in the manner described in Chapter 6 before performing the T32GRD fits in an attempt to extract the resonance parameters. The extracted values are presented in Table 12-5. The resonance parameters extracted from the rotated data may be questionable because of the rotation of the data necessary for analysis. Also, the analyzing-power cross section $\sigma \cdot A_y$ is not invariant under the rotation for the 139.4° and 163.6° data as it is for some of the rotated data, as discussed in Chapter 6. As in the case of the second and the fourth resonances, only the beam-plus-Doppler resolution parameter can be extracted.

12.7 Seventh T=3/2 Resonance in ^{29}P. The seventh T=3/2 resonance in ^{29}P was measured by ^{28}Si($\vec{p}$,p)^{28}Si scattering as shown in Figure 12-8. This resonance was observed within 1.5 keV of the energy predicted from the ^{31}P(p,t)^{29}P measurements. A summary of the resonance parameters is given in Table 12-6. The beam-plus-Doppler distribution was the only resolution parameter which was extracted. The beam-energy resolution during this experiment was not particularly good, although the terminal stripping foil had the Formvar burned off. The resolution problems resulted from terminal charging problems (the charging belt occasionally hitting the column and losing charge).

12.8 Summary of A=29 Measurements. The selection of ^{29}P for a detailed study of the T=3/2 states resulted in the measurements of five T=3/2 resonances never previously studied. The resonance parameters

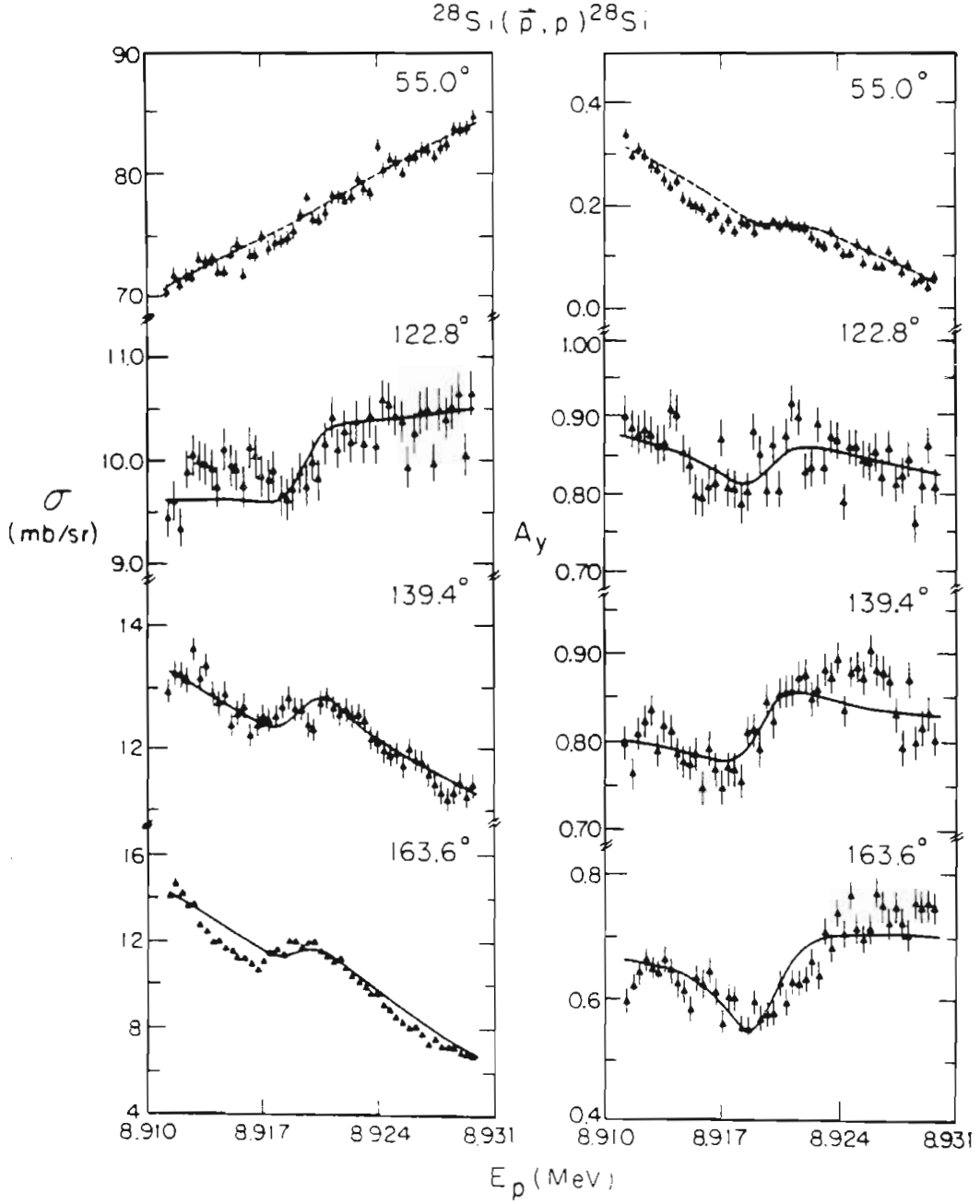

Figure 12-7 $^{28}Si(\vec{p},p)^{28}Si$ sixth T=3/2 isospin-forbidden resonance in ^{29}P. Cross-section and analyzing-power excitation functions are shown at four angles. See text and Table 12-5 for details.

Table 12-5 6^{th} T=3/2 State in ^{29}P Preliminary Resonance Parameters.

Preliminary $^{28}Si(\vec{p},p)^{28}Si$ sixth T=3/2 isospin-forbidden resonance parameters and measurement conditions.

1. Preliminary Resonance Parameters.

E_R = 8.9196 ± .002 MeV $J^\pi = 5/2^+$ γ_p^2 = 59 ± 20 eV

Γ = 3538 ± 527 eV Γ_p = 108 ± 20 eV Γ_p / Γ^* = 0.031

Δ_{BD}^* = 1100 ± 200 eV Δ_{ST} = 115 ± 12 eV

Angles used in analysis : 122.8°, 139.4°, 163.6°

*) See text and Table 11-1 for explanation of these parameters.

2. Excitation Function Measurement Parameters.

Energy Region Covered = 18.56 keV
Energy Step Size = 386.6 eV
Average Beam Intensity = 145 nA
Average Beam Pol. = 0.70

Target : H-55 7.09 μg/cm² SiO / 6.2 μg/cm² C

Target Nuclei = $9.442 \cdot 10^{16}$ /cm²
Incident Particles = $4.993 \cdot 10^{14}$

3. Chamber Geometry.

Det. Pair	θ_{lab} (deg)	θ_{cm} (deg)	Total Dis. (inches)	Coll. Hi. (inches)	Coll. Wi. (inches)	Solid Angle (msr)
1L-R	53.3	55.0	4.0	0.50	0.0625	3.801
2L-R	121.0	122.8	4.75	0.50	0.125	5.243
3L-R	138.0	139.4	4.1	0.50	0.125	7.037
4L-R	163.0	163.6	4.0	0.50	0.125	7.393

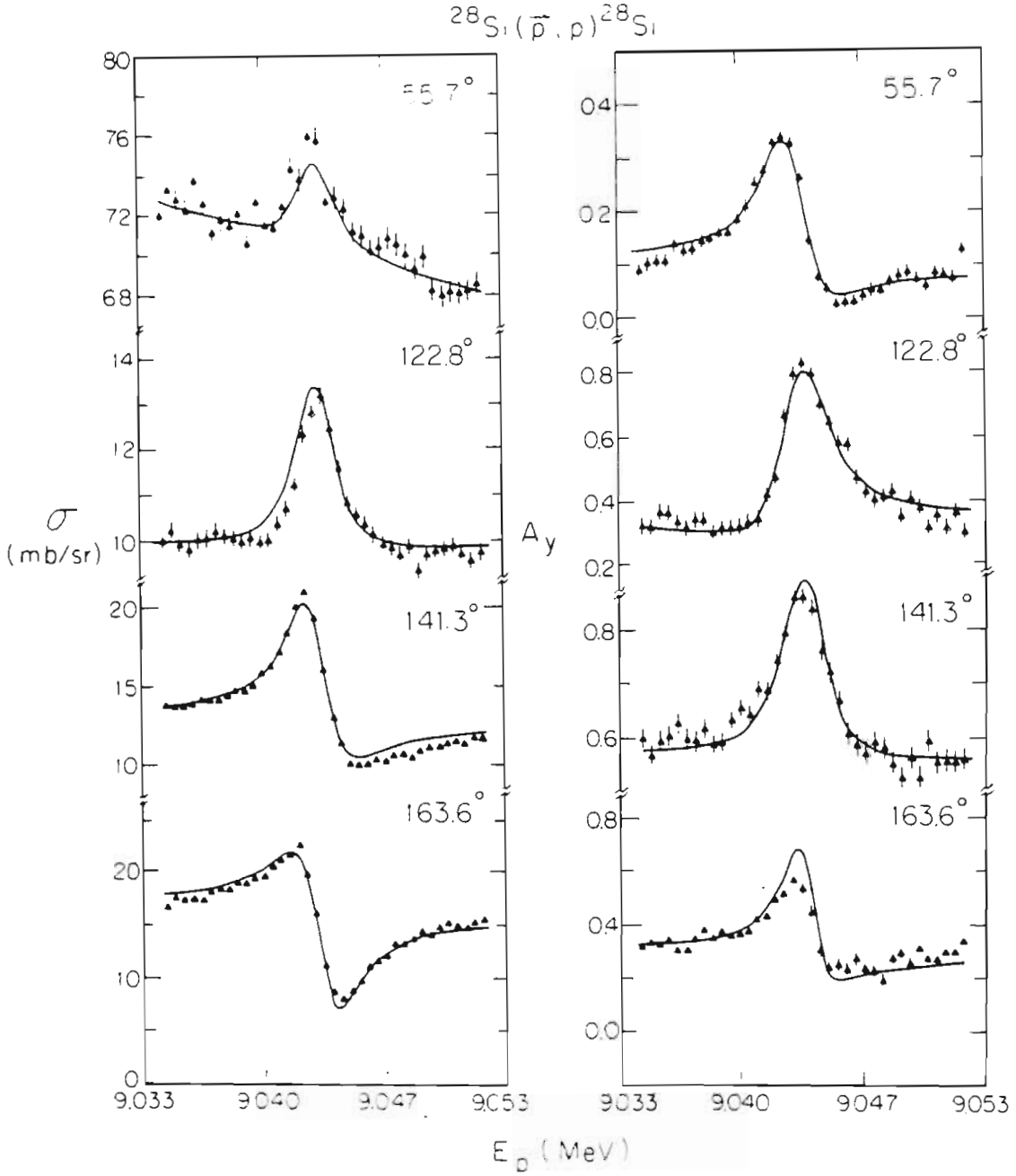

Figure 12-8 $^{28}Si(\vec{p},p)^{28}Si$ seventh T=3/2 isospin-forbidden resonance in ^{29}P. Cross-section and analyzing-power excitation functions are shown at four angles. See text and Table 12-6 for details.

Table 12-6 7^{th} T=3/2 State in ^{29}P Resonance Parameters.

$^{28}Si(\vec{p},p)^{28}Si$ seventh T=3/2 isospin-forbidden resonance parameters and measurement conditions.

1. Resonance Parameters.

$E_R = 9.0435 \pm .002$ MeV $J^\pi = 5/2^+$ $\gamma_p^2 = 199 \pm 11$ eV

$\Gamma = 1526 \pm 120$ eV $\Gamma_p = 371 \pm 21$ eV $\Gamma_p / \Gamma = 0.243 \pm .023$

$\Delta_{BD}^{*} = 1411 \pm 111$ eV $\Delta_{ST} = 211 \pm 21$ eV

Angles used in analysis : 55.7^o, 122.8^o, 141.3^o, 163.6^o

*) See text and Table 11-1 for explanation of these parameters.

2. Excitation Function Measurement Parameters.

Energy Region Covered = 17.50 keV
Energy Step Size = 486.4 eV
Average Beam Intensity = 95 nA
Average Beam Pol. = 0.76

Target : AA17 12.4 $\mu g/cm^2$ SiO / 6.1 $\mu g/cm^2$ C

Target Nuclei = $16.969 \cdot 10^{16}$ /cm^2
Incident Particles = $2.996 \cdot 10^{14}$

3. Chamber Geometry.

Det. Pair	θ_{lab} (deg)	θ_{cm} (deg)	Total Dis. (inches)	Coll. Hi. (inches)	Coll. Wi. (inches)	Solid Angle (msr)
1L-R	54.0	55.7	4.0	0.50	0.0625	3.801
2L-R	121.0	122.8	4.0	0.50	0.125	7.393
3L-R	140.0	141.3	4.3	0.50	0.125	6.398
4L-R	163.0	163.6	4.0	0.50	0.125	7.393

Table 12-7 T=3/2 ^{29}P Resonance Parameters.

Measurement of T=3/2 resonance parameters by ^{28}Si($\vec{p}$,p)^{28}Si.

- The E_x in column 9 is the predicted excitation energy in ^{29}P from the ($\vec{p}$,p) measurements.
- The E_x in column 10 is the excitation energy in ^{29}P measured from the (p,t) experiments.

	Previous Measurement Results [Iko76]			Present Measurement Results					
				($\vec{p}$,p)				^{29}P	(p,t)
T=3/2 State	E_R (MeV)	Γ (eV)	Γ_p (eV)	E_R (MeV)	J^π	Γ (eV)	Γ_p (eV)	E_x (MeV)	E_x (MeV)
1	5.834 ± .002	360 ± 50	300 ± 40	5.8392 ± .002	5/2$^+$	271 ± 10	216 ± 5	8.385	8.384
2	-----	-----	-----	7.1632 ± .002	1/2$^+$	3066 ± 54	2431 ± 41	9.663	9.659
3	-----	-----	-----	7.654 ± .002	7/2$^+$	----	----	10.137	10.136
4	-----	-----	-----	8.0192 ± .002	3/2$^+$	884 ± 170	99 ± 11	10.490	10.48
6	-----	-----	-----	8.9196 ± .002	5/2$^+$	3538 ± 527	108 ± 20	11.359	11.356
7	-----	-----	-----	9.0435 ± .002	5/2$^+$	1526 ± 120	371 ± 21	11.479	11.480

using polarized beam high-resolution data were extracted for the first, second, fourth, sixth (preliminary), and seventh T=3/2 states. Table 12-7 presents a summary of the data and a comparison with previous measurements. The conclusions based on the new information revealed from these measurements will be presented in Chapter 14.

13. $(\vec{p},p)$ and (p,p) Data III. - A = 33 and 37

13.1 Introduction. This chapter presents the $^{32}S(\vec{p},p)^{32}S$ and $^{36}Ar(\vec{p},p)^{36}Ar$ polarized beam high-resolution excitation-function data measured for T=3/2 states in ^{33}Cl and ^{37}K. The locations of several of these states were determined by the (p,t)-(p,^{3}He) single-angle cross section and analyzing power measurements made at Princeton.

13.2 First T=3/2 Resonance in ^{33}Cl. The first T=3/2 state in ^{33}Cl was the initial resonance we observed by polarized beam high resolution $(\vec{p},p)$ measurements. The $^{32}S(\vec{p},p)^{32}S$ data and T32GRD calculated fits are shown in Fig. 13-1. The resonance was measured during the same experiment in which the third T=3/2 resonance in ^{33}Cl was measured. The remeasurement of this lowest T=3/2 state was used to check our measurement and analysis methods.

The lack of information on the lattice structure of the Sb_2S_3 target made it impossible to calculate the Doppler broadening distribution. Because this first T=3/2 resonance occurs at such a low proton energy, thin (1.9 $\mu g/cm^2$) terminal stripping foils, with the Formvar backings burned off by unpolarized beam, were used. The straggling contribution from a foil of this thickness is 165 eV (FWHM). Thus, the overall machine energy fluctuation resolution was very good. The polarization of the beam was determined by the quench-ratio method [Ohl71] before and after each data point measurement. The resonance

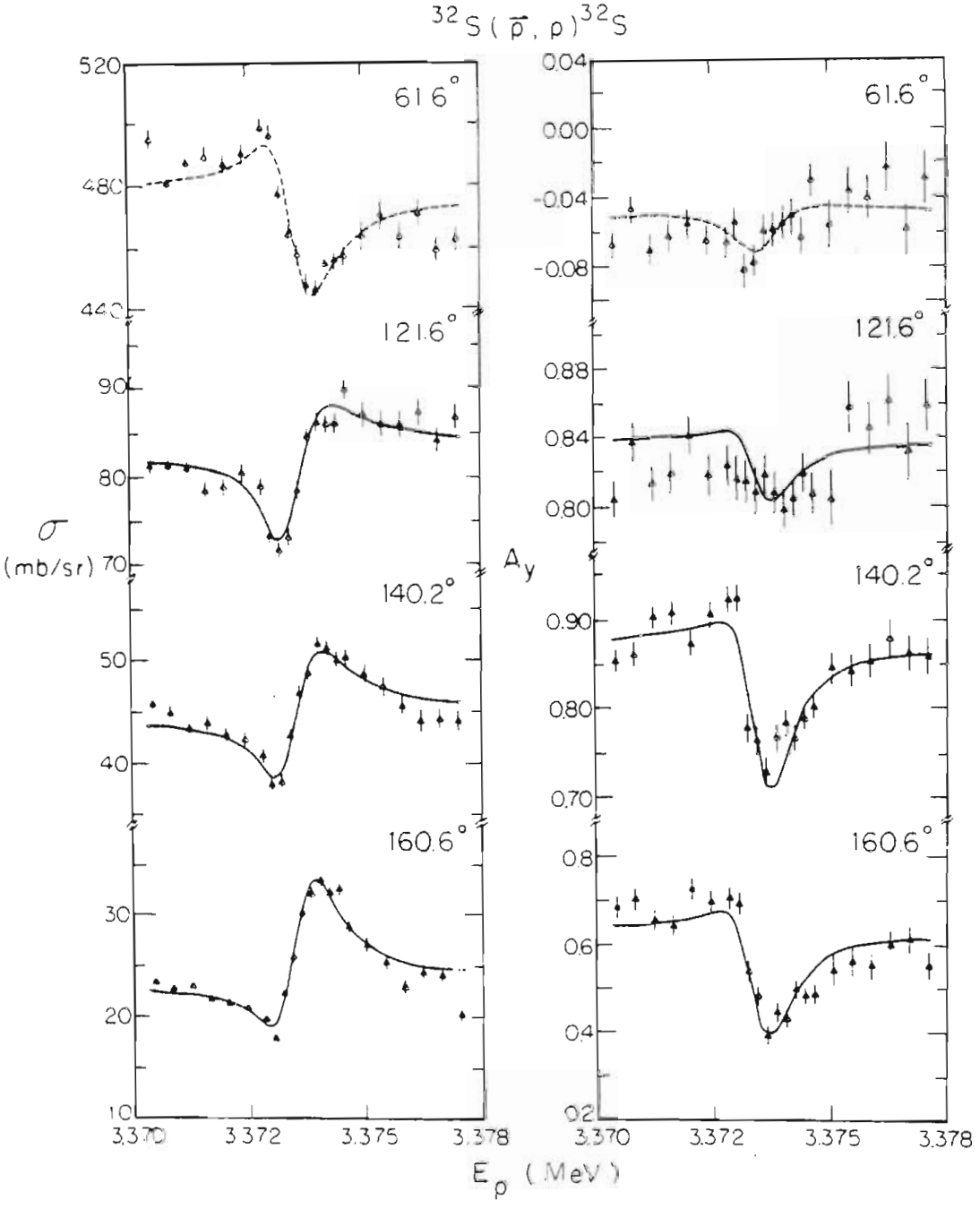

Figure 13-1 $^{32}S(\vec{p},p)^{32}S$ first T=3/2 isospin-forbidden resonance in ^{33}Cl. Data and fits for cross-section and analyzing-power excitation functions are shown at four angles. See text and Table 13-1 for details.

Table 13-1 1st T=3/2 State in ^{33}Cl Resonance Parameters.

$^{32}S(\vec{p},p)^{32}S$ first T=3/2 isospin-forbidden resonance parameters and measurement conditions.

1. Resonance Parameters.

E_R = 3.3745 ± .002 MeV $J^\pi = 1/2^+$ γ_p^2 = 121 ± 11 eV

Γ = 99.6 ± 9 eV Γ_p = 98.4 ± 9 eV Γ_p/Γ = 0.988 ± .08

Δ_{BD}^* = 712 ± 70 eV Δ_{ST} = 404 ± 40 eV

Angles used in analysis : 121.6°, 140.2°, 160.6°

*) See text and Table 11-1 for explanation of these parameters.

2. Excitation Function Measurement Parameters.

Energy Region Covered = 6.90 keV
Energy Step Size[1] = 418.1 eV
Average Beam Intensity = 25 nA
Average Beam Pol. = 0.83

Target : JF-1 10.6 μg/cm^2 Sb_2S_3 / 10.1 μg/cm^2 C

Target Nuclei = $5.631 \cdot 10^{16}$ /cm^2
Incident Particles* = $2.247 \cdot 10^{14}$

*) See text for special note

3. Chamber Geometry.

Det. Pair	θ_{lab} (deg)	θ_{cm} (deg)	Total Dis. (inches)	Coll. Hi. (inches)	Coll. Wi. (inches)	Solid Angle (msr)
1L-R	60.0	61.6	4.5	0.25	0.125	2.755
2L-R	120.0	121.6	4.5	0.50	0.125	5.842
3L-R	139.0	140.2	4.0	0.50	0.125	7.393
4L-R	160.0	160.6	4.0	0.50	0.125	7.393

parameters from the polarized beam measurement are shown in Table 13-1.

See Table 13-6 for a comparison of the polarized beam results and the earlier unpolarized beam [Iko76] measurements. The results from the polarized beam measurements are in excellent agreement with the earlier results obtained from an analysis of (p,p) excitation functions using a Γ_p / Γ value determined from β^+ delayed proton decay measurements.

13.3 Second T=3/2 Resonance in ^{33}Cl. The second T=3/2 state in ^{33}Cl was identified from the (p,t)-(p,^{3}He) single-angle comparisons. Before the Princeton (p,t) and (p,^{3}He) experiments were performed, significant beam time (three separate experiments) was used at TUNL attempting to locate this resonance. Problems occurred in searching for this resonance because the Sb_2S_3 targets had the natural isotopic abundances of sulfur (95 % ^{32}S and 4.21 % ^{34}S). It was not possible to obtain enriched ^{32}S in the form of Sb_2S_3. Strong resonances in ^{35}Cl were observed several times as small effects in the excitation function cross sections. However, when these bumps ('Ghosts in the night') were re-examined with tight windows set around the ^{32}S peak, but excluding the ^{34}S peak, the bumps in the excitation functions disappeared.

Our (p,p) searches had relied on the parent-analog energy location method for locating T=3/2 states, as detailed in Chapter 2. The negative results in searching for the second T=3/2 resonance in ^{33}Cl using these search techniques was a prime motivating factor in deciding to make the off-site (p,t) and (p,^{3}He) measurements.

After acquiring the Princeton (p,t) and (p,^{3}He) data, the second resonance was observed during the first $^{32}S(\vec{p},p)^{32}S$ energy excitation measurement attempt within 3 keV of the predicted resonance energy. This location is in strong disagreement with the previous identification of [Abb73] which assigns the T=3/2 state to the wrong resonance. In fact the work of [Abb73] is plagued with the same natural sulfur target problems described above. However, the authors did not realize the problems, and this resulted in the incorrect identification of many weak bumps in their data to be high-spin (7/2 or 9/2) negative-parity states. A quick check of known ^{35}Cl states reveals that most of the supposed ^{33}Cl high spin negative parity states occur at the same incident proton energy as strong ^{35}Cl states.

The data and T32GRD fits for our measurement of the second T=3/2 state are presented in Fig. 13-2. Data from only three angles are presented for this measurement. Because of the uncertainty of the beam energy resolution, the terminal stripping, and the Doppler broadening, only the beam-plus-doppler broadening width was obtained.

The extracted resonance parameters have a large uncertainty due to the fact that the T=3/2 resonance occurs within 2-4 keV of a very large T=1/2 resonance. At 163.5^o the cross section excitation function shows that the narrow T=3/2 resonance occurs at the T=1/2 resonance maximum. The T=1/2 resonance analyzing power excitation function does not change as rapidly. Because the cross section and analyzing power excitation functions surrounding the T=3/2 resonance are not constant with energy, the resonance parameters extracted from these data are questionable.

However, the identification as the second T=1/2 state is not in question. It may be possible to find angles where both the off-resonance cross section and analyzing powers are nearly constant. However, the T=3/2 resonances observed thus far suggest that this may be difficult. Table 13-2 summarizes the extracted resonance parameters. The comparison of the resonance parameters with the earlier [Abb73] work is shown in Table 13-6. This comparison is not between measurements of the same resonance since the [Abb73] work identified the wrong resonance as being the T=3/2 level.

13.4 Third T=3/2 Resonance in ^{33}Cl. The third T=3/2 resonance in ^{33}Cl observed by the $^{32}S(\vec{p},p)^{32}S$ reaction is shown in Fig. 13-3. The resonance parameters for this state are given in Table 13-3. The resonance energy of this state is in agreement with the energy assigned by (p,γ) measurements [Esw72]. This third T=3/2 state was incorrectly assigned to a nearby broad T=1/2 state by [Abb73]. Figure 2-5 shows the [Abb73] data and our measurement of the true T=3/2 state. The actual T=3/2 state can be seen as a bump of one data point in the [Abb73] work. The comparison of the two measurements is shown in Table 13-6. It should be mentioned that (p,p) work done elsewhere [Wam80] is in agreement with our reported measurements [Wil79] for this state.

The resolution parameters could not be completely extracted. Hence, only the beam-plus-Doppler parameter is given. The beam polarization for this resonance was determined by the quench-ratio method.

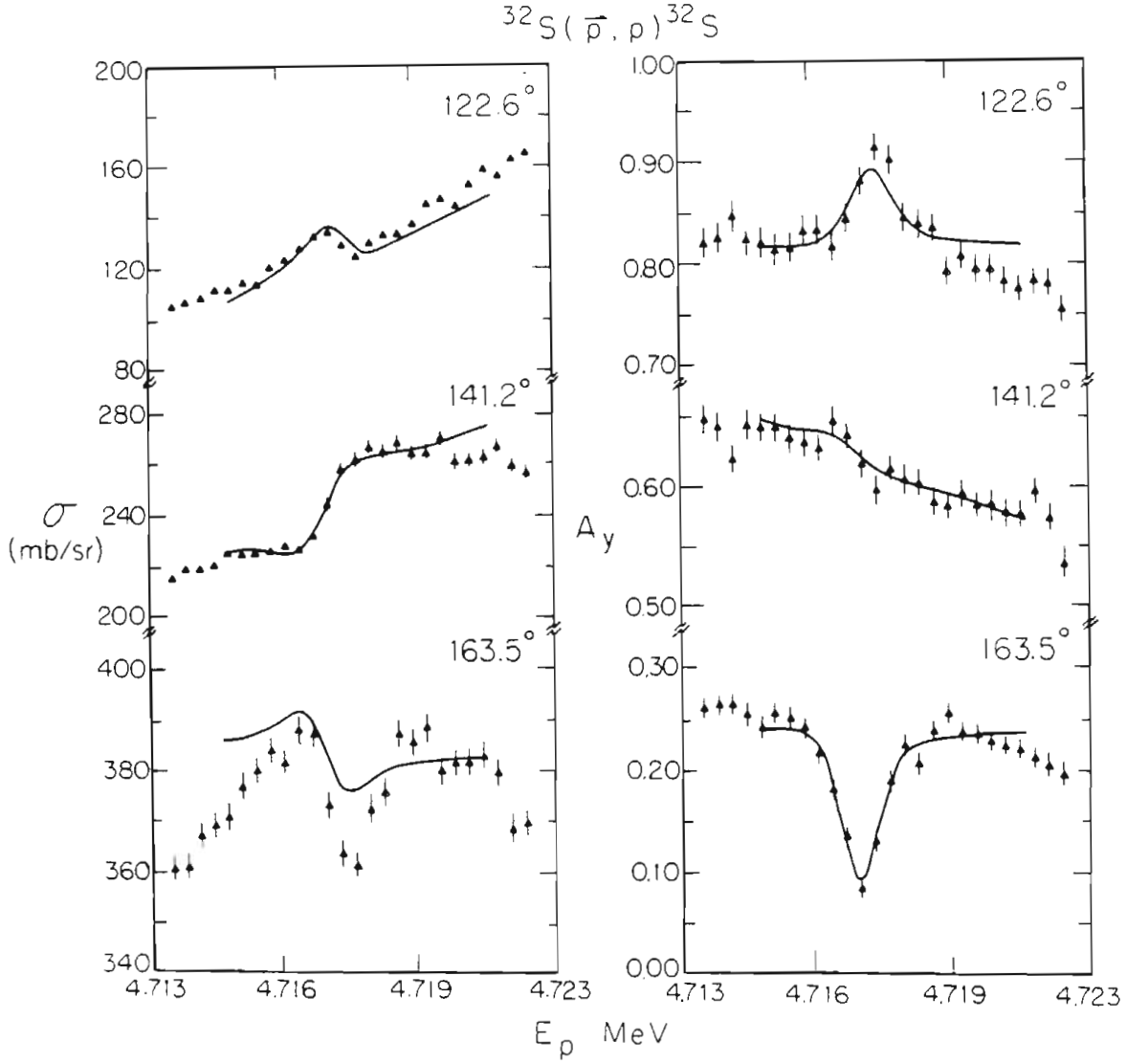

Figure 13-2 $^{32}S(\vec{p},p)^{32}S$ second T=3/2 isospin-forbidden resonance in ^{33}Cl. Data and fits for cross-section and analyzing-power excitation functions are shown at three angles. See text and Table 13-2 for details.

Table 13-2 2^{nd} T=3/2 State in ^{33}Cl Preliminary Resonance Parameters.

Preliminary $^{32}S(\vec{p},p)^{32}S$ second T=3/2 isospin-forbidden resonance parameters and measurement conditions.

1. Preliminary Resonance Parameters.

E_R = 4.7174 ± .002 MeV $J^\pi = 3/2^+$ γ_p^2 = 303 ± 90 eV

Γ = 356 ± 145 eV Γ_p = 100 ± 15 eV Γ_p / Γ^* = 0.28

Δ_{BD}^* = 970 ± 220 eV Δ_{ST} = 172 ± 17 eV

Angles used in analysis : 122.6°, 141.2°, 163.5°

*) See text and Table 11-1 for explanation of these parameters.

2. Excitation Function Measurement Parameters.

Energy Region Covered = 12.00 keV
Energy Step Size = 352.9 eV
Average Beam Intensity = 90 nA
Average Beam Pol. = 0.76

Target : H-30 6.3 $\mu g/cm^2$ Sb_2S_3 / 5.0 $\mu g/cm^2$ C

Target Nuclei = $3.350 \cdot 10^{16}$ $/cm^2$
Incident Particles = $2.497 \cdot 10^{14}$

3. Chamber Geometry.

Det. Pair	θ_{lab} (deg)	θ_{cm} (deg)	Total Dis. (inches)	Coll. Hi. (inches)	Coll. Wi. (inches)	Solid Angle (msr)
1L-R	54.0	55.5	4.0	0.50	0.0625	3.801
2L-R	121.0	122.6	4.0	0.50	0.125	7.393
3L-R	140.0	141.2	4.3	0.50	0.125	6.398
4L-R	163.0	163.5	4.0	0.50	0.125	7.393

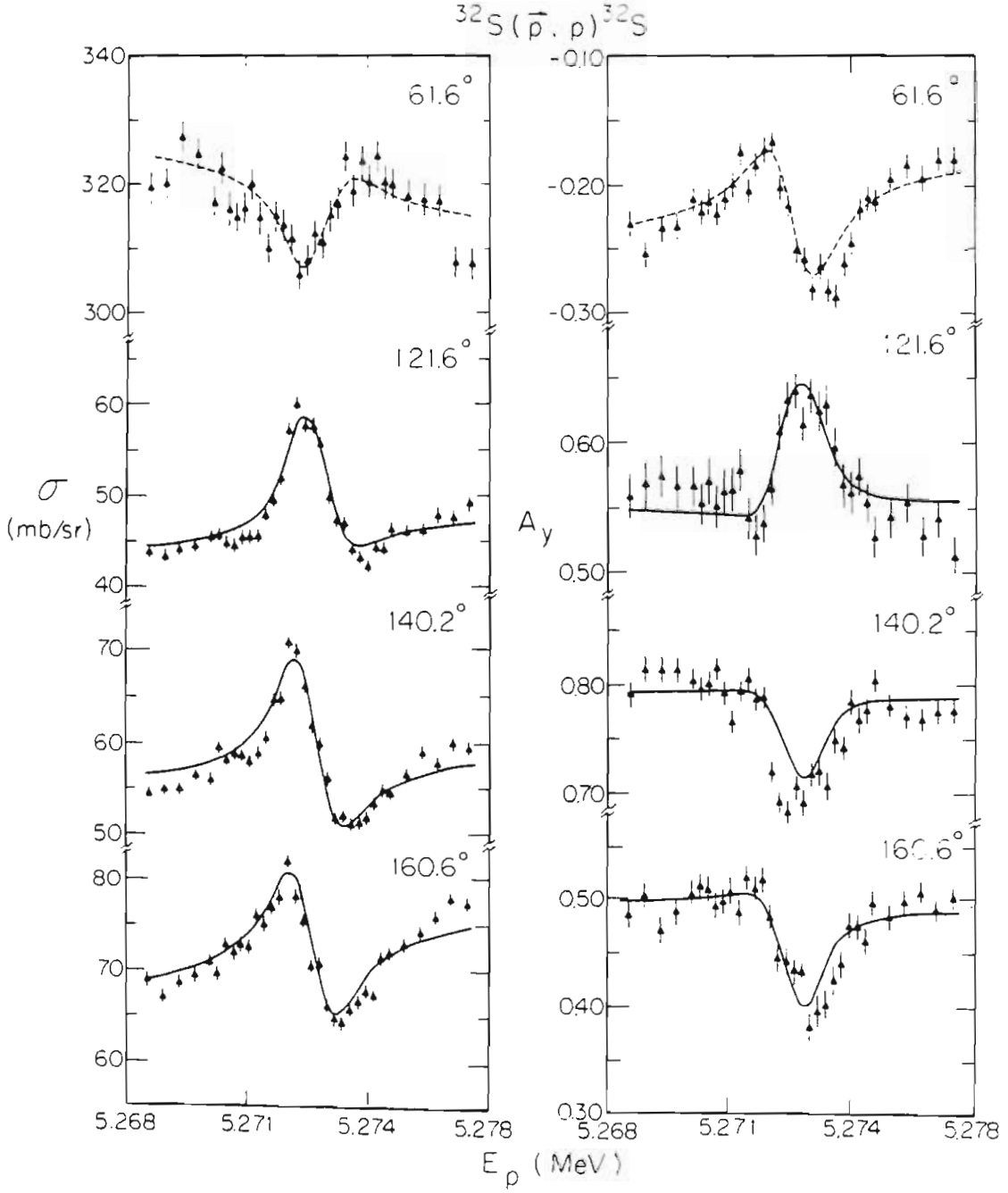

Figure 13-3 $^{32}S(\vec{p},p)^{32}S$ third T=3/2 isospin-forbidden resonance in ^{33}Cl. Data and fits for cross-section and analyzing-power excitation functions are shown at four angles. See text and Table 13-3 for details.

Table 13-3 3rd T=3/2 State in ^{33}Cl Resonance Parameters.

$^{32}S(\vec{p},p)^{32}S$ third T=3/2 isospin-forbidden resonance parameters and measurement conditions.

1. Resonance Parameters.

E_R = 5.2734 ± .002 MeV $J^\pi = 5/2^+$ γ_p^2 = 199 ± 3.3 eV

Γ = 108 ± 7 eV Γ_p = 95.6 ± 2 eV Γ_p/Γ = 0.884 ± .06

Δ_{BD}* = 1000 ± 130 eV Δ_{ST} = 260 ± 26 eV

Angles used in analysis : 121.6°, 140.2°, 160.6°

*) See text and Table 11-1 for explanation of these parameters.

2. Excitation Function Measurement Parameters.

Energy Region Covered = 8.26 keV
Energy Step Size[1] = 201.4 eV
Average Beam Intensity = 50 nA
Average Beam Pol.* = 0.84

Target : JF-1 10.6 μg/cm^2 Sb_2S_3 / 10.1 μg/cm^2 C

Target Nuclei = $5.631 \cdot 10^{16}$ /cm^2
Incident Particles = $2.996 \cdot 10^{14}$

*) See text for special note

3. Chamber Geometry.

Det. Pair	θ_{lab} (deg)	θ_{cm} (deg)	Total Dis. (inches)	Coll. Hi. (inches)	Coll. Wi. (inches)	Solid Angle (msr)
1L-R	60.0	61.6	4.5	0.25	0.125	2.755
2L-R	120.0	121.6	4.5	0.50	0.125	5.842
3L-R	139.0	140.2	4.0	0.50	0.125	7.393
4L-R	160.0	160.6	4.0	0.50	0.125	7.393

13.5 Higher T=3/2 Resonances in ^{33}Cl. The unpolarized beam (p,p) excitation- function data were taken over energy regions in the ^{33}Cl compound nucleus corresponding to possible T=3/2 state locations. The predicted T=3/2 state locations were based on the ^{35}Cl(p,t)^{33}Cl and ^{35}Cl(p,^{3}He)^{33}S measurements made at Princeton. No effort was made to make polarized beam measurements over these same energy regions. These higher-lying resonance excitation function data exhibit many resonances.

13.6 First T=3/2 Resonance in ^{37}K. The first T=3/2 state in ^{37}K was observed by ^{36}Ar($\vec{p}$,p)^{36}Ar scattering using the ion-implanted ^{36}Ar targets discussed in Chapter 10. The resonance is shown in Fig. 13-4. The resonance parameters are given in Table 13-4.

The analysis of this resonance was complicated by the mistake of using two ion implant energies (of 10 keV and 50 keV) to make the target. The two implant energies give a double-peaked distribution of ^{36}Ar ions implanted into a region of ~ 12 $\mu g/cm^2$ in the carbon foil. In order to calculate the resonance distribution, a constant density of ^{36}Ar ions implanted to a depth of ~ 12 $\mu g/cm^2$ was assumed. Based on the calculated distribution [SPI01], this is not an unrealistic assumption. The effect of energy straggling in the carbon foil was thus folded into the resolution distribution. However, it is not clear how the actual density distribution of ^{36}Ar affects the observed resonance shape.

The Doppler broadening distribution for the ^{36}Ar can be calculated based on two models describing the lattice coupling of the ^{36}Ar ions in the carbon. In the calculation that provides the largest Doppler

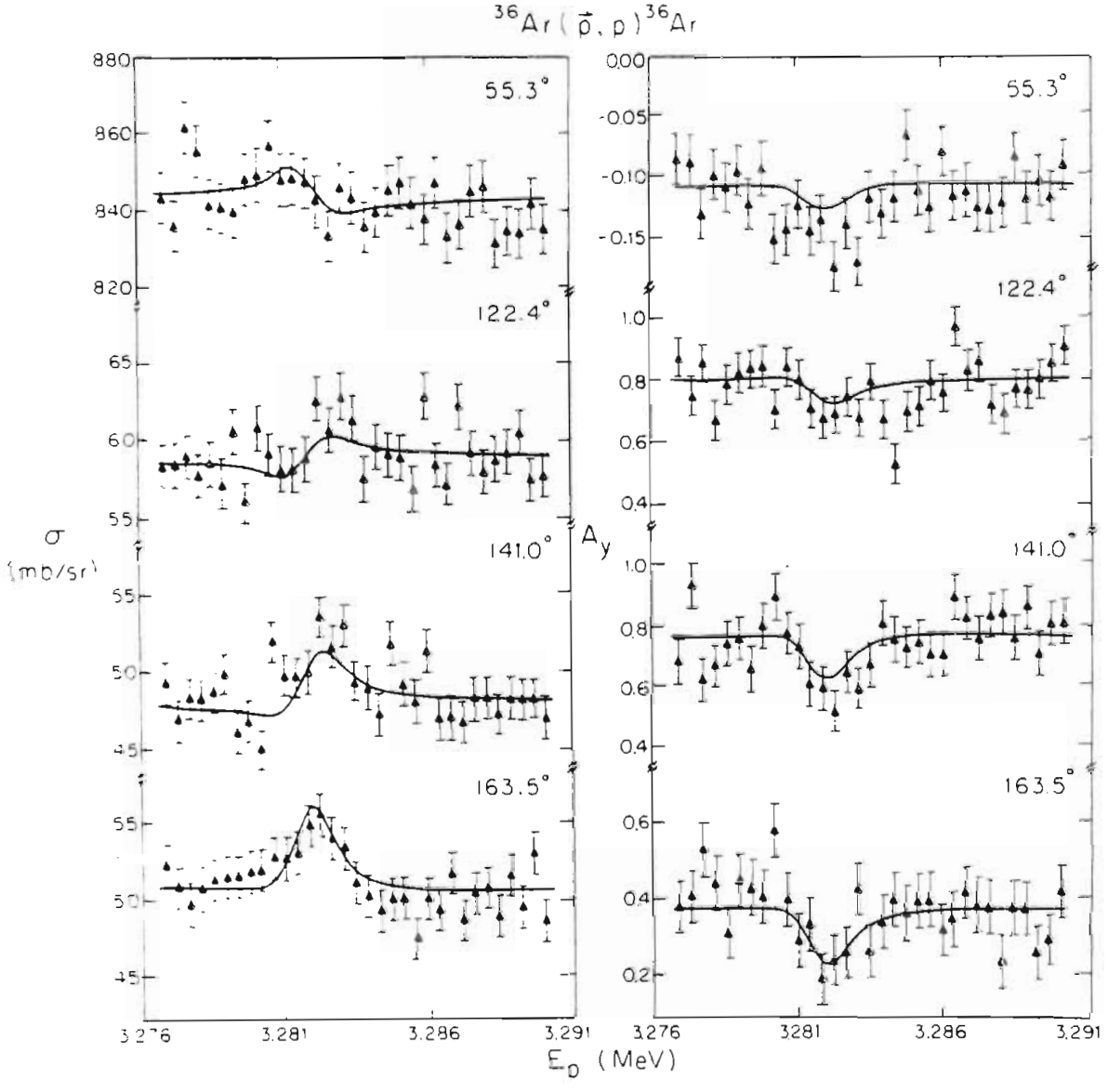

Figure 13-4 $^{36}Ar(\vec{p},p)^{36}Ar$ first T=3/2 isospin-forbidden resonance in ^{37}K. Data and fits for cross-section and analyzing-power excitation functions are shown at four angles. See text and Table 13-4 for details.

Table 13-4 1^{st} T=3/2 State in ^{37}K Resonance Parameters.

$^{36}Ar(\vec{p},p)^{36}Ar$ first T=3/2 isospin-forbidden resonance parameters and measurement conditions.

1. Resonance Parameters.

$E_R = 3.2840 \pm .002$ MeV $J^\pi = 3/2^+$ $\gamma_p^2 = 561 \pm 83$ eV

$\Gamma = 38 \pm 6$ eV $\Gamma_p = 34 \pm 5$ eV $\Gamma_p / \Gamma = 0.900 \pm .10$

$\Delta_{BD}^{*} = 1250 \pm 100$ eV $\Delta_{ST} = 665 \pm 100$ eV

Angles used in analysis : 122.4^o, 141.0^o, 163.5^o

*) See text and Table 11-1 for explanation of these parameters.

2. Excitation Function Measurement Parameters.

Energy Region Covered = 13.0 keV
Energy Step Size = 409.5 eV
Average Beam Intensity = 32 nA
Average Beam Pol. = 0.75

Target* : C-1 2.1 $\mu g/cm^2$ ^{36}Ar / 91 $\mu g/cm^2$ C

Target Nuclei = $3.513 \cdot 10^{16}$ $/cm^2$
Incident Particles = $1.498 \cdot 10^{14}$

*) See text for special note

3. Chamber Geometry.

Det. Pair	θ_{lab} (deg)	θ_{cm} (deg)	Total Dis. (inches)	Coll. Hi. (inches)	Coll. Wi. (inches)	Solid Angle (msr)
1L-R	54.0	55.3	4.0	0.50	0.0625	3.801
2L-R	121.0	122.4	4.3	0.50	0.125	6.398
3L-R	140.0	141.0	4.0	0.50	0.125	7.393
4L-R	163.0	163.5	4.0	0.50	0.125	7.393

broadening effect, one can assume that the ^{36}Ar has the same quantal energy due to vibrations as the surrounding carbon lattice structure for which the quantal energy is known. Using this assumption, the Doppler broadening distribution width for a 3.28-MeV incident proton beam would be 260 eV (FWHM). The other model assumes that the ^{36}Ar ions are in interstitial lattice locations. For the interstitial ^{36}Ar ion locations, the Doppler broadening distribution width is 150 eV.

Because of the uncertainties in the Doppler broadening and in the resolution effects resulting from the dual implant energies, only the beam-plus-Doppler distribution width is presented. These data are in general agreement with the previously measured results [Goo67]. However, the earlier results relied on comparisons of the elastic and inelastic proton yields to obtain the branching ratio.

13.7 Second T=3/2 Resonance in ^{37}K. Only a preliminary analysis of the second T=3/2 resonance in ^{37}K observed by $^{36}Ar(\vec{p},p)^{36}Ar$ scattering was performed. The location of this resonance was found within 6 keV of the energy predicted from our $^{39}K(p,t)^{37}K$ measurements. The excitation function data are shown in Fig. 13-5. The rapidly varying off-resonance cross section and analyzing power, coupled with the small resonance effects at 141.0° and 163.5°, made analysis of these two angles impossible, and thus no fits are shown. The T32GRD analysis of 55.3° and 122.4° data is not very reliable due to the necessary rotation. Table 13-5 presents the very preliminary resonance parameters extracted from analyzing the 55.3° and 122.4° data. The beam-plus-Doppler resolution parameter is the only resolution parameter presented because

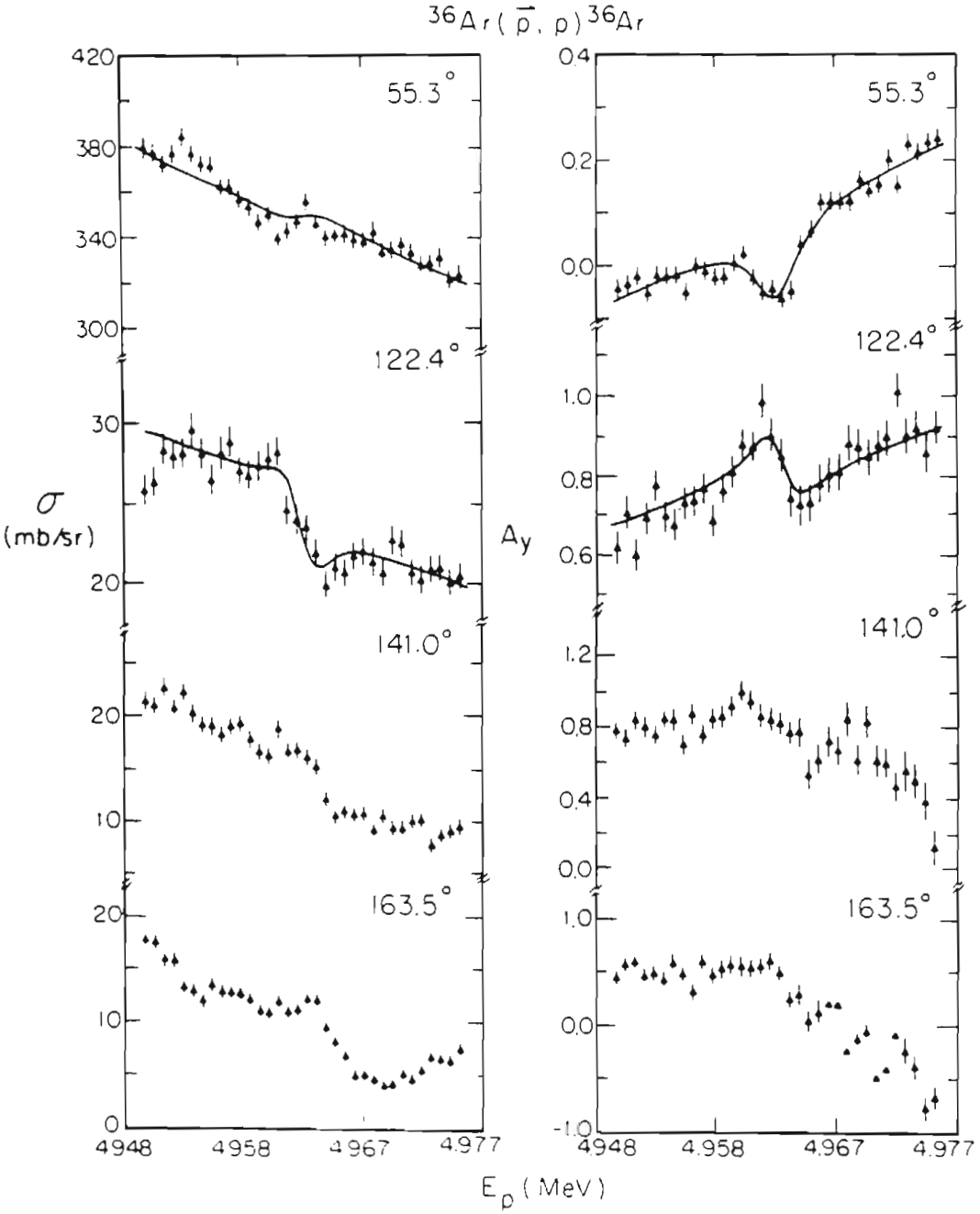

Figure 13-5 $^{36}Ar(\vec{p},p)^{36}Ar$ second T=3/2 isospin-forbidden resonance in ^{37}K. Data for cross-section and analyzing-power excitation functions are shown at four different angles. See text and Table 13-5 for details.

Table 13-5 2nd T=3/2 State in ^{37}K Preliminary Resonance Parameters.

Preliminary $^{36}Ar(\vec{p},p)^{36}Ar$ second T=3/2 isospin-forbidden resonance parameters and measurement conditions.

1. Preliminary Resonance Parameters.

E_R = 4.9634 ± .002 MeV $J^\pi = 1/2^+$ γ_p^2 = 330 ± 190 eV

Γ = 2750 ± 1061 eV Γ_p = 553 ± 320 eV Γ_p/Γ = 0.21 ± .14

Δ_{BD}^* = 1400 ± 400 eV Δ_{ST} = 335 ± 100 eV

Angles used in analysis : 55.3°, 122.4°

*) See text and Table 11-1 for explanation of these parameters.

2. Excitation Function Measurement Parameters.

Energy Region Covered = 25.85 keV
Energy Step Size = 760.2 eV
Average Beam Intensity = 65 nA
Average Beam Pol. = 0.73

Target* : C-23 1.6 μg/cm^2 ^{36}Ar / 91 μg/cm^2 C

Target Nuclei = $2.643 \cdot 10^{16}$ /cm^2
Incident Particles = $1.997 \cdot 10^{14}$

*) See text for special note

3. Chamber Geometry.

Det. Pair	θ_{lab} (deg)	θ_{cm} (deg)	Total Dis. (inches)	Coll. Hi. (inches)	Coll. Wi. (inches)	Solid Angle (msr)
1L-R	54.0	55.3	4.0	0.50	0.0625	3.801
2L-R	121.0	122.4	4.3	0.50	0.125	6.398
3L-R	140.0	141.0	4.0	0.50	0.125	7.393
4L-R	163.0	163.5	4.0	0.50	0.125	7.393

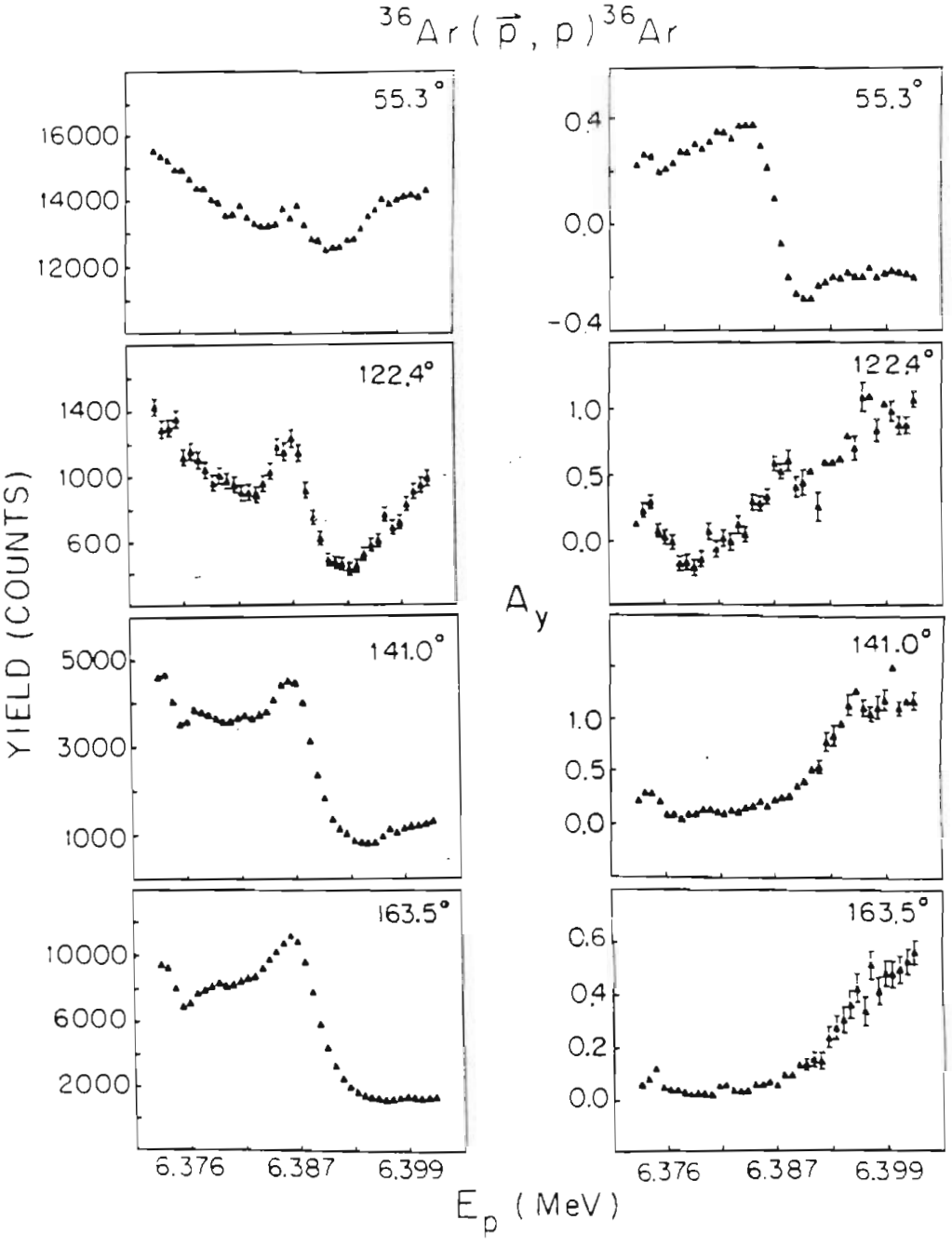

Figure 13-6 $^{36}Ar(\vec{p},p)^{36}Ar$ yield curve and analyzing-power excitation functions covering the energy region where the third T=3/2 isospin-forbidden resonance is predicted from $^{39}K(p,t)^{37}K$ data to occur.

Table 13-6 T=3/2 ^{33}Cl and ^{37}K Resonance Parameters.

Measurement of T=3/2 resonance parameters by $^{32}S(\vec{p},p)^{32}S$ and $^{36}Ar(\vec{p},p)^{36}Ar$.

- The E_x in column 10 is the predicted excitation energy from the $(\vec{p},p)$ measurements.
- The E_x in column 11 is the excitation energy measured from the (p,t) experiments.

Compound Nucleus	T=3/2 State	Previous Measurement Results			Present Measurement Results					
					$(\vec{p},p)$					(p,t)
		E_R (MeV)	Γ (eV)	Γ_p (eV)	E_R (MeV)	J^π	Γ (eV)	Γ_p (eV)	E_x (MeV)	E_x (MeV)
^{33}Cl	1	3.370 ± .001 [a]	115 ± 15 [b]	115 ± 15 [b]	3.3745 ± .002	1/2$^+$	100 ± 9	98 ± 9	5.549	5.548
	2	4.855 ± .003 [c]	10000 ± 1000 [c]	7000 ± 700 [c]	4.7174 ± .002	3/2$^+$	356 ± 145	100 ± 15	6.851	6.848
	3	5.284 ± .003 [c]	11000 ± 1100 [c]	10400 ± 1040 [c]	5.2734 ± .002	5/2$^+$	108 ± 7	96 ± 2	7.391	7.390
^{37}K	1	3.278 ± .003 [d]	40 ± 20 [d]	40 ± 20 [d]	3.2840 ± .002	3/2$^+$	38 ± 6	34 ± 5	5.052	5.052
	2	----	----	-----	4.9634 ± .002	1/2$^+$	2750 ± 1061	553 ± 320	6.686	6.692
	3	------	-----	-----	6.374 ± .004	5/2$^+$	------	------	8.058	8.071

a) [Abb70] energy determination.

b) [Iko76] using (p,p) scattering.

c) [Abb73] using (p,p) scattering.

d) [Goo67] and [Sex73] using (p,p) scattering.

of the problems in estimating resolution effects discussed in Section 13.6 for the first T=3/2 resonance in ^{37}K.

13.8 Third T=3/2 Resonance in ^{37}K. The third T=3/2 resonance in ^{37}K was observed by $^{36}Ar(\vec{p},p)^{36}Ar$ scattering. Two resonances were observed in the energy region predicted from the $^{39}K(p,t)^{37}K$ measurements. The energy excitation data are shown in Fig. 13-6. The energy of the small resonance on the far left is 6.374 MeV, and the energy of the large resonance is 6.388 MeV. However, the 6.374-MeV resonance which is much narrower than the 6.388-MeV resonance is most likely the third T=3/2 state. This resonance is within 13 keV of the $^{39}K(p,t)^{37}K$ predicted resonance energy.

No analysis of the 6.374-MeV resonance was attempted because of the lack of off-resonance excitation function data and the large step sizes used.

13.9 Summary of Measurements. A summary of the resonances measured in ^{33}Cl and ^{37}K and a comparison with the previous measurements are given in Table 13-6. The behavior of the reduced proton widths for all the resonance measurements presented in Chapters 11, 12, and 13 will be discussed in the next chapter.

14. Isospin Mixing and Proton Reduced Widths

14.1 Introduction. The existence of T=3/2 isospin-forbidden resonances with total widths of 40 eV to several keV implies that the T=3/2 compound-nucleus state and/or the T=0 target and final-state wave functions are not pure isospin states. Several different models based on various isospin-mixing mechanisms have been used previously to estimate the strength of isospin impurities in the above mentioned states. It may be helpful to review Section 1.1 which summarizes some of the formalism and definitions used in describing isospin mixing. A review of Sections 1.1.2-1.1.3 which detail the previous experimental results of measurements of the T=3/2 and T=2 isospin-forbidden resonances may also be helpful.

14.1.1 Isospin-Mixing Mechanisms. The isospin admixtures present in the T=0, $J^{\pi}=0^{+}$ target nucleus can possibly result from the mixing of the unperturbed pure T=0 state with the $T_{>}$ (T=1,2,...) levels of identical spin and parity [Rad53, MDo60, Boh67, Moh69, Sop69, Lee72, Ber72]. According to conventional mixing models [MDo56, Ari71, Aue71, Lev73, Ber72], the isospin admixtures present in the compound T=3/2 state result from three possible mechanisms:

(1) Mixing with nearby $T_{<}$ levels of the same spin and parity [MDo60, Ari71, Lev73].

(2) Mixing with the $T_{<}$ "monopole" states in the compound nucleus

(i.e. states described by the shell model having the same ℓ and j as the compound $T_>$ state, but different principal orbit numbers n'). These states occur at higher excitation energies then the T=3/2 states in the compound nucleus [Ari71, Lev73]. (This mixing is sometimes referred to as continuum mixing [Ari71].)

(3) Mixing with the "antianalog" state, the isospin $T_<$ state described by the shell model as having the identical configuration $(n\ell j)$. This state will occur at a lower excitation energy than the T=3/2 state [Aue71, Ari71].

There is also the possibility of direct mixing between the compound T=3/2 state and the T=0 target [Aue71]. The three mechanisms described above mix through intermediate states. However, the direct mixing occurs between the compound nucleus state and the target final state. The mixing results from a two-body interaction, such as the two-body Coulomb interaction which is described below. In shell model formalism, the direct mixing changes the orbits of both of the two interacting particles.

None of the calculations using these mixing mechanisms predict the A=8 periodic behavior exhibited by the decay of the first T=3/2 states in A=4n+1 T_z=-1/2 nuclei to the T=0 ground states of the target nuclei. Therefore, other mixing mechanisms may exist which result in admixtures in the compound analog state, the final state, or both.

14.1.2 Isospin-Mixing Interactions. The possible charge-dependent forces which introduce the isospin admixtures are the electromagnetic and the hadronic forces. The electromagnetic force is manifested in the

Coulomb interaction, neutron-proton mass differences, and magnetic interactions. In order to investigate any possible charge dependence of the nuclear force, the contributions of the electromagnetic force must be totally accounted for. Calculations using the Coulomb interaction alone are able to account for the charge dependences observed in most of the measurements of charge-dependent processes [Hen69, Ber72].

The Coulomb interaction operator can be described in isospin formalism as [Sop69]

$$C = \sum_{i<j} \frac{e^2}{r_{ij}} \left(\frac{1}{2} - t_z^i\right)\left(\frac{1}{2} - t_z^j\right), \qquad 14\text{-}1$$

where t_z^i is the isospin operator for nucleon i, and r_{ij} is the separation of a pair of nucleons. Operating on a state of definite isospin T, $\phi_o(T, T_z)$ with the Coulomb operator C yields a state $C\phi_o$ which no longer has pure isospin T, but can be described by a superposition of pure isospin states

$$C\phi_o = V_o\phi_o + \sum_{\lambda\, T'} V_\lambda(T')\phi_\lambda(T', T_z) \qquad 14\text{-}2$$

where V_o is the original amplitude of state ϕ_o and $V_\lambda(T')$ are the amplitudes of the λ different orthogonal states of various isospins. The amplitudes $V_\lambda(T')$ are calculated in first-order perturbation theory by the Coulomb-interaction matrix elements between the states

$$V_\lambda(T') = \langle\phi_\lambda(T', T_z)|C|\phi_\lambda(T, T_z)\rangle. \qquad 14\text{-}3$$

The total isospin impurity in the wave function, in first-order perturbation theory is [Ber72]

$$\alpha^2 = \sum_{\lambda\, T'} V_\lambda^2(T')/(\varepsilon_\lambda - \varepsilon_o)^2 \qquad 14\text{-}4$$

where ε_o is the energy of the state of pure isospin and ε_λ are the energies of the λ orthogonal states. The Coulomb interaction can be divided into three parts representing its transformation properties under isospin rotations, isoscalar, isovector, and isotensor:

$$C = S + T^{(1)} + T^{(2)} \qquad 14\text{-}5a$$

$$S = \sum_{i<j} \left(\frac{1}{4} + \frac{1}{3}t^i \cdot t^j\right) \frac{e^2}{r_{ij}} \qquad \text{(isoscalar)} \qquad 14\text{-}5b$$

$$T^{(1)} = -\sum_{i<j} \frac{1}{2}\left(t_z^i + t_z^j\right) \frac{e^2}{r_{ij}} \qquad \text{(isovector)} \qquad 14\text{-}5c$$

$$T^{(2)} = \sum_{i<j} \left(t_z^i t_z^j - \frac{1}{3}t^i \cdot t^j\right) \frac{e^2}{r_{ij}} \qquad \text{(isotensor).} \qquad 14\text{-}5d$$

The scalar term S operates only between states of the same isospin and can be included in the charge-independent part of the Hamiltonian. The isovector term $T^{(1)}$ can change the isospin by $\Delta T = 0, \pm 1$ while the isotensor term $T^{(2)}$ has $\Delta T = 0, \pm 1$, and ± 2. Therefore, in our experiments, in which $\Delta T=1$, isovector and isotensor terms may contribute.

14.1.3 Isospin-Mixing Calculations. A review of the different calculations of isospin mixing in light nuclei can be found in [Sop69,

Ber72]. Calculations of isospin mixing in T=0, $J^{\pi}=0^{+}$ N=Z self-conjugate nuclei using a Fermi gas model and including mixing from only T=1 states predict isospin impurities in nuclear ground states ranging from $3 \cdot 10^{-5}$ (^{4}He) to $9 \cdot 10^{-3}$ (^{40}Ca) [Ber72]. Shell-model harmonic-oscillator monopole state mixing calculations using only T=1 states indicate admixtures of $1 \cdot 10^{-5}$ (^{4}He) and $1.2 \cdot 10^{-2}$ (^{40}Ca) [Ber72]. Both of these calculations replaced the two-body Coulomb interactions with a one-body Coulomb interaction and are isovector in character. The isospin admixtures in the Z=N target nuclei result in a Z dependence of the reduced widths from $Z^{1.7}$ to $Z^{3.5}$ [Iko76] depending on the models used [MDo60, Boh67, Sop69, Moh69, Lee72, Ber72]. None of these models were used to predict the magnitudes of the reduced widths.

All of these calculations include only isovector forces and were calculated with one-body Coulomb interaction. ($\Delta T = 0, \pm 1$). However, as explained in Sections 1.1.1-1.1.3, it is necessary to include isotensor terms to describe the experimentally measured reduced widths. For example, the observed order of magnitude differences of the lowest T=3/2 T_z=+1/2 neutron reduced widths magnitudes compared to the T_z=-1/2 proton reduced widths sizes cannot be described by isovector interactions alone [McD78]. The T=3/2 T_z=+1/2 and T=3/2 T_z=-1/2 state decays are mirror decays to the same A=4n target nuclei ground state. Having only isovector mixing requires the isospin admixtures for the two decays to be equal. Thus, the isospin-mixing calculations must include significant isotensor contributions.

Calculations have been performed by Auerbach and Lev [Aue71] to estimate the direct Coulomb (two-body) mixing between the analog state and the final state, and also the contribution from the analog-state mixing with the antianalog state. The antianalog mixing used one-body Coulomb interaction and ignored any isotensor interaction contributions. The calculations were performed for the proton decay of the first T=3/2 states in ^{13}N, ^{17}F, ^{33}Cl, and ^{41}Sc [Aue71]. These calculations predicted very small effects from the direct Coulomb mixing compared to the antianalog contributions. The predicted magnitudes of the reduced widths were larger by an order of magnitude than the observed reduced widths. No regular A dependence could be inferred from these results.

Calculations for the analog state mixing in the compound nucleus with the nearby $T_<$ states and the monopole states have also been performed [Ari71, Lev73]. The [Lev73] calculations indicated that the monopole contribution to the mixing should be an order of magnitude smaller than the mixing with the nearby $T_<$ states. These results disagreed with Arima and Yoshida [Ari71], which reported greater contributions from the monopole mixing terms than the $T_<$ states. However, the [Ari71] calculations using configuration-mixed shell model wave functions were found to be very sensitive to the single-particle well depth and did not include many-body correlations which may reduce the size of the monopole mixing [Aue71].

As mentioned in Section 1.1.3, the lowest T=3/2 and T=2 isospin-forbidden decays exhibit similar widths and A dependences. This similarity in widths, implies that the chance mixing with nearby $T_<$

states is not a dominant contribution to the observed isospin mixing, because the excitation regions in the different nuclei where these T=3/2 and T=2 nuclear levels occur have very different nuclear structure. None of the calculations for mixing of the T=3/2 compound states predict the observed A=8 oscillatory behavior of the T_z=-1/2 elastic proton reduced widths. Also, only the [Ari71] calculation included two-body isotensor terms (through direct Coulomb mixing). The mixing mechanisms which which have been used to produce isospin admixtures in the compound nucleus do not have significant isotensor components and do not explain the experimental results [McD78].

There is one model which can predict the general trends with A observed in the reduced widths for the first T=2 and T=3/2 analog state measurements [McD78]. This schematic model includes isotensor mixing and hence can predict differences between T=3/2 neutron and proton decays. The model, which relates off-diagonal isospin-mixing matrix elements to isobaric multiplet mass differences, is essentially a parameterization of the observed data with little physical interpretation. Most importantly, the model cannot account for the A=8 oscillations displayed by the first T=3/2 proton-decay reduced widths.

14.2 Systematic Behavior of Reduced Widths. A summary of the systematic behavior of previously measured proton elastic scattering reduced widths for the lowest T=3/2 and T=2 resonances was presented in Section 1.1.3. Several of the first T=3/2 resonances in A=4n+1 T_z=|-1/2| nuclei were remeasured in the present work by using $(\vec{p},p)$ scattering and the helicity amplitude analysis method. See Chapters 5-13. A summary of

these first T=3/2 state reduced widths, the 9 high-lying T=3/2 state reduced widths extracted from measurements made by the present work, and the reduced widths extracted from previously measured high-lying T=3/2 states follows.

14.2.1 Comparison of A-Dependences of Reduced Widths. A comparison of the elastic proton reduced widths extracted for the first T=3/2 resonances in A=4n+1 nuclei using the previous measurements and the results from the present measurements is shown in Fig. 14-1. The reduced widths are plotted against the mass number A of the A=4n target nucleus. The reduced widths for all cases shown were calculated using Eq. 1-1 with a matching radius value r_o=1.4. The agreement between the two methods is excellent. The disagreement between the ^{13}N first T=3/2 reduced width measurements results partially from the inclusion of atomic effects in the present analysis. The new measurements of the first T=3/2 resonances in A=4n+1 T_z=-1/2 nuclei did not change any of the conclusions on isospin mixing presented in Section 1.1.3.

The new $(\vec{p},p)$ reduced widths based on a method which utilized only one type of measurement are assumed to be more accurate than the previous widths extracted by combining several experiments. Figure 14-2 shows the best-value first T=3/2 p_o reduced widths including the new width values extracted from the polarized beam measurements. The resonance parameters are presented in Table 14-1. Notice that the values of $\gamma^2_{p_o}$ for the A=8n and A=8n+4 nuclei appear to be converging with increasing A.

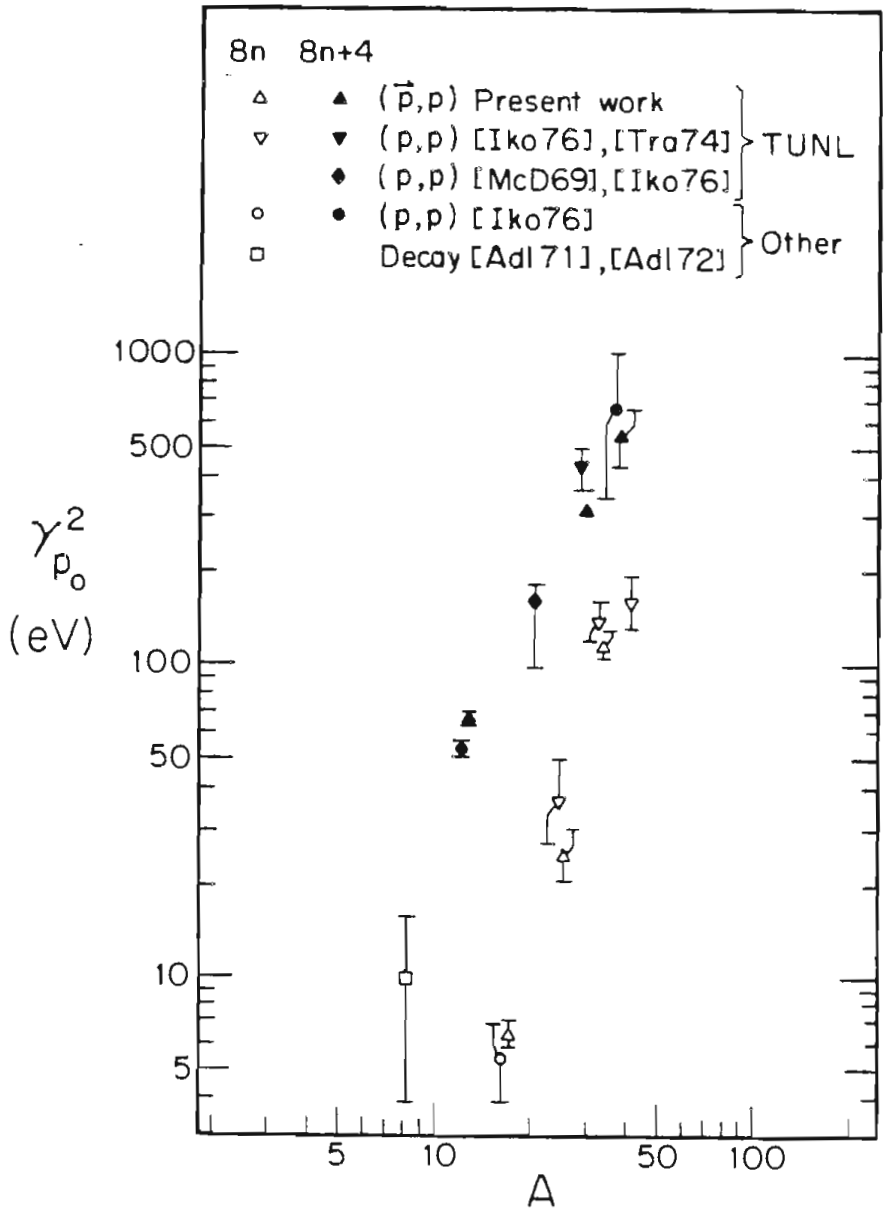

Figure 14-1 A comparison of measurements by the present and previous methods of the proton reduced widths γ_p^2 for the p_o decays of the first T=3/2 states in A=4n+1 T_z=-1/2 nuclei to the T_z=0 A=4n ground states. The reduced widths are plotted versus mass number A. The oscillation of the reduced widths for A=8n (open points) and A=8n+4 (solid points) target nuclei is apparent. See Table 1-1, Table 14-1, and Section 14.2.1 for discussion. The reduced widths were all calculated with a matching radius of r_o=1.4.

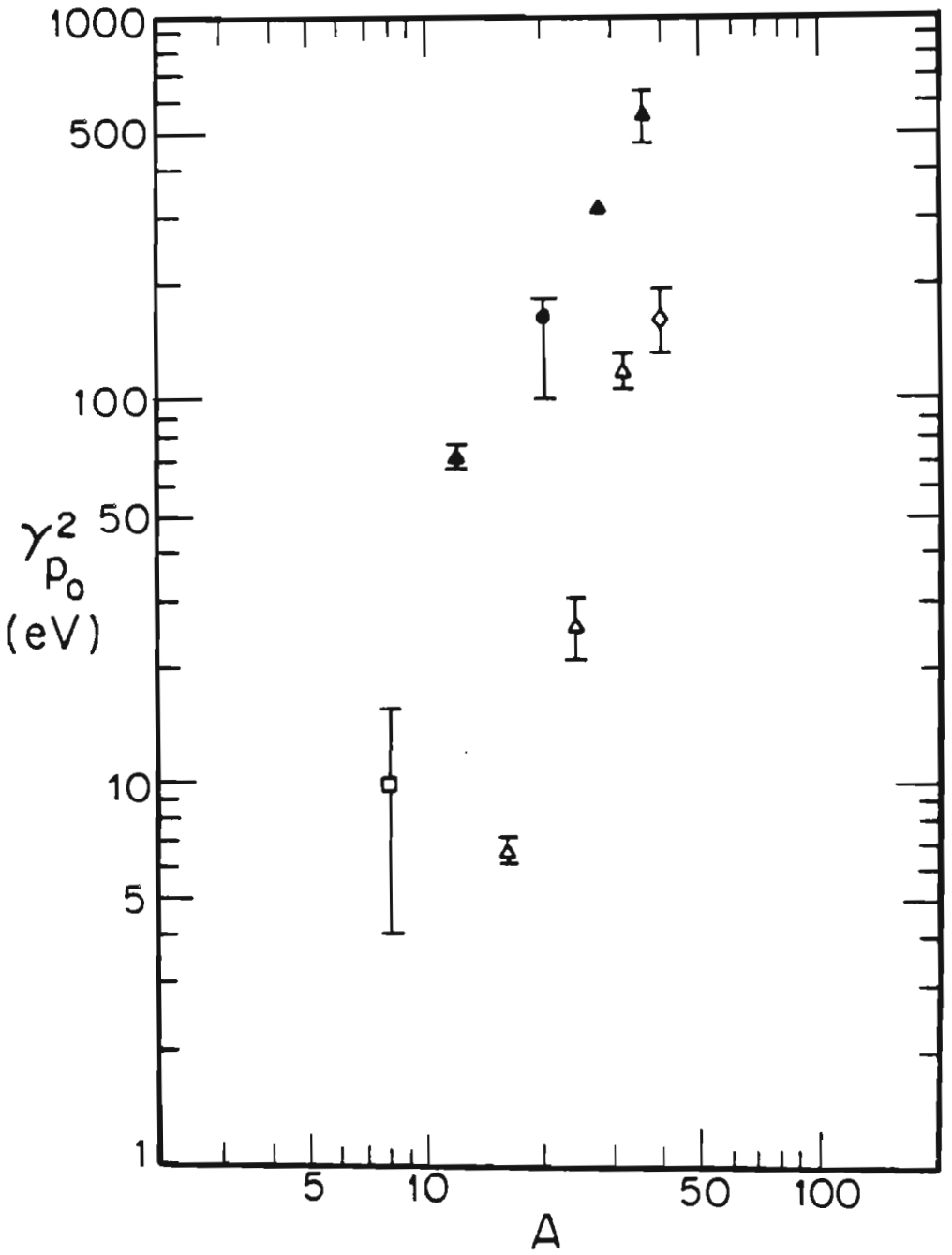

Figure 14-2 The proton reduced widths γ_p^2 for the p_o decays of the first T=3/2 states in A=4n+1 T_z=-1/2 nuclei to the T_z=0 A=4n ground states are plotted versus mass number A. The oscillation of the reduced widths between A=8n (open points) and A=8n+4 (solid points) target nuclei is apparent. The triangles are reduced widths determined from the present measurements. The sources for the other symbols are: open box - [Ad171, Ad172], solid dot [Iko76], and open diamond [Tra74]. See Table 14-1 and Section 14.2.1 for discussion.

Table 14-1 Resonance Parameters for the First T=3/2 States in A=4n+1 T_z=-1/2 Nuclei as Determined in Present and Previous Measurements.

See Tables 1-1, 11-7, 11-8, 12-7, and 13-6 and Section 14.2.1.

A=4n T_z=0	A=4n+1 T_z=-1/2	J^π	E_R (MeV)	Γ (eV)	Γ_p (eV)	$\gamma_{p_o}^2$ (eV)
^{8}Be	^{9}B	$3/2^-$	16.695 [b]	275 ± 93	30 ± 17 [f]	10 ± 6
^{12}C	^{13}N	$3/2^-$	14.2308 ± .0002 [c]	1010 ± 30	281 ± 15 [a]	71 ± 4
^{16}O	^{17}F	$1/2^-$	11.2642 ± .002 [a]	183 ± 13	23 ± 2 [a]	7 ± 1
^{20}Ne	^{21}Na	$5/2^+$	6.872 ± .005 [d]	750^{+50}_{-250}	150^{+10}_{-50} [d]	165^{+13}_{-65}
^{24}Mg	^{25}Al	$5/2^+$	5.8671 ± .002 [a]	105 ± 18	18 ± 4 [a]	26 ± 5
^{28}Si	^{29}P	$5/2^+$	5.8392 ± .002 [a]	271 ± 10	216 ± 5 [a]	319 ± 6
^{32}S	^{33}Cl	$1/2^+$	3.3744 ± .002 [a]	100 ± 9	98 ± 9 [a]	121 ± 11
^{36}Ar	^{37}K	$3/2^+$	3.284 ± .002 [a]	38 ± 6	34 ± 5 [a]	561 ± 83
^{40}Ca	^{41}Sc	$3/2^+$	4.967 ± .004 [e]	55 ± 5	55 ± 5 [e]	165 ± 30

a) [Present] b) [Ajz79] c) [Hue74] d) [McD69] e) [Tra74]

f) [McD76]

The elastic proton reduced widths $\gamma^2_{p_o}$ which have been determined for the second T=3/2 levels are presented in Fig. 14-3 and Table 14-2. The present measurements of the second T=3/2 states in in ^{17}F, ^{25}Mg, ^{29}P, and ^{33}Cl are shown along with the extracted reduced width for the second T=3/2 level in ^{21}Na measured by [McD69]. The ^{33}Cl point has a dashed, large error bar resulting from the uncertainty of the resonance analysis which was complicated by the presence of a nearby, wide T=1/2 resonance (see Section 13.3). The reduced width for the ^{37}K second T=3/2 state is not shown because of the poor quality of the $^{36}Ar(\vec{p},p)^{36}Ar$ data and the non-constant off-resonance cross sections and analyzing powers. The properties exhibited by these second T=3/2 reduced widths are:

(1) The second T=3/2 reduced widths are slightly larger than the first T=3/2 state reduced widths.

(2) The general trend of the second T=3/2 reduced widths with A is similar to that of the first T=3/2 states.

(3) There is evidence that the A=8 periodic behavior displayed by the first T=3/2 A=4n+1 nuclei might persist for the second T=3/2 resonances. However, the magnitude of the difference between reduced widths resulting from the A=8n and A=8n+4 target nuclei is not as great as for the first T=3/2 states. Also, note that the reduced widths for the A=8n and A=8n+4 nuclei do not converge in the same A region as the widths from the first T=3/2 states.

14.2.2 Comparison of A-Dependences of Average Reduced Widths. The average reduced widths for each A=4n+1 T_z=-1/2 nucleus were calculated by summing the individual T=3/2 resonance proton elastic reduced widths

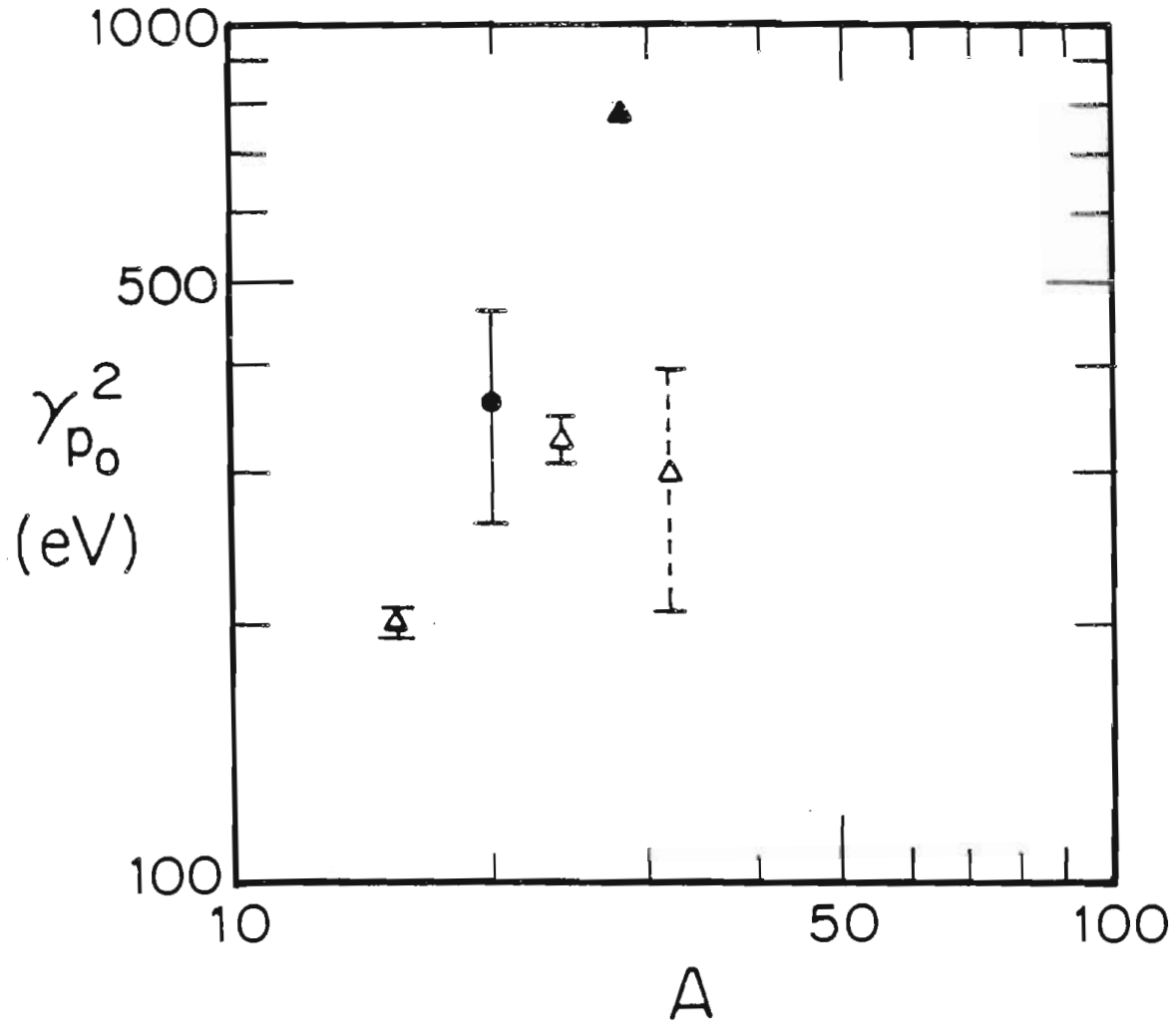

Figure 14-3 The proton reduced widths γ_p^2 for the p_o decays of the second T=3/2 states in A=4n+1 T_z=-1/2 nuclei to the T_z=0 A=4n ground states are plotted versus mass number A. The reduced widths are plotted as open points for A=8n target nuclei and as solid points for A=8n+4 target nuclei. The triangles are reduced widths determined from the present measurements. The solid dot was determined by (p,p) measurements [McD69]. The dashed error bar indicates uncertainty in the extraction of the ^{33}Cl width (see Section 13.3). See Table 14-2 and Section 14.2.1.

Table 14-2 Resonance Parameters for the Second T=3/2 States in A=4n+1 T_z=-1/2 Nuclei as Determined in Present and Previous Measurements.

See Tables 11-7, 11-8, 12-7, and 13-6 and Section 14.2.1.

A=4n T_z=0	A=4n+1 T_z=-1/2	J^π	E_R (MeV)	Γ (eV)	Γ_p (eV)	$\gamma^2_{p_o}$ (eV)
^{16}O	^{17}F	$3/2^-$	12.7077 ± .002 [a]	2600 ± 200	766 ± 24 [a]	203 ± 6
^{20}Ne	^{21}Na	$1/2^+$	7.128 ± .005 [b]	2300 ± 500	1100 ± 300 [b]	362 ± 99
^{24}Mg	^{25}Al	$3/2^+$	5.9410 ± .002 [a]	1300 ± 135	232 ± 12 [a]	330 ± 17
^{28}Si	^{29}P	$1/2^+$	7.1632 ± .002 [a]	3066 ± 54	2431 ± 41 [a]	789 ± 13
^{32}S	^{33}Cl	$3/2^+$	4.7174 ± .002 [a]	367 ± 145	100 ± 15 [a]	303 ± 46
^{36}Ar	^{37}K	$1/2^+$	4.9634 ± .002 [a]	(2750) ±1061	(553) ± 316 [a]	(330) ±189

a) [Present] b) [McD69]

which had been determined, and then this sum was divided by the number of resonances included in the sum. These average elastic proton reduced widths $\bar{\gamma}^2_{p_o}$ are shown in Fig. 14-4. Table 14-3 presents the $\bar{\gamma}^2_{p_o}$ for all of these nuclei for which at least two resonances were measured and reduced widths extracted. The errors were calculated by adding the individual errors together in quadrature.

There is no doubt that the A=8 oscillations persist for the average reduced widths. The initial reaction would be to conclude that the average widths are dominated by the first T=3/2 states. However, this conclusion is not true. An examination of the magnitude of the individual reduced widths indicates that for many of the nuclei, the high-lying T=3/2 reduced widths are much greater than those of the first state. The ^{17}F point shown in Fig. 14-4 includes only the first two T=3/2 levels. The effect of adding higher T=3/2 reduced widths determined from [Skw74] measurements to the ^{17}F average reduced width is shown in in Table 14-3. Adding the reduced widths for states which have only isospin-forbidden particle decays does not make much difference to the average width. However, adding the states which have isospin-allowed particle decay channels does make quite a difference on the ^{17}F average width. It should be remembered, as pointed out in Section 5.4.2, that some of the T=3/2 levels identified by [Skw74] may not be T=3/2 states.

14.2.3 Comparison of Excitation-Energy Dependences of Reduced Widths. The most complete set of T=3/2 states measured in a given nucleus is that for ^{17}F, observed in ^{16}O(p,p)^{16}O. However, the assignment of isospin T=3/2 to some of these states may be questionable

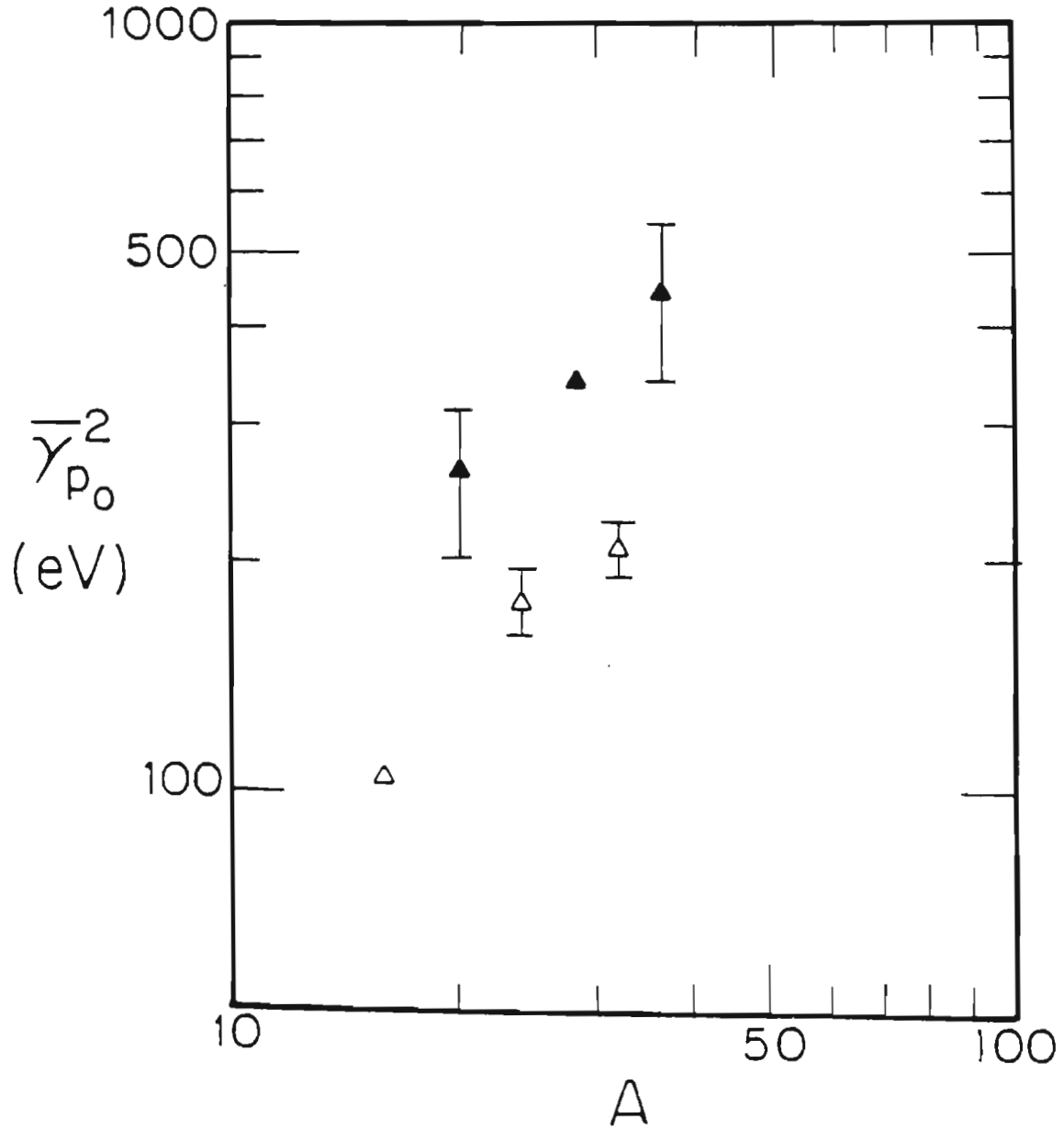

Figure 14-4 The average proton reduced widths $\overline{\gamma}_p^2$ for p_o decays of T=3/2 states in A=4n+1 T_z=-1/2 nuclei to the T_z=0 A=4n ground states are plotted versus mass number A. The oscillation of the reduced widths for A=8n (open points) and A=8n+4 (solid points) target nuclei is apparent. See Table 14-3 and Section 14.2.2 for a summary of which states were included in the calculations.

Table 14-3 Averaged Elastic Scattered Reduced Widths for the T=3/2 States in A=4n+1 T_z=-1/2 Nuclei as Determined in Present and Previous Measurements.

From Tables 5-2, 11-7, 11-8, 12-7, 13-6, and 14-1.

See Section 14.2.2 for discussion.

A=4n T_z=0	A=4n+1 T_z=-1/2	T=3/2 States	$\bar{\gamma}^2_{p_o}$ (eV)
^{16}O	^{17}F	1,2	105 ± 6
		1,2,3,4	130 ± 127
		1-7	308 ± 203
^{20}Ne	^{21}Na	1,2	263 ± 110
^{24}Mg	^{25}Al	1,2	178 ± 18
^{28}Si	^{29}P	1,2,4,7	343 ± 19
^{32}S	^{33}Cl	1,2,3	208 ± 47
^{36}Ar	^{37}K	1,2	445 ± 206

because of poor resolution and lack of determination of the isospin by other measurement methods (as discussed in Section 5.4.2). Furthermore, the order of occurrence of the T=3/2 states in the T_z=−1/2 nuclei is not the same as the order of occurrence of the states in the parent T_z=+3/2 nucleus. Although it is possible that the ordering of states might change, we have never observed this to happen in any other nuclei studied. The excitation energy dependences for the proton elastic reduced widths $\gamma^2_{p_o}$ of the T=3/2 states in ^{17}F are given in Fig. 14-5 and Table 14-4. It is difficult to deduce any general features of the reduced widths with excitation energy, other than that the reduced widths increase with energy. The uncertainty of the isospin assignments to these states makes any conclusions questionable.

The behavior of the ^{29}P reduced widths versus the effective excitation energy U, which has been corrected for nucleon pairing effects [Gil65], is presented in Fig. 14-6 and Table 14-5. The advantage of showing the data versus the effective excitation energy is that it allows comparison of reduced widths determined from other nuclei. All of these ^{29}P T=3/2 states have only isospin-forbidden particle decays. The most noticeable feature of the data is that the reduced widths generally decrease with excitation energy. Dividing the reduced widths by the average level density of states with the same J^π and same effective excitation energy, calculated using the level density equations of [Gil65] only magnifies the decrease of widths with excitation energy. The reduced widths divided by the average level densities are shown in Fig. 14-7. This implies that the average contribution to the isospin admixtures from the chance mixing with individual T=1/2 states is

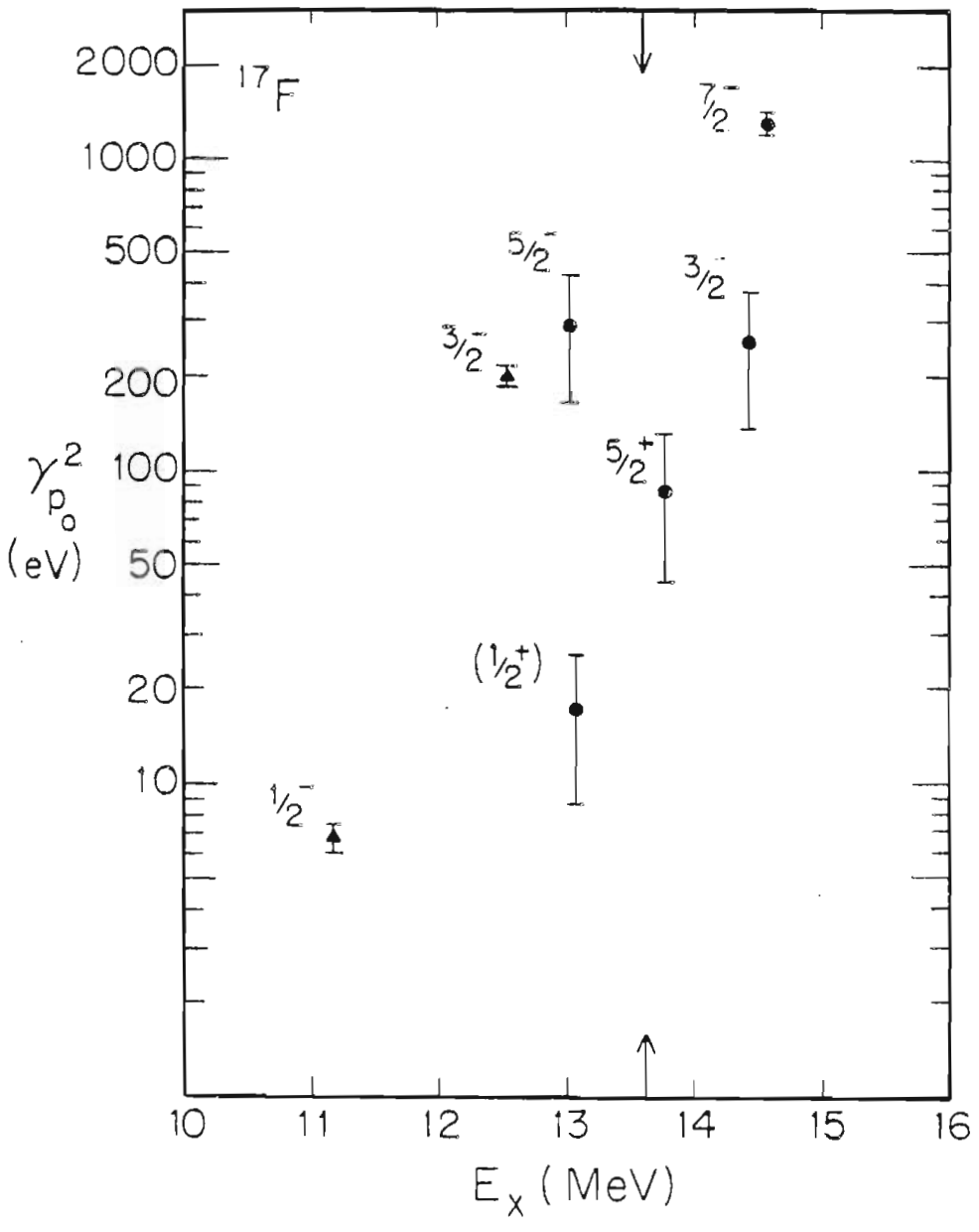

Figure 14-5 The proton reduced widths γ_p^2 for the p_o decays of the T=3/2 states in ^{17}F to the T_z=0 ^{16}O ground state are plotted versus excitation energy in MeV. The spins and parities are indicated. The triangles are reduced widths determined from the present measurements, The sources for the solid dots are [Skw74, Hin76]. The arrows on the top and bottom of the figure indicate where the T=1 isospin-allowed decay channel to the first T=1 state in ^{16}O becomes energetically available. See Table 14-4 and Section 14.2.3 for discussion.

Table 14-4 Resonance Parameters of T=3/2 States in ^{17}F as Determined in Present and Previous Measurements.

See Tables 5-2 and 12-7 and Section 14.2.2.

T=3/2 State (MeV)	E_x (MeV)	E_R (MeV)	J^π	Γ (keV)	Γ_p (keV)	$\gamma^2_{p_o}$ (eV)	REF
1	11.202	11.2642 ± .002	$1/2^-$	0.18 ± 0.01	0.023± 0.002	6.8 ± 1	Present
2	12.562 ± .002	12.7097 ± .002	$3/2^-$	2.60 ± 0.10	0.77 ± 0.024	203 ± 6	Present
3	13.080	13.271 ± .004	$(1/2^+)$	2.0 ± 1.0	0.08 ± 0.04	17 ± 9	[Skw74]
4	13.061	13.250 ± .004	$5/2^-$	2.0 ± 1.0	0.30 ± 0.15	294 ± 127	[Skw74]
5	13.782	14.017 ± .004	$5/2^+$	12.0 ± 5.0	0.24 ± 0.12	88 ± 44	[Skw74]
6	14.3042 ± .0033	14.3040 ± .003	$7/2^-$	19.3 ± 1.6	1.65 ± 0.12	1292 ± 94	[Bin76]
7	14.177	14.4438 ± .006	$3/2^-$	27.0 ± 5.0	1.08 ± 0.50	258 ± 119	[Skw74]

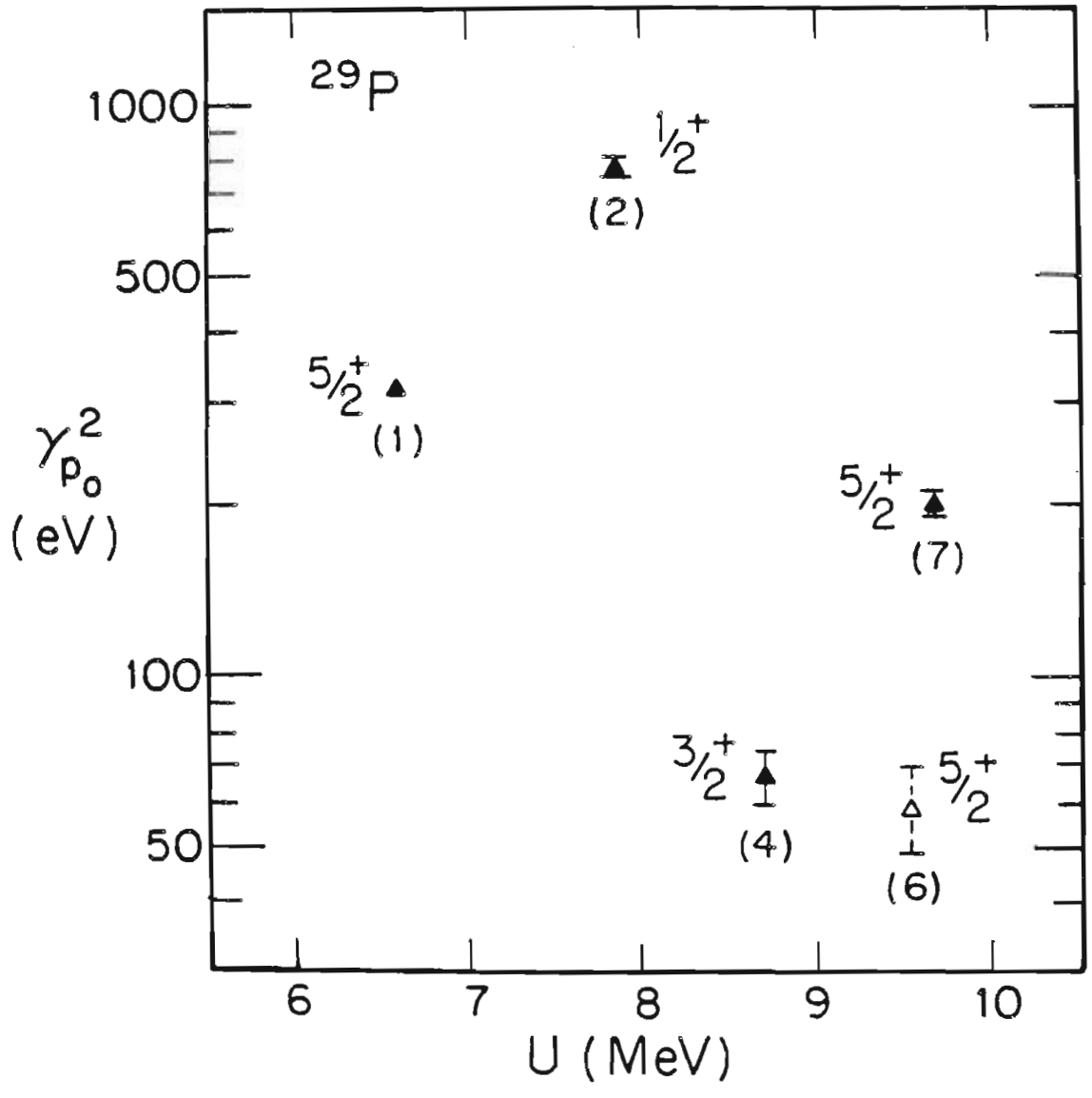

Figure 14-6 The proton reduced widths γ_p^2 for the p_o decays of the T=3/2 states in ^{29}P to the T_z=0 ^{28}Si ground state are plotted versus adjusted excitation energy U in MeV. The spins and parities are indicated. All measurements are from the current work. The dashed error bar indicates uncertainty in the extraction of the sixth T=3/2 reduced width (see Section 12.6). See Table 14-5 and Section 14.2.3 for discussion.

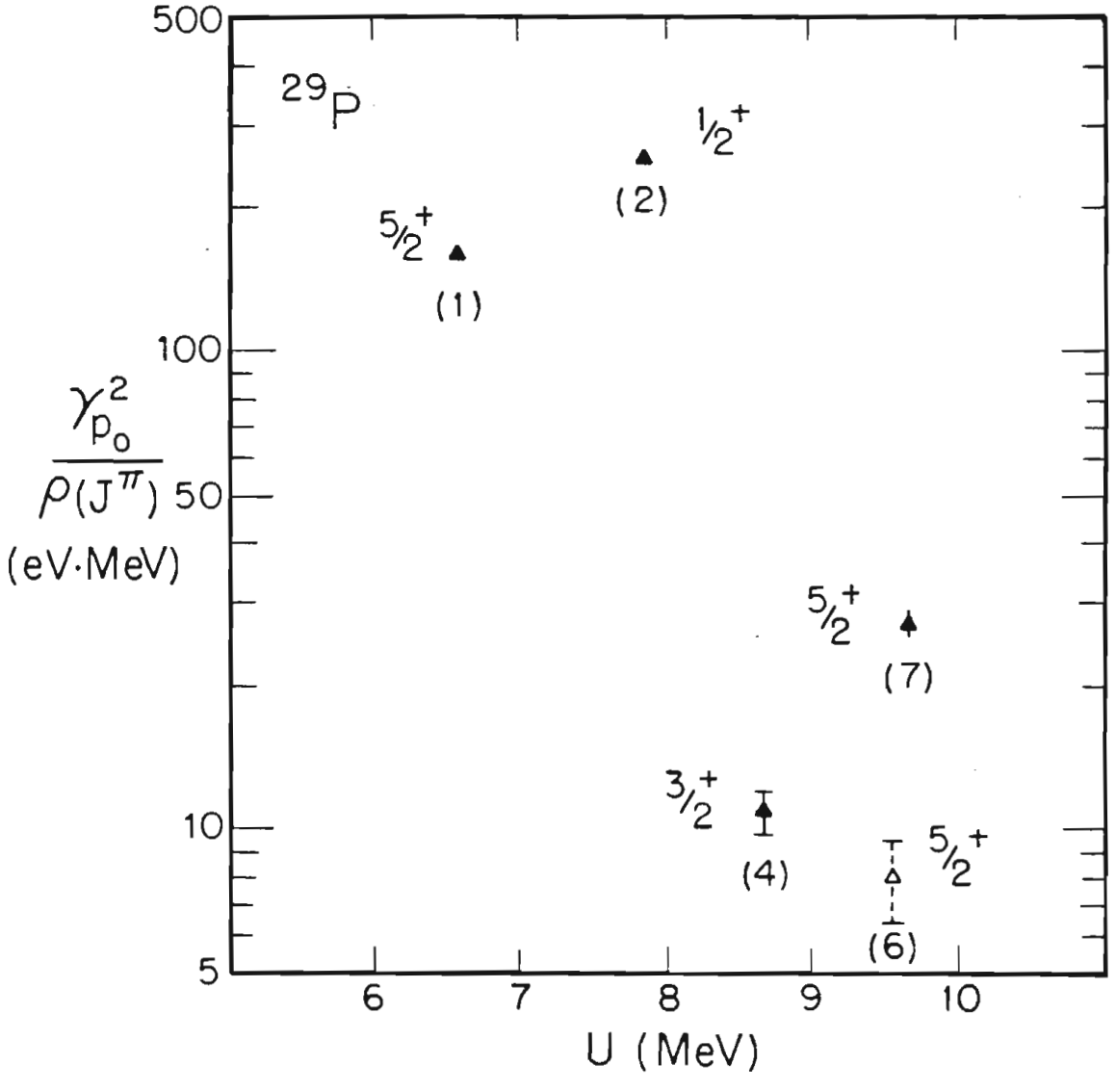

Figure 14-7 The proton reduced widths divided by the average density of states $\gamma_p^2/\rho_{ave.}$ for the p_0 decays of the T=3/2 states in ^{29}P to the T_z=0 ^{28}Si ground state are plotted versus adjusted excitation energy U. The spins and parities are indicated. All measurements are from the current work. The dashed error bar indicates uncertainty in the extraction of the sixth T=3/2 reduced width (see Section 12.6). See Section 14.2.3 for discussion.

decreasing with increasing energy with respect to the elastic proton decay. The ^{17}F data were not examined relative to the level densities because the level density equations are not valid for such a light mass target.

The proton elastic reduced widths versus the effective excitation energy U are shown in Fig. 14-8 and Table 14.5 for the three measured T=3/2 resonances in ^{33}Cl. The reduced widths divided by the average level density of states with the same J^{π} actually decreases with excitation energy as shown in Fig. 14-9 in a similar fashion to the ^{29}P states, possibly indicating that the isospin admixture contribution resulting from chance mixing with nearby T=1/2 states is decreasing.

14.2.4 Comparison of Spin and Parity Dependences of Reduced Widths. The $1/2^+$, $3/2^+$, and $5/2^+$ T=3/2 resonances' reduced widths are plotted versus effective excitation energy U in Figs. 14.10, 14.11, and 14.12. The significance of any of the observed trends with excitation energy is not apparent. However, the reduced widths divided by the average level densities generally decrease with excitation energy for all three sets of spins as shown in Figs. 14-13, 14-14, and 14-15. The systematics of the states in ^{13}N and ^{17}F were not included because of the lack of information on how to calculate the average excitation energies or average density levels for these light nuclei.

14.3 Summary of Observed T=3/2 States Reduced Widths Behavior. The basic trends exhibited by the proton elastic reduced widths $\gamma^2_{p_o}$ observed by $(\vec{p},p)$ population of T=3/2 isospin-forbidden resonances are as follows:

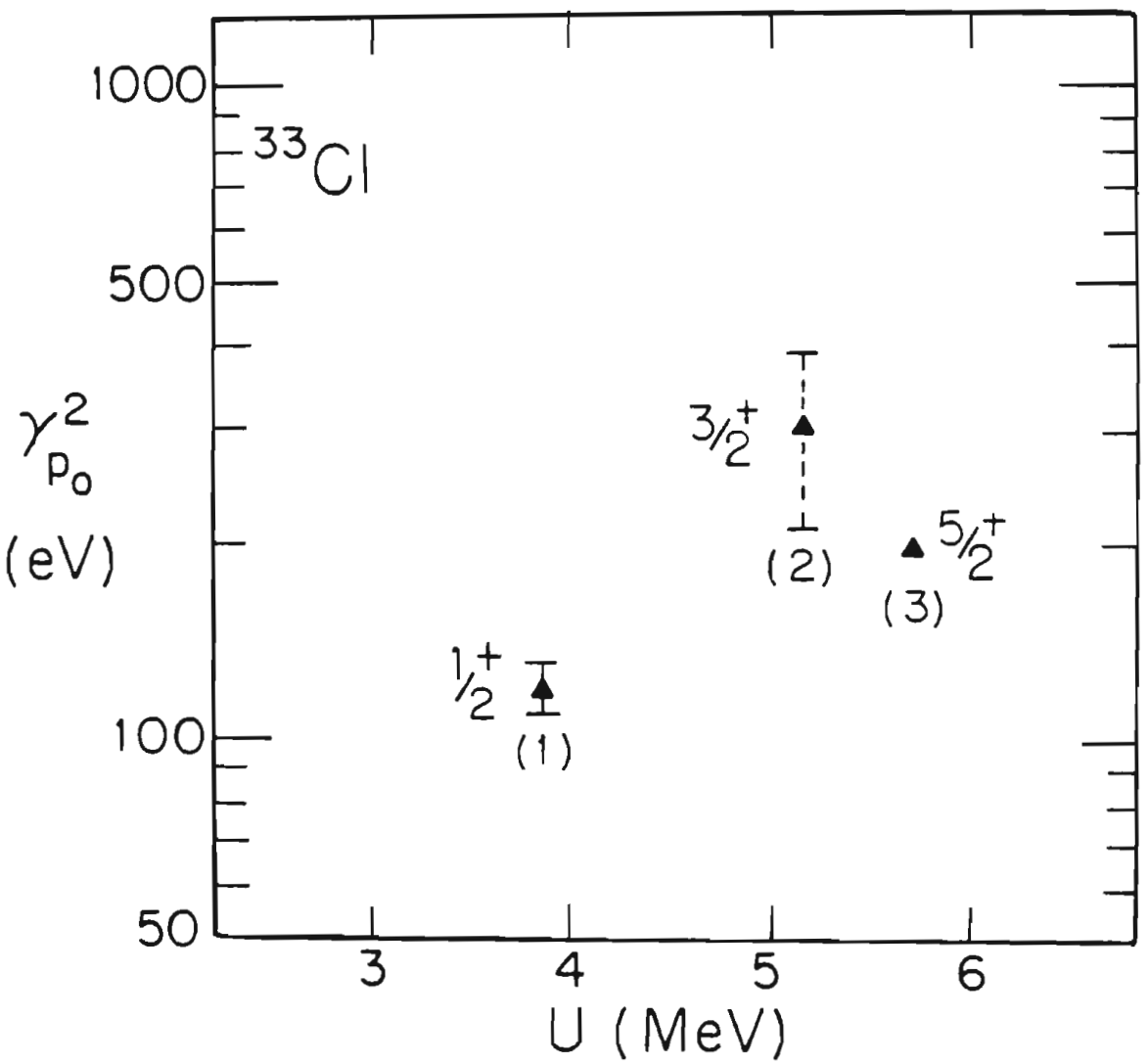

Figure 14-8 The proton reduced widths γ_p^2 for the p_o decays of the T=3/2 states in ^{33}Cl to the T_z=0 ^{32}S ground state are plotted versus adjusted excitation energy U. The spins and parities are indicated. All measurements are from the current work. The dashed error bar indicates uncertainty in the extraction of the second T=3/2 reduced width. (See Section 13.3.) See Table 14-5 and Section 14.2.3 for discussion.

Table 14-5 Resonance Parameters of T=3/2 States in ^{29}P and ^{33}Cl as Determined in Present Measurements.

See Tables 12-7 and 13-6 and Section 14.2.2.

T=3/2 State	U (MeV)	E_R (MeV)	J^π	Γ (eV)	Γ_p (eV)	$\gamma_{p_o}^2$ (eV)
^{29}P						
1	6.585	5.8392 ± .002	$5/2^+$	271 ± 10	216 ± 5	319 ± 6
2	7.863	7.1632 ± .002	$1/2^+$	3066 ± 54	2431 ± 41	789 ± 13
4	8.690	8.0192 ± .002	$3/2^+$	884 ± 170	99 ± 11	67 ± 7
6	9.559	8.9196 ± .002	$5/2^+$	3538 ± 527	108 ± 20	(59) ± 10
7	9.679	9.0435 ± .002	$5/2^+$	1526 ± 120	371 ± 21	199 ± 11
^{33}Cl						
1	3.879	3.3745 ± .002	$1/2^+$	100 ± 9	98 ± 9	121 ± 11
2	5.181	4.7174 ± .002	$3/2^+$	356 ± 145	100 ± 15	(303) ± 46
3	5.721	5.2734 ± .002	$5/2^+$	108 ± 7	96 ± 2	199 ± 3

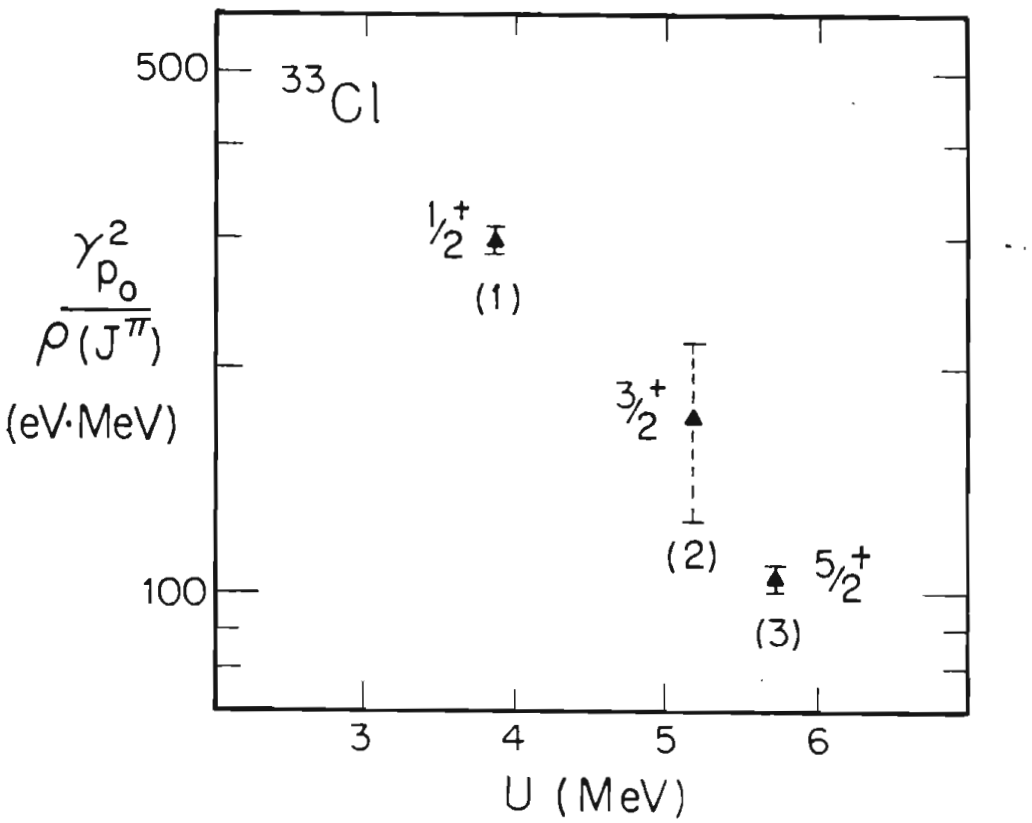

Figure 14-9 The proton reduced widths divided by the average density of states $\gamma_p^2/\rho_{ave.}$ for the p_o decays of the T=3/2 states in ^{33}Cl to the T_z=0 ^{32}S ground state are plotted versus adjusted excitation energy U. The spins and parities are indicated. All measurements are from the current work. The dashed error bar indicates uncertainty in the extraction of the second T=3/2 reduced width. (See Section 13.3.) See Section 14.2.3 for discussion.

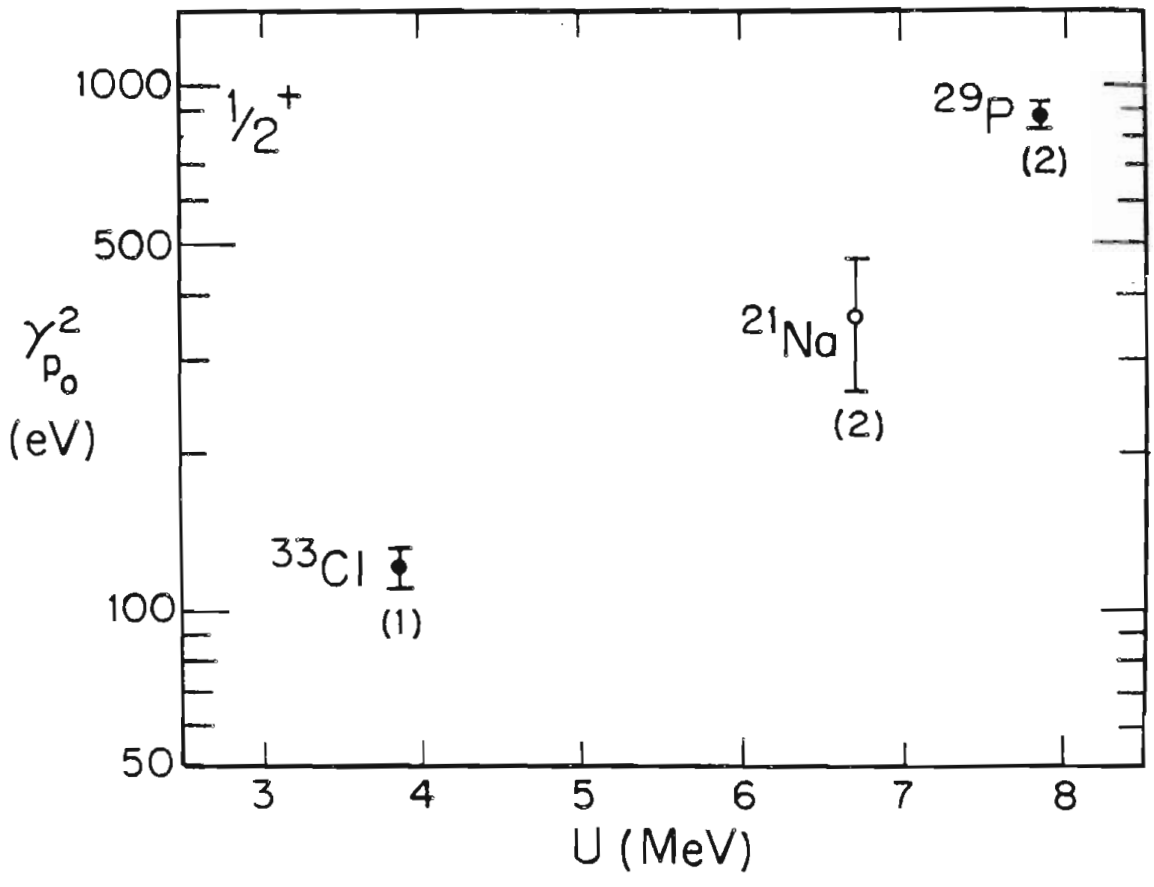

Figure 14-10 The proton reduced widths γ_p^2 for the p_o decays of the T=3/2 states with $J^\pi=1/2^+$ to the $T_z=0$ A=4n ground states are plotted versus adjusted excitation energy U. The A=4n+1 compound nucleus and T=3/2 level are indicated for each point. The solid dots represent the current work and the open dot is from [McD69]. See Section 14.2.4 for discussion.

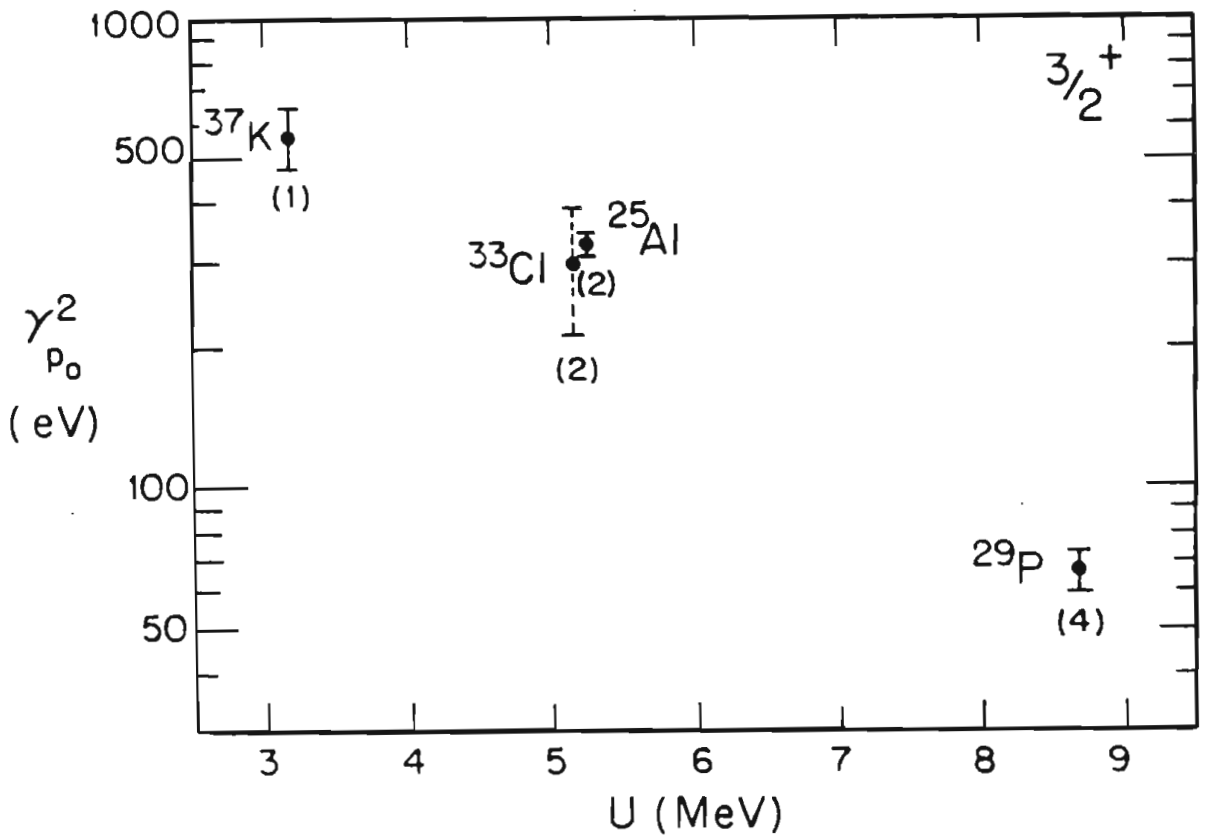

Figure 14-11 The proton reduced widths γ_p^2 for the p_0 decays of the T=3/2 states with $J^\pi=3/2^+$ to the $T_z=0$ A=4n ground states are plotted versus adjusted excitation energy U in MeV. The A=4n+1 compound nucleus and T=3/2 level are indicated for each point. All data points are from the current work. The dashed error bar indicates uncertainty in the extraction of the ^{33}Cl width. (See Section 13.3.) See Section 14.2.4 for discussion.

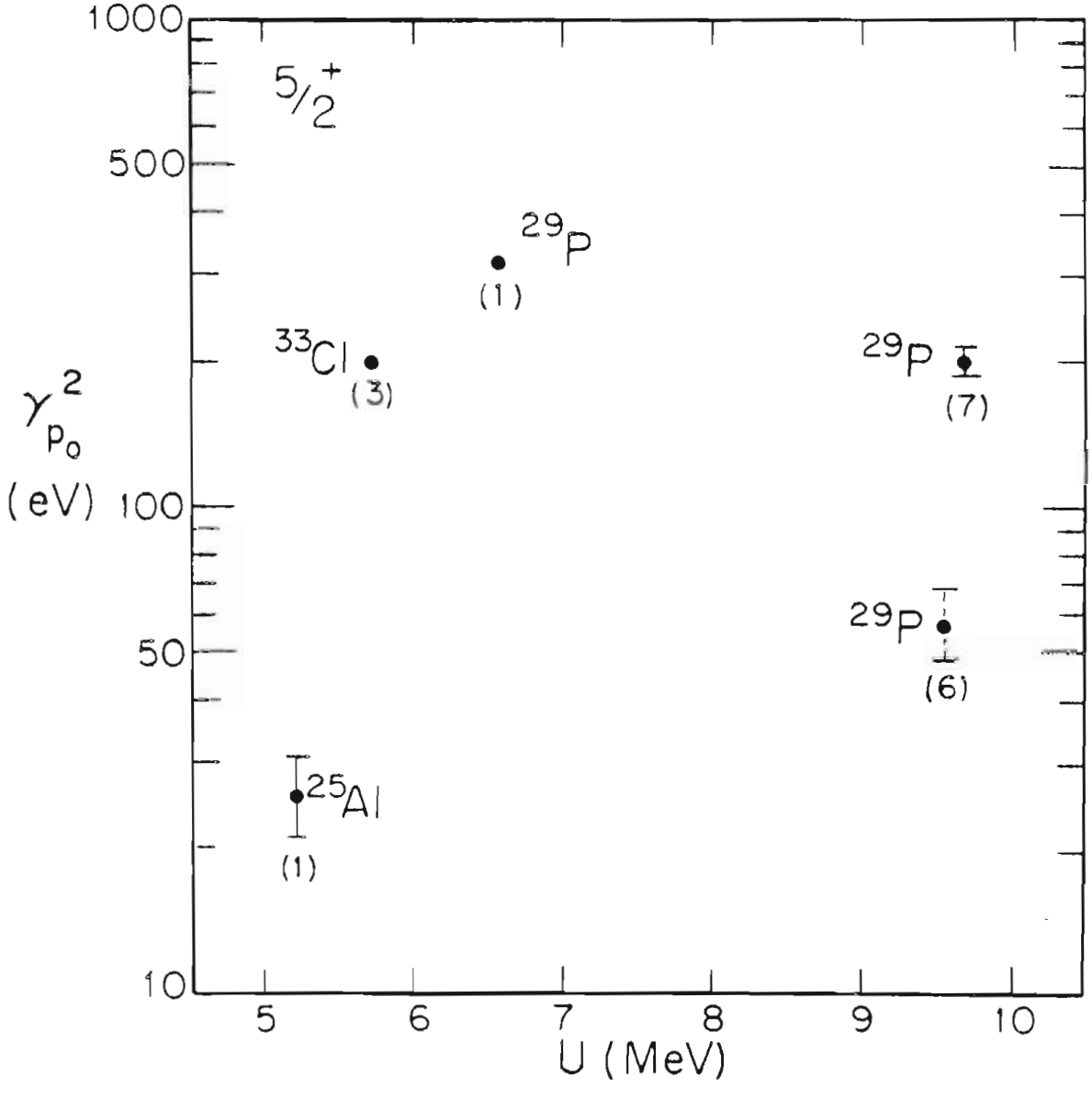

Figure 14-12 The proton reduced widths γ_p^2 for the p_o decays of the T=3/2 states with $J^\pi=5/2^+$ to the $T_z=0$ A=4n ground states are plotted versus adjusted excitation energy U in MeV. The A=4n+1 compound nucleus and T=3/2 level are indicated for each point. All data points are from the current work. The dashed error bar indicates uncertainty in the extraction of the ^{29}P width. (See Section 12.6.) See Section 14.2.4 for discussion.

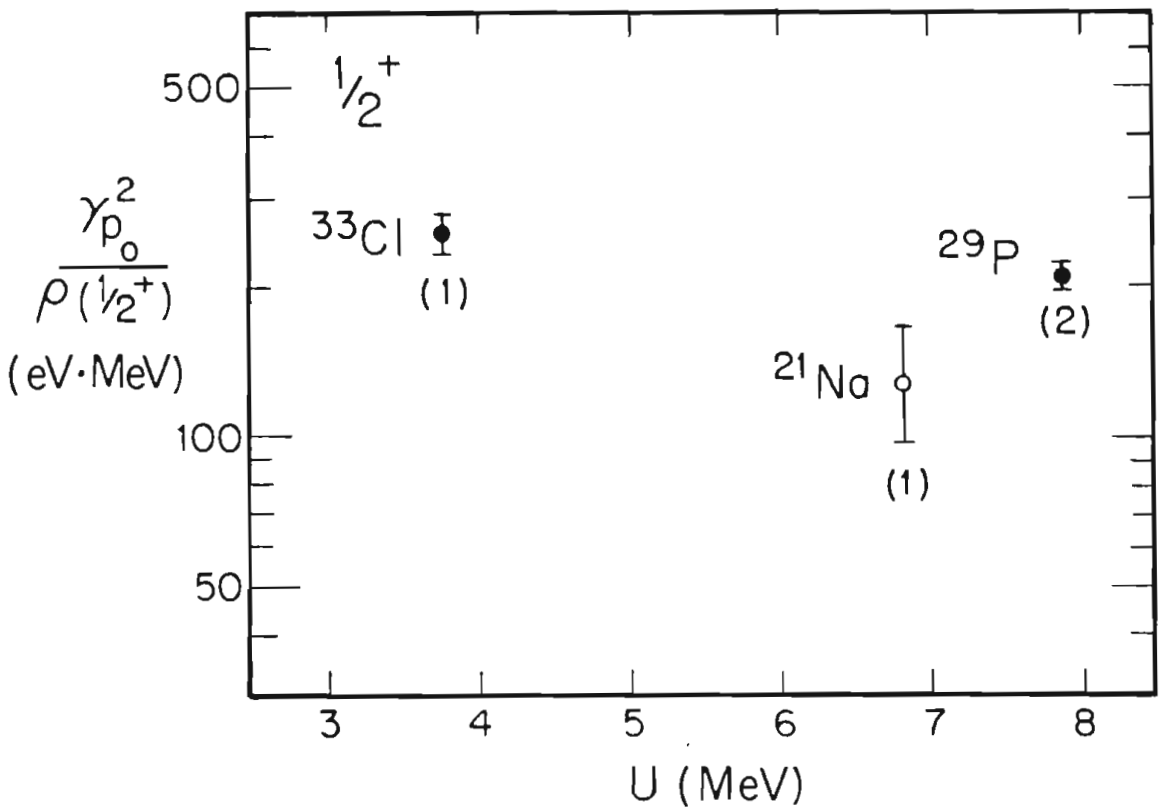

Figure 14-13 The proton reduced widths divided by the average density of states $\gamma_p^2/\rho_{ave.}$ for the p_o decays of the T=3/2 states with $J^\pi=1/2^+$ to the $T_z=0$ A=4n ground states are plotted versus adjusted excitation energy U. The A=4n+1 compound nucleus and T=3/2 level are indicated for each point. The solid dots represent the current work and the open dot is from [McD69]. See Section 14.2.4 for discussion.

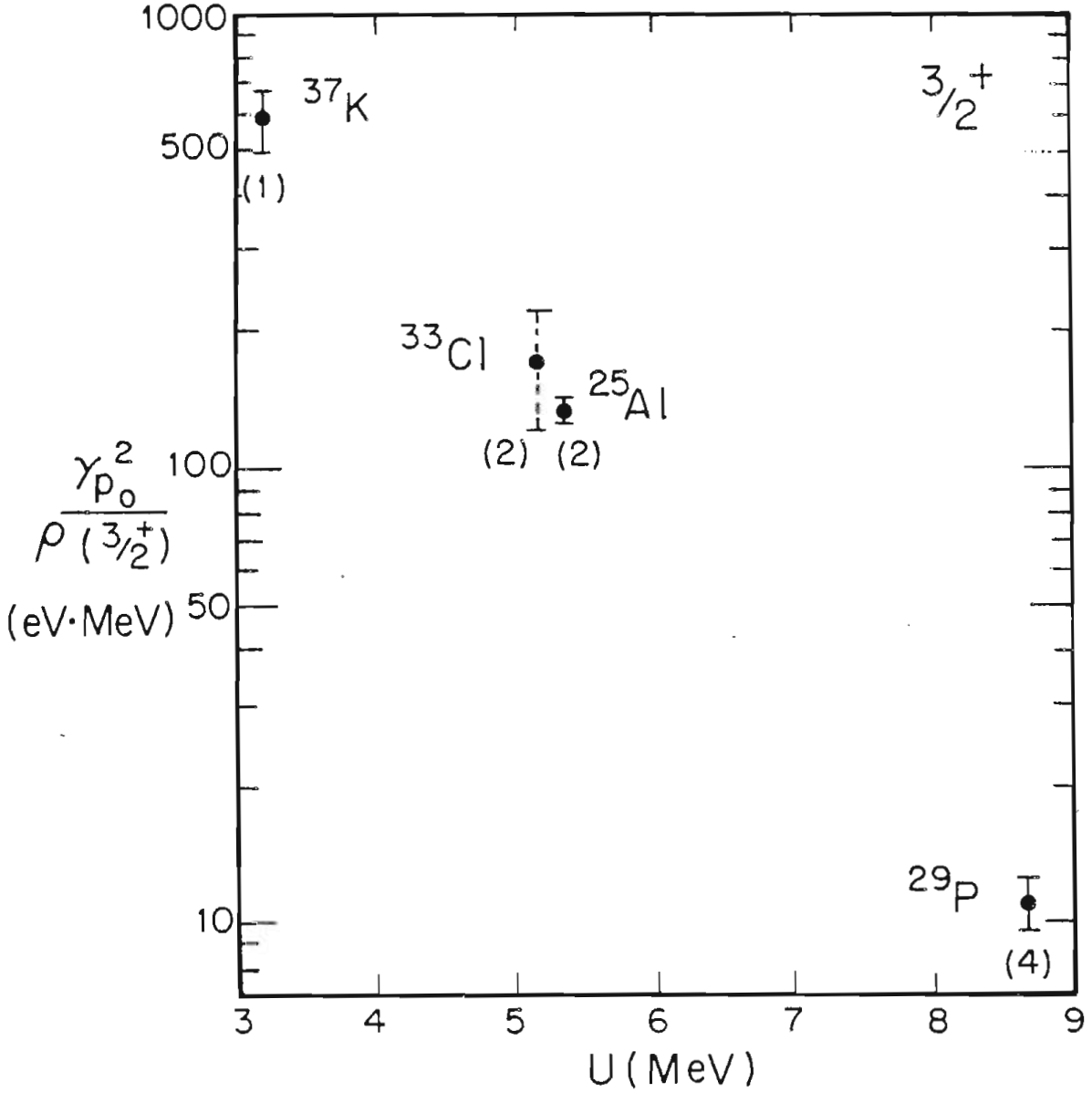

Figure 14-14 The proton reduced widths divided by the average density of states $\gamma_p^2/\rho_{ave.}$ for the p_o decays of the T=3/2 states with $J^\pi=3/2^+$ to the $T_z=0$ A=4n ground states are plotted versus adjusted excitation energy U in MeV. The A=4n+1 compound nucleus and T=3/2 level are indicated for each point. All data points are from the current work. The dashed error bar indicates uncertainty in the extraction of the ^{33}Cl width. (See Section 13.3.) See Section 14.2.4 for discussion.

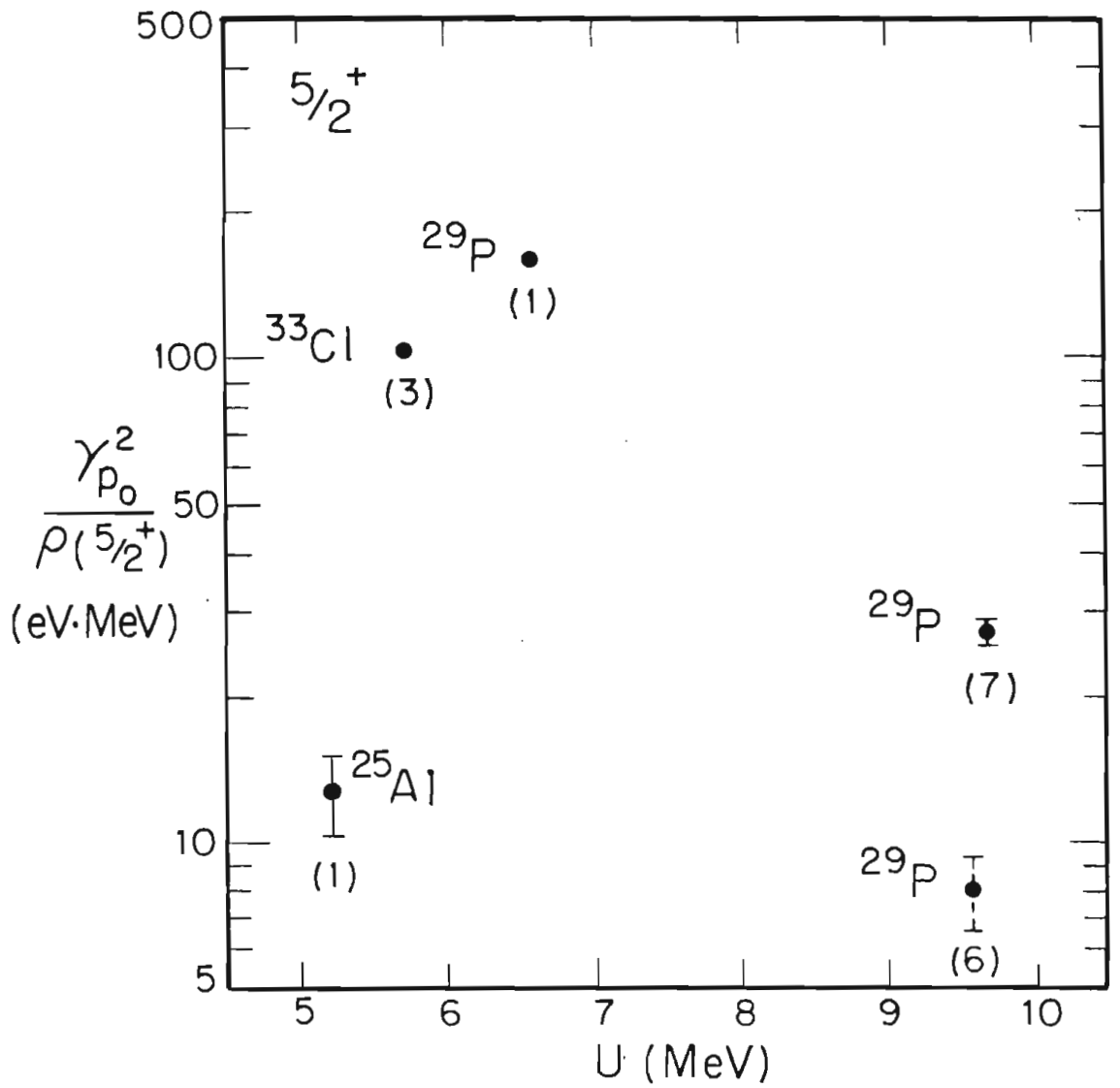

Figure 14-15 The proton reduced widths divided by the average density of states $\gamma_p^2/\rho_{ave.}$ for the p_0 decays of the T=3/2 states with $J^\pi=5/2^+$ to the $T_z=0$ A=4n ground states are plotted versus adjusted excitation energy U in MeV. The A=4n+1 compound nucleus and T=3/2 level are indicated for each point. All data points are from the current work. The dashed error bar indicates uncertainty in the extraction of the ^{29}P width. (See Section 12.6.) See Section 14.2.4 for discussion.

(1) The first, second, and average T=3/2 state have reduced widths which all exhibit a gradual, smooth increase of width with A.

(2) The first T=3/2 states and average T=3/2 states have reduced widths which show a distinctive oscillation of period A=8 in the magnitude of the widths as a function of A.

(3) The second T=3/2 states reduced widths may exhibit the behavior of oscillation of widths with period A=8. The magnitude of the differences between the A=8n and A=8n+4 reduced widths is not as great as for the lowest T=3/2 states. However, the lack of measurements of all the possible second T=3/2 state reduced widths and the error bars on the ^{21}Na and ^{33}Cl make this conclusion less certain.

(4) For a given nucleus, the reduced widths do not always increase monotonically with increasing excitation energy. In fact, narrow total and partial width resonances are observed at excitation energies several MeV above the first T=3/2 states.

(5) For several nuclei the proton elastic reduced widths $\gamma^2_{p_o}$ divided by the average level density of states show a decrease in width with increasing excitation energy.

14.4 Conclusion on Isospin Mixing. The fundamental conclusions revealed by these measurements of isospin mixing in high-lying T=3/2 isospin-forbidden resonances are:

(1) The isospin-mixing mechanisms are largely independent of nuclear structure effects in each compound nucleus. This includes the location of the antianalog states, the monopole states, and the nearby T=1/2 states.

(2) The isospin-mixing mechanisms must be caused by some general, smoothly varying effect which increases regularly with A.

(3) The oscillatory behavior exhibited by the reduced widths for the first T=3/2 states is not an accidental effect seen only for these levels and resulting from some subtle effects in isospin mixing for these levels. The possible persistence of this oscillation in the second T=3/2 states and the distinct oscillation of the average reduced widths indicate that some general isospin-mixing mechanism is causing this behavior.

(4) The isospin mixing of the T=3/2 state with nearby T=1/2 states in the compound nucleus decreases with increasing excitation energy for several of the nuclei studied.

When all of the evidence from the T=3/2 and T=2 measurements [Iko76, McD76, Fre79] is considered, several other conclusions concerning the isospin-mixing mechanisms can be reached:

(1) The isospin-mixing mechanisms considered or proposed thus far cannot explain the observed oscillation of the T=3/2 states proton-decay reduced widths.

(2) Proposed isospin-mixing mechanisms and calculations have failed to consider the importance of isotensor mixing contributions. (As discussed in Section 1.1.1-1.1.3 and 14.1.3.)

(3) The proton reduced widths for the first T=3/2 states in the T_z=-1/2 nuclei which populate the first 2^+ states in the A=4n target nuclei do not exhibit any periodic behavior [McD76]. This fact, coupled with the proton elastic reduced widths oscillatory behavior, strongly indicates that the mixing mechanisms may be directly related

to the isospin admixtures in the target-nucleus ground states.

(4) The increase in magnitude of the T_z=+1/2 neutron reduced widths [McD76] and the lack of oscillation for these widths suggest a difference in the contributions from different decay mechanisms for the neutron and proton decays. It might be possible that the mechanism which produces the oscillation of proton reduced widths also contributes to the neutron reduced widths, but that the oscillations are not visible because the other mixing mechanisms which contribute to the larger neutron widths dominate.

15. Recommendations and Summary

15.1 Suggestions for Theoretical Investigations. All of the conclusions regarding isospin mixing obtained from the evaluation of the experimental evidence (see Chapter 14) indicate that a new theoretical effort should be made to understand the processes involved in isospin mixing and the isospin-forbidden particle decays. Clearly, there is now sufficient reliable experimental data to justify and motivate such a study. However, initial emphasis should be placed on considering new mixing mechanisms and not on performing extremely complicated, detailed calculations.

In addition to the fundamental theoretical questions posed above, there are several other interesting studies that should be investigated as a result of this research:

(1) The (p,t), (p,^{3}He), and ($\vec{p}$,p) studies have yielded new energy assignments and more accurate energy assignments for previously identified high-lying T=3/2 states in A = 25, 29, 33, and A=37 mass systems. In several instances, the parent-state energies are also known. Thus, calculations of the coefficients of the isobaric mass multiplet equation (IMME) can be performed [Jan69, Ben79]. The IMME calculations can help understand the dependence of Coulomb energies on Z and A and can be used to look at charge dependent forces. These calculations were not performed in this research, because detailed

investigations of the experiments which have determined the energies and masses of the other multiplet members are required.

(2) An investigation of Coulomb displacement energies for excited states using the methods developed by [She75, Kou78] might be useful in investigating the locations of the T=3/2 states and predicting the expected location of other high-lying T=3/2 states, as well as understanding isospin-mixing mechanisms.

(3) A study of the systematic behavior of the high-lying $T_z=+1/2$ neutron widths [Wei76, Cie78, Kla81, Hin81] would be useful. The behavior of the average neutron reduced widths can be investigated and compared to the $T_z=-1/2$ results in a few cases. Such a program, using high-energy-resolution neutron beams would require a very large developmental effort at TUNL.

(4) The investigation of the extremely strong states populated and observed in the $^{27}Al(p,t)^{25}Al$ spectra (at 9.14 MeV and 10.34 MeV) would be useful. We currently do not understand why such strong states appear in the $^{27}Al(p,t)^{25}Al$ spectra.

(5) Consideration should be given to developing better methods to analyze narrow resonances which are not in a region with constant off-resonance cross sections and analyzing powers. However, such methods necessarily require more parameters to characterize the off-resonance amplitudes.

(6) A solid-state physics project to investigate carefully Doppler broadening in compounds would be useful and would eliminate ambiguities in the analysis of the resonance data, while eventually allowing the selection of targets yielding optimum Doppler

broadening. Alternatively, narrow, specially-selected resonances might be used to determine lattice vibrational properties in light elements.

15,2 Suggestions for Future Experimental Investigations. The investigation of additional second T=3/2 A=4n+1 T_z=-1/2 states seems to be completely justified. Both the second states in ^{21}Na and ^{37}K should be remeasured with either high quality ion-implanted ^{20}Ne and ^{36}Ar foils or with a differentially-pumped gas cell. The latter would be a better method of study with smaller uncertainties because of the resolution effects. The ^{21}Na state has never been studied with polarized beam but only with unpolarized beams of moderate energy resolution [McD69]. An investigation of the ^{37}K state will require answering the problems of non-constant off-resonance cross section and analyzing power mentioned in (5) above. It may be possible to locate angles where the off-resonance excitation functions are nearly flat. The angular distributions above and below resonance should be studied with high-resolution beams. If better analysis methods are developed, it would also be worthwhile to remeasure the second T=3/2 state in ^{33}Cl which lies within ~ 4 keV of a T=1/2 resonance.

Investigations of second T=3/2 states which have not been previously studied will be difficult, and in the cases of ^{9}B and ^{13}N, possibly not useful. The second T=3/2 states in both ^{9}B and ^{13}N have isospin-allowed particle decays. Other possible T=3/2 states in ^{41}Sc have to be located. The ^{40}Ca(p,p)^{40}Ca energy excitation function region where this second T=3/2 state occurs is extremely resonant [Bro62].

Thus, some other method of identifying the state should be used. Unfortunately, the direct (p,t) and (p,^{3}He) method is not possible because ^{43}Sc has a half-life of only 3.89 hours. It might be possible to use ^{39}K(^{3}He,n)^{41}Sc (see Section 2.4) or perhaps ^{40}Ca(p,γ)^{41}Sc.

Further studies of third T=3/2 states might also be justified. The third T=3/2 state in ^{33}Cl has been studied with ($\vec{p}$,p) energy excitation functions in the current work. The third T=3/2 state in ^{17}F has been studied by (p,p) work [Skw74], and the third T=3/2 state in ^{25}Al has been measured with polarized beam but not yet analyzed [Lud82]. The locations of the third T=3/2 states in ^{29}P and ^{37}K are known from the present work and have been observed by ($\vec{p}$,p). However, the ^{37}K resonance needs to be remeasured because insufficient data were taken off-resonance. It is not certain whether the third state in ^{29}P can be studied by ($\vec{p}$,p) because of its high J^π value ($7/2^+$) and therefore low penetrability of the ℓ=4 angular-momentum barrier. Also, the state which has been tentatively identified as the T=3/2 state lies on the edge of a T=1/2 resonance which has rapidly varying cross section and analyzing powers.

More (p,t) and (p,^{3}He) measurements to locate and study high-lying T=3/2 states are justified, based on the success of the current measurements. The measurements should certainly be taken with polarized beam and the best possible energy resolution. The combination of measurements from Princeton and IUCF might be the best method of making these measurements. Preliminary acquisition of single-angle (p,t) and (p,^{3}He) measurements at IUCF on ^{23}Na^{35}Cl targets indicate that ^{21}Na

would be a good system to study by measuring angular distributions.

There are several possible improvements or changes to the $(\vec{p},p)$ data acquisition and analysis:

(1) Acquire energy excitation functions by fast ramping of the target rod instead of changing the entire machine energy. This method, which requires event-mode data acquisition, was attempted with the DDP-224 computers, which proved to be too slow. However, with the VAX/11-780, event-mode acquisition should be feasible. This method would eliminate the problem of beam wandering and the resulting yield shifts in the cross section. It would also reduce problems of beam energy jumps during excitation function measurements, which currently cannot be detected unless they are extremely large. Both of these effects would result in higher quality data.

(2) Determining the spins and parities of the states using the present T32GRD analysis code is difficult and time consuming. It would be useful to modify the code to calculate the fits for a selection of ℓ and J values.

(3) Increasing the number of detector pairs from the present number of 4 to 5 or 6 detector pairs would increase the number of values used in calculating the average resonance parameters and increase the reliability of these parameters. The new XSYS data acquisition system should allow expansion with no difficulty.

(4) The beam-energy-spread measurement system should be improved, as suggested in Chapter 8. The knowledge of the resolution would remove ambiguities in the analysis, and would also allow instantaneous evaluation of the beam resolution quality, thereby saving experimental

time.

15.3 Summary. The measurements of isospin mixing in high-lying T=3/2 resonances in light nuclei which are described in this research utilized a broad array of experimental methods and analysis techniques. Several new techniques were developed, and several other techniques were extended to new regions.

The (p,t) and (p,^{3}He) angular distribution experiments which had previously been used to locate the first one or two T=3/2 states in A=4n+1 nuclei were shown to provide a reliable method of locating high-lying T=3/2 states. Also, the importance of having high-resolution (p,t) and (p,^{3}He) spectra in order to locate and resolve T=3/2 and T=1/2 states was demonstrated. Generally, such data require proton energies of 40, 60, or perhaps higher energies, not available at TUNL.

The direct measurement of beam energy spread, developed during this research, was important for reliable estimates of the beam energy spread of the $(\vec{p},p)$ measurements. Although only a few measurements of the beam energy spread were measured during the present research, these beam energy spread widths confirmed that the resolution widths obtained through fitting the $(\vec{p},p)$ excitation functions were reasonable. Finally, the development of the polarized high-resolution beam, and the extension of the helicity-amplitude analysis method for $(\vec{p},p)$ measurements, was critical to extracting the final resonance parameters.

Although each of these experiments can stand on its own merit, their combination led to very accurate, systematic measurements of

isospin mixing. Hopefully, these new results will stimulate further experiments and renewed theoretical interest and investigation.

APPENDIX A.

Useful Computer Codes

1. CSTRAGL - (TUNL/VAX) - [Wil82].

   Two-material energy straggling calculation. This code convolutes two individual energy straggling distributions. Uses code STRAGL for straggling calculations. See Section 6.3.1.

2. DIFSIG - (TUCC) - [Wil82].

   Calculates differential cross sections and analyzing powers for energy excitation functions. Also can rotate excitation functions in order to produce constant off-resonance cross sections and analyzing powers. See Section 6.4.1.

3. ENE90(D) - (TUNL/VAX) - [Wil82].

   Subroutine which returns energy in MeV when given frequency in MHz for the dual-90^{o} magnet system. Based on the magnet calibration from the present work. Single and double precision.

4. FREQ - (TUNL/VAX) - [Wil82].

   Generates tables of NMR frequency and energies for all TUNL beam lines. Dual-90^{o} magnet system based on the magnet calibration from the present work.

5. LVDN - (TUNL/VAX) - [Wil82, Nel82].

   Level density code based on [Gil65] equations. Can calculate individual spin and parity level density or total level density.

6. MULTI - (TUNL/VAX) - [Nel82, Sel69].

   Multiple resonance, R-matrix code.

7. NMR90(D) - (TUNL/VAX) - [Wil82].

   Subroutine which returns frequency in MHz when given energy in MeV for the dual-90^{o} magnet system. Based on the magnet calibration from the present work. Single and double precision.

8. PENET - (TUNL/VAX) - [Tho81].

   Coulomb penetrability calculation.

9. RESDIS - (TUNL/VAX) - [Wil82].

   Resolution convolution calculation. Convolutes a Gaussian and one- or two-target energy straggling distribution. See Section 6.4.2.

10. SPECTR - (TUNL/VAX) - [Var82].

    Spectra peak-fitting code which runs in conjunction with XSYS.

11. STRAGL - (TUNL/VAX) - [Wil82, Sch74].

    Calculates the energy straggling distributions for straggling in the Landau, Vavilov, or Gaussian regions. See Section 6.3.1.

12. THRESH - (TUNL/VAX) - [Wil82].

    Code to determine threshold energies for (p,n) data. See Section 9.4.1.

13. TRANSPORT - (TUNL/VAX) - [Bro67, Bro70].

    Current version of beam transport code TRANSPORT.

14. T32GRD - (TUCC) - [Wil82].

    Helicity-amplitude resonance analysis code. See Section 6.4.3.

15. T32P - (TUCC) - [Wil82].

    Code to produce Calcomp or Tektronix plots and tables of final energy excitation function data and calculated fits.

16. T32PLOT - (TUNL/VAX) - [Bro67, Bro70]

    Code to produce plots and tables of energy excitation function yield curves and analyzing powers. See Section 6.4.1.

APPENDIX B.

T32GRD Analysis File Name Format

1. Explanation.

Due to the large amount of $(\vec{p},p)$ and (p,p) data generated, it was necessary to establish a file coding system to bring order to the large number of files needed in the analysis of the T=3/2 resonance data. The following file format covers both files at TUNL on the VAX and also files at TUCC.

2. File Code Format.

(i) General format.

AABC.DEEE.DATA

(a) AA - Designates target nucleus periodic table symbol. One or two characters. (All capital letters)

(b) B - T=3/2 suspect state number relative to parent state.

(c) C - OPTIONAL This can denote several different things.
One Letter - Designates different off-line analysis.
Two Letters - 1. Designates different energy suspect states.
2. Designates different off-line analysis.
Numbers - Designates different off-line analysis.
WARNING THIS HAS NOT ALWAYS BEEN USED CONSISTENTLY.

(d) D - File type code. (Only one possible at a time.)
S : Stripped elastic data file from DDP-224 to VAX.
I : Stripped inelasic data file(s) from DDP-224 to Vax.
D : Input file for DIFSIG program.
O : Output file from DIFSIG program.
T : Input file for T32GRD program. (PDS)
F : Output file from T32GRD program. (PDS)

(e) EEE - Date experiment was performed.
eg. 1-5-81 : 181

(ii) Partitioned Data Set format (PDS).

AABC.DEEE.DATA(FGGG)

(a)-(e) As above.

(f) F - Data information code.
(A and R are mutually exclusive but either may have C.)
A : Standard T32GRD input or output.
R : Rotated input or output data.
C : Truncated data base on high or low energy side of the excitation function.

(g) GGG - Center of mass angle to nearest degree.

3. Example.

SI2A.T181.DATA(AC139) - T32GRD input file for the second T=3/2 state in $^{28}Si(\vec{p},p)^{28}Si$ for unrotated 139° data. This is the lowest energy resonance observed in the region where the second T=3/2 state is expected..

REFERENCES

Abb70 U. Abbondanno et al., Nuovo Cim. A70 (1970) 391.

Abb73 U. Abbondanno et al., Nuovo Cim. 13A (1973) 321.

Abr64 M. Abramowitz and T.A. Stegun, editors, Handbook of Mathematical Functions with Formulas, Graphs and Mathematical Tables, (AMS-55), (National Bureau of Standards, 1964).

Ada66 J.L. Adams et al., Nucl. Phys. 89 (1966) 377.

Ade69 E.G. Adelberger et al., Nucl. Phys. A124 (1969) 49.

Ade73 E.G. Adelberger et al., Phys. Rev. C7 (1973) 889.

Adl71 J.C. Adloff et al., Phys. Rev. C3 (1971) 1808.

Adl72 J.C. Adloff et al., Phys. Rev. C5 (1972) 664.

Ajz79 F. Ajzenberg-Selove, Nucl. Phys. A320 (1979) 1.

Ajz81 F. Ajzenberg-Selove, Nucl. Phys. A360 (1981) 1.

Ajz82 F. Ajzenberg-Selove, Nucl. Phys. A375 (1982) 1.

ANA01 Auckland Nuclear Accessory Company, 3200 Scott Blvd., Santa Clara, CA 95051.

Aok82 Y. Aoki, private communication, 1982.

ARI01 The Arizona Carbon Foil Company, Tuscon Arizona 85711.

Ari71 A. Arima and S. Yoshida, Nucl. Phys. A161 (1971) 1.

Ash76 N.W. Ashcroft and N.D. Mermin, Solid State Physics, (Holt, Rinehart, and Winston, New York 1976).

Aue71 N. Auerbach and A. Lev, Phys. Lett. 34B (1971) 13.

Aus70 N. Austern, Direct Nuclear Reaction Theories, (John Wiley and Sons, New York 1970).

Bae73 H.W. Baer et al., Ann. Phys. 76 (1973) 437.

Bar72 T.T. Bardin et al., Phys. Rev. C5 (1972) 1351.

Bar81 P.H. Barker et al., Second International Conference on Precision Measurements and Fundamental Constants, Gaithersburg MD, 1981, to be published.

Bea70 R.C. Bearse et al., Phys. Rev. C1 (1970) 608.

BEL01 Bell Laboratories, Documents for use with GR-Z, Murray Hill, N.J. 07974, 1977.

Ben73a W. Benenson et al., Phys. Rev. C7 (1973) 1143.

Ben73b W. Benenson et al., Phys. Rev. C8 (1973) 210.

Ben73c R.D. Bent et al., IUCF Internal Report No. 1-73 (unpublished) 1973.

Ben74 W. Benenson and E. Kashy, Phys Rev. C10 (1974) 173.

Ben79 W. Benenson and E. Kashy, Rev. Mod. Phys. 51 (1979) 527.

Ber70 B.L. Berman et al., Phys. Rev. Lett. 24 (1970) 319.

Ber72 G.F. Bertsch and A. Mekjian, Ann. Rev. Nucl. Sci. 22 (1972) 25.

Ber73 J.C. Bergstrom et al., Phys. Rev. C7 (1973) 2228.

Ber76 D. Berghofer et al., Nucl. Phys. A263 (1976) 109.

Bic75 H. Bichsel and R.P. Saxon, Phys. Rev. A11 (1975) 1286.

Ble78 M.E. Bleck, Ph.D. dissertation, Duke University, 1978 (unpublished), available from University Microfilms International, 300 N. Zeeb Rd., Ann Arbor, Michigan 48106.

Bli73 R.J. Blin-Stoyle, Fundamental Interactions and the Nucleus, (North-Holland Publishing Company, Inc., Amsterdam, 1973).

Boh15 N. Bohr, Phil. Mag. 30 (1915) 581.

Boh67 A. Bohr et al., in Nuclear Structrure, eds. A. Hossain, H-Ar-Rashid, and M. Islam, (North-Holland Publishing Company, Inc., Amsterdam, 1967) p. 1.

Bri81 J.S. Briggs and A.M. Lane, Phys. Lett. 106B (1981) 436.

Bro62 N.A. Brown, Ph.D. dissertation, Rice University, 1962 (unpublished).

Bro67 K.L. Brown, SLAC Report No. 75 (1967); Advances in Particle Phys. 1 (1967) 71.

Bro70 K.L. Brown and S.K. Howry, SLAC Report No. 91 (1970).

Bur81 B.L. Burks and F.L. Midler, Bull. Am. Phys. Soc. 26 1981 1235.

But68 G.W. Butler et al., Phys. Rev. 166 (1968) 1096.

Cac71 A. Cachard et al., Phys. Stat. Sol. (a) 5 (1971) 637.

Cai74 J.E. Cairns et al., Nucl. Instr. and Meth. 114 (1974) 489.

Cer64 J. Cerny and R.H. Pehl, Phys. Rev. Lett. 12 (1964) 619.

Cer66 J. Cerny et al., Phys. Lett. 20 (1966) 35.

Cer68 J. Cerny, Ann. Rev. Nucl. Sci. 18 (1968) 27.

Chu78 W.-K. Chu and M.-A. Nicolet, Backscattering Spectrometry, (Academic Press, New York, 1978).

Cie78 S. Cierjacks et al., Phys. Rev. C17 (1978) 12.

Cie80 S. Cierjacks et al., Nucl. Instr. and Meth. 169 (1980) 185.

Cla71 R.G. Clarkson and N. Jarmie, Comp. Phys. Comm. 2 (1971) 433.

Cle74 T.B. Clegg et al., Nucl. Instr. and Meth. 57 (1974) 167.

Cri49 C.L. Critchfield and D.C. Dodder, Phys. Rev. 76 (1949) 602.

Dav69 J.C. Davis and F.T. Noda, Nucl. Phys. A134 (1969) 361.

Deh67 D. Dehnhard and J.L. Yntema, Phys. Rev. 160 (1967) 964.

Det65 C. Detraz et al., Phys. Rev. Lett. 14 (1965) 708.

Det69 C. Detraz and H.H. Duhm, Phys. Lett. 29B (1969) 29.

Det70 C. Detraz and R. Richter, Nucl. Phys. A158 (1970) 393.

Dzu72 T.G. Dzubay et al., Nucl. Instr. and Meth. 101 (1972) 407.

End78 P.M. Endt and C. Van der Leun, Nucl Phys. A310 (1978) 1.

Ell66 R.V. Elliott and R.H. Spear, Nucl. Phys. 84 (1966) 209.

Esw72 M.A. Eswaran et al., Phys. Rev. C5 (1972) 1270.

Fan63 U. Fano, Ann. Rev. Nucl. Sci. 13 (1963) 1.

Fau82 R.E. Fauber, D.M. Janac, and J.F. Wilkerson, private communication, 1982.

Fea79 J.M. Feagin, Ph.D. dissertation, University of North Carolina, 1979, (unpublished), available from University Microfilms International, 300 N. Zeeb Rd., Ann Arbor, Michigan 48106.

Fle68 D.G. Fleming et al., Phys. Rev. 165 (1968) 1153.

FLU01 Hearth Liner V-1, Flurocarbon Process Systems Division, Anaheim, California 92803.

FLU02 Fluke Frequency Synthesizer, Model 6039A, manufactured by John Fluke Mfg. Co., Inc., Everett, Washington 98206.

Fra74 H. Frauenfelder and E.M. Henley, Subatomic Physics, (Prentice-Hall, Inc., Englewood Cliffs, N.J., 1974).

Fre76 J.M. Freeman, Nucl. Instr. and Meth. 134 (1976) 153.

Fre79 S.J. Freedman et al., Phys. Rev. C19 (1979) 1907.

Gil65 A. Gilbert and A.G.W. Cameron, Can. J. of Phys. 43 (1965) 1446.

Gle75 N.K. Glendenning, in Nuclear Spectroscopy and Reactions, Part D., edited by J. Cerny (Academic Press, New York, 1975) p. 319.

Goo57 T.J. Gooding and R.M. Eisberg, Phys. Rev. 105 (1957) 357.

Goo67 R.D. Goosman and R.W. Kavanagh, Phys. Rev. 161 (1967) 1156.

Gou81 C.R. Gould et al., IEEE Trans. Nucl. Sci. NS-28 (1981) 3708.

Gru81 W. Gruebler and P.A. Schmelzbach, in Polarization Phenomena in Nuclear Physics - 1980, eds. G.G. Ohlsen et al., AIP Conference Proceedings, No. 69, (American Institute of Physics, N.Y. 1981) p. 848.

Hae65 W. Haeberli et al., Phys. Rev. Lett. 15 (1965) 267.

Har64 J.C. Hardy and R.J. Verall, Phys. Lett. 13 (1964) 148.

Har65 J.C. Hardy and R.E. Bell, Can. J. Phys. 43 (1965) 1.

Har66 J.C. Hardy and D.J. Skyrme, in Isobaric Spin in Nuclear Physics, J.D. Fox and D. Robson editors, (Academic Press, New York, 1966) p. 701.

Har66a J.C. Hardy et al., Nucl. Phys. 81 (1966) 113.

Har69 J.C. Hardy et al., Phys. Rev. Lett. 22 (1969) 1439.

Har70 J.C. Hardy et al., Phys. Rev. Lett. 25 (1970) 298.

Har71 J.C. Hardy et al., Phys. Rev. C3 (1971) 700.

Har72 R.A. Hardekopf, Ph.D. dissertation, Duke University, 1972 (unpublished), available from University Microfilms International, 300 N. Zeeb Rd., Ann Arbor, Michigan 48106.

Har74 J.C. Hardy, in Nuclear Spectroscopy and Reactions, Part C., edited by J. Cerny (Academic Press, New York, 1974) p. 417.

Har75 M.N. Harakeh et al., Phys. Rev. C11 (1975) 998.

Hei32 W. Heisenberg, Z. Phys. 77 (1932) 1.

Hen68 D.C. Hensley, Phys. Lett. 27B (1968) 644.

Hen69 E.M. Henely, in Isospin in Nuclear Physics, edited by D.H. Wilkinson (North-Holland Publishing Company, Amsterdam, 1969), p. 15.

Hen79 E.M. Henely and G.A. Miller, in Mesons in Nuclei eds. M. Rho and D.H. Wilkinson (North-Holland Publishing Company, Amsterdam, 1979), Chapter 10.

Hin75 F. Hinterberger et al., Nucl. Instr. and Meth. 130 (1975) 347.

Hin75a F. Hinterberger et al., Nucl. Phys. 253 (1975) 125.

Hin76 F. Hinterberger et al., Nucl. Phys. 263 (1976) 460.

Hin81 F. Hinterberger et al., Nucl. Phys. A352 (1981) 93.

Hol61 L. Holland, Vacuum Deposition of Thin Films, (Chapman and Hall, London 1961).

Hoo64 B.W. Hooton, Nucl. Instr. and Meth. 27 (1964) 338.

How82 C.R. Howell and S.A. Wender, Nucl. Instr. and Meth. 195 (1982) 443.

Hue73 E. Huenges et al., Phys. Lett. 46B (1973) 361.

Hue74 E. Huenges et al., Nucl. Instr. and Meth. 121 (1974) 307.

Iko75 P.G. Ikossi, Ph.D. dissertation, University of North Carolina, 1975, (unpublished), available from University Microfilms International, 300 N. Zeeb Rd., Ann Arbor, Michigan 48106.

Iko76 P.G. Ikossi et al., Phys. Rev. Lett. 36 (1976) 1357; Nucl. Phys. A274 (1976) 1; erratunm, Phys. Rev. Lett. 42 (1979) 1382.

Iko80 P.G. Ikossi, University of Washington Progress Report 1980 (unpublished).

Jac75 D.F. Jackson, Nuclear Reactions, (Chapman and Hall, London, 1975).

Jan69 J. Janecke, in Isospin in Nuclear Physics, edited by D.H. Wilkinson (North-Holland Publishing Company, Amsterdam, 1969), p. 297.

Jar78 N. Jarmie et al., Comp. Phys. Comm. 13 (1978) 317.

KEP01 Kepco Inc., 131-38 Stanford Avenue, Flushing, N.Y. 11352.

Kou74 R.T. Kouzes, Ph.D. dissertation, Princeton University, 1974 (unpublished), available from University Microfilms International, 300 N. Zeeb Rd., Ann Arbor, Michigan 48106.

Kla81 H.O. Klages et al., Annual Report on Nuclear Physics Activities, July 1, 1980 - June 30, 1981, Institut fur Kernphyski, Kernforschungszentrum Karlsruhe.

Kou75 R. Kouzes and A. Broad, IUCF Internal Report No. 75-6 (unpublished) 1975.

Kou78 R.T. Kouzes, Nucl. Instr. and Meth. 155 (1978) 261.

Kou80 R.T. Kouzes, private communication, 1980.

Kru53 J. Krumhansl and H. Brooks, J. Chem. Phys. 21 (1953) 1663.

Kun74 P.D. Kunz, DWUCK4 computer code, University of Colorado, unpublished 1974.

Lam39 W.E. Lamb Jr., Phys. Rev. 15 (1939) 190.

Lan44 L. Landau, J. Phys. U.S.S.R. 4 (1944) 201.

Lan58 A.M. Lane and R.G. Thomas, Rev. Mod. Phys. 30 (1958) 257.

Lau56 J. de Launay, in Solid State Physics Vol 2., F. Seitz and D. Turnbull eds., (Academic Press, New York, 1956).

Law65 G.P. Lawrence, R.K. Beauchamp, and J.L. McKibben, Bull. Am. Phys. Soc., Ser 2, 10 (1965) 23.

Law77 J.D. Lawson, The Physics of Charged Particle Beams, (Oxford University Press, Oxford, 1977).

Lee72 H.C. Lee and R.Y. Cusson, Ann. Phys. 72 (1972) 353.

Lev69 M.J. Levine and P.D. Parker, Phys Rev. 186 (1969) 1021.

Lev73 A. Lev and N. Auerbach, Nucl. Phys. A206 (1973) 563.

Liv37 M.S. Livingston and H.A. Bethe, Rev. Mod. Phys. 9 (1937) 245.

Loz80 W.R. Lozowski, IUCF Scientific and Technical Report 1980, (unpublished) p. 149.

Loz81 W.R. Lozowski, private communication, 1981.

Lud82 E.J. Ludwig et al., private communication, 1982.

Lyn68 J.E. Lynn, The Theory of Neutron Resonance Reactions, (Clarendon Press, Oxford, 1968).

Mac68 H.D. Maccabee et al., Phys. Rev. 165 (1968) 469.

Mai77 G. Mairle et al., Nucl. Phys. A280 (1977) 97.

Mar66 J. B. Marion, Rev. Mod. Phys. 38 (1966) 660.

Mar77 R.E. Marrs et al., Phys. Rev. C16 1977) 61.

McD68 A.B. McDonald and E.G. Adelberger, Phys. Lett. 26B (1968) 380.

McD69 A.B. McDonald et al., Nucl. Phys. A137 (1969) 545.

McD76 A.B. McDonald et al., Nucl. Phys. A273 (1976) 477.

McD76a A.B. McDonald et al., Nucl. Phys. A273 (1976) 464.

McD78 A.B. McDonald et al., Phys. Rev. Lett. 40 (1978) 1692.

McP65 R. McPherson and J.C. Hardy, Can. J. Phys. 43 (1965) 1.

MDo56 W.M. MacDonald, Phys. Rev. 101 (1956) 271.

MDo60 W.M. MacDonald, in Nuclear Spectroscopy, Part B., edited by F. Ajzenberg-Selove (Academic Press, New York, 1960) p. 932.

Mic75 S. Micheletti et al., Phys. Rev. C11 (1975) 64.

Mil82 D.W. Miller et al., Phys. Rev. C26 (1982) 1793.

Moh69 R. Mohan, Ph.D. dissertation, Duke University, 1969 (unpublished), available from University Microfilms International, 300 N. Zeeb Rd., Ann Arbor, Michigan 48106.

Mor68 G.C. Morrison et al., Phys. Rev. 174 (1968) 1366.

Mor76 R. Moreh et al., Nucl. Phys. A262 (1976) 221.

Mor79 R. Moreh et al., Nucl. Instr. and Meth. 166 (1979) 45.

Mor82 R. Moreh, private communication, 1982.

Mug79 A.H.F. Muggleton, J. Phys. E12 (1979) 780.

Nan74 H. Nann and W. Benenson, Phys. Rev. C10 (1974) 1880.

Nan81 H. Nann, private communication, 1981.

Nan82 H. Nann, private communication, 1982.

Nan82a H. Nann and B.H. Wildenthal, private communication, 1982.

Nay77 H. Naylor and R. E. White, Nucl. Instr. and Meth. 144 (1977) 331.

Nel70 J.M. Nelson et al., Nucl. Phys. A156 (1970) 406.

Nel74 J.M. Nelson et al., Nucl. Phys. A218 (1974) 441.

Nel82 R.O. Nelson, private communication, 1982.

New74 H.W. Newson et al., Nucl. Instr. and Meth. 122 (1974) 99.

Nic72 R. Nicklow et al., Phys. Rev. B5 (1972) 4951.

OAK01 Oak Ridge National Laboratory, Isotope Sales Division, Post Office Box X, Oak Ridge, TN 37830.

Off75 V.C. Officer et al., Bull. Am. Phys. Soc. 20 (1975) 1169.

Ohl71 G.G. Ohlsen et al., Phys. Rev. Lett. 27 (1971) 599.

OPA01 Opamp Labs Inc., 1033 North Syacamore Avenue, Los Angeles, California 90038.

Ove69 J. C. Overley, P. D. Parker, and D. A. Bromley, Nucl. Instr. and Meth. 68 (1969) 61.

PEN01 Penn Spectra Tech., Inc., Wellingford Pennsylvania 19086.

Pen61 S. Penner, Rev. Sci. Instrum. 32 (1961) 150.

Pig74 M. Pignanelli et al., Phys. Rev. C10 (1974) 445.

Pre73 K. Preled and Th. Sluyters, Rev. Sci. Instrum. 44 (1973) 1451.

Pre75 M.A. Preston and R.K. Bhaduri, Structure of the Nucleus, (Addison-Wesley Publishing Company, Inc., Reading, Massachusetts, 1975).

Pur71 F.O. Purser, private communication, 1971.

Rad53 L.A. Radicatti, Proc. Phys. Soc. A66 (1953) 139.

Ree66 P.L. Reeder et al., Phys. Rev. 147 (1966) 781.

Rog77 D.W.O. Rogers et al., Can. J. Phys. 55 (1977) 206.

Rot74 G.W. Roth and W.G. Weitkamp, Nucl. Instr. and Meth. 115 (1974) 501.

Sal77 M. Salzmann et al., Nucl. Phys. A282 (1977) 317.

Sat80 G.R. Satchler, Introduction to Nuclear Reactions, (Wiley and Sons, New York, 1980).

Sch71 P. Schwandt et al., Nucl. Phys. A163 (1971) 432.

Sch82 P. Schwandt et al., Phys. Rev. C26 (1982) 55.

Sch74 B. Schorr, Comp. Phys. Comm. 7 (1974) 215.

Sel64 S.M. Selzer and M.J. Berger, Nucl. Sci. Series Report No. 39, Studies in Penetration of Charged Particles in Matter, NAS-NRC Publ. 1133 (1964) p. 187.

Sel69 D.L. Sellen, Ph.D. dissertation, Duke University, 1969 (unpublished), available from University Microfilms International, 300 N. Zeeb Rd., Ann Arbor, Michigan 48106.

Sex73 R.G. Sextro et al., Phys. Rev. C8 (1973) 258; R.G. Sextro, Ph.D. dissertation, University of California, 1973 (unpublished).

Sex74 R.G. Sextro et al., Nucl. Phys. A234 (1974) 130.

She75 R. Sherr and G. Bertsch, Phys. Rev. C12 (1975) 1671.

Shu67 P Shulek et al., Sov. J. Nucl. Phys. 4 (1967) 400.

Skw74 B.M. Skwiersky et al., Phys. Rev. C9 (1974) 910.

SL001 Deposit Control Master, Model OMNI-II, Sloan Technology Corporation, Santa Barbara, California 93103.

Sop69 J.M. Soper, in Isospin in Nuclear Physics, edited by D.H. Wilkinson (North-Holland Publishing Company, Amsterdam, 1969), p. 229.

SPI01 Spire Corporation, Patriots Park, Bedford Massachusetts 01730.

Ste67 N.V. Steere, Handbook of Laboratory Safety, The Chemical Rubber Company, Cleveland, Ohio (1967).

Tak66 S. Takayanagi et al., Nucl. Instr. and Meth. 45 (1966) 345.

Tak72 J. Takacs, Nucl. Instr. and Meth. 103 (1972) 587.

Tei69 B. Teitelman and G.M. Temmer, Phys. Rev. 177 (1969) 1656.

Tem81 G.M. Temmer et al., IEEE Trans. Nucl. Sci. NS-28 (1981) 1540.

Tze78 H-S. Tzeng et al., Nucl. Instr. and Meth. 150 (1978) 143.

Thi74 P. Thieberger et al., Nucl. Instr. and Meth. 122 (1974) 527.

Tho68 W.J. Thompson et al., Phys. Rev. 173 (1968) 975.

Tho79 W.J. Thompson, private communication, 1979.

Tho80 W.J. Thompson et al., Phys. Rev. Lett. 45 (1980) 703.

Tho81 W.J. Thompson, private communication, 1981.

Ton80 S.A. Tonsfeldt, Ph.D. dissertation, University of North Carolina, 1980, (unpublished), available from University Microfilms International, 300 N. Zeeb Rd., Ann Arbor, Michigan 48106.

Tow69 I.S. Towner and J.C. Hardy, Adv. Phys. 18 (1969) 401.

Tra74 T.A. Trainor et al., Phys. Rev. Lett. 33 (1974) 229.

VAR01 Nuclear Magnetic Resonance Fluxmeter, Model 5002, manufactured by Varian Radiation Division, (now Spectromagnetics a subsidiary of The Cyclotron Corporation, Berkeley California 97410).

Var82 R.L. Varner, private communication, 1982.

Vav57 P.V. Vavilov, Soviet phys.-JETP 5 (1957) 749.

VEE01 Electron Beam Gun System, Model VeB-6, Veeco Instruments Inc., Plainview, New York 11803.

Ver75 A. Vermeer and B.A. Strasters, Nucl. Instr. and Meth. 131 (1975) 213.

Vig71 B. Vignon et al., Nucl. Phys. A162 (1971) 82.

Vig74 D.A. Viggers, J. Phys. A7 (1974) 360.

Wam80 H.R. Wampfler and V. Meyer, Helv. Phys. Acta 53 (1980) 317.

Wei76 H. Weigmann et al., Phys. Rev. C14 (1976) 1328.

Wes76 C.R. Westerfeldt and W.K. Wells, private communication, 1976.

Wes77 C.R. Westerfeldt, Masters thesis, North Carolina State University 1977, (unpublished).

Wes82 C.R. Westerfeldt et al., to be published.

Wil60 D.H. Wilkinson, in Nuclear Spectroscopy, Part B., edited by F. Ajzenberg-Selove (Academic Press, New York, 1960) p. 852.

Wil69 D.H. Wilkinson, editor, Isospin in Nuclear Physics, (North-Holland Publishing Company, Amsterdam, 1969).

Wil79 J.F. Wilkerson et al., Bull. Am. Phys. Soc. 24 (1979) 818.

Wil82 J.F. Wilkerson and W.J. Thompson, T32GRD source code and documentation, (unpublished) 1982.